The Pennsylvania State University

The Graduate School

Department of Geosciences

SHALE WEATHERING ACROSS A LATITUDINAL CLIMOSEQUENCE

A Dissertation in

Geosciences

by

Ashlee Laura Denton Dere

Submitted in Partial Fulfillment
of the Requirements
for the Degree of

Doctor of Philosophy

August 2014

The dissertation of Ashlee Laura Denton Dere was reviewed and approved* by the following:

Dr. Susan L. Brantley
Distinguished Professor of Geosciences
Dissertation Co-Advisor
Chair of Committee

Dr. Timothy S. White
Senior Research Associate
Dissertation Co-Advisor

Dr. Jason Kaye
Professor of Biogeochemistry

Dr. Lee Kump
Professor of Geosciences
Head of the Department of Geosciences

*Signatures are on file in the Graduate School

ABSTRACT

The thin layer of weathered rock, or regolith, at the Earth's surface supports most terrestrial life, yet the rates and mechanisms of regolith formation are poorly quantified. Furthermore, the role of climate in controlling regolith formation is unclear, limiting our ability to predict the future availability of soil. To investigate the influence of climate on weathering rates and regolith depth, a transect of study sites across a range of climates in the northern hemisphere was established on a single lithology – iron-rich, organic-poor Silurian shale – as part of the Susquehanna Shale Hills Critical Zone Observatory, Pennsylvania, USA. Sites increase in mean annual temperature (MAT) from Wales to New York, Pennsylvania, Virginia, Tennessee, Alabama and Puerto Rico. Mean annual precipitation (MAP) is high in Wales and Puerto Rico and increases slightly from north to south through the Appalachian Mountain sites. Across these sites, ridgetop regolith depth increases with temperature from north to south (35 – 632 cm). Regolith depth on slopes, however, vary less than ridgetop sites and range from 52–86 cm across the Appalachian sites. Based on meteoric ^{10}Be inventories in the augerable regolith, soil residence times, an approximation of the weathering duration, increase from 10 ky at the northern sites to 120 ky in Puerto Rico but erosion rates remain constant within error across the climosequence (~40 m My^{-1}). Thus, climate appears to have a larger effect on the thickness and residence time of regolith on the ridgetop than on the slope.

Using Na as a proxy for plagioclase feldspar weathering, the extent of Na depletion at the soil surface (estimated using the mass transfer coefficient) increases from 20% in Wales and Pennsylvania to 100% Na depletion at the surface in Puerto Rico. These observations are consistent with a transition from kinetically-limited weathering in the north, where weathering rates are limited by mineral dissolution kinetics, to transport-limited weathering in Puerto Rico, where weathering rates are limited by the removal of weathered material. Na loss is the deepest reaction observed in the augerable regolith. Na release during plagioclase dissolution may therefore represent the chemical initiation of regolith formation as fractured bedrock is transformed to finer-grained material. The time-integrated Na release rates increase exponentially with MAT and linearly with

MAP: calculating an Arrhenius-type temperature dependence yields an apparent activation energy for feldspar dissolution across the climosequence of 115 ± 25.0 kJ mol^{-1} (excluding New York). This value is equal to the sum of the activation energy and enthalpy of the feldspar dissolution reaction, as expected for kinetically-limited sites. Presumably, if we had more sites along the climosequence, the Arrhenius plot would show a break in slope related to the decrease in apparent activation energy as transect sites are increasingly transport-limited to the south and the apparent activation energy decreases to equal the enthalpy of feldspar dissolution.

Although feldspar may initiate the chemical changes responsible for regolith formation, this mineral constitutes < 12% of the bulk shale. Mg depletion can be used as a proxy for the dissolution of the more abundant chlorite-like minerals in the shale, including vermiculite and hydroxy-interlayered vermiculite (HIV). The extent of Mg depletion at the land surface also increases toward the south but in contrast to Na, Mg is also re-precipitated in secondary clay minerals, maintaining Mg concentrations in the soil. Therefore, although the loss of Mg from regolith along the climosequence can be described with an apparent activation energy of 64.0 ± 14.4 kJ mol^{-1} (excluding New York), the calculated temperature dependence is not interpreted with respect to an activation energy of dissolution (although the value is within the range of laboratory estimates of chlorite activation energy).

New York, the only site underlain by locally-derived shale till, provides a test of the kinetic limitation of regolith formation in the north. At this site, Na release rates are faster than Pennsylvania, a site with similar MAT and MAP. Enhanced Na release in New York shows that the interpretation of kinetic limitation at the northern sites is valid, i.e., an increase in mineral surface area created by glacial grinding causes an increase in weathering rate. Thus, glaciers affect shale weathering rates by increasing mineral surface area and accelerating weathering rates for kinetically limited systems.

These observations are consistent with simple reactive transport models for weathering of rock on a convex hillslope. The regolith data can also be considered using a quantitative pedogenic energy model, i.e. the Effective Energy and Mass Transfer (EEMT) model. EEMT combines the effects of precipitation, temperature and biota as a

predictor of soil development. According to the model, the biota do not drive the observed differences in regolith depth and weathering. In fact, the variable that is the best predictor of ridgetop regolith depth or weathering extent is MAT. The effect of temperature on the weathering of feldspar and chlorite minerals is observable because variables other than climate have been held constant (e.g. erosion and lithology). Results from this investigation will inform quantitative models of soil formation and hillslope evolution as a function of climate and lithology.

TABLE OF CONTENTS

LIST OF FIGURES

LIST OF TABLES

ACKNOWLEDGEMENTS

I am grateful for the guidance and support of my advisors, Susan Brantley and Tim White. They helped shape me both as a scientist and a person, impressing upon me the importance of going forth with courage and practicing imperfection. I am thankful for the rich science discussions with Sue and for her guidance and patience. I am grateful for the many hours of time spent in the field with Tim, learning about geology and life. He also provided me with many opportunities to grow in teaching and working with undergraduate students, for which I am extremely thankful. I also thank Lee Kump and Jason Kaye for providing insightful comments on this work over the years. I also appreciate support from Rick Stehouwer who has continued to provide mentorship during my foray into the world of geosciences. I appreciate the rich experiences with colleagues in the PSU CarbonEARTH program, including the opportunity to work with Laura Warner and 4th grade students at Philipsburg Elementary School.

This work was carried out with the help of numerous individuals across the Northern Hemisphere. Brian Reynolds provided excellent mentorship and I greatly benefited from interactions with David Robinson, Inma Robinson, Simon Grant, David Norris and many others at the Centre for Ecology and Hydrology (CEH). Rich April and Di Keller at Colgate University provided a great deal of assistance and guidance in this work. I also thank Tom Miller at the University of Puerto Rico, Mayaguez, Elizabeth Knapp at Washington and Lee University, Larry McKay and Chris Fedo at the University of Tennessee and Mezemir Wagaw at Alabama A&M University.

Chapter 1

Shale Weathering in the Critical Zone

Introduction

The Critical Zone is the layer at the Earth's surface that supports most terrestrial life on Earth (Brantley et al., 2007). The thin layer of weathered regolith at the surface, commonly referred to as soil, is a central constituent of this zone. Soil serves as an interface for gas and water exchange between the atmosphere and the subsurface as well as a locus of nutrient cycling that supports ecosystems (Amundson et al., 2007). Soil is also vital to the agricultural activities that support humans and is increasingly important as human population continues to grow while arable land available for agriculture declines (Foley et al., 2005). By some estimates, a 50% increase in agricultural production by 2030 will be necessary to sustain Earth's growing population (Godfray et al., 2010).

The drastic alteration of Earth by humanity is becoming increasingly apparent (Hooke, 2000). For example, soil depletion rates resulting from human activities have been estimated to be 30 times greater than pre-human rates, effectively lowering Earth's land surface by approximately 6 cm (Wilkinson and McElroy, 2007). Soil erosion from agricultural activities alone can exceed 1 mm y^{-1}, resulting in soil loss that far outpaces soil production (Montgomery et al., 2007). At present, the ability to predict how such

changes will impact the soil resources we depend upon for food and ecosystem services is limited.

Geologists and soil scientists have long studied the slow rates of natural weathering and soil formation, yet rates of soil formation are still poorly quantified. Given the dependence of terrestrial life on the sustained production of soil, and the potential denudation of soil due to human activities, it is imperative to understand the rates at which soil forms to replace what is lost (NRC, 2004; Brantley et al., 2007). Furthermore, the role of climate in controlling soil formation rates is not well quantified. This is especially problematic as global temperatures are projected to increase 2 to 4 ℃ in the near future, along with changes in precipitation patterns (IPCC, 2013). In response to projected global climate change, many soil properties are expected to change, which may in turn affect soil production and erosion rates (Smith et al., 2013). For example, a study from 1978 – 2003 across the UK has documented a 0.6% annual loss of soil organic carbon, likely as a result of increasing temperatures accelerating carbon decomposition (Bellamy et al., 2005). Quantifying the influence of climate on weathering and soil formation is vital to effectively managing soil resources that sustain humans and ecosystems alike.

Soil formation and climate

The formation of soil can be considered in the context of a theoretical framework introduced by Dokuchaev (1883) and formalized by Jenny (1941):

$$S = f(\text{cl, o, r, p, t}) \tag{1}$$

Here, a soil property or function, S, results from various environmental factors including climate (cl), organisms (o), relief (r), parent material (p) and time (t). More recently, humans are recognized as an additional important variable (Amundson, 2004; Richter 2007). These factors ultimately influence the type of soil formed, including the depth and degree of development. Vegetation varies with climate, thus these two variables cannot be evaluated exclusively.

In general, deeper soils occur in warm, wet climates (e.g. Strakhov, 1967; Bockheim, 1980; Ruhe, 1984). For example, across the northern hemisphere in humid climates, increasing thickness of the weathered zone is expected as temperatures increase from high to low latitudes (Brady and Weil, 2008). Near the equator, weathered regolith can be up to 1000 m thick (Ollier, 1984). Moisture and temperature are the dominant climate variables controlling weathering. Temperature generally accelerates the rates of chemical and biological processes while moisture affects physical, chemical and biological processes in a soil (Jenny, 1980). Climate is often approximated as mean annual temperature (MAT) and precipitation (MAP), but such quantification fails to account for seasonal variability in temperature and precipitation. For example, moisture deficits can periodically restrict soil leaching and water-rock interactions (Rasmussen et al., 2011) or freezing temperatures, and consequently frozen water, can result in enhanced physical weathering (Anderson et al., 2012).

Regolith is often characterized as two separate layers: saprolite, where bedrock is chemically altered but retains the original structure of the bedrock, and soil, which consists of weathered material that has been subjected to pedogenic processes or biotic disturbance (Dixon and von Blanckenburg, 2012). Not all soils contain saprolite, in

which case bedrock weathers directly to soil. In the geomorphic literature, soil and saprolite are often referred to as the mobile and immobile layers, respectively; the mobile layer is soil material that can be transported downslope through erosional processes while the immobile layer is unaffected by erosional processes except in the case where the mobile layer is completely removed (i.e. by landslides) (Heimsath et al., 2001). The transition from soil to saprolite can be difficult to identify and may not be discrete, especially in deep weathering environments.

In some regimes, chemical weathering could be the initiator of regolith formation as minerals are broken down to form soil (White, 1995). Increasing temperature results in faster reaction rates while increasing precipitation delivers more dilute water that is far from equilibrium with mineral surfaces, enhancing mineral dissolution (Kump et al., 2000). Physical processes are also important in initiating weathering, increasing mineral surface area and opening new conduits for water that can enhance chemical dissolution (Stallard, 1995). Vegetation, which is inherently coupled with climate, can have a direct influence on weathering by physically breaking rocks during root growth in fractures and by enhancing chemical weathering through carbon dioxide production and the uptake of weathering products (Anderson, 1988). Conversely, the presence of vegetation stabilizes weathered material, preventing erosion and increasing the time for weathering reactions to occur (Dupré et al., 2003). Both chemical and physical weathering occur simultaneously to produce weathered regolith. Assuming a system is in steady state, the production of regolith by physical and (biogeo)chemical processes, the sum of which equals total denudation, will be balanced by erosion of material from the landscape (Riebe et al., 2004).

Numerous studies have highlighted the significance of climate on weathering rates (White and Blum, 1995; Dahlgren et al., 1997; White et al., 1999; Dessert et al., 2001; Stewart et al., 2001; Oliva et al., 2003; Williams et al., 2010). For example, White and Blum (1995) documented an exponential temperature and linear precipitation dependence of Si and Na loss from granitic watersheds across the globe. Dessert et al. (2001) concluded temperature and precipitation were dominant factors controlling basalt weathering in the Deccan Traps, India. Similarly, Williams et al. (2010) documented a temperature dependence of feldspar weathering in loess-derived soils across a latitudinal gradient along the Mississippi River Valley, USA. Egli et al. (2008) also observed that climate influenced weathering of till in the Swiss Alps, but only indirectly through vegetation.

In contrast, Rasmussen et al. (2011) identified that both climate and erosion rates influence Na loss from granitic weathering profiles. In that study, a temperature dependence was only observed when mean annual precipitation exceeded 100 cm yr^{-1}. Other researchers, however, have concluded that the effects of climate on weathering are secondary to erosion driven by tectonics (Riebe et al., 2001, 2003, 2004). For example, Riebe et al. (2001) reported that physical erosion rates correlated strongly with chemical weathering rates in granitic landscapes. In contrast, they reported only a weak correlation between chemical weathering rates and either temperature or precipitation. A compilation of global denudation rates in non-glaciated landscapes by von Blanckenburg (2005) also showed that weathering rates vary primarily with erosion rather than temperature or precipitation. Thus, while laboratory studies consistently document a strong temperature dependence of mineral dissolution, the effects of climate are not always observable under

field conditions (Kump et al., 2000). This necessitates investigating sites where all environmental variables other than climate are held constant as much as possible to isolate the influence of climate on weathering rates in the field.

Many researchers have used environmental gradients as a way to investigate weathering rates and mechanisms as a function of one of the state variables presented in Eq. 1 (White and Brantley, 1995). Such an approach attempts to minimize all variables except for the factor of interest (i.e. parent material or climate) (Birkeland, 1999). Given the inherent complexity of natural systems, it is impossible to completely eliminate variability among multiple factors. However, careful site selection can minimize variability such that the effects of one environmental parameter can be isolated and studied. Such an environmental gradient approach has been used to quantify physical erosion (e.g. Rinaldo et al., 1995; Riebe et al., 2004), pedogenic development (e.g. Chadwick et al., 1990; White et al., 1999) and geochemical fluxes (White and Blum, 1995; White et al., 2008; Rasmussen et al., 2011) across a variety of lithologies and climates. This approach can be used at multiple scales, including the laboratory, clast, pedon, watershed and global scale, providing different rates of weathering depending on the scale (Navarre-Sitchler and Brantley, 2007).

Although the relationship between deeper and more weathered soils in warmer and wetter climates has long been observed, modeling this relationship with climate has been challenging (Amundson, 2004; Minasny et al., 2008). Mathematical models of hillslope evolution are increasingly capable of integrating geochemical and geomorphic processes to model soil formation in a variety of landscapes (Gabet and Mudd, 2009; Lebedeva et al., 2007; Ferrier and Kirchner, 2008; Yoo and Mudd, 2008; Lebedeva and

Brantley, 2013). Simple reactive transport models are used to simulate weathering on a

hillslope (Lebedeva and Brantley, 2013) and fluid flux through regolith (Maher, 2010).

Recently, models include climate parameters to identify the role of climate in hillslope

weathering processes (Hilley et al., 2010; Norton et al., 2014). Such modeling efforts are

instrumental in moving toward more quantitative predictions of Critical Zone evolution,

especially the effects of climate on the landscape. However, more field-based

observations are necessary to validate and refine these models.

The temperature dependence of the weathering rate constant (k) can be quantified

using the Arrhenius equation:

$$k = A^{\frac{-Ea}{RT}} \tag{2}$$

Here, A is the pre-exponential factor, Ea is the activation energy, T is the temperature and

R is the universal gas constant. The slope of a plot of the natural log of the rate constant

as a function of inverse temperature yields the activation energy (Ea). In laboratory

studies investigating elementary reactions under controlled conditions, the activation

energy determined from such a plot represents the minimum energy required for a

reaction to proceed (Brantley and Conrad, 2008). In examining natural weathering

profiles, however, mineral dissolution reactions usually involve multiple steps and the

temperature dependence of the rate does not yield the true activation energy. For

example, the temperature dependence can include the enthalpy of a reaction (ΔH), which

describes the temperature dependence of the equilibrium constant. For such complex

reactions, the slope of the Arrhenius plot could equal the activation energy plus the

enthalpy of other steps in the reaction at equilibrium. For example, weathering model

experiments have demonstrated that for some soil systems, the temperature dependence of the albite dissolution reaction could be as large as the sum of the activation energy and the enthalpy of the dissolution reaction for weathering limited systems or equal to the enthalpy of the dissolution reaction for transport limited systems where fluids are in equilibrium with the mineral (Lebedeva et al., 2010).

In a steady state weathering profile, where the rate of regolith production is balanced by denudation, the denudation rate can be limited by dissolution kinetics or by transport of weathering products (Brantley and White, 2009). Thus, weathering regimes can be characterized as kinetically limited (sometimes referred to as the weathering-limited regime) or transport limited (Stallard and Edmond, 1983). In the case of kinetic limitation, denudation rates increase if the rate of chemical reactions increase. In this regime, denudation is affected by both the temperature dependence of the mineral rate constant (the activation energy) and by equilibrium solubility (the enthalpy of reaction) (Lebedeva et al., 2010). In the case of transport limitation, denudation is controlled by the transport of material out of the profile. Slow removal of regolith results in thick profiles where porefluids are in local equilibrium with weathering minerals. If erosive transport is increased, it can expose fresh, unweathered material to weathering fluids. Profiles weathering in the transport limited regime are affected by temperature only through the temperature dependence of the equilibrium solubility. Weathering profiles can also be characterized as occurring in the transition regime, where changes in the dissolution rate constant and the erosion rate can affect denudation. The classification of weathering profiles is useful to understand mechanisms controlling weathering fluxes and regolith thickness.

Shale weathering

Shale is of particular interest because, as the dominant sedimentary rock on Earth, it constitutes 25% of surface rock (Amiotte-Suchet et al., 2003) (Fig. 1-1). Given the large geographic extent of shale, it also serves as an important parent material for soil development. Although the chemical composition of shale can vary greatly, including organic-poor or iron-rich shales, the mineralogical composition generally includes quartz, feldspars and clay minerals, with some carbonates (Shaw and Weaver, 1965; Garrels and Mackenzie, 1972) (Fig. 1-2). Given that shale is dominated by silt and clay-sized particles, it is expected to erode quickly but weather slowly compared to crystalline rocks (Birkeland, 1974).

The majority of studies investigating shale have focused on the economically important, organic-rich ("black") shale (e.g. Littke et al., 1991; Jaffe et al., 2002; Kolowith and Berner, 2002; Peng et al., 2004; Tuttle and Breit, 2009; Woodruff et al., 2009; Mathur et al., 2012; Jin et al., 2013). In addition, field studies investigating shale weathering have often focused on outcrops without investigation of the upper soil layer (e.g. Tuttle and Breit, 2009). Organic-poor shale weathering has been investigated at the laboratory scale (Kohler et al., 2005; Liermann et al., 2011) as well as from buried shale chips (Day et al., 1980). For example, one study comparing laboratory dissolution rates of organic-rich and organic-poor shale documented higher elemental release rates from organic-rich shale than its organic-poor counterpart (Liermann et al., 2011).

Recently, however, an extensive study of the organic-poor, iron-rich shale-bearing Rose Hill Formation has been conducted in central Pennsylvania at the Susquehanna

Shale Hills Critical Zone Observatory (SSHO) (e.g. Lin, 2006; Qu and Duffy, 2007; Jin

et al., 2010; Ma et al., 2010; Andrews et al., 2011; Yesavage et al., 2012; Brantley et al.,

2013; Thomas et al., 2013). The shale mineralogy at this site is dominantly quartz (30%),

illite (61%) and 'chlorite' (6%), which includes vermiculite and hydroxy-interlayered

vermiculite (HIV), with minor iron oxides, potassium and plagioclase feldspar and

calcite. The deepest weathering reactions at this site are hypothesized to be the

dissolution of calcite and pyrite (~20 m deep), with plagioclase beginning to dissolve

around 5 m below the surface and 'chlorite' and illite weathering to vermiculite and HIV

beginning at approximately 50 cm below the soil surface (Jin et al, 2010; Brantley et al.,

2013).

The shale transect

In order to isolate the effect of climate on shale weathering, an environmental

gradient approach was used to identify sites similar to SSHO with respect to lithology

and topography but varying in climate (Dere et al., 2010). The Rose Hill Formation

underlying SSHO is geographically extensive, extending throughout the Appalachian

Mountains, with a coeval formation also present in mid-Wales, UK. Fortuitously, the site

at the Plynlimon Experimental Forest, UK, has been investigated since 1968 by the

Centre for Ecology and Hydrology (CEH), providing long-term measurements of

temperature, precipitation and solute chemistry (Neal et al., 2011) (Appendix D). In

addition to the well-established SSHO and Plynlimon sites, new sampling sites were

selected near collaborating institutions to maximize scientific engagement and facilitate

the establishment of satellite research sites to the SSHO. Additional study sites were

located in: Chadwicks, New York, USA; Whipple Dam State Park, Pennsylvania, USA;

Goshen National Wildlife Refuge, Virginia, USA; Big Ridge State Park, Tennessee,

USA; Lake Guntersville State Park and Scottsboro, Alabama, USA; and Juncal, Puerto

Rico, USA. The Rose Hill Formation is not present in Puerto Rico, however, so a site was

identified in shale of the Oligocene San Sebastian Formation.

Geographic Information Systems (GIS) software was used to identify sites similar

to SSHO with respect to lithology, aspect, topography and land use (Dere et al., 2010).

Field work was conducted at each site to confirm similarities. Initial sampling focused on

ridgetop topographic positions to represent the simplest example of soil-rock interaction

(Jin et al., 2010). Here, water is assumed to flow largely vertically through the weathering

profile until bedrock at which point lateral flow occurs. In addition, we assume no inputs

other than precipitation are added to the site (Brantley and White, 2009). The

stratigraphic location of each sampling site was carefully documented to determine the

best parent shale composition. Finally, sites were chosen so that contributions from

glacial till, colluvium or human disturbance were minimized (where possible). Although

vegetation differs across the climosequence, we assume that biota are cycling elements

near the surface (without net removal) in these stable landscapes and are therefore not

greatly influencing ridgetop regolith chemistry or thickness.

Despite the large geographic extent of this study and the inherent natural

variability of shale, initial chemical analysis of the shale across the climosequence is

quite similar (Fig. 1-3). There were some notable differences in the shale depending on

location, however. For example, shale in VA exhibits alternating fine- to coarse-grained

laminations, consistent with a depositional environment closer to the edge of the Silurain

foreland basin and far from the open ocean (Folk, 1960). Conversely, at the site in AL

that was closest to the open ocean during the Silurian, the shale matrix is very fine-

grained and lacks laminations. In addition, chert nodules are present in the shale at this

site, reflecting the accumulation of silicious biogenic skeletons in the deep-sea

depositional environment (Blatt et al., 1980).

Following previous work at the SSHO (Jin et al., 2010; Yesavage et al., 2012), the

determination of weathering rates across the climosequence was completed using

geochemical and mineralogical analyses of soil and rocks. A geochemical mass balance

approach is a common method to estimate the weathering extent over the duration of soil

formation (April et al., 1986; Brimhall and Dietrich, 1987; White, 2008; Brantley and

White, 2009; Chadwick et al., 2003). This approach compares elemental concentrations

of unweathered rock and soil relative to an immobile element not involved in weathering.

Following the estimation of the total mass of elemental loss, a weathering rate can be

determined if the weathering duration has been estimated (Brantley and White, 2009).

Elemental depletion of Na or Mg can be used as a proxy for mineral weathering reactions

such as the dissolution of feldspar (Na loss) (White and Brantley, 2003) or chlorite (Mg

loss) (Jin et al., 2010). In natural systems, however, proper identification of the original

parent composition as well as the weathering duration can be difficult.

One approach to estimating a weathering duration is the use of cosmogenic

isotopes. Meteoric cosmogenic [10]Be is delivered via precipitation to Earth's surface and

tightly binds to clay particles, where it accumulates over the lifetime of the soil

(Willenbring and von Blanckenburg, 2010). Thus, soils serve as a reservoir in which [10]Be

accumulates such that older soils have a greater inventory of ^{10}Be (Pavich et al., 1986).

Under steady state conditions, the inventory of ^{10}Be in soils can also be used to estimate

erosional fluxes on a hillslope (Jungers et al., 2009; West et al., 2013). The use of

meteoric ^{10}Be has already been effectively employed at SSHO, documenting ridgetop soil

residence times of approximately 11 ky and hillslopes that are eroding at a rate of ~26 m

My^{-1} (West et al., 2013, 2014).

Using data collected from the shale climosequence, the overall object of this

research is to quantify the extent of weathering in residual shale soils to understand how

soil depth and weathering vary as a function of climate. The overarching hypothesis of

this work is that when lithology and landscape position are held constant, climate

systematically influences shale weathering and can therefore be used to predict depth,

chemistry and formation rates of soils derived from shale.

Summary of chapters

The second chapter, *Climate dependence of feldspar weathering in shale soils*

across a latitudinal climate gradient, documents the initial characterization of the study

sites in an investigation of the influence of climate on feldspar weathering rates (Dere et

al., 2013). The experimental design of the study is outlined in detail, including the choice

of sites located on ridgetop topographic positions and underlain by the same shale parent

material. Extensive effort was expended to identify the parent material of the soils at each

site in order to effectively document elemental depletion. The dissolution of plagioclase

feldspar was chosen as the initial weathering reaction to investigate because Na is largely

contained in plagioclase and is not precipitated as secondary minerals or used as a primary nutrient by biota. Thus, the loss of Na can be used as a proxy for plagioclase weathering. Geochemical depletion profiles, which document the loss of an element relative to initial parent concentrations (Brantley and Lebedeva, 2011), were used to determine the extent of Na depletion and the weathering regimes of each site. Finally, this chapter quantifies the temperature and precipitation dependence of Na release rates by using erosion rate estimates from the literature. This chapter has been published (Dere et al., 2013) and represents a collaborative effort where the first author participated in identifying site locations and sampling as well as geochemical and mineralogical analyses and coauthors helped locate and establish study sites and provided overall geological (T. White) and geochemical insights (S. Brantley).

The third chapter investigates both weathering and erosion across the climosequence to further investigate the role of climate in landscape evolution. Both ridgetop and slope sites were sampled across the climosequence, providing regolith depth and geochemical data for the convex-up portion of the landscape. The results of ridgetop and slope weathering are compared to a simple reactive transport model for a model rock weathering on an idealized hillslope to further investigate the transition from kinetic to transport-limited weathering. In addition to Na, we also investigate the loss of Mg from the sampled profiles, which serves as a proxy for 'chlorite' weathering. Herein, 'chlorite' represents the mixture of chlorite, vermiculite and hydroxy-interlayered vermiculite (HIV) that is found in the shale bedrock. Upon weathering, Mg dissolves from 'chlorite' and some re-precipitates as secondary vermiculite and HIV, maintaining Mg concentrations in the soil. In addition, this chapter includes meteoric ^{10}Be data for the

ridgetop profiles that are used to calculate a soil residence time as well as erosion rates for each site. The ^{10}Be-based estimates of weathering duration were used to calculate new estimates of the temperature dependence of Na and Mg loss. The geochemical data included in this chapter were analyzed and interpreted by A. Dere with guidance from S. Brantley and T. White. The ^{10}Be data were measured by coauthor N. West in collaboration with E. Kirby and P. Bierman. In addition, M. Lebedeva assisted with modeling efforts.

The final chapter includes detailed characterizations of the weathering profiles across the climosequence. Specifically, the results of bulk and clay mineralogical analyses are shown in relation to soil morphology and geochemistry to allow inferences about the main weathering reactions responsible for initiating the weathering profiles. Additional characterization of soil and solute fluxes at the Plynlimon site in Wales are presented in Appendix D. In Chapters 2 and 3, climate is parameterized as mean annual temperature (MAT) and mean annual precipitation (MAP). In Ch. 3, a relatively new quantitative pedogenic energy model is tested to see if it is helpful in understanding soil development along the climosequence. Basic meteorological stations were installed at each transect site to monitor temperature, precipitation, solar radiation, wind speed and soil moisture and temperature. Data from the meteorological stations were used in the quantitative pedogenic energy model to determine the flux of energy into the system. The model, called Effective Energy and Mass Transfer (EEMT), is based on basic thermodynamic principles that relate incoming energy in the form of solar radiation to energy forms that are available to do work in the subsurface (Rasmussen et al., 2012). In short, EEMT parameterizes climate in one variable. EEMT was calculated for each

transect site and used to predict soil properties such as soil depth or the chemical depletion fraction (CDF). These results were compared to other climate variables, including MAT and MAP, to determine the best predictor of soil depth, clay content, average depth-weighted kaolinite and the CDF. Geochemical and mineralogical data included in this chapter were measured and analyzed by A. Dere with insight from R. April, T. White and S. Brantley. C. Rasmussen provided assistance with the EEMT model.

Conclusions

A transect of sites was established to investigate regolith thickness and rates of shale weathering and erosion as a function of climate. Despite the large scale of the study and difficulty of constraining variables in natural systems, the effects of climate on weathering could be observed. This experimental design allowed for the first detailed investigation of the role climate plays in controlling shale weathering and moves toward better quantification of soil formation.

Across this climosequence, the thickness of the regolith at ridgetops increase over twenty-fold from north to south with increasing temperature. The thickness of the mobile regolith (soil), defined as the layer that moves downslope along a hillside, also increases to the south along the climosequence but to a much smaller extent (12-fold increase). Total regolith depth on slopes is thinner than the total depth of ridgetop regolith. Apparently, factors controlling ridgetop thickness are more affected by climate than factors controlling slope regolith thickness. The soil residence time (SRT) is defined here

as the duration of time that a particle spends in the regolith on average during transformation from bedrock to regolith. The SRT increases linearly from north to south but erosion rates are constant across the climosequence within the uncertainties of the meteoric [10]Be inventories measured at each site. The sites in this study are considered to be at steady state with respect to ridgetop regolith thickness, i.e. the thickness of the regolith is constant in time and the production of weathered material is balanced by denudation (chemical and physical weathering).

The deepest weathering reaction observed in the regolith at these shale sites was the dissolution of plagioclase feldspar followed by the transformation of 'chlorite' and illite to vermiculite and hydroxy-interlayered vermiculite (HIV). Here 'chlorite' represents a mixture of true chlorite, vermiculite and HIV phases; these secondary minerals are present in higher concentrations at the warmest sites of the climosequence. True chlorite is only present in the bedrock and soils in Wales but has not been documented with XRD at any other site.

Using Na release rates as a proxy for feldspar weathering, we observe an exponential increase of Na release rates as a function of temperature and a linear increase as a function of precipitation and calculate an apparent activation energy of 115 ± 25.0 kJ mol^{-1} (excluding NY). This value is higher than laboratory-derived activation energies for albite dissolution but similar to field estimates of the temperature dependence of plagioclase dissolution. Feldspar weathering in Puerto Rico approaches local equilibrium, where the rate-limiting step of dissolution is the removal of weathered material. In contrast, feldspar weathering approaches kinetic limitation to the north in Wales, where dissolution is limited by the mineral reaction rate. Thus, there appears to be a transition

from kinetic limitation to increasing transport limitation of feldspar dissolution from north to south across the climosequence. The temperature dependence of Na loss is therefore likely equal to the activation energy plus the enthalpy of the plagioclase dissolution reaction across the range in sites that are kinetically limited while the temperature dependence approximates the enthalpy of plagioclase dissolution in the southernmost part of the transect near Puerto Rico. In other words, the importance of solubility equilibrium in controlling plagioclase feldspar dissolution increases toward the south.

Although New York is underlain by a different parent material (locally-derived shale till), the faster Na release rates at this site compared to the similar MAT and MAP Pennsylvania site demonstrates that the interpretation of kinetic limitation at the northern sites is valid. In New York, grinding by the glacier increased mineral surface area of the parent material. Thus, an increase in mineral weathering rates due to increased mineral surface area (as is the case in New York) or mineral dissolution rate constant across the climosequence (with increasing temperature) increases the denudation rate of the system at kinetically-limited sites.

Using Mg as a proxy for 'chlorite' weathering, Mg loss also increases from north to south across the climosequence. Contrary to Na, however, all sites retain significant Mg in the surface soils, which is often a sign that a soil is kinetic limited. However, retention of Mg at the land surface likely results from partial re-precipitation of Mg in secondary vermiculite and HIV. In fact, the content of vermiculite and HIV in weathered regolith increases from north to south, consistent with enhanced production of secondary Mg-bearing minerals toward the south. The temperature dependence of 'chlorite'

dissolution exhibited along the climosequence thus cannot be easily interpreted with respect to the 'chlorite' weathering reaction. Therefore, although the loss of Mg from regolith along the climosequence can be described with an apparent activation energy of 64.0 ± 14.4 kJ mol^{-1} (excluding New York), the calculated temperature dependence is not interpreted with respect to an activation energy of dissolution although this value is within the range of chlorite activation energies estimated in the laboratory ($40.5 - 94.3$ kJ mol^{-1}) (Ross, 1967; Lowson et al., 2007).

Results from this study can also be reviewed in the context of previously developed models. Observations of increasing transport limitation across the climosequence are roughly consistent with a simple reactive transport model of albite dissolution on a convex-up hillslope (Lebedeva and Brantley, 2013). In addition, applying a quantitative pedogenic energy model (EEMT) that combines multiple climate parameters into one term highlights the importance of quantifying the precipitation flux to the subsurface. Furthermore, biota do not appear to be driving observed differences in weathering across the climosequence. Greater EEMT is associated with enhanced chemical weathering, but ultimately temperature is the best predictor of soil properties and weathering across the climosequence. EEMT does not correlate as well with soil properties at the northern sites that were highly impacted by the last glaciation, likely due to the fact that the model ignores energy associated with freeze/thaw or snowmelt as well as changes in energy fluxes since the last glaciation, both of which are important in northern latitudes. In contrast to the conclusions of Riebe et al. (2001) who observed little effect of temperature on the extent of granite weathering across a range of climates, the effect of temperature on shale weathering was easily discerned in this study where

erosion rates were low and relatively constant and the effects of biota were maintained relatively constant.

Results from this transect are a first step toward more quantitative approaches to estimating regolith depth and weathering rates on shale. For example, a full reactive transport model could be investigated as a function of climate variables along the climosequence. The investigation of additional shale sites in the intervening landscapes (i.e. West Virginia) or replicate samples at existing sites would also strengthen the quantification of climate influence on regolith depth and weathering presented here. Furthermore, identifying sites with climates not included in this study would contribute to this dataset. The data from this study will also be integral for testing mathematical models of hillslope evolution. Ultimately, the information presented here will be useful in predicting the future availability of soil as climate changes in the future.

References

Amiotte-Suchet P., Probst J. L. and Ludwig W. (2003) Worldwide distribution of continental rock lithology: Implications for the atmospheric/soil CO_2 uptake by continental weathering and alkalinity in river transport to the oceans. *Global Biogeochem. Cyc.* DOI:10.1029/2002GB001891.

Amundson R. (2004) Soil formation. *In*: Treatise in Geochemistry (Eds.) J. I. Drever, H. D. Holland, and K. K. Turekian. Elsevier, Amsterdam. pp. 1-35.

Amundson R., Richter D. D., Humphreys G. S., Jobbagy E. G. and Gaillardet J. (2007) Coupling between biota and earth materials in the critical zone. *Elements* **3**:327-332.

Anderson D. W. (1988) The effect of parent material and soil development on nutrient cycling in temperate ecosystems. *Biogeochem.* **5**:71-97.

Anderson R. S., Anderson S. P. and Tucker G. E. (2012) Rock damage and regolith transport by frost: an example of climate modulation of the geomorphology of the critical zone. *Earth Surf. Process. Landforms* DOI:10.1002/esp.3330.

Andrews D. M., Lin H., Zhu Q., Jin L. and Brantley S. L. (2011) Hot spots and hot moments of dissolved organic carbon export and soil organic carbon storage in the Shale Hills catchment. *Vadose Zone J.* **10**:943-954.

April R. H., Hluchy M. M. and Newton R. M. (1986) Chemical weathering in two Adirondack watersheds: Past and present-day rates. *Geol. Soc. Am. Bull.* **97**:1232-1238.

Bazilevskaya E., Lebedeva M., Pavich M., Rother G., Parkinson D. Y., Cole D. and Brantley S. L. (2013) Where fast weathering creates thin regolith and slow weathering creates thick regolith. *Earth Surf. Process. Landforms* DOI:10.1002/esp.3369.

Bellamy P. H., Loveland P. J., Bradley R. I., Lark R. M. and Kirk G. J. D. (2005) Carbon losses from all soils across England and Wales 1978-2003. *Nature* **437**:245-248.

Birkeland P. W. (1974) Pedology, weathering and geomorphological research. Oxford University Press, New York. 372 p.

Birkeland P. W. (1999) Soils and Geomorphology. Oxford University Press, New York. 430 p.

Bockheim J. G. (1980) Solution and use of chronofunctions in studying soil development. *Geoderma* **24**:71-85.

Boski T. and Herbosch A. (1990) Trace elements and their relation to the mineral phases in the lateritic bauxites from southeast Guinea Bissau. Chem. *Geol*. **82**:279-297.

Brady N. C. and Weil R. R. (2008) The Nature and Properties of Soils. Pearson Prentice Hall, New Jersey. 965 p.

Brantley S. L. and Conrad C. F. (2008) Analysis of rates of geochemical reactions. *In*: (Eds.) Brantley S. L., Kubicki J. D. and White A. F. Kinetics of Water-Rock Interaction. Springer, New York. pp. 1-37.

Brantley S. L. and Lebedeva M. (2011) Learning to read the chemistry of the regolith to understand the critical zone. *Annu. Rev. Earth Plan. Sc*i. **39**:387-416.

Brantley S. L. and White A. F. (2009) Approaches to modeling weathered regolith. *Rev. Mineral. Geochem.* **70**:435-484.

Brantley S. L., Goldhaber M. B. and Ragnarsdottir K. V. (2007) Crossing disciplines and scales to understand the critical zone. *Elements* **3:**307–314.

Brantley S. L., Holleran M. E., Jin L. and Bazilevskaya E. (2013) Probing deep weathering in the Shale Hills Critical Zone Observatory, Pennsylvania (USA): the hypothesis of nested chemical reaction fronts in the subsurface. *Earth Surf. Process. Landforms* DOI:10.1002/esp.3415.

Brimhall G. H. and Dietrich W. E. (1987) Constitutive mass balance relations between chemical composition, volume, density, porosity, and strain in metasomatic hydrochemical systems: Results on weathering and pedogenesis. *Geochim. Cosmochim. Acta* **51**:567-587.

Brumsack H. J. (1980) Geochemistry of Cretaceous black shales from the Atlantic Ocean (DSDP Legs 11, 14, 36 and 41). *Chem. Geol*. **31**:1-25.

Chadwick O. A., Brimhall G. H. and Hendricks D. M. (1990) From a black to a gray box – a mass balance interpretation of pedogenesis. *Geomorph.* **3**:369-390.

Chadwick O. A., Gavenda R. T., Kelly E. F., Ziegler K., Olson C. G., Elliott W. C. and Hendrick D. M. (2003) The impact of climate on the biogeochemical functioning of volcanic soils. *Chem. Geol*. **202**:195-223.

Dahlgren R. A., Boettinger J. L., Huntington G. L. and Amundson R. G. (1997) Soil development along an elevational transect in the western Sierra Nevada, California. *Geoderma* **78**:207-236.

Day, M. J., Leigh, C., Young, V. and Young A. (1980) Weathering of rock discs in temperate and tropical soils. Z. *Geomorph. N. F*. **35**:11-15.

Dere, A. L., White T. S., April R. H., Reynolds B., Miller T. E., Knapp E. P., McKay L. D. and Brantley S. L. (2013) Climate dependence of feldspar weathering along a latitudinal gradient. *Geochim. Cosmochim. Acta*. **122**:101-126.

Dessert C., Dupré B., Francois L. M., Schott J., Gaillardet J., Chakrapani G. and Bajpai S. (2001) Erosion of Deccan Traps determined by river geochemistry: impact on the global climate and the $^{87}Sr/^{86}Sr$ ratio of seawater. *Earth Planet. Sci. Lett*. **188**:459-474.

Dixon J. L. and von Blanckenburg F. (2012) Soils as pacemakers and limiters of global silicate weathering. *Comptes Rendus Geosci*. **344**:597-609.

Dokuchaev V. V. (1883) Russian chernozems (Russkii chernozem). Israel Prog. Sci. Trans., Jerusalem, 1967. Transl. from Russian by N. Kraner. Available from U.S. Dep. Of Commerce, Springfield, Virginia.

Dupré B., Dessert C., Oliva P., Goddéris Y., Viers J., Francois L., Millot R. and Gaillardet J. (2003) Rivers, chemical weathering and Earth's Climate. *Comptes Rendus Geosci*. **335**:1141-1160.

Egli M., Mirabella A. and Sartori G. (2008) The role of climate and vegetation in weathering and clay mineral formation in late Quaternary soils of the Swiss and Italian Alps. *Geomorph.* **102**:307-324.

Ferrier K. L. and Kirchner J. W. (2008) Effects of physical erosion on chemical denudation rates: A numerical modeling study of soil-mantled hillslopes. *Earth Planet. Sci. Lett*. **272**:591-599.

Foley J. A., DeFries R., Asner G. P., Barford C., Bonan G., Carpenter S. R., Chapin F.S., Coe MT., Daily G.C., Gibbs H.K., Helkowski J.H., Holloway T., Howard E.A., Kucharik C.J., Monfreda C., Patz J.A., Prentic I.C., Ramankutty N. and Snyder P. K. (2005) Global consequences of land use. *Science* **309**:570-574.

Gabet E. J. and Mudd S. M. (2009) A theoretical model coupling chemical weathering rates with denudation rates. *Geol*. **37**:151-154.

Garrels R. M. and Mackenzie F. T. (1972) A quantitative model for the sedimentary rock cycle. *Marine Chem*. **1**:27-41.

Godfray H. C. J., Beddington J. R., Crute I. R., Haddad L., Lawrence D., Muir J. F., Pretty J., Robinson S., Thomas S. M. and Toulmin C. (2010) Food security: The challenge of feeding 9 billion people. *Science* **327**:812-818.

Heimsath A. M., Dietrich W. E., Nishizumi K. and Finkel R. C. (2001) Stochastic processes of soil production and transport: erosion rates, topographic variation and cosmogenic nuclides in the Oregon Coast Range. *Earth Surf. Process. Landforms* **26**:531-552.

Hilley G. E., Chamberlain C. P., Moon S., Porder S. and Willett S. D. (2010) Competition between erosion and reaction kinetics in controlling silicate-weathering rates. *Earth Planet. Sci. Lett.* **293**:191-199.

Hooke R. L. (2000) On the history of humans as geomorphic agents. Geology. 28:843-846.

Intergovernmental Panel on Climate Change (IPCC) (2013) Climate change 2013 The physical science basis, working group I contribution to the Fifth Assessment report of the Intergovernmental Panel on Climate Change. (Eds.) Stocker T.F. and Qin D. Cambridge University Press, New York.

Jaffe L. A., Peucker-Ehrenbrink B. and Petsch S. T. (2002) Mobility of rhenium, platinum group elements and organic carbon during black shale weathering. *Earth Planet. Sci. Lett*. **198**:339-353.

Jenny H. (1941) Factors of soil formation. McGraw Hill, New York. 281 p.

Jenny H. (1980) The soil resource, origin and behavior. Springer, New York. 377 pp.

Jin L., Mathur R., Rother G., Cole D., Bazilevskaya E., Williams J., Carone A. and Brantley S. (2013) Evolution of porosity and geochemistry in Marcellus Formation black shale during weathering. *Chem. Geol*. **356**:50-63.

Jin, L., Ravella R., Ketchum B., Heaney P. and Brantley S. L. (2010) Mineral weathering and elemental transport during hillslope evolution at the Susquehanna Shale Hills Critical Zone Observatory. *Geochim. Cosmochim. Acta*. **74**:3669-3691.

Jungers M. C., Bierman P. R., Matmon A., Nichols K., Larsen J. and Finkel R. (2009) Tracing hillslope sediment production and transport with in situ and meteoric [10]Be. *J. Geophys. Res*. DOI:10.1029/2008JF001086.

Kendall B., Creaser R. A.., Gordon G. W. and Anbar A. D. (2009) Re-Os and Mo isotope systematics of black shales from the Middle Proterozoic Velkerri and Wollogorang Formations, McArthur Basin, northern Australia. *Geochim. Cosmochim. Acta* **73**:2534-2558.

Khan M. R. (1987) Influence of weathering and low-temperature preoxidation on oil shale and coal devolatilization. *Energy & Fuels* **1**:366-376.

Kidder D. L., Krishnaswamy R. and Mapes R. H. (2003) Elemental mobility in phosphatic shales during concretion growth and implications for provenance analysis. *Chem. Geol.* **198**:335-353.

Kohler S. J., Bosbach D. and Oelkers E. H. (2005) Do clay mineral dissolution rates reach steady state? *Geochim. Cosmochim. Acta* **69**:1997-2006.

Kolowith L. C. and Berner R. A. (2002) Weathering of phosphorus in black shales. *Biogeochem. Cyc*. DOI:10.1029/2001GB001887.

Kump L. R., Brantley S. L. and Arthur M. A. (2000) Chemical weathering, atmospheric CO_2, and climate. *Annu. Rev. Earth Planet. Sci*. **28**:611-667.

Lavergren U., Astrom M. E., Falk H. and Bergback B. (2009) Metal dispersion in groundwater in an area with natural and processed black shale - Nationwide perspective and comparison with acid sulfate soils. *Applied Geochem*. **24**:359-369.

Lebedeva M. I. and Brantley S. L. (2013) Exploring geochemical controls on weathering and erosion of convex hillslopes: beyond the empirical regolith production function. *Earth Surf. Process. Landforms* **38**:1793-1807.

Lebedeva M. I., Fletcher R. C., Balashov V. N. and Brantley S. L. (2007) A reactive diffusion model describing transformation of bedrock to saprolite. *Chem. Geol*. **244**:624-645.

Lebedeva M. I., Fletcher, R. C. and Brantley, S. L. (2010) A mathematical model for steady-state regolith production at constant erosion rate. *Earth Surf. Process. Landforms* **35**: 508–524.

Lee Y. I. (2009) Geochemistry of shales of the Upper Cretaceous Hayang Group, SE Korea: Implications for provenance and source weathering at an active continental margin. *Sedimen. Geol*. **215**:1-12.

Leventhal J. S. and Hosterman J. W. (1982) Chemical and mineralogical analysis of Devonian Black-Shale samples from Martin County, Kentucky; Caroll and Washington counties, Ohio; Wise County, Virginia; and Overton County, Tennessee, U.S.A. *Chem. Geol*. **37**:239-264.

Li Y. H. and Schoonmaker J. E. (2005) Chemical composition and mineralogy of marine sediments. *In*: Sediments, Diagenesis, and Sedimentary Rocks. (Eds.) Mackenzie F.T., Holland H.D. and Turekian, K.K. Treatise on Geochemistry, vol. 7. Elsevier-Pergamon, Oxford. pp. 1–35.

Liermann L. J., Mathur R., Wasylenski L. E., Nuester J., Anbar A. D. and Brantley S. L. (2011) Extent and isotopic composition of Fe and Mo release from two Pennsylvania shales in the presence of organic ligands and bacteria. *Chem. Geol*. **281**:167-180.

Lin H. (2006) Temporal stability of soil moisture spatial pattern and subsurface preferential flow pathways in the Shale Hills Catchment. *Vadose Zone J*. **5**:317-340.

Littke, R., Klussmann U., Krooss B., and Leythaeuser D. (1991) Quantification of loss of calcite, pyrite, and organic matter due to weathering of Toarcian black shales and effects on kerogen and bitumen characteristics. *Geochim. Cosmochim. Acta* **55**:3369-3378.

Lowson R. T., Brown P. L., Josick Comarmond M. C. and Rajaratnam G. (2007) The kinetics of chlorite dissolution. *Geochim. Cosmochim. Acta*. **71**:1431-1447.

Ma L., Chabaux F., Pelt E., Blaes E., Jin L. and Brantley S. (2010) Regolith production rates calculated with uranium-series isotopes at Susquehanna/Shale Hills Critical Zone Observatory. *Earth Plan. Sc. Lett*. **297**:211-225.

Maher K. (2010) The dependence of chemical weathering rates on fluid residence time. *Earth Planet. Sci. Lett.* **294**:101-110.

Mathur R., Jin L., Prush V., Paul J., Ebersole C., Fornadel A., Williams J. Z. and Brantley S. (2012) Cu isotopes and concentrations during weathering of black shale of the Marcellus Formation, Huntingdon County, Pennsylvania (USA). *Chem. Geol*. **304**:175-184.

Minasny B., McBrantney A. B. and Salvador-Blanes S. (2008) Quantitative models for pedogenesis – A review. *Geoderma* **144**:140-157.

Montgomery D. R. (2007) Soil erosion and agricultural sustainability. *Proc. National Academies Sci.* **104**:13268-13272.

National Research Council (NRC) (2001) Basic Research Opportunities in Earth Science. National Academy Press, Washington, 154 p.

Navarre-Sitchler A. and Brantley S. L. (2007) Basalt weathering across scales. *Earth Planet. Sci. Lett.* **261**:321-334.

Neal C., Reynolds B., Norris D., Kirchner J. W., Neal M., Rowland P., Wickham H., Harman S., Armstrong L., Sleep D., Lawlor A., Woods C., Williams B., Fry M., Newton G. and Wright D. (2011) Three decades of water quality measurements from the Upper Severn experimental catchments at Plynlimon, Wales: an openly accessible data resource for research, modelling, environmental management and education. *Hydrol. Process.* DOI: 10.1002/hyp.8191.

Norton K. P., Molnar P. and Schlunegger F. (2014) The role of climate-driven chemical weathering on soil production. *Geomorph.* **204**:510-517.

Oliva P., Viers J. and Dupré B. (2003) Chemical weathering in granitic environments. *Chem. Geol.* **202**:225-256.

Patterson J. H. and Lindner A. W. (1990) Inorganic geochemistry and mineralogy of Unit B, Duaringa oil shale deposit. *Fuel* **69**:1081-1085.

Pavich M. J., Brown L., Harden J., Klein J. and Middleton R. (1986) ^{10}Be distribution in soils from Merced River terraces, California. *Geochim. Cosmochim. Acta* **50**:1727-1735.

Peng B., Song Z., Tu X., Xiao M., Wu F. and Lv H. (2004). Release of heavy metals during weathering of the Lower Cambrian Black Shales in western Hunan, China. Environ. *Geol.* **45**:1137-1147.

Qu Y. and Duffy C. J. (2007) A semidiscrete finite volume formulation for multiprocess watershed simulation. *Water Resourc. Res.* DOI:10.1029/2006WR005752.

Rasmussen C., Brantley S., Richter D., Blum A., Dixon J. and White A. F. (2011) Strong climate and tectonic control on plagioclase weathering in granitic terrain. *Earth Planet. Sc. Lett.* **301:**521-530.

Rasmussen C. (2012) Thermodynamic constraints on effective energy and mass transfer and catchment function. *Hydrol. Earth Syst. Sci.* **16**:725-739.

Richter D. D. (2007) Humanity's transformation of Earth's soil: pedology's new frontier. *Soil Sci.* **172**:957-967.

Richter D. D. and Markewitz D. (1995) How deep is soil? *BioSci.* **45**:600-609.

Riebe C. S., Kirchner J. W. and Finkel R. C. (2003) Long-term rates of chemical weathering and physical erosion from cosmogenic nuclides and geochemical mass balance. *Geochim. Cosmochim. Acta* **67**:4411-4427.

Riebe C. S., Kirchner J. W. and Finkel R. C. (2004) Erosional and climatic effects on long-term chemical weathering rates in granitic landscapes spanning diverse climate regimes. *Earth Planet. Sc. Lett.* **224**:547-562.

Riebe C. S., Kirchner J. W., Granger D. E. and Finkel R. C. (2001) Strong tectonic and weak climatic control of long-term chemical weathering rates. *Geol.* **29**:511-514.

Rinaldo A., Dietrich W. E., Rigon R., Vogel G. K. and Rodriguez-Iturbe I. (1995) Geomorphological signatures of varying climate. *Nature* **374**:632-635.

Ross G. J. (1967) Kinetics of acid dissolution of an orthochlorite mineral. *Canadian J. Chem.* **45**:3031-3034.

Ruhe R. V. (1984) Loess-derived soil of the Mississippi Valley region: II. Soil-climate system. *Soil Sci. Soc. Am. J.* **48**:864-867.

Shaw D. B. and Weaver C. E. (1965) The mineralogical composition of shales. *J. Sedimen. Petrol*. **35**:213-222.

Slack J. F., Dumoulin J. A., Schmidt J. M., Young L. E. and Rombach C. S. (2004) Paleozoic Sedimentary Rocks in the Red Dog Zn-Pb-Ag District and Vicinity, Western Brooks Range, Alaska: Provenance, Deposition, and Metallogenic Significance. *Economic Geol*. **99**:1385-1414.

Smith P., Ashmore M. R., Black H. I., Burgess P. J., Evans C. D., Quine T. A., Thomson A.M., Hicks K. and Orr H. G. (2013). The role of ecosystems and their management in regulating climate, and soil, water and air quality. *J. Applied Ecol*. **50**:812-829.

Strakhov N. M. (1967) Principles of lithogenesis, Vol. 1. Oliver and Boyd Ltd., Edinburgh, 245 p.

Stallard R. F. (1995) Relating chemical and physical erosion. *In*: Chemical Weathering Rates of Silicate Minerals (Eds.) White A.F. and Brantley S.L. Reviews in Mineralogy Vol. 31. Mineralogical Society of America, Washington, D.C. pp. 543-564.

Stewart B. W., Capo R. C. and Chadwick O. A. (2001) Effects of rainfall on weathering rate, base cation provenance, and Sr isotope composition of Hawaiian soils. *Geochim. Cosmochim. Acta* **65**:1087-1099.

Thomas E. M., Lin H., Duffy C. J., Sullivan P. L., Holmes G. H., Brantley S. L. and Jin L. (2013) Spatiotemporal patterns of water stable isotope compositions at the Shale Hills Critical Zone Observatory: Linkages to Subsurface Hydrologic Processes. *Vadose Zone J*. DOI: 10.2136/vzj2013.01.0029.

Tuttle M. L. W. and Breit G. N. (2009) Weathering of the New Albany Shale, Kentucky, USA: I. Weathering zones defined by mineralogy and major-element composition. *Appl. Geochem*. **24**:1549-1564.

Tuttle M. L. W., Breit G. N. and Goldhaber M. B. (2003) Geochemical Data from New Albany Shale, Kentucky: A Study in Metal Mobility During Weathering of Black Shales. U.S. Geological Survey, Denver, CO.

West N., Kirby E., Bierman P. and Clarke B. A. (2014) Aspect-dependent variations in regolith creep revealed by meteoric ^{10}Be. *Geol*. **6**:507-510.

West N., Kirby E., Bierman P., Slingerland R., Ma L., Brantley S. and Rood D. (2013) Regolith transport on hillslopes in the Susquehanna Shale Hills Critical Zone Observatory inferred from meteoric ^{10}Be. *J. Geophys. Res-Earth*. **118**:1877-1896.

White A. F. (1995) Chemical weathering rates of silicate minerals in soils. *In*: Chemical Weathering Rates of Silicate Minerals (Eds.) White A.F. and Brantley S.L. Reviews in Mineralogy Vol. 31. Mineralogical Society of America, Washington, D.C. pp. 407-461.

White A. F. (2008) Quantitative approaches to characterizing natural chemical weathering rates. In Kinetics of Water-Rock Interactions. S. L. Brantley, J. D. Kubicki and A. F. White (eds.) Springer, New York. pp. 469-544.

White A. F. and Blum A. E. (1995) Effects of climate on chemical weathering in watersheds. *Geochim. Cosmochim. Acta* **59**:1729-1747.

White A. F. and Brantley S. L. (1995) Chemical weathering rates of silicate minerals: An overview. *In*: Chemical Weathering Rates of Silicate Minerals (Eds.) White A.F. and

Brantley S.L. Reviews in Mineralogy Vol. 31. Mineralogical Society of America, Washington, D.C. pp. 1-22.

White A. F. and Brantley S. L. (2003) The effect of time on the weathering of silicate minerals: why do weathering rates differ in the laboratory and field? *Chem. Geol*. **202**:479-506.

White A. F., Blum A. E., Bullen T. D., Vivit D. V., Schulz M. and Fitzpatrick J. (1999) The effect of temperature on experimental and natural chemical weathering rates of granitoid rocks. *Geochim. Cosmochim. Acta* **63**:3277-3291.

White A. F., Bullen T. D., Schulz M. S., Blum A. E., Huntington T. G. and Peters N. E. (2001) Differential rates of feldspar weathering in granitic regolith. *Geochim. Cosmochim. Acta* **65**:847-869.

White A. F., Schulz B. N., Vivit D. V., Blum A., Stonestrom D. and Anderson S. P. (2008) Chemical weathering of a Marine Terrace Chronosequence, Santa Cruz, California I: interpreting the long-term controls on chemical weathering based on spatial and temporal element and mineral distributions. *Geochim. Cosmochim. Acta* **72**:36-68.

Wilkinson B. H and McElroy B. J. (2007) The impact of humans on continental erosion and sedimentation. *Geol Soc. Am. Bull*. **119**:140-156.

Williams J. Z., Bandstra J. Z., Pollard D. and Brantley S. L. (2010) The temperature dependence of feldspar dissolution determined using a coupled weathering-climate model for Holocene-aged loess soils. *Geoderma* **156**:11-19.

Willenbring J. K. and von Blanckenburg F. (2010) Meteoric cosmogenic Beryllium-10 adsorbed to river sediment and soil: Applications for Earth-surface dynamics. *Earth Sci. Rev*. **98**:105-122.

Woodruff L. G., Cannon W. F., Eberl D. D., Smith D. B., Kilburn J. E., Horton J. D., Garrett R. G. and Klassen R. A. (2009) Continental-scale patterns in geochemistry and mineralogy: Results from two transects across the United States and Canada. *Appl. Geochem*. **24**:1369-1381.

Wyborn L. A. I. and Chappell, B. W. (1982) Chemistry of the Ordovician and Silurian Greywackes of the Snowy Mountains, Southeastern Australia: An example of chemical evolution of sediments with time. *Chem. Geol*. **39**:81-92.

von Blanckenburg F. (2005) The control mechanisms of erosion and weathering at basin scale from cosmogenic nuclides in river sediment. *Earth Planet. Sci. Lett*. **237**:462-479.

Yesavage T., Fantle M. S., Vervoort J., Mathur R., Jin L., Liermann L. J. and Brantley S. L. (2012) Fe cycling in the Shale Hills Critical Zone Observatory, Pennsylvania: An analysis of biogeochemical weathering and Fe isotope fractionation. *Geochim. Cosmochim. Acta* **99**:18-38.

Yoffe O., Nathan Y., Wolfarth A., Cohen S. and Shoval S. (2002) The chemistry and mineralogy of the Negev oil shale ashes. *Fuel* **81**:1101-1117.

Yoo K. and Mudd S. M. (2008) Toward process-based modeling of geochemical soil formation across diverse landforms: A new mathematical framework. *Geoderma* **146**:248-260.
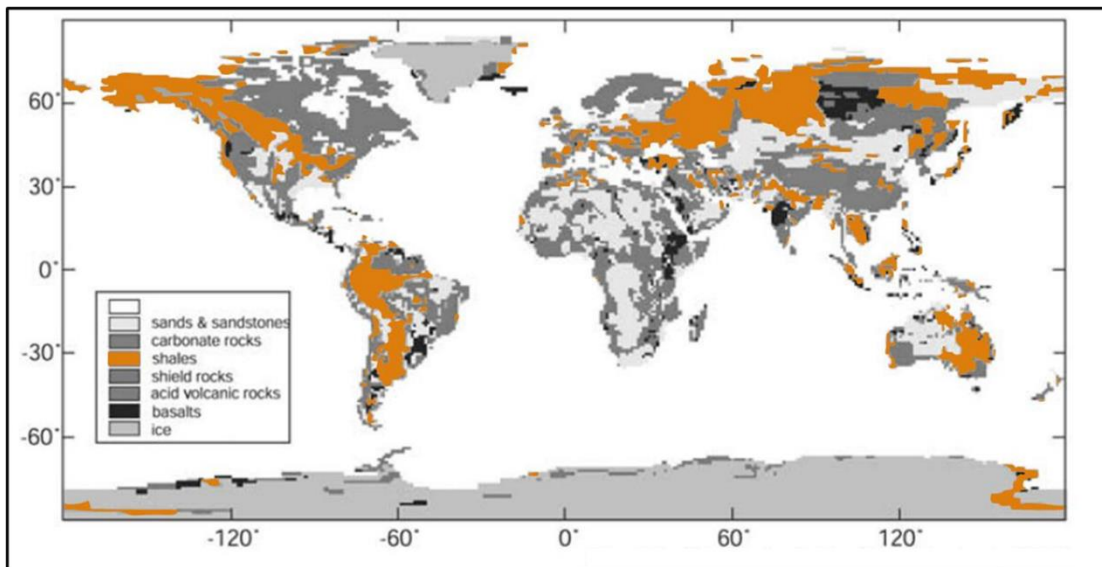
Figure 1-1. Global map of shale distribution, highlighted in orange. Modified from Amiotte-Suchét et al. (2003).
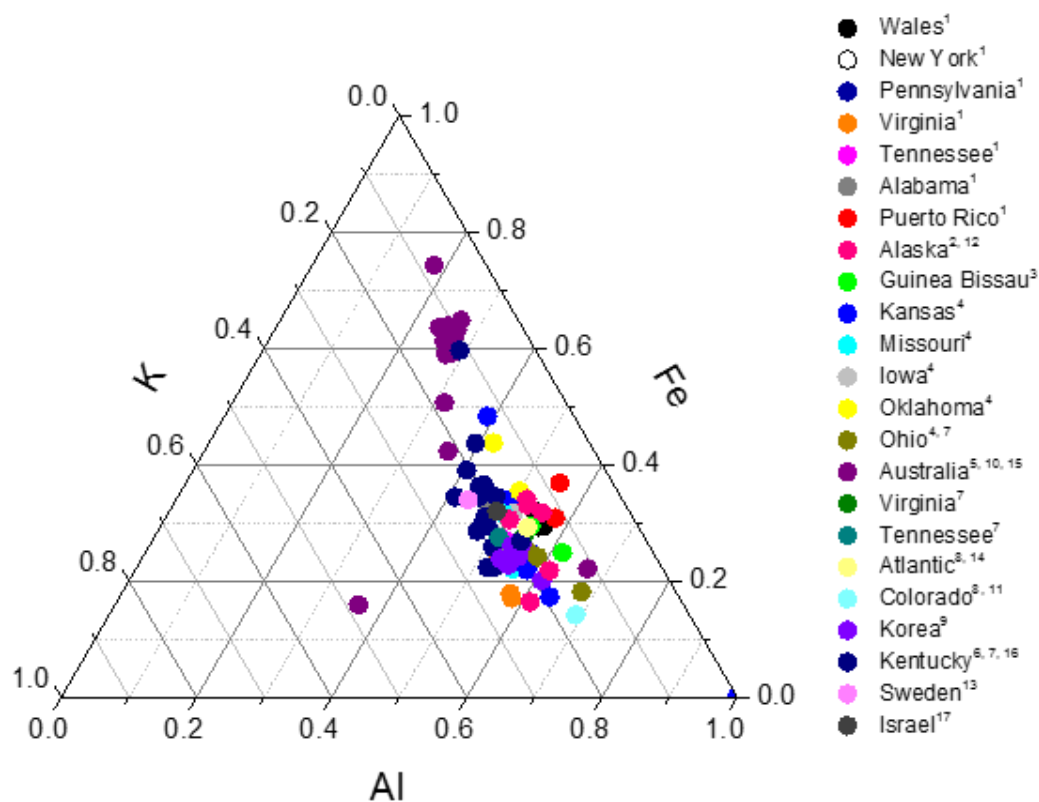
Figure 1-2. Ternary plot of Al, Fe and K shale chemistry compiled from the literature compared to data from this study. The majority of shale chemistry reported in the literature is for the "black" shale end member, but chemistry may be similar at other sites and could be compared to data from this study to expand the dataset. Data from: [1]This study; [2]Unpublished data from T. White; [3]Boski and Herbosh, 1989; [4]Kidder et al., 2003; [5]Wyborn and Chappell, 1982; [6]Tuttle et al., 2003; [7]Leventhal et al., 1982; [8]Brumsack, 1980; [9]Lee, 2009; [10]Patterson and Lindner, 1990; [11]Khan, 1987; [12]Slack et al., 2004; [13]Lavergren et al., 2009; [14]Li and Schoonmaker, 2005; [15]Kendall et al., 2009; [16]Tuttle and Breit, 2009; [17]Yoffe et al., 2002.
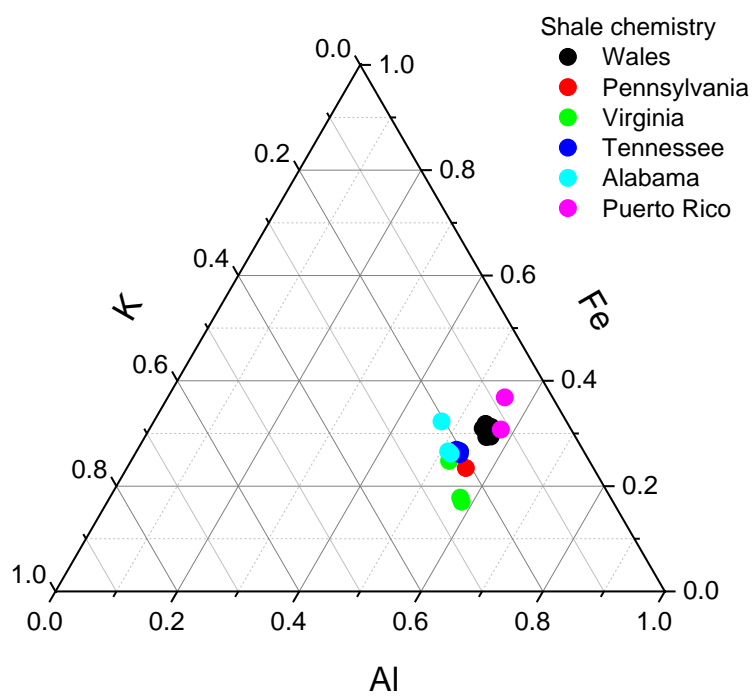
Figure 1-3. Ternary plot of Al, Fe and K shale chemistry from across the climosequence.

Chapter 2

Climate dependence of feldspar weathering in shale soils along a latitudinal gradient

Abstract

Although regolith, the mantle of physically, chemically, and biologically altered material overlying bedrock, covers much of Earth's continents, the rates and mechanisms of regolith formation are not well quantified. Without this knowledge, predictions of the availability of soil to sustain Earth's growing population are problematic. To quantify the influence of climate on regolith formation, a transect of study sites has been established on the same lithology -- Silurian shale -- along a climatic gradient in the northern hemisphere as part of the Susquehanna Shale Hills Critical Zone Observatory, Pennsylvania, USA. The climate gradient is bounded by a cold/wet end member in Wales and a warm/wet end member in Puerto Rico; in between, mean annual temperature (MAT) and mean annual precipitation (MAP) increase to the south through New York, Pennsylvania, Virginia, Tennessee and Alabama. The site in Puerto Rico does not lie on the same shale formation as the Appalachian sites but is similar in composition. Soils and rocks were sampled at geomorphologically similar ridgetop sites to compare and model shale weathering along the transect. Focusing on the low-concentration, non-nutrient element Na, we observe that the extent and depth of Na depletion is greater where mean annual temperature (MAT) and precipitation (MAP) are higher. Na depletion, a proxy for feldspar weathering, is the deepest reaction documented in the augerable soil profiles. This may therefore be the reaction that initiates the transformation of high bulk-density

bedrock to regolith of low bulk density. Based on the shale chemistry along the transect, the time-integrated Na release rate (Q_{Na}) increases exponentially as a function of MAT and linearly with MAP. NY, the only site with shale-till parent material, is characterized by a Q_{Na} that is 18 times faster than PA, an observation which is attributed to the increased surface area of minerals due to grinding of the glacier and kinetically limited weathering in the north. A calculated apparent Arrhenius-type temperature dependence across the transect (excluding NY) for the dissolution of feldspar (Na depletion) is 99 ± 15 kJ mol^{-1}, a value similar to field-measured values of the activation energy (14 to 109 kJ mol^{-1}) or laboratory-measured values of the enthalpy of the albite reaction (79.8 kJ mol^{-1}). Observations from this transect document that weathering losses of Na from Silurian shale can be understood with models of regolith formation based on chemical and physical factors such that weathering progresses from kinetically limited sites (Wales to AL) to the transport-limited site in Puerto Rico. Significant advances in our ability to predict regolith formation will be made as we apply more quantitative models to such transect studies on shales and other rocks types.

Introduction

The Critical Zone, which supports most terrestrial life on Earth, extends from the top of the vegetation canopy to the lower limits of aquifers beneath Earth's continental surfaces (National Research Council, 2001; Brantley et al., 2007). As a central constituent of this zone, soil is the interface between gas and water exchange connecting the atmosphere and aquifers and plays a major role in nutrient cycling that supports

ecosystems and humans alike (Amundson et al., 2007). The rate at which soil forms,

however, cannot be quantified from soil state factors (Amundson, 2004; Minasny et al.,

2008) even though many researchers have sought to quantify physical erosion,

pedogenesis and geochemical fluxes as a function of climate and parent material (e.g.

Chadwick et al., 1990; Rinaldo et al., 1995; White and Blum, 1995; Steefel and Lichtner,

1998; White et al., 1999; Riebe et al., 2003; Goddéris et al., 2006; Rasmussen et al.,

2007; Buss et al., 2008; Dixon et al., 2009a and b; Jin et al., 2010; Maher, 2010;

Rasmussen et al., 2011; Moore et al., 2012). Predictions of the long-term availability of

soil to sustain agriculture for Earth's growing population are problematic given this lack

of knowledge.

Shale is of particular interest because it is a common sedimentary rock at Earth's

surface, constituting approximately 25% of mapped bedrock (Amiotte-Suchet et al.,

2003) and 51% of the sedimentary lithosphere (Lerman and Wu, 2008). In addition, shale

has relatively limited diversity of mineralogy given its origin from previously weathered

materials, meaning modeling soil formation on shale may be simpler than such models

for crystalline rocks. Previous field studies of shale weathering have largely focused on

organic-rich ("black") shale weathering, a small subset of all shales (e.g. Littke et al.,

1991; Kolowith and Berner, 2002; Tuttle and Breit, 2009; Woodruff et al., 2009, Mathur

et al., 2012). Laboratory studies of shale dissolution have been performed on both

organic-poor and organic-rich shales (Liermann et al., 2011). Likewise, detailed studies

of shale weathering are under way at the Susquehanna Shale Hills Critical Zone

Observatory (SSHO) in central Pennsylvania, USA (Lin et al., 2006; Jin et al., 2010; Ma

et al., 2010; West et al., 2013). The research presented here builds upon the work at

SSHO and thus focuses on weathering of organic-poor shale along a climosequence spanning from tropical to high mid-latitude temperate regimes. In this paper we provide the first description of the soils along the climosequence to catalyze efforts to formulate quantitative models of regolith formation.

Background

The formation of soil has long been considered within the theoretical framework proposed by Jenny (1941), where observed soil properties are a function of climate, landscape position, organisms, parent material and time. The type of soil and the depth and degree of development are influenced by these five factors. Today, we recognize that the effect of biota must also include anthropogenic influences (Amundson et al., 2007; Wilkinson and McElroy, 2007; Richter, 2007). An environmental gradient approach has often been used by pedologists to isolate the influence of each variable (e.g. Bockheim, 1980; Birkeland, 1999; Williams et al., 2010). For the investigation reported here, study sites were carefully selected along a 34° latitudinal climate gradient (18°N to 52°N) primarily on Rose Hill shale within the Appalachian Mountains, holding state factors other than climate as constant as possible (discussed further below). Additional sites beyond the Appalachian Mountains include a similar shale in the tropics (Puerto Rico) and a shale in Wales, United Kingdom that is stratigraphically and geochemically equivalent to the Rose Hill Formation in the United States. Sites were chosen only in regimes where precipitation is greater than evapotranspiration and strictly from ridge top positions. All sites therefore experience net water flow into the subsurface that

approaches vertical without the complexity of downslope transport of water or sediments (Jin et al., 2010). In summary, the variables of lithology, vegetation, erosion rate and human disturbance are held relatively constant while temperature, precipitation, relief and bedrock orientation vary along the transect.

One method for determining the extent of weathering is to measure the mass loss from an observed soil profile relative to the original concentrations in unweathered rock (April et al., 1986; Brimhall and Dietrich, 1987; Brimhall et al., 1992; White et al., 1998; Brantley et al., 2008; Brantley and White, 2009; Brantley and Lebedeva, 2011). Using this approach, relative changes in the concentration of the mobile elements which are removed from the soil profile during weathering are compared to the concentration of an immobile element not involved in weathering. This approach has been used to estimate field weathering extents of the dominant crystalline rocks (granite and basalt) as well as shale (e.g. April et al., 1986; White et al., 2001; Chadwick et al., 2003; Jin et al., 2010). The method is contingent upon the proper identification of the parent material. Once the mass loss of an element has been calculated, an estimation of the duration of weathering allows determination of a weathering rate (White, 2002; Brantley and White, 2009; Brantley and Lebedeva, 2011). Depletion of an individual element can be used as a proxy for the extent of mineral reactions provided the element is found in one mineral. For example, Na loss is often attributed to feldspar weathering (White and Brantley, 2003) and Mg loss can indicate biotite, hornblende, or chlorite weathering (Luce et al., 1972; Buss et al., 2008; Jin et al., 2010). Such methods have also been used across large latitudinal gradients. For example, elemental release rates have been used to quantify the effect of climate on weathering. Most recently, Williams et al. (2010) concluded that the

apparent activation energy of albite dissolution from loess along a 12° latitudinal gradient equaled 75 ± 14 kJ mol-1 and this same transect of sites was then modeled as a function of climate parameters by Goddéris et al. (2010). Importantly, such studies of climosequences also facilitate model projections of the effect of future climate on soil and porefluid chemistry (Goddéris et al., 2013).

Methods

Site Selection

The climosequence comprises the following seven sites listed from highest to lowest latitude: Plynlimon, Wales, United Kingdom; Chadwicks, New York (NY), USA; Whipple Dam State Park and SSHO, Pennsylvania (PA), USA; Goshen National Wildlife Management Area, Virginia (VA), USA, Big Ridge State Park, Tennessee (TN), USA; Lake Guntersville State Park, Alabama (AL), USA; and Juncal, Puerto Rico (PR), USA (Fig. 2-1). These locations span 34º of latitude (Table 2-1), mostly lying within the Appalachian Mountains of the USA (Table 2-1). Soil and rock samples were collected from Whipple Dam State Park, approximately 4 km NE of SSHO in PA because the location of the sampled soil within the Rose Hill Formation was better constrained than at SSHO and therefore more easily compared to the other transect sites. We also present observations from SSHO and use it as a way to estimate error. Geographic Information Systems (GIS) software was used to locate potential sites that were subsequently evaluated by field visits. Extreme care was taken to choose sites on parent rock that

would be well constrained lithologically and geochemically as described further below. Maps were used in the field and exploratory cores were taken at each site to confirm the presence of residual shale soil profiles at ridge top geographic positions until sites with the requisite characteristics (described below) were discovered.

Mean annual temperature (MAT) and mean annual precipitation (MAP) were estimated for each site using data from proximal weather stations at similar elevations with at least 20 y of complete records (NOAA, 2011). Monthly averages of temperature and precipitation were obtained from the weather stations and averaged for all years, excluding any years where monthly data were incomplete. See Appendix A for more details.

The variability of parent material bedrock composition (Figure 2-2) was minimized by choosing sites located on Silurian iron-rich, organic-poor Clinton Group shale, known as the Rose Hill Formation in NY (Gillette, 1947), PA (Folk, 1960) and VA (Kozak, 1965), the Rockwood Formation in TN (Finlayson, 1964), the Red Mountain Formation in AL (Sanford, 1966), and the Gwestyn Formation in Wales (British Geological Survey, 2005). In PR, the Oligocene San Sebastian Formation (Tobish and Turner, 1971) was identified as the most geochemically similar formation in PR to the Rose Hill Formation.

The stratigraphic position within the formation was also considered; i.e., stratigraphic sections of local outcrops in NY, PA, VA, TN and AL were mapped to measure local variability in texture and chemistry. A detailed geochemical characterization in central PA (not presented here) showed less geochemical variability in the lower part of the Rose Hill formation compared to higher strata (unpub. data). Thus,

sampling was accomplished in the basal 10 m of the Rose Hill Formation wherever possible.

As discussed in detail below, the soils in our study have estimated soil residence times (SRT) of less than 250 ka. The maximum SRT we estimate is for the PR site (250 ka) where the largest climate transition occurred from marine isotope stage (MIS) 5 to the Last Glacial Maximum (LGM) (~ 5°C) (Imbrie et al., 1984). The other soils have an estimated SRT less than 100 ka. Over that time period, the largest climate change in North America occurred during the transition from the Last Glacial Maximum (LGM) to the present (Cadwell et al., 2004; Clark et al., 2004). The LGM directly impacted Wales and NY by glaciation, while PA was subjected to periglacial conditions until at least 15 ka (Ciolkosz et al., 1986; Clark and Ciolkosz, 1988; Gardner et al., 1991). Previous researchers have also found periglacial features present in VA and the Great Smoky Mountains in TN (King and Ferguson, 1960; Clark and Ciolkosz, 1988), but we did not observe these features at our sites. Although till is prevalent in other localities in Wales, at our site a residual shale soil that was developed on bedrock was investigated. It is well known that thickness of till can vary significantly over a small spatial scale (Stephenson et al., 1988). In contrast, no till-free residual soil was found in NY despite a significant search; instead, the NY regolith developed on a parent material that consisted of locally-derived shale till and therefore will be treated separately in the following discussion.

In this study, we defined regolith operationally as the material that can be augered by hand either from the land surface or from a soil pit; everything below what we can manually auger is considered "bedrock". The regolith in the northern part of the transect is comprised of soil which sits on rock without intervening saprolite (Wales, PA).

Regolith in NY is soil developed from till. In VA, soil developed from shale that extends right into the weathered sandstone layer below. Regolith in the southern part of the transect consists of soils overlying saprolite (TN, AL, PR), and the base of saprolite in some localities had rock fragments. Our augering did not penetrate into saprock or fresh bedrock beneath the saprolite at the southern sites. At SSHO, Jin et al. (2011) argued that fresh bedrock was only encountered at depths of 26 m and that an intervening layer of "saprock" was found between fresh bedrock and soil.

The soil residence time (SRT) was defined as the duration of time particles spent in this augerable layer. In the two sites north of the extent of the furthest advance of the LGM (Wales and NY), SRT was estimated based on the time since deglaciation (see discussion below). For the other sites, the observed soil thickness (L) was used to calculate SRT from the erosion rate (E) for each ridgetop soil:

$$SRT = \frac{L}{E} \tag{1}$$

Erosion rates in PA on the Rose Hill shale in the SSHO have been well constrained by [10]Be studies at 17 ± 6 m My^{-1} (West et al., 2013). South of PA along the Appalachians, erosion rates have not been measured precisely at our study sites but are estimated to range from $8 - 26$ m My^{-1} across numerous lithologies (including shale), provinces and elevations (Portenga and Bierman, 2011; Appendix A). For all calculations, we therefore assumed the erosion rate at the non-Pennsylvania Appalachian study sites equal 17 ± 9 m My^{-1}. Implications of potential variations in this erosion rate are explored in the Discussion section.

We know of no measured erosion rates on shale in Puerto Rico. However, erosion rates of 43 m My^{-1} have been measured on quartz diorite in the Luquillo Forest of PR (elevation 700 m, MAP 430 cm) (Brown et al., 1995). Given the significantly greater relief and rainfall in the Luquillo Mountains compared to the transect site (elevation 366 m, MAP 250 cm), the erosion rate is expected to be slower for the shale in PR, but faster than the shale in Appalachia. Therefore, an erosion rate of 25 m My^{-1} was assumed as the midpoint value within a possible range from 8 - 43 m My^{-1} (Portenga and Bierman, 2011) for PR.

The use of Eq. (1) is equivalent to the assumption that the soil production rate and erosion rate are equal. This assumption has been shown to be true within error at SSHO where soil production and erosion rates have both been measured (Ma et al., 2010 and 2013; West et al., 2013). Furthermore, it has been argued that the Southern Appalachian Mountains have been eroding at a similar rate for the past $10^2 – 10^8$ yr (Matmon et al., 2003). This long period of denudation and lack of rapid uplift lead to the inference that soil production rates equal erosion rates. The assumption that erosion rate is equal to soil production rate was also shown to be reasonable for a soil in Puerto Rico, albeit developed on a different lithology (Chabaux et al., 2013). These assumptions are discussed and explored more extensively in the Discussion section.

Although we recognize the impossibility of isolating biota across a climosequence, we chose forested sites to minimize biotic variability. Vegetation along the Appalachian Mountain portion of the transect remains fairly constant with a canopy of temperate hardwood species, while Wales largely supports Sitka Spruce plantations and Puerto Rico has tropical species. In NY, tree species include Spruce, White Pine,

American Beech and Striped and Red Maple. Tree species in PA are dominantly oak, with hickory and Virginia Pine. The site in VA is dominated by Chestnut Oak and hickory, with an understory of Mountain Laurel and Sugar Maple. Maple, beech, oak and Pawpaw are all common tree species observed in TN. The site in AL has Pitch Pine, White Oak and hickory trees as well as Sweetgum, Hornbeam and Persimmon. Vegetation in Puerto Rico largely includes banana plants and palm trees.

While sampling sites are presently undisturbed and forested, the Appalachian Mountains have been deforested at least two to three times over the last 300 years (Walter and Merritts, 2008). At the Wales site, spruce trees are intensively managed for timber production and the most recent harvesting occurred ~40 years ago. In the SSHO, the forest was cleared during colonial times. The site in Puerto Rico was once a farm but has been fallow for 40 years and trees are now cut only as needed to manage the land.

Rock and soil sampling

Rock samples were collected from bedrock exposed at the bottom of hand-dug soil pits or from outcrops proximal to soil sampling sites (Table 2-2). We measured exposed geologic sections and sampled at one meter intervals for geochemical analyses. Outcrop rock samples from these sections were collected from the base through lowermost 40 – 50 cm of the Rose Hill Formation in NY (n = 36), VA (n = 47), TN (n = 68) and AL (n = 43). A drill core from SSHO was used to constrain shale variability, but due to the uncertainty in the stratigraphic position of SSHO, a rock sample from the bottom of our sampled site at Whipple Dam was used as parent material. Rock samples

collected in Puerto Rico include shale from nearby road cuts and stream beds (n = 21). At

each outcrop, we used a Jacob's staff and an Abney Level to measure off the top of the

Tuscarora Sandstone, a prominent stratigraphic marker and resistant landscape element,

to estimate the location of soil pits within the stratigraphy of the Rose Hill Shale.

Appendix A summarizes detailed rock sampling locations.

Soil samples were collected using a 5 cm diameter hand auger from the mineral

soil surface to the depth of refusal, where auger penetration ceased. Soils were sampled

every 5 cm in the upper 20 cm of the soil and every 10 cm below 20 cm. The organic

horizon was collected separately by hand before augering and the interface between the

organic and mineral horizon was defined as 0 cm. Each sample was placed in a

resealable plastic bag for storage. In addition to hand augering, soil pits were hand dug as

deeply as possible (maximum depth of 2 m) and described (Soil Survey Staff, 1993).

Augering was completed at each site to the deepest depth possible.

Soil bulk density

Soil bulk density (ρ_b, g cm^{-3}) was measured at several soil depths at each site by

driving a sampler of known volume laterally into soil pit walls. Samples were dried at

105 °C and then weighed and bulk density was calculated using the known volume and

dry mass of the sample (Grossman and Reinsch, 2002). Bulk density versus depth data

were then fit to the following equation:

$$\rho_b = \rho_b^0 + \frac{(\rho_b^{max} - \rho_b^0)Kz}{1 + Kz} \qquad (2)$$

Here, ρ_b^0 is the bulk density at depth z = 0 and ρ_b^{max} is the maximum bulk density achieved at depth. K is an empirical fit parameter. To determine K, ρ_b^0 and ρ_b^{max}, transect data were plotted along with data for proximal soils obtained from the Natural Resource Conservation Service (NRCS) soils database (Soil Survey Staff, 2012) and were fit to Eq. (2). Fit parameters for each site are listed in Table 2-1. Example fits are shown in the Supplementary Material.

Soil and rock chemistry

Bedrock samples were ground in the laboratory with a ceramic mortar and pestle and the entire ground sample was passed through a 100-mesh sieve (< 150 μm). Bulk soil samples (including all particle size fractions) were air dried, homogenized by mixing in the plastic bag, and split four times using a riffle soil splitter. One of the four splits was ground to < 150 μm. For both rocks and bulk soils, 100 mg of ground sub-sample were fused with 1 g of lithium metaborate at 950 °C for 10 minutes and then dissolved in 5% nitric acid for thirty minutes (Medlin et al., 1969). Major elements were analyzed on the solutions by inductively coupled plasma atomic emission spectroscopy (ICP-AES) (Perkin-Elmer Optima 5300DV ICP-AES, Waltham, MA), with an estimated analytical error of ± 3% for each element, at the Materials Characterization Laboratory at Penn State University (MCL).

Soil samples from NY were analyzed using the < 2 mm fraction to avoid the inclusion of minor fragments of Adirondack Mountains-derived gneiss in the till. Elemental concentrations for the NY samples were obtained using a Phillips PW2404 X-

ray Fluorescence Spectrometer (PANalytical, Almelo, The Netherlands) at Colgate

University, Hamilton, NY.

Loss on ignition (LOI) was measured by heating to 750 °C overnight followed by

heating to 900 °C for three hours the following morning. The ash was cooled, weighed

and weight loss was calculated. For some samples, LOI was calculated by subtracting

total oxides from 100. See Appendix A for data obtained by these two common LOI

methods.

Mineralogy

Selected samples from each site were analyzed using x-ray diffraction (XRD) on

ground bulk soil samples (< 150 μm) randomly mounted onto a metal holder by a side

loading technique (Whittig and Allardice, 1986). A Scintag PAD-V powder x-ray

diffractometer (Scintag, Inc. (currently Thermo Scientific), Cupertino, CA) with Cu-Kα

radiation ($\gamma = 1.54178$ Å) and a Ge solid state detector was used at 35 kV voltage and 30

mA current to scan samples from 2° to 70° 2θ and collect diffraction patterns using a step

size of 0.020° 2θ at 1° 2θ per minute. Peak patterns were analyzed using JADE software,

which displays patterns generated by XRD analysis and matches these patterns to a

mineral database. Samples were prepared for quantitative mineral analysis by adding 0.25

g corundum standard to 1 g of ground sample and micromilling with ethanol in a

McCrone mill (Eberl, 2003). After drying, samples were shaken with Vertrel, sieved,

then mounted on a side loading sample holder to maximize random orientation of

minerals. Following XRD analysis as described above, mineral abundances were

quantified using the USGS RockJock program that uses the added corundum standard to quantify mineral abundances (Eberl, 2003).

Thin sections were prepared perpendicular to bedding for select rock samples by Spectrum Petrographics (Vancouver, WA) and observed under a petrographic microscope.

Results

Parent composition

Rock samples collected from outcrops and the bottom of pits across the climosequence are geochemically similar (Fig. 2-2). Of the major elements, Ca, Al and Si (Table 2-2) showed significant variability, most notably at the PR site. Across the transect, Ca occurs at <1 wt. % in most samples but up to 20 wt. % in PR samples. Overall, the composition of the shale in PR differs to the greatest extent from the other sites, as expected given its younger age and different depositional history. However, given the large geographic extent of this study and the inherent variability of shale composition, we have minimized geochemical variability as much as possible.

Thin sections of select shale samples from VA display alternating fine- to coarse-grained laminations. Such textures are expected in VA where deposition in the Silurian foreland basin was farthest from the open ocean (Folk, 1960). Less distinct fine laminae were observed in TN and a very fine-grained matrix lacking distinct laminations was observed in shale from AL, the site which had been closest to the open Silurian ocean.

AL is the only site where chert nodules are present in the shale and the soil, also reflecting the deep-sea depositional environment where silicious biogenic skeletons accumulated (Blatt et al., 1980).

Bedding angles vary along the transect with gently dipping beds in Wales, NY, AL and PR, and more steeply dipping beds in PA, VA and TN (Table 2-2). One site was somewhat anomalous. Specifically, the bedding of the shale formation at the VA site has the steepest dip. In addition, the formation at that point has the thinnest exposure of Rose Hill shale observed for any of the sites in our study. As discussed further below, the thin shale was entirely weathered down to the underlying sandstone, truncating the soil profile.

Shale rock fragments were observed in the bottom of soil pits in Wales and PA and the soil core in TN. In VA, the bottom of the profile was truncated by the underlying sandstone layer – i.e., weathering had extended completely through the shale layer – and no shale fragments were recovered. No shale rock fragments were observed at the bottom of augered holes in AL and PR.

In Wales and PA, these rock fragments (samples PlynQ-RF and ALD-10-158, respectively) are chemically similar to rocks from outcrops, which in conjunction with physical observations from soil pits dug to bedrock, confirm that augerable depth (L) is congruent with the depth to parent material at these sites. In TN, however, small, soft shale chips recovered from the bottom of the soil core where augering became impossible were chemically distinct from the shale bedrock samples: specifically, Na, Ca and Mg were depleted while Si and Al were not (Table 2-2, sample ALD-10-432).

Extreme care was used in defining protolith chemistry, given the known heterogeneity of shale compositions depending upon depositional environment. Rock samples used as parent (Table 2-2) were chosen based on stratigraphic observations from nearby outcrops and measurement of soil sampling locations within the formation. In Wales, the choice for parent includes all rock samples collected at the site and one rock sample collected from the bottom of the soil pit. Parent in PA was determined from a rock at the bottom of the soil pit. In VA, TN and AL, stratigraphic sections of local outcrops were measured and strata were correlated to soil sampling locations to identify which part of the formation was the parent for the soil we sampled. For PR, parent was defined as two rock samples collected in close proximity to the soil sampling site. The variability in parent composition was estimated as the standard deviation around the mean of the bedrock samples used as parent at each of the sites (Table 2-2). In PA, variability was estimated from the rock sample collected at Whipple Dam and a drill core from SSHO (Jin et al., 2010).

Soil depth

Significant effort was expended to choose sites where we could sample all the way to shale bedrock; however, several problems plagued our site choice given the constraints of local geology as well as land use. Nonetheless, total augerable soil depth (i.e. including augering at the base of soil pits) was observed to generally increase from north to south from roughly 30 cm in Wales and PA to 632 cm in PR (Fig. 2-3a, b).

In Wales and PA, augering was possible through 35 and 28 cm, respectively, of soil. Although unaugerable, the underlying parent material consisted of approximately 5 to 20 cm of highly fragmented shale that was observed at the bottom of soil pits in Wales and PA, respectively, and this material was observed in turn to lie above less fractured shale. In contrast, weathering in VA was observed to have proceeded through the entire steeply dipping Rose Hill Shale unit (80 cm) and 20 cm into the underlying Tuscarora Sandstone. In addition, remnants of overlying sandstone units that had been almost entirely weathered away were observed to still remain in the shale soil. In TN, the depth of refusal for the deepest augered core was 398 cm. Given that the shale chips recovered from that depth were weathered, and augering is difficult in clay-rich soils beneath several meters depth, the augering likely had not reached parent material in that location. Likewise, augerable soil depth in AL was 220 cm, but the abundance of chert nodules limited the augering. Therefore the augerable depth in VA (weathered all the way through the shale layer to the underlying sandstone), TN (bottom-most rock fragments depleted with respect to parent composition) and AL (chert nodules precluded deeper augering) are considered minima, represented by the upward arrows in Fig. 2-3a.

Along most of the sites, we did not auger multiple cores. To assess within-site variability of augerable soil depth for Wales and PR, we assumed that the variability of 22 ridgetop cores in PA at the SSHO CZO, 34 ± 15 cm (Jin et al., 2010; Herndon et al., 2011), was a good approximation of variability. Using this estimate of relative error (44%), variability is smaller than the symbol size for Wales and PA in Fig. 2-3a.

The till present in NY represents a substantially different parent material from all other sites and accordingly has an augerable soil depth that greatly exceeds that of

similar-latitude transect sites (Table 2-1). Given the difference in parent material, NY is treated separately from the rest of the transect in the following discussion.

Discussion

Soil depth and residence time

Across the transect, MAT varies relatively consistently from north to south. Of these sites, however, two are extremely wet (Wales and PR, MAP ~ 240 cm yr^{-1}) whereas the five others are only moderately wet (NY, PA, VA, TN, AL, 100 cm < MAP < 140 cm).

The soils increase in L from north to south across the transect (Fig. 2-3a), consistent with many findings in the literature that soils formed in warm, wet climates tend to be deeper than those in cold climates (Strakhov, 1967; Bockheim, 1980; Ruhe, 1984). A least squares regression line (not shown) fit to the soil depth data does not fit all the depth estimates within error because Wales and PA have similar soil depths while the minimum soil depths estimated for the more southern soils are significantly thicker. In fact, the observed values of L versus MAT in Fig. 2-3a require a sigmoidal curve to incorporate all observations. Some of this sigmoidal variation is likely due to the fact that both MAT and MAP vary along the transect. In addition, as discussed later, the rate-limiting step of feldspar weathering likely changes from mineral reaction-limited in the north to transport-limited in the south (see Discussion).

As expected since erosion rates do not vary to great extent along the transect as discussed above, soil residence times show a similar trend to that of depth with respect to MAT (Fig. 2-3c). Error bars in Fig. 3c include maximum and minimum estimates of SRT based on the range of erosion rates in the literature summarized in Table 2-1 and Appendix A. The SRT was set to the time since deglaciation in Wales and NY (Cadwell et al., 2004; Clark et al., 2004). Likewise, detailed [10]Be studies at SSHO in PA have constrained erosion rates between 11 and 23 m My^{-1}, used in the calculations as 17 ± 6 m My^{-1} (West et al., 2013). For all sites in the Appalachians south of PA, a constant erosion rate of 17 ± 9 m My^{-1} was used for calculations of SRT and plotted in the figure assuming those error bars, but the values of both L and SRT are minima due to various issues described above. In PR, where we were only able to constrain E to within $8 - 43$ m My^{-1}, the data point and error bars were calculated assuming $E = 25 \pm 17$ m My^{-1}.

Na depletion profiles

A previous study of weathering of the Rose Hill Formation near the transect site in PA reported Na as largely present in plagioclase feldspar (Jin et al., 2010). The observed loss of Na across the transect was therefore attributed to dissolution of plagioclase:

$$2NaAlSi_3O_8 + 2H_2CO_{3\,(aq)} + 9H_2O \rightarrow Al_2Si_2O_5(OH)_4 + 2Na^+ + 2HCO_3^- + 4H_4SO_4 \quad (3)$$

XRD analyses of shale from across the transect confirm the presence of plagioclase feldspar in the parent material (Table 2-3). Quantitative mineral estimates often have uncertainties of up to 2-3% arising from factors such as variability in mineral

composition, degree of crystallinity and preferred orientation, especially when attempting to quantify low-abundance mineral phases (Jenkins and Snyder, 1996; Hillier, 2000; Ferrier et al., 2010). Calculations of the plagioclase content based on bulk Na, however, shows similar quantities of plagioclase as those obtained from the quantitative powder XRD analyses (Table 2-3). Furthermore, Na is not taken up to a large extent by biota or precipitated in authigenic minerals and no other Na-bearing minerals were identified. Therefore even with uncertainties associated with quantitative XRD, the Na loss is assumed to be from plagioclase dissolution.

To quantify the loss of Na, we normalized its concentration using an immobile element to account for changes in concentrations of other elements. Both Ti and Zr were tested as possible immobile elements by calculating $\tau_{i,j}$ with j = Ti and i = Zr and vice versa (see Eq. 5) (Brimhall and Dietrich, 1987; Chadwick et al., 1990). At northern sites, including Wales, PA and VA, both Ti and Zr appear equally immobile for data in Table 2-4. However, Jin et al. (2010) concluded that Zr was less mobile than Ti in PA where highly resistant zircons were observed in bedrock and soils. Although no scanning electron microscopy (SEM) analysis was completed on other soils to confirm, we expect zircons are also present in soils and bedrock at the other sites. Consistent with Zr as the more immobile element, Ti was observed to be slightly mobile in TN and highly mobile in AL (Table 2-4). The high mobility of Ti observed in AL, and to a lesser extent in PA (Jin et al., 2010) and TN, is likely the result of colloidal transport of clays that contain Ti and not Zr (Bern et al., 2011; Bern and White, 2011) or Fe-Al-Si-Ti particles (Yesavage et al., 2012). Consistent with such mobility, the Ti enrichments at depth observed in AL and PR can be attributed to the accumulation of Ti-bearing particles at depth rather than

Zr mobility (Table 2-4) (Bern et al, 2011). Given these observations and other studies

reporting higher Ti mobility compared to Zr in some lithologies (Gardner, 1980; Cornu et

al., 1999; Neaman et al., 2006), Zr is the best choice of immobile element for this

transect.

Strain (ε_i) was also calculated for each soil profile (Brimhall et al., 1992):

$$\varepsilon_i = \frac{\rho_p}{\rho_w} \frac{C_{i,p}}{C_{i,w}} - 1 \tag{4}$$

Here, ρ_p and ρ_w are the bulk density of the parent (p) and weathered soil (w), respectively.

Strain values greater than 0 indicate expansion relative to initial rock volume and values

less than zero indicate soils have collapsed. Soil profiles across the transect generally

exhibit strain values greater than one consistent with significant expansion, i.e., addition

of air and plant and organic matter into soil.

Relative depletion of Na from transect soils was assessed by calculating the mass

transfer coefficient:

$$\tau_{i,j} = \frac{C_{j,w}}{C_{j,p}} \frac{C_{i,p}}{C_{i,w}} - 1 \tag{5}$$

Here, τ is a dimensionless coefficient representing the ratio of the concentration, C, of an

element of interest (j) relative to an immobile element (i) in the weathered soil (w) and

the parent (p) (Brimhall and Dietrich, 1987; Anderson et al., 2002). When $\tau = 0$, element j

is neither enriched nor depleted with respect to element j in the parent; when $\tau < 0$, the

element has been lost relative to immobile element i in parent and $\tau > 0$ indicates the

element has been added to the profile relative to parent (Brantley and White, 2009).

One problem arose when we used Zr as the immobile element in VA where the

soil is truncated by sandstone at 80 cm depth. The Rose Hill Shale at this latitude is thin,

coarse and contains sandstone interbeds, as observed in outcrop. At that site, Zr

concentrations throughout the entire soil profile are 3 – 5 times greater than Zr

concentrations in the parent shale (Tables 2-2, 2-4). The high Zr concentrations in the soil

resemble Zr concentrations measured in sandstone collected 25 cm below the shale soil

(800 ppm) and two outcrop sandstone samples collected stratigraphically above and

below the parent shale (679 and 881 ppm, respectively) (Table 2-2). Therefore, we

concluded that the high Zr concentrations in the soil are residuals from the overlying

sandstone formation, i.e. overlying sandstone units were weathered, leaving behind

zircon-rich material that was incorporated into the shale soil. Supporting this conclusion,

the soil Zr concentrations are more variable with depth than any of the other transect

soils. Given that we could not use Zr as the immobile element for the VA soil, we relied

on corrected Ti concentrations in the soil as the immobile element. To correct the values

to account for Ti mobility, we assumed similar proportions of Ti were lost from the upper

80 cm of the VA core as were observed in the upper 80 cm of TN (Table 2-4):

$$[Ti]_{VA,corr} = [Ti]_{VA,actual} + \left(\tau_{Zr,Ti}^{TN} * [Ti]_{VA,actual} \right) \tag{6}$$

$[Ti]_{VA,corr}$ (wt %) was used as a proxy for Zr as the immobile element in VA for all

subsequent calculations. Such a Ti correction was also used successfully for a few

profiles by Jin et al. (2010) for Rose Hill shale in PA.

Plots of $\tau_{Zr,Na}$ show increasing loss of Na at the surface (increasingly negative

values of $\tau_{Zr,Na}$) with increasingly warmer and wetter climates (Fig. 2-4). The value of

$\tau_{Zr,Na}$ at the soil surface (z = 0) documents the greatest extent of depletion for a ridgetop

soil. However, this value is sometimes affected by dust deposition or bioturbation

(Williams et al., 2010). A better approximation of the greatest extent of Na depletion for

each soil can be attained by extrapolating linearly to the surface as shown by the dashed lines in Fig. 2-4; values of Na loss at the land surface across the transect vary from approximately 10 - 20% in Wales and PA, 70% in VA, 80% in TN, 95% in AL and 100% in PR. Na depletion profiles from Wales, PA, VA, TN and AL are not 100% Na-depleted at the land surface and are thus termed incompletely developed profiles whereas the soil in PR is 100% depleted and is termed a completely developed profile (Brantley and White, 2009).

Fig. 2-4 also shows that the depth of return to parent composition (L_{parent}) is generally deeper in warmer, wetter soils than cooler, drier soils. Profiles from VA, TN and AL, however, do not return to parent composition at the point of refusal of hand-augering (L does not equal L_{parent}). To determine L_{parent} accurately would have required drilling in the southern profiles and we were unable to do this. The point of refusal is shown on Fig. 2-4 as the deepest solid symbol for each site. For those sites where the deepest augered sample did not show a composition within error of the parent, an approximation of the depth of parent is shown with an open symbol. In effect, the open symbols on the figure represent our best estimate or model of the depth of weathering at each site, constrained as described in the next paragraph.

Estimated values of L_{parent} were chosen by assuming that the profiles would describe sigmoidal concentration-depth profiles (Brantley et al., 2008) while simultaneously being consistent with constraints based on the depths reported in Fig. 2-3a which are based on our field observations. The sigmoids are shown on the figure as dashed lines. The depth interval across which τ varies from -1 to 0 (i.e. the bottom of a completely developed profile) or $\tau_{surface}$ to 0 (incompletely developed profile) documents

the reaction front for the mineral. The slope of τ versus depth across the reaction front is related to the rate of solute transport divided by the rate of reaction of the mineral: on a plot such as Fig. 2-4, shallower fronts document faster reaction rates and steeper fronts represent slower rates as long as the rate of solute transport is roughly constant (April et al., 1986; White, 2002; Brantley and White, 2009). This concept was used as a constraint on the dashed curves as described below.

For example, in VA the profile does not return to parent composition because the entire shale layer is weathered: for this soil, a sigmoidal curve has simply been hypothesized such that the slope for the reaction front is shallower than that observed in PA. Extrapolation of the τ plot to parent for AL (where augering was difficult due to the prevalence of chert nodules) was completed by fitting the data to a sigmoidal curve (Brantley et al., 2008). In TN, shale chips recovered from the bottom-most sample are still slightly weathered and Na depletion therefore likely also extends deeper into the underlying but unaugerable material (Table 2-2). The TN curve for τ was extrapolated with a sigmoidal function (dashed line) defined with a slope for the reaction front (between 370 and 520 cm depth) roughly consistent with that plotted for AL. The chert nodules at the AL site may explain the observed shallower value of L in AL compared to TN. Importantly, although the curves for VA, TN, AL and PR in Fig. 2-4 are hypothesized at depth, this assumed depth of parent is not used for subsequent calculations. In addition, the value of L does not markedly change the values of the temperature or precipitation dependence which we calculate in the next section.

The extent of depletion at the land surface can be used to infer weathering regimes (Lebedeva et al., 2007; Brantley and White, 2009; Williams et al., 2010). Na

depletion profiles from Wales, PA, VA, TN and AL are all incompletely developed profiles. Such a profile can develop if, for example, the element of interest is dissolved from one mineral but re-precipitated as a secondary mineral at the land surface, maintaining the concentration above 0. However, we observed no Na-containing mineral precipitates at the surface or at depth. Therefore, this incomplete profile development is interpreted to be consistent with weathering that is kinetically limited as concluded for the PA SSHO by Jin et al. (2010). For kinetic limitation, the erosive Damkohler number, Da, is << 1. According to Lebedeva et al. (2007 and 2010), the Damkohler number for erosion for a given mineral reaction is related to the ratio of the mineral reaction rate to the erosion rate; a kinetically limited weathering regime would be described as having higher erosion rates compared to reaction rates. In PR, however, the profile is completely developed (100% Na depletion at the surface) and is thus consistent with the local equilibrium regime, where the erosive Damkohler number is >> 1 and erosion rates are small relative to reaction rates (Lebedeva et al., 2007; Brantley and Lebedeva, 2011). In the case of local equilibrium, the reaction front is relatively narrow and at most depths the pore fluids are equilibrated with the reacting mineral. Such a transition from kinetic limitation in the north to local equilibrium in the south is consistent with our interpretation that the erosion rate is relatively constant along the transect while the chemical reactivity increases with MAT and MAP. Here we assume that MAP is a proxy for fluid flux through the profile and mineral reactivity increases with MAP (higher precipitation maintains more dilute and thus more corrosive pore fluids with concentrations that are farther from equilibrium).

Kinetic limitation of a mineral in a soil means that increasing the reaction rate, for example by increasing the surface area of the mineral, should increase the solute flux which will in turn affect the slope of the weathering front. According to models summarized by Lebedeva et al. (2010), while holding all other variables constant, soil thickness in kinetically limited systems should increase with increasing MAP (porefluid advection velocity) and decrease with MAT. Furthermore, the models are consistent with an increase in depletion at the surface ($\tau_{surface}$ becomes increasingly negative) with an increase in MAT (Lebedeva et al., 2010). In TN and AL, MAP is roughly the same while temperature increases between the two sites. The models of Lebedeva et al. (2010) thus are at least broadly consistent with the deeper soil and lesser extent of surface Na depletion in TN compared to AL. PA and VA also have similar MAP but VA is warmer than PA, so the models of Lebedeva et al. (2010) would predict shallower soils in VA than PA. However, PA was more strongly impacted by periglacial conditions than VA. Ma et al. (2013) have shown that soils in the PA CZO are likely thickening, even though they are within error of steady state (soil production balanced by denudation).

NY provides a test of the idea of kinetic limitation. Data from NY have not been directly compared so far to the other transect sites because the parent material is till rather than shale bedrock. The till largely consists of shale (with minor inclusion of metamorphic rock fragments from the Adirondack Mountains) ground up by glaciation and therefore has greater specific surface area available for weathering. Given the similar MAT, MAP and bedrock between NY and PA (8.3 °C, 106 cm and 10 °C, 107 cm respectively), similar Na depletion profiles would be expected if the parent material had been identical. Rather, the Na depletion profile in NY (depletion at surface = 45%)

approaches that of VA (depletion at surface = 71%). In contrast, the depth at which soil

particles approach the composition of the parent (~ 60 cm) (Fig. 2-5) is within the range

of soil depths observed for 22 ridgetop soils sampled in the SSHO in PA (Herndon et al.,

2011). In fact, model simulation of weathering soils as a function of increasing mineral

reaction rate (i.e. increasing specific surface area) show that the depth of weathering does

not change as fast as the slope of the reaction front as long as the profile remains

incompletely developed (Brantley and Lebedeva, 2011). Thus, incompletely developed

reaction fronts calculated for a given duration of weathering (holding all other pertinent

variables constant) tend to show increasingly shallower slopes in models as the assumed

mineral surface area is increased up until the profile becomes completely developed. The

augerable soil depth in NY (L = 220 cm) is also deeper than expected for shale parent

material at that latitude (compare L = 28 cm for PA, Fig. 2-3a). All of these discrepancies

are attributed to the till parent material and are consistent with the conclusion that

plagioclase weathering in the NY and PA soils are kinetically limited.

Temperature and precipitation effects on Na release rates

The total mass of an element lost from a weathered profile can be calculated by

integrating the area under the curve of the τ plot (Chadwick et al., 1990; Egli and Fitze,

2000; Brantley and Lebedeva, 2011):

$$M_j = \rho_p C_{j,p} \int_0^L \frac{\tau_j(z)}{(\varepsilon_i(z)+1)} dz \tag{7}$$

Here, L is the depth of today's soil, which we equated to the observed augerable depth

(bottom closed symbol in Fig. 2-4). Arguably, the integration could be completed to

L$_{parent}$ instead of L (Fig. 2-4), but we instead did the calculation strictly based on the

observable L rather than the model value (L$_{parent}$) so as not to bias the calculations. M$_j$ is

the total mass loss of element *j* from the soil profile, ρ_p is the density of the parent, C$_{j,p}$ is

the concentration of element *j* in the parent and z is the depth interval of the sample.

Calculating M$_{Na}$ for soil profiles across the transect, we observe a nonlinear increase in

the total mass of Na, M$_{Na}$, lost with increasing MAT (Fig. 2-6). Again, a straight line

cannot be fit to include all the best constrained data (Wales, PA, PR) while being

simultaneously consistent with our minimum estimates of M$_{Na}$ at VA, TN and AL.

Importantly, the value of M$_{Na}$ for PA is the most well established of the entire transect

because of the many observations not only from our transect site but also from the nearby

CZO, as we have discussed previously. Likewise, observations from PR showed a

completely developed profile that is well constrained in terms of Na loss and is unlikely

to be overestimated by more than ± 44%, the relative error we estimated for 22

measurements of soil depth along the ridge at the SSHO.

The average integrated rate of Na loss (Q$_{Na}$) from each profile was also

calculated:

$$Q_{Na} = \frac{M_{Na}}{SRT} \tag{8}$$

Values of Q$_{Na}$ cannot be compared easily as a function of MAT because the transect

consists of very wet and moderately wet subsets. To determine the dependence on MAT,

the Q$_{Na}$ values were averaged for the very wet sites Wales and PR (average = Q$_{Na,very\ wet}$)

and for the moderately wet sites PA, VA, TN, AL (Q$_{Na,moderately\ wet}$). The very wet sites

were re-scaled to the average MAP for the moderately wet sites, Q$_{Na,MAP-adj}$, by

subtracting the average "moderately wet" Q_{Na} value from the average "very wet" Q_{Na}

values as follows:

$$Q_{Na,MAP-adj} = Q_{Na} - \left(Q_{Na,very\ wet} - Q_{Na,moderately\ wet}\right) \qquad (9)$$

The natural log of these adjusted values, $Q_{Na,MAP-adj}$, for Wales and PR (very wet sites),

along with unadjusted Q_{Na} values for PA, VA, TN and AL (moderately wet sites) were

plotted against inverse temperature and the slope was calculated for this plot (Fig. 2-7).

Treating the temperature dependence as an activation energy, the slope was set equal to

$(- E_a/R)$ where R is the universal gas constant, and our best estimate of the apparent

activation energy E_a was determined: 99.0 ± 15.0 kJ mol^{-1}.

We can also return to the NY site and treat it similarly. Although data from NY

are not plotted on Fig. 2-6, M_{Na} for NY was calculated using Eq. (8) as 91.6 mol Na m^{-2},

about 11 times larger than that of PA. Likewise, the weathering rate calculated for the

NY till site (SRT = 10 ka), equals 0.0092 mol Na m^{-2} yr^{-1}, approximately 18 times the

rate observed for PA. Once again the NY site documents the effect of an increase in

mineral surface area for the kinetically limited plagioclase dissolution reaction.

Uncertainty in erosion rates

In recognizing the uncertainty of erosion rates at all sites except PA, we tested the

sensitivity of the apparent activation energy determined above to our erosion rate

assumptions. Our initial assumption is for constant erosion rates along the Appalachians

equal to 17 ± 9 m My^{-1} (Portenga and Bierman, 2011; Appendix A). This value is robust

in that it is also the average erosion rate measured in several detailed studies of Shale

Hills (Ma et al., 2010, 2013; West et al., 2013) and by many measurements (Portenga and

Bierman, 2011). The major uncertainty in erosion rate lies in PR, where the only

available erosion measurements are for a quartz diorite in the Luquillo rain forest (~43 m

My^{-1}), with double the precipitation and relief of our study site. Conservatively, the range

of possible erosion rates in PR could therefore be as low as the lowest measured

Appalachian sites (8 m My^{-1}) or as high as Luquillo (43 m My^{-1}). In our calculation we

assumed an average of these extremes, 25 ± 17 m My^{-1}. Therefore, if, for example, the

erosion rate in PR is in fact as high as that measured in Luquillo (43 m My^{-1}) and our

assumed Appalachian rate of 17 m My^{-1} is correct, the apparent activation energy would

be 117 ± 14.6 kJ mol^{-1}. If on the other hand, erosion in PR is similar to the Appalachians

(E = 17 m My^{-1}), we calculate an apparent activation energy of 86.1 ± 15.5 kJ mol^{-1}.

Across the range of most likely erosion rates across the transect, we therefore

expect the apparent activation energy to lie between ~80 to 120 kJ mol^{-1}. Error in the

assumed erosion rate in PR, the warmest site of the transect, is the strongest control on

inferred activation energy. Varying erosion rate across the Appalachians within the

constraints of Portenga and Bierman (2011) has little effect on the calculated temperature

dependence of feldspar weathering.

The range in activation energies reported here are not dissimilar to the range of

activation energies calculated for the dissolution of plagioclase in other field studies (77 -

109 kJ mol^{-1}) (Velbel, 1994; Dorn and Brady, 1995; White and Blum, 1995; Williams et

al., 2010). An anomalously low value of 14 kJ mol^{-1} was measured by Riebe et al. (2004)

in granitic, actively eroding, unglaciated sites where an additional term was added to Eq.

(11) to account for denudation rates. However, the range of values inferred here are on

the high end or higher than those measured in laboratory studies (59 – 89 kJ mol^{-1})

(Helgeson et al., 1984; Chou and Wollast, 1985; Knauss and Wolery, 1986; Rose, 1991;

Hellman, 1994; Blum and Stillings, 1995; Stillings and Brantley, 1995; Chen and

Brantley, 1997). This is discussed further below.

Precipitation dependence

We used another form of the Arrhenius equation to isolate the dependence of

precipitation on Q_{Na}:

$$ln Q_{Na(298\ K)} = ln Q_{Na(actual)} + \left(\frac{E_a}{R} \left(\frac{1}{T} - \frac{1}{298} \right) \right) \tag{10}$$

Assuming $E_a = 99$ kJ mol^{-1} as described above, $Q_{Na(298K)}$ refers to the Na dissolution rate

scaled to 298K and $Q_{Na(actual)}$ is the Na dissolution rate calculated for each site (all values

summarized in Table 2-5). A plot of $Q_{Na(298K)}$ versus MAP reveals a linear dependence of

Na dissolution rate at 298 K on precipitation alone: $Q_{Na(298K)} = 0.01$ (MAP) - 0.005 ($R^2 =$

0.79) (see Appendix A).

The exponential dependence on temperature and linear dependence on

precipitation for Q_{Na} is similar to observations for granite weathering reported by White

and Blum (1995). In their study, the influence of MAT and MAP on Si and Na fluxes

were assessed for watersheds underlain by granite. They proposed a simple equation to

evaluate the combined effects of temperature and precipitation on weathering rates:

$$Q_{Na} = (a_1 * MAP) exp \left[- \frac{E_a}{R} \left(\frac{1}{T} - \frac{1}{T_0} \right) \right] \tag{11}$$

Here, Q_{Na} is the Na dissolution rate, a_1 is the slope of the relationship between Q_{Na} and

MAP, MAP is the average precipitation at each site, E_a is the activation energy, R is the

universal gas constant, T is the temperature of the study site and T_0 is a reference

temperature, here chosen to be the average temperature of all the studied sites. Taking our

measured values of Q_{Na} along with measured values of MAP and MAT (Table 2-1) and a

T_0 of 13°C (the average temperature for our study sites), we used this equation to

quantify the effect of both precipitation and temperature on Na depletion across the

transect. The best fit of our measured Q_{Na} to Eq. (11) produces values of $a_1 = 0.0015$ mol

Na m^{-3} yr^{-1}and $E_a = 81.5$ kJ mol^{-1} ($r^2 = 0.93$). The effect of temperature on feldspar

weathering is therefore accentuated at wetter sites (Fig. 2-8). White and Blum (1995)

reported values of $a_1 = 0.097$ mol Na m^{-3} yr^{-1} and $E_a = 62.5$ kJ mol^{-1} when they fit their

Na fluxes from granite weathering to Eq. (11) (note that they used a reference

temperature of 5°C, which is close to the mean temperature of their study sites). The

smaller E_a and larger $a_1$values calculated by White and Blum (1995) are likely due to the

fact that their study included the Rio Icacos watershed in Puerto Rico, which receives 430

cm of annual precipitation and heavily controls the fit of the equation, as well as sites

with MAP < 100 cm. Our study does not include sites with such large variability in MAP.

Rasmussen et al. (2011), in a study of plagioclase weathering across granitic

watersheds, also observed that the extent of Na depletion at the land surface of soils was

highly correlated to the annual water balance at sites that were not water-limited (sites

with a humidity index > 1, where the index equals MAP divided by mean annual

potential evapotranspiration (PET)). For their study, this corresponded to sites with MAP

> 74 cm. They reported an exponential dependence of plagioclase weathering on

temperature and an apparent activation energy of 69 ± 15 kJ mol^{-1}, but only when data

from wet sites were evaluated separately from dry sites. They also concluded that their

data demonstrated threshold behavior at MAP = 74 cm. In other words, sites with low

MAP have insufficient water for removal of weathering products and a short water

residence time whereas sites with greater MAP are not restricted by these factors. All

sites included in our study are wet according to their definition and therefore we cannot

evaluate whether there is a threshold that matches their observations.

In contrast to our conclusion that climate is important in these shale soils, Riebe et

al. (2001 and 2004) concluded that climate is not as important a variable as erosion in

controlling long-term granite weathering rates. Specifically, Riebe et al. (2004) reported

that chemical weathering rates inferred from soil data are highly correlated with erosion

rates but only weakly correlated with climate across 14 sites in North America with

temperatures ranging from 2 to 22°C and precipitation spanning 22 to 420 cm yr^{-1}. They

concluded that tectonic controls on erosion are more important in driving chemical

weathering than climate. In contrast to the sites reported by Riebe et al., across our

transect, erosion rates are estimated to be low and relatively constant (~17 m My^{-1} to at

most 43 m My^{-1}) as compared to the range in denudation rates measured by Riebe et al.

(2004) (8.5 – 230 m My^{-1}). In fact, it is estimated that the Southern Appalachian

Mountains have been eroding at a similar rate for the past $10^2 - 10^8$ yr and rock uplift is

balanced by denudation over the time the soils have been forming along our transect

(Matmon et al., 2003). The uniformity of erosion rates and lack of significant tectonic

uplift apparently allows us to observe a strong climate signal in our study. In effect, the

natural experiment of Riebe et al. was more likely to document the effect of erosion while ours was more likely to document the effect of climate.

Furthermore, Riebe et al. (2004) determined weathering rates from values of the chemical depletion fraction (CDF). The CDF can be calculated for an individual element j to indicate the fractional loss of j or can be calculated to indicate the fractional loss of all elements during weathering. When the chemical depletion fraction of an individual element j is calculated for a sample this value of CDF equals -τ_j (Brantley and Lebedeva, 2011). When the CDF is calculated for all mobile elements, Riebe et al. (2004) use this formula:

$$CDF = \left(1 - \frac{[Zr]_{rock}}{[Zr]_{soil}}\right) \tag{12}$$

In this formulation, the CDF is the fraction of all elements that have been lost from the soil sample compared to the parent material, assuming Zr is immobile. Brantley and Lebedeva (2011) showed that this value of CDF is equivalent to a summation over all the depleted components in a soil and thus can be calculated from values of τ_j summed over all j.

To interpret the contribution of chemical weathering to total denudation, Riebe et al. (2004) interpret one single CDF value from surface soils collected from randomly chosen $1 - 2$ m^2 grids within the study areas ($0.5 - 10$ ha) at each field site. Calculating CDF for an entire soil requires assessment of one concentration value for Zr in the soil to use in Eq. (12), even though that concentration can vary with depth. In the case of Riebe et al., average Zr concentration of soils collected at depth from soil pits were generally similar to surface soil Zr concentrations, therefore surface soil concentrations were

deemed representative of the entire soil. One can assess the overall Zr concentration either by analyzing one homogenized sample of the entire soil or by integrating depth-weighted average Zr concentrations for each sample interval. This latter approach is generally what is done and therefore relies upon taking an adequate number of samples versus depth, measurements of bulk density and an appropriate summation.

Riebe et al. (2001, 2004) have argued that CDF calculated for an entire soil in this way is equivalent to the percent of total denudation that has occurred by chemical weathering processes for that soil. For our transect, CDF calculated as per this method varies from almost 0% in Wales to 50% in Puerto Rico, consistent with the relative contribution of chemical weathering as a fraction of total denudation increasing linearly south along the transect (Table 2-4). One interpretation of these CDF values is that in Wales almost all denudation is due to physical erosion, whereas half the total denudation in tropical PR is due to chemical weathering. While it might be tempting to infer that weathering of shale is more sensitive to climate than that of granite, this conclusion may not make sense given the differences in sampling (surface soil samples, Riebe et al., 2004) versus soil depth profiles (herein).

One subtlety should be noted here, however. Jin et al. (2010) concluded that much of the mass loss of Fe, Al, Si and some other elements from the PA SSHO soil occurred through transport of fine particles out of the soil column rather than by solubilization. The importance of clay-sized particle transport is likely high in PA and in the other transect soils given the shale parent material. Therefore, the CDF for these soils most likely does not refer solely to *chemical* depletion (solubilization) but likely refers to transport as solutes as well as fine particles. The CDF in this case is thus the loss of mass

as solutes and fine particles in the subsurface (i.e. loss of material that differs in composition from parent material), and loss of mass as particles due to erosion at the land surface.

Weathering advance rate

The interpretation that the temperature dependence as expressed in Eq. (10) and Fig. 2-7 is an activation energy is overly simplistic. According to weathering model experiments of Lebedeva et al. (2010), the temperature dependence of Q_{Na} as shown in Fig. 2-7 should approximate $E_a + \Delta H$ for weathering that is controlled kinetically, as observed for Wales through AL. Here ΔH is the enthalpy change of the albite dissolution reaction. Given this relationship and a laboratory value for E_a of albite dissolution of 65.3 $\pm$ 3.4 kJ mol^{-1} (Chen and Brantley, 1997) and ΔH of 79.8 kJ mol^{-1} (Johnson et al., 1992), we predict the temperature dependence for albite dissolution for data from Wales to AL as shown in Fig. 2-7 should equal 145.1 kJ mol^{-1} for strict kinetic limitation. This is within error of the value of 131 ± 31.3 kJ mol^{-1} we calculate when we regress the data from only the kinetically limited transect sites (excluding PR).

In contrast, the entire transect is not comprised of incompletely developed profiles developed in the kinetic regime. For a completely developed profile such as that observed in PR, many researchers have shown that the weathering advance rate (w) is not influenced by the kinetics of dissolution at all but rather only by equilibrium solubility (Lichtner, 1988; Brantley et al., 2008; White, 2008; Maher, 2010; Lebedeva et al., 2010). In effect, w represents the rate that a near-equilibrium fluid infiltrates downward,

solubilizing minerals. The weathering advance rate for a completely developed profile,

i.e., the linear rate that a weathering profile advances into the subsurface (cm yr^{-1}), is

therefore often approximated by the following equation (Brantley and Lebedeva, 2011):

$$w = \frac{Q_{water}\, C_{eq}}{C_0} \tag{13}$$

Here, Q_{water} is the fluid advection rate (cm yr^{-1}) through the soil profile. For the case of

Na feldspar, C_{eq} is the aqueous concentration of Na in equilibrium with feldspar (mol cm^{-3}) and C_0 is the initial concentration of Na in parent material (mol cm^{-3}). Based on this

equation, the variation of w with temperature could reflect the change in the product,

$Q_{water}C_{eq}$, with temperature along the transect instead of the rate of change in the albite

dissolution rate constant. (We implicitly assume here that the parent composition C_0 is

relatively constant along the transect). The rate of change of C_{eq} with temperature is

described by the Van't Hoff equation:

$$\frac{d \ln K}{d\frac{1}{T}} = -\frac{\Delta H}{R} \tag{14}$$

Here R is the universal gas constant and K is the equilibrium constant, for example for

reaction (3). C_{eq} changes with temperature according to K. In effect, for the PR profile

which is not kinetically controlled, the temperature dependence should approach the ΔH

of albite dissolution (79.8 kJ mol^{-1}) (Johnson et al., 1992). Therefore an alternate

interpretation of Q_{Na} in Fig. 2-7 is that the temperature dependence decreases across the

transect from north to south from Ea + ΔH (131 kJ mol^{-1}) to ΔH (99 kJ mol^{-1}). In effect,

Fig. 2-7 is an Arrhenius plot where the mechanism of reaction changes across the transect

somewhere between the Appalachians and PR. Theoretically, we should fit two lines to

the data where the line at low T is consistent with 131 kJ mol^{-1} and the slope at high T is consistent with 99 kJ mol^{-1}.

Conclusions

A transect of sites has been established across a latitudinal climate gradient to investigate rates of shale weathering as a function of climate. The time-integrated Na release rates inferred for the soils as a proxy for feldspar weathering are higher in warmer wetter climates and lower in cold climates. We found that Na release rates increased exponentially with temperature and linearly with precipitation across these sites. We calculated a temperature dependence for feldspar weathering of 99 ± 15 kJ mol^{-1} across all sites, which is not dissimilar to laboratory-derived values of the activation energy or the enthalpy of reaction for albite dissolution. However, we infer that the rate-limiting step of dissolution varies across the transect from the interfacial mineral reaction to erosive transport. In the kinetically limited profiles from Wales to AL, the temperature dependence of feldspar dissolution (131 ± 31.3 kJ mol^{-1}) is consistent with $E_a + \Delta H$ (145 kJ mol^{-1}), as predicted by weathering model experiments (Lebedeva and Brantley, 2011). Somewhere between the southern Appalachian sites and PR we conclude that the profiles become limited by transport and are likely to be described by a lower activation energy. Such quantitative treatments of weathering are being pursued using numerical models.

Although we observe a quantifiable influence of climate on plagioclase weathering, plagioclase generally constitutes less than 5% of the unweathered shale mineralogy. The dissolution of feldspar is one of the deepest reactions observed and may

be a profile-initializing reaction, i.e., a reaction that initiates the weathering process, but is unlikely to be the main control of regolith depth. Feldspar dissolution therefore does not entirely explain weathering rates across the transect, but these measurements are a first step toward better quantification of such weathering. More detailed studies of mineral reactions, especially the weathering of illite and chlorite, the dominant shale minerals, will be necessary to better quantify the influence of climate on weathering rates.

Acknowledgements

References

Amiotte-Suchet P., Probst J. L. and Ludwig W. (2003) Worldwide distribution of continental rock lithology: Implications for the atmospheric/soil CO_2 uptake by continental weathering and alkalinity in river transport to the oceans. *Global Biogeochem. Cy.* DOI:10.1029/2002GB001891.

Amundson R. (2004) Soil formation. In *Treatise in Geochemistry* (eds. J. I. Drever, H. D. Holland , and K. K. Turekian). Elsevier, Amsterdam. pp. 1-35.

Amundson R., Richter D. D., Humphreys G. S., Jobbagy E. G. and Gaillardet J. (2007) Coupling between biota and earth materials in the critical zone. *Elements* **3**:327-332.

Anderson S. P., Dietrich W. E. and Brimhall G. H. (2002) Weathering profiles, mass-balance analysis, and rates of solute loss: Linkages between weathering and erosion in a small, steep catchment. *Geol. Soc. Am. Bulletin* **114:**1143-1158.

April R. H., Hluchy M. M. and Newton R. M. (1986) Chemical weathering in two Adirondack watersheds: Past and present-day rates. *Geol. Soc. Am. Bull.* **97**:1232-1238.

Bern C. R. and White A. F. (2011) A model for assessing, quantifying, and correcting for index element mobility in weathering studies. *Appl. Geochem.* **26**:S9-S11.

Bern C. R., Chadwick O. A., Hartshorn A. S., Khomo L. M. and Chorover J. (2011) A mass-balance model to separate and quantify colloidal and solute redistributions in soil. *Chem. Geol.* **282**:113-119.

Bierman P. R., Jungers, M., Reusser, L. and Pavich, M. (2008) Look again: meteoric 10-Be Is a useful tracer of hillslope and basin-scale process. *Geol. Soc. Am. Abstracts Program*. pp. 165–166.

Bierman P. R., Reusser, L. and Pavich, M. (2009) New ways of using an old isotopic system – meteoric 10-Be is back and ready to do geomorphology. *Geophys. Res. Abstracts*, **11**:EGU2009-0.

Birkeland P. W. (1999) Soils and Geomorphology. Oxford University Press, New York. p. 430.

Blatt H., Middleton G. and Murray R. (1980) Origin of sedimentary rocks. Prentice-Hall, New Jersey. 577 p.

Blum A. F. and Stillings L. L. (1995) Feldspar dissolution kinetics. *Rev. Mineral. Geochem.* **31**:291-351.

Bockheim J. G. (1980) Solution and use of chronofunctions in studying soil development. *Geoderma* **24**:71-85.

Brantley S. L. and Lebedeva M. (2011) Learning to read the chemistry of the regolith to understand the critical zone. *Annu. Rev. Earth Pl. Sc.* **39**:387-416.

Brantley S. L. and White A. F. (2009) Approaches to modeling weathered regolith. *Rev. Mineral. Geochem.* **70**:435-484.

Brantley S. L., Goldhaber M. B. and Ragnarsdottir K. V. (2007) Crossing disciplines and scales to understand the critical zone. *Elements* **3**:307–314.

Brantley S. L., Bandstra J., Moore J. and White A. F. (2008) Modeling chemical depletion profiles in regolith. *Geoderma* **145**:494-504.

Brimhall G. H. and Dietrich W. E. (1987) Constitutive mass balance relations between chemical composition, volume, density, porosity, and strain in metasomatic hydrochemical systems: Results on weathering and pedogenesis. *Geochim. Cosmochim. Acta* **51:**567-587.

Brimhall G. H., Chadwick O. A., Lewis C. J., Compston W., Williams I. S., Danti K. J., Dietrich W. E., Power M. E., Hendricks D. and Bratt J. (1992) Deformational mass transport and invasive processes in soil evolution. *Science* **255**:695-702.

British Geological Survey (2005) Digital Geological Map of Great Britain 1:10 000 scale (DiGMapGB-10) data [CD-Rom]. Version 1.11. Keyworth, Nottingham: British Geological Survey. Tile TQ69SW. Release date 20-04-2005.

Brown E. T., Stallard R. F., Larsen M. C., Bourles D. L., Raisbeck G. M. and Yiou F. (1998) Determination of predevelopment denudation rates of an agricultural watershed (Cayaguas River, Puerto Rico) using in-situ-produced ^{10}Be in river-borne quartz. *Earth Planet. Sci. Lett*. **160**:723-728.

Brown E. T., Stallard R. F., Larsen M. C., Raisbeck G. M. and Yiou F. (1995) Denudation rates determined from the accumulation of in situ-produced ^{10}Be in the Luquillo Experimental Forest, Puerto Rico. *Earth Plan. Sc. Lett.* **129**:193-202.

Buss H. L., Sak P. B., Webb S. M. and Brantley S. L. (2008) Weathering of the Rio Blanco quartz diorite, Luquillo Mountains, Puerto Rico: Coupling oxidation, dissolution, and fracturing. *Geochim. Cosmochim. Acta* **72**:4488-4507.

Cadwell D. H. and Muller E. H. (2004) New York glacial geology, U.S.A. *In:* Quaternary Glaciations – Extent and Chronology. Part II: North America. (Eds.) Ehlers J. and Gibbard P. L. Elsevier, Netherlands. pp. 201-205.

Chabaux F., Blaes E., Stille P., di Chiara Roupert R., Dosseto A., Pelt E., Ma L., Buss H.L. and Brantley S.L. (2013) Regolith formation rate from U-series nuclides: Implications from the study of a spheroidal weathering profile in the Rio Icacos watershed (Puerto Rico), *Geochim. Cosmochim. Acta.* **100**:73-95.

Chadwick O. A., Brimhall G. H. and Hendricks D. M. (1990) From a black to a gray box – a mass balance interpretation of pedogenesis. *Geomorph.* **3**:369-390.

Chadwick O. A., Gavenda R. T., Kelly E. F., Ziegler K., Olson C. G., Elliott W. C. and Hendrick D. M. (2003) The impact of climate on the biogeochemical functioning of volcanic soils. *Chem. Geol*. **202**:195-223.

Chen Y. and Brantley S. L. (1997) Temperature- and pH-dependence of albite dissolution rate at acid pH. *Chem. Geo*. **135:**275-290.

Ciolkosz E. J., Cronce R. C. and Sevon W. D. (1986) Periglacial features in Pennsylvania. Pa. State Univ., Agron. Ser. 92. 52 p.

Chou L. and Wollast R. (1985) Steady-state kinetics and dissolution mechanisms of albite. *Amer. J. Sci.* **285**:9663-993.

Clark G. M. and Ciolkosz E. J. (1988) Periglacial geomorphology of the Appalachian highlands and interior highlands south of the glacial border – a review. *Geomorph.* **1:**191-220.

Clark C. D., P. L. Gibbard and Rose J. (2004) Pleistocene glacial limits in England, Scotland and Wales. *In:* Quaternary Glaciations – Extent and Chronology. Part I: Europe. (Eds.) Ehlers J. and Gibbard P. L. Elsevier, Netherlands. pp. 47-82.

Clifton T. and Granger D. (2005). Erosion rate of the Appalachian plateau in the vicinity of the New River Gorge, West Virginia. *Geol. Soc. Am. Abstr. Prog.* **37**:18.

Cornu S., Lucas Y., Lebon E., Abrosi J. P., Luizao F., Rouiller J., Bonnay M. and Neal C. (1999) Evidence of titanium mobility in soil profiles, Manaus, central Amazonia. *Geoderma* **91**:281-295.

Dixon J. L., Heimsath A. M. and Amundson R. (2009a) The critical role of climate and saprolite weathering in landscape evolution. *Earth Surf. Process. Landforms* **34**:1507-1521.

Dixon J. L., Heimsath A. M., Kaste J. and Amundson R. (2009b) Climate-driven processes of hillslope weathering. *Geol.* **37**:975-978.

Dorn R. I. and Brady P. V. (1995) Rock-based measurement of temperature-dependent plagioclase weathering. *Geochim. Cosmochim. Acta* **59**:2847-2852.

Duxbury J. (2009) Erosion rates in and around Shenandoah National Park, VA, determined using analysis of cosmogenic [10]Be: University of Vermont, 134 p.

Eberl D. D. (2003) User's guide to RockJock – a program for determining quantitative mineralogy from powder x-ray diffraction data. U.S. Geological Survey, Open-file report 03-78.

Egli M. and Fitze P. (2000) Formulation of pedogenic mass balance based on immobile elements: a revision. *Soil Sci.* **165**:437-443.

Ferrier K. L., Kirchner J. W., Riebe C. S. and Finkel R. C. (2010) Mineral-specific chemical weathering rates over millennial timescales: Measurements at Rio Icacos, Puerto Rico. *Chem. Geol.* **277**:101-114.

Finlayson C. P. (1964) Geology map and mineral resources summary of the White Hollow quadrangle, Tennessee. Tennessee Div. Geol. Geologic Map GM-145-SW.

Folk R. L. (1960) Petrography and origin of the Tuscarora, Rose Hill, and Keefer Formations, Lower and Middle Silurian of Eastern West Virginia. *J. Sedim. Res.* **30**:1-58.

Gardner L. R. (1980) Mobilization of Al and Ti during weathering – isovolumetric geochemical evidence. *Chem. Geol.* **30**:151-165.

Gardner T. W., Ritter J. B., Shuman C. A., Bell J. C. Sasowsky K. C. and Pinter N. (1991) A periglacial stratified slope deposit in the valley and ridge province of central Pennsylvania, USA: sedimentology, stratigraphy and geomorphic evolution. *Permafrost Periglac. Process.* **2**:141-162.

Gillette T. (1947) The Clinton of western and central New York. N.Y. State Mus. Bull. 341.

Goddéris Y., Brantley S. L., Francois L. M., Schott J., Pollard D., Déqué M. and Dury M. (2013) Rates of consumption of atmospheric CO2 through the weathering of loess during the next 100 yr of climate change. *Biogeosci.* **10**:135-148.

Goddéris Y., Francois L. M., Probst A., Schott J., Moncoulon D., Labat D. and Viville D. (2006) Modelling weathering processes at the catchment scale: The WITCH numerical model. *Geochim. Cosmochim. Acta* **70**:1128-1147.

Goddéris Y., Williams J. Z., Schott J., Pollard D. and Brantley S. L. (2010) Time evolution of the mineralogical composition of Mississippi Valley loess over the last 10 kyr: Climate and geochemical modeling. *Geochim. Cosmochim. Acta* **74**:6357-6374.

Grossman R. B. and Reinsch T. G. (2002) Bulk density and linear extensibility. *In:* Methods of soil analysis. Part 4. Physical Methods. (Eds.) Dane J. H. and Topps G. C. Soil Sci. Soc. Am. Book Series No. 5. ASA and SSSA, Madison, WI. pp. 201-228.

Hancock G. and Kirwan M. (2007) Summit erosion rates deduced from 10Be: Implications for relief production in the central Appalachians. *Geol.* **35**:89-92.

Helgeson H. C., Murphy W. M. and Aagaard P. (1984) Thermodynamic and kinetic constraints on reaction rates among minerals and aqueous solution. II. Rate constants, effective surface area, and the hydrolysis of feldspar. Geochim. Cosmochim. Acta 48:2405-2432.

Hellman R. (1994) The albite-water system: Part II. The time-evolution of the stoichiometry of dissolution as a function of pH at 100, 200, and 300 °C. *Geochim. Cosmochim. Acta* **58**:595-611.

Herndon E. M., Jin L. and Brantley S. L. (2011) Soils reveal widespread manganese enrichment from industrial inputs. *Environ. Sci. Technol.* **45**:241-247.

Hillier S. (2000) Accurate quantitative analysis of clay and other minerals in sandstones by XRD: comparison of a Rietveld and a reference intensity ratio (RIR) method and the importance of sample preparation. *Clay Min*. **35**:291-302.

Imbrie J., Hays J. D., Pisias N. G., Prell W. L. and Shackleton N. J. (1984) The orbital theory of Pleistocene climate: support from a revised chronology of the marine $\delta^{18}O$ record. *In:* Milankovitch and climate. (Eds.) Berger J. I. A., Hays J., Kukla G. and Saltzman B. Reidel, Dordrecht, Netherlands.

Jenkins R. and Snyder R. L. (1996) Introduction to X-ray Powder Diffractometry. John Wiley and Sons, Inc., New York. 403 p.

Jenny H. (1941) Factors of soil formation. McGraw Hill, NY. 281 p.

Jin L. Ravella R., Ketchum B., Heaney P. and Brantley S. L. (2010) Mineral weathering and elemental transport during hillslope evolution at the Susquehanna/Shale Hills Critical Zone Observatory. *Geochim. Cosmochim. Acta* **74**:3669-3691.

Jin L., Rother G., Cole D. R., Mildner D. F. R., Duffy C. J. and Brantley S. L. (2011) Characterization of deep weathering and nanoporosity development in shale – A neutron study. *Amer. Min*. **96**:198-512.

Johnson J. W., Oelkers E. H. and Helgeson H. C. (1992) Supcrt92. *Computers & Geosci.* **18**:899-947.

King P. B. and Ferguson H. W. (1960) Geology of northeasternmost Tennessee: U.S. Geol. Survey Prof. Paper 311. 136 p.

Knauss K. G. and Wolery T. J. (1986) Dependence of albite dissolution kinetics on pH and time at 25°C and 10°C. *Geochim. Cosmochim. Acta* **50**:2481-2497.

Kolowith L.C. and Berner R.A. (2002) Weathering of phosphorus in black shales. *Biogeochem. Cyc.* DOI:0.1029/2001GB001887.

Kozak S. J. (1965) Geology of the Millboro Quadrangle, Virginia. Virginia Div. Mineral. Resources Rep. Invest. 8. 19 p.

Lebedeva M. I., Fletcher, R. C. and Brantley, S. L. (2010) A mathematical model for steady-state regolith production at constant erosion rate. *Earth Surf. Process. Landforms* **35**: 508–524.

Lebedeva M.I., Fletcher R.C., Balashov V.N. and Brantley S.L. (2007) A reactive diffusion model describing transformation of bedrock to saprolite. *Chem. Geol.* **244**:624-645.

Lerman A. and Wu L. (2008) Kinetics of Global Geochemical Cycles. *In*: *Kinetics of Water-Rock Interaction* (Eds.) Brantley S. L., Kubicki J. D. and White A. F. Springer, New York. pp. 655-736.

Lichtner P. C. (1988) The quasi-stationary state approximation to coupled mass transport and fluid-rock interaction in a porous medium. *Geochim. Cosmochim. Acta* **49**:779-800.

Liermann L. J., Mathur R., Wasylenski L. E., Nuester J., Anbar A. D. and Brantley S. L. (2011) Extent and isotopic composition of Fe and Mo release from two Pennsylvania shales in the presence of organic ligands and bacteria. *Chem. Geo.* **281**:167-180.

Lin H. (2006) Temporal stability of soil moisture spatial pattern and subsurface preferential flow pathways in the Shale Hills Catchment. *Vadose Zone J.* **5**:317-340.

Lin H., Kogelmann W., C. Walker and M. A. Bruns. (2006) Soil moisture patterns in a forested catchment: a hydropedological perspective. *Geoderma* **131**:345-368.

Littke R., Klussmann U., Krooss B. and Leythaeuser D. (1991) Quantification of loss of calcite, pyrite, and organic matter due to weathering of Toarcian black shales and effects on kerogen and bitumen characteristics. *Geochim. Cosmochim. Acta* **55**:3369-3378.

Luce R. W., Bartlett R. W. and Parks G. A. (1972) Dissolution kinetics of magnesium silicates. *Geochim. Cosmochim. Acta* **36**:35-50.

Ma L., Chabaux F., Pelt E., Blaes E., Jin L. and Brantley S. (2010) Regolith production rates calculated with uranium-series isotopes at Susquehanna/Shale Hills Critical Zone Observatory. *Earth Plan. Sc. Lett.* **297**:211-225.

Ma L., Chabaux F., West N., Kirby E., Jin L. and Brantley S. (2013) Regolith production and transport in the Susquehanna Shale Hills Critical Zone Observatory, Part I: Insights from U-series isotopes. *J. Geophys. Res.* DOI: 10.1002/jgrf.20037.

Maher K. (2010) The dependence of chemical weathering rates on fluid residence time. *Earth Planet. Sci. Lett.* **294**:101-110.

Mathur R., Jin L., Prush V., Paul J., Ebersole C., Fornadel A., Williams J. Z. and Brantley S. (2012) Cu isotopes and concentrations during weathering of black shale of the Marcellus Formation, Huntingdon County, Pennsylvania (USA). *Chem. Geol.* **304**:175-184.

Matmon A. S., Bierman P. R., Larsen J. Southworth S., Pavich M., Finkel R. and Caffee M. (2003) Erosion of an ancient mountain range, the Great Smoky Mountains, North Carolina and Tennessee. *Amer. J. Sci.* **303**:817-855.

Medlin J. H., Suhr N. H. and Bodkin J. B. (1969) Atomic Absorption Analysis of Silicates Employing LiBO2 Fusion. *Atomic Absorption Newsletter* **8**:25-29.

Minasny B., McBrantney A. B. and Salvador-Blanes S. (2008) Quantitative models for pedogenesis – A review. *Geoderma* **144**:140-157.

Moore J., Lichtner P. C., White A. F. and Brantley S. L. (2012) Using a reactive transport model to elucidate differences between laboratory and field dissolution rates in regolith. *Geochim. Cosmochim. Acta*. **93**:235-261.

National Research Council (NRC) (2001) Basic Research Opportunities in Earth Science. National Academy Press, Washington, 154 p.

National Oceanographic and Atmospheric Administration (NOAA) (2011) Climate Data Online: Monthly Observational Data. U.S. Department of Commerce, National Oceanic and

Atmospheric Administration, National Environmental Satellite Data and Information Service, National Climatic Data Center. http://www.ncdc.noaa.gov/cdo-web/

Neaman A., Chorover J. and Brantley S. L. (2006) Effects of organic ligands on granite dissolution in batch experiments at pH 6. *Amer. J. Sci.* **306**:451-473.

Portenga E. W. (2011) Using [10]Be to constrain erosion rates of bedrock outcrops globally and in the central Appalachian Mountains: University of Vermont, 174 p.

Portenga E. W. and Bierman P. R. (2011) Understanding Earth's eroding surface with [10]Be. *GSA Today* **21**:4-10.

Rasmussen C., Matsuyama N., Dahlgren R. A., Southard R. J. and Brauer N. (2007) Soil genesis and mineral transformation across an environmental gradient on andesitic lahar. *Soil Sci. Soc. Am. J.* **71**:225-237.

Rasmussen C., Brantley S., Richter D., Blum A., Dixon J. and White A.F. (2011) Strong climate and tectonic control on plagioclase weathering in granitic terrain. *Earth Planet. Sc. Lett.* **301**:521-530.

Reuter J. M. (2005) Erosion rates and patterns inferred from cosmogenic [10]Be in the Susquehanna River basin: University of Vermont, 172 p.

Richter D. D. (2007) Humanity's transformation of Earth's soil: pedology's new frontier. *Soil Science* **172**:957-967.

Riebe C. S., Kirchner J. W. and Finkel R. C. (2003) Long-term rates of chemical weathering and physical erosion from cosmogenic nuclides and geochemical mass balance. *Geochim. Cosmochim. Acta* **67**:4411-4427.

Riebe C. S., Kirchner J. W. and Finkel R. C. (2004) Erosional and climatic effects on long-term chemical weathering rates in granitic landscapes spanning diverse climate regimes. *Earth Planet. Sc. Lett.* **224**:547-562.

Riebe C. S., Kirchner J. W., Granger D. E. and Finkel R. C. (2001) Strong tectonic and weak climatic control of long-term chemical weathering rates. *Geol.* **29**:511-514.

Rinaldo A., Dietrich W. E., Rigon R., Vogel G. K. and Rodriguez-Iturbe I. (1995) Geomorphological signatures of varying climate. *Nature 374*:632-635.

Rose N. M. (1991) Dissolution rates of prehnite, epidote, and albite. *Geochim. Cosmochim. Acta* **55**:3273-3286.

Ruhe R. V. (1984) Loess-derived soil of the Mississippi Valley region: II. Soil-climate system. *Soil Sci. Soc. Am. J.* **48**:864-867.

Sanford T. H. (1966) Generalized geologic map of Marshall County, Alabama. Alabama Geol. Survey Map 60.

Soil Survey Staff (1993) National Soil Survey Handbook, Title 430-VI. U.S. Govt. Printing Office, Washington, D.C.

Soil Survey Staff (2012) Natural Resources Conservation Service, United States Department of Agriculture. Soil Survey Geographic (SSURGO) Database for [Survey Area, State]. Available online at http://soildatamart.nrcs.usda.gov. Accessed 02/09/2012.

Strakhov N. M. (1967) Principles of lithogenesis Vol. 1. Oliver and Boyd Ltd., Edinburgh. 245 p.

Steefel C. I. and Lichtner P. C. (1998) Multicomponent reactive transport in discrete fracture: I. Controls on reaction front geometry. *J. Hydrol.* **209**:186-199.

Stephenson, D. A., Fleming A. H. and Mickelson D. M. (1988) Glacial deposits. *In:* Hydrogeology. The Geology of North America Vol. 0-2. (Eds.) Back W., Rosenshein J. S. and Seaber P. R. Geol. Soc. of Am., Boulder, Colorado, pp 301-314.

Stillings L. L. and Brantley S. L. (1995) Feldspar dissolution at 25 °C and pH 3: reaction stoichiometry and the effect of cations. *Geochim. Cosmochim. Acta* **59**:1483-1496.

Sullivan C. L. (2007) [10]Be erosion rates and landscape evolution of the Blue Ridge Escarpment, southern Appalachian Mountains: University of Vermont, 76 p.

Tobish O. and Turner M. (1971) Geologic map of the San Sebastian Quadrangle, Puerto Rico. Puerto Rico: U.S. Geol. Survey Misc. Invest. Series Map I-661.

Tuttle M. L. W. and Breit G. N. (2009) Weathering of the New Albany Shale, Kentucky, USA: I. Weathering zones defined by mineralogy and major-element composition. *Appl. Geochem.* **24**:1549-1564.

Velbel M. A. (1994) Temperature dependence of silicate weathering in nature: How strong a negative feedback on long-term accumulation of atmospheric CO_2 and global greenhouse warming? *Geol.* **21**:1059-1062.

Walter R. C. and Merritts D. J. (2008) Natural streams and the legacy of water-powered mills. *Science* **319**:299-304.

West N., Kirby E., Bierman P., Slingerland R., Ma L., Brantley S. and Rood D. (2013) Regolith transport on hillslopes in the Susquehanna Shale Hills Critical Zone Observatory inferred from meteoric [10]Be. *J. Geophys. Res-Earth.* **118**:1877-1896.

White A. F. (2002) Determining mineral weathering rates based on solid and solute weathering gradients and velocities: application to biotite weathering in saprolites. *Chem. Geol.* **190**:69-89.

White A. F. (2008) Quantitative approaches to characterizing natural chemical weathering rates. *In:* Kinetics of Water-Rock Interactions. (Eds.) Brantley S. L., Kubicki J. D. and White A. F. Springer, New York. pp. 469-544.

White A. F. and Blum A. E. (1995) Effects of climate on chemical weathering in watersheds. *Geochim. Cosmochim. Acta* **59**:1729-1747.

White A. F. and Brantley S. L. (2003) The effect of time on the weathering of silicate minerals: why do weathering rates differ in the laboratory and field? *Chem. Geol.* **202**:479-506.

White A. F., Blum A. E., Schulz M. S., Vivit D. V., Stonestrom D. A., Larsen M., Murphy S. F. and Eberl D. (1998) Chemical weathering in a tropical watershed, Luquillo Mountains, Puerto Rico: I. Long-term versus short-term weathering fluxes. *Geochim. Cosmochim Acta* **62**:209-226.

White A. F., Blum A. E., Bullen T. D., Vivit D. V., Schulz M. and Fitzpatrick J. (1999) The effect of temperature on experimental and natural chemical weathering rates of granitoid rocks. *Geochim. Cosmochim. Acta* **63**:3277-3291.

White A. F., Bullen T. D., Schulz M. S., Blum A. E., Huntington T. G. and Peters N. E. (2001) Differential rates of feldspar weathering in granitic regolith. *Geochim. Cosmochim. Acta* **65**:847-869.

Whittig L. D. and Allardice W. R. (1986) X-ray diffraction techniques. *In:* Klute, A. (Ed.) Methods of Soil Analysis, Part 1: Physical and Mineralogical Methods. Soil Sci. Am. Book Series No. 9. ASA and SSSA, Madison, WI.

Wilkinson B. H and McElroy B. J. (2007) The impact of humans on continental erosion and sedimentation. *Geol. Soc. Am. Bull.* **119**:140-156.

Williams J. Z., Bandstra J. Z., Pollard D. and Brantley S. L. (2010) The temperature dependence of feldspar dissolution determined using a coupled weathering-climate model for Holocene-aged loess soils. *Geoderma* **156**:11-19.

Woodruff L. G., Cannon W. F., Eberl D. D., Smith D. B., Kilburn J. E., Horton J. D., Garrett R. G. and Klassen R. A. (2009) Continental-scale patterns in geochemistry and mineralogy: Results from two transects across the United States and Canada. *Appl. Geochem.* **24**:1369-1381.

Yesavage T., Fantle M. S., Vervoort J., Mathur R., Jin L., Liermann L. J. and Brantley S. L. (2012) Fe cycling in the Shale Hills Critical Zone Observatory, Pennsylvania: An analysis of biogeochemical weathering and Fe isotope fractionation. *Geochim. Cosmochim. Acta* **99**:18-38.
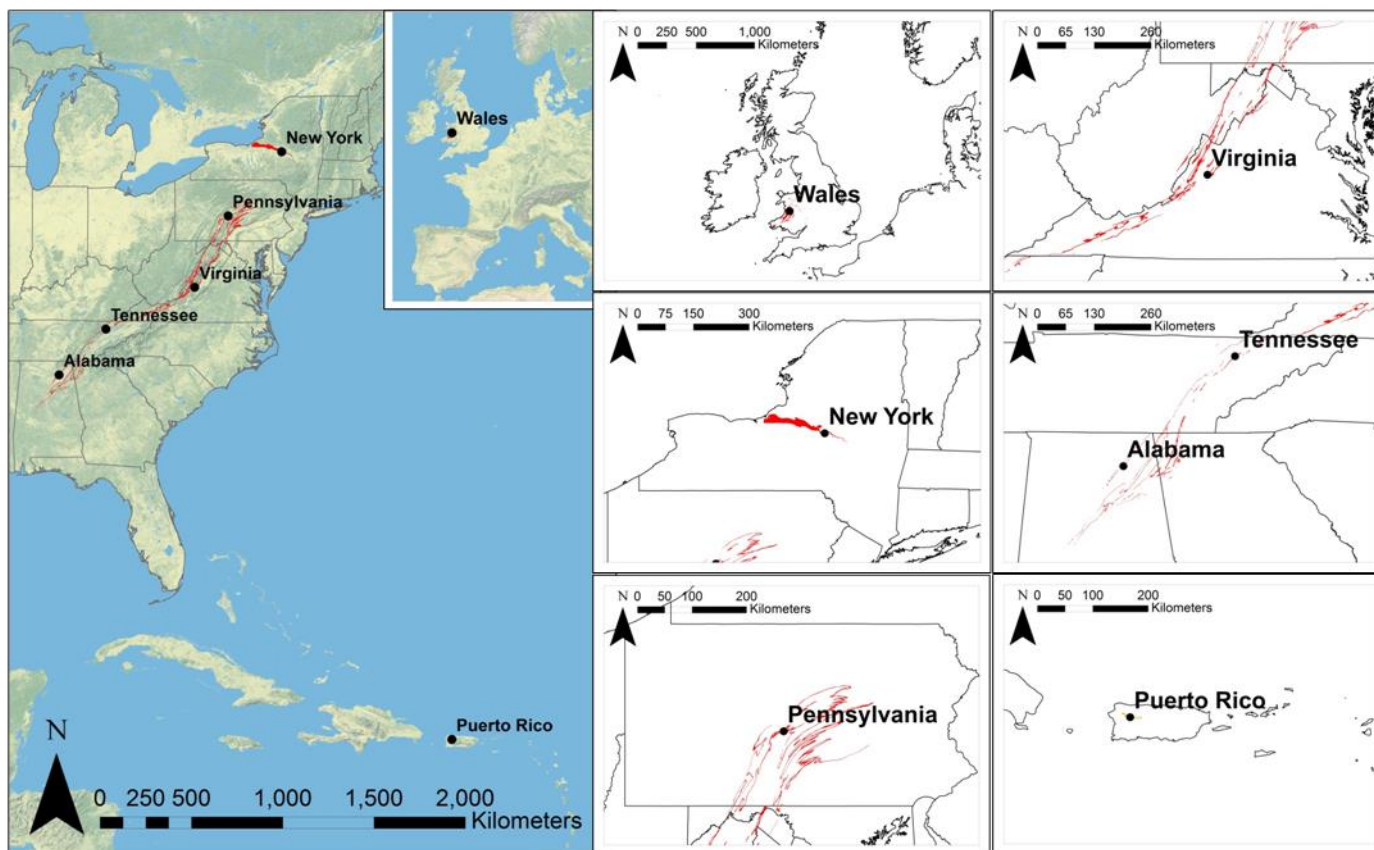
Figure 2-1. Map of shale transect sampling sites. All sites were located on ridgetop positions. Only the soil in NY was developed on till.
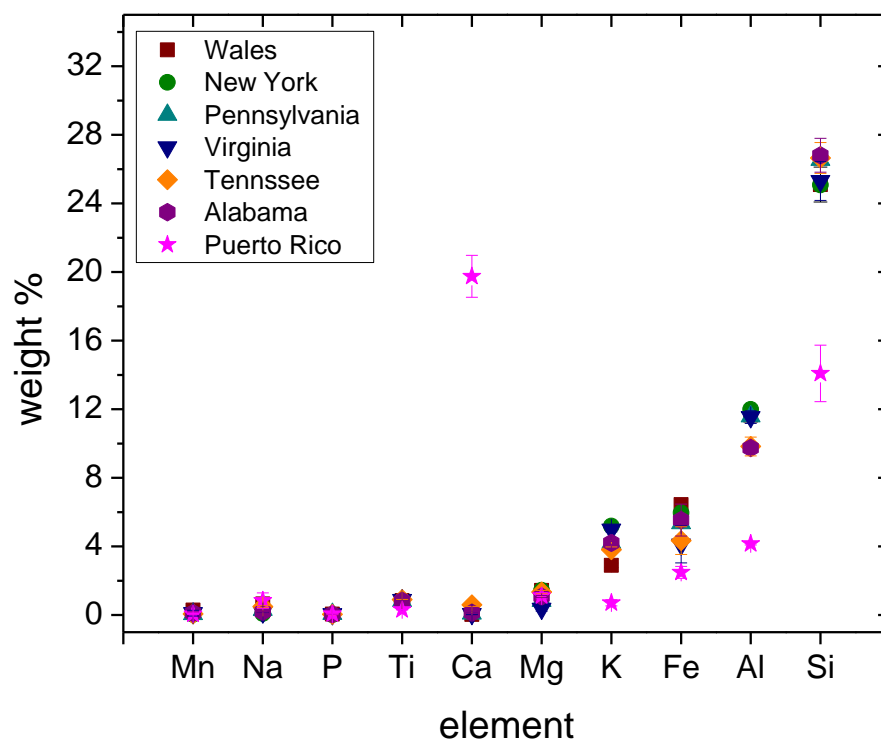
Figure 2-2. Plot of elemental weight percent measured in rock fragments collected from parent material at transect sites. See text for further discussion.
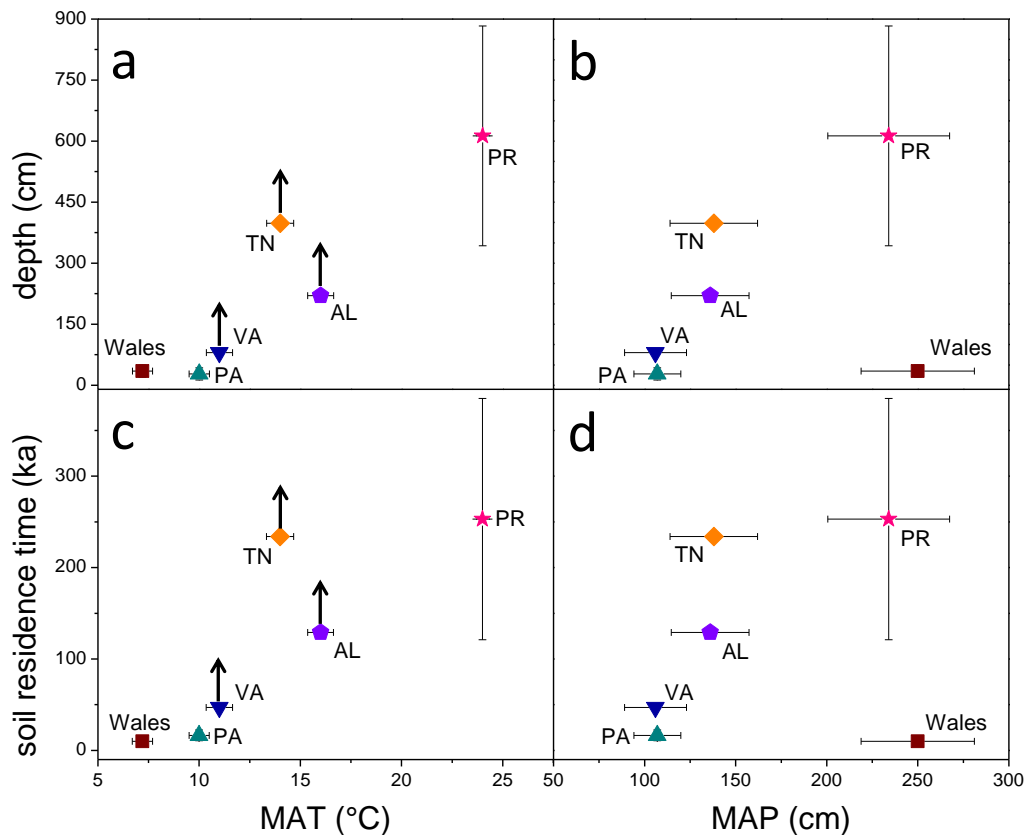
Figure 2-3. Augerable soil depth and soil residence time (SRT) as a function of mean annual temperature (MAT) and precipitation (MAP) for transect sites. Arrows represent sites where depth to unweathered shale may be deeper than augerable soil depth (see text) and therefore the plotted depths and the soil residence times are minima. NY is the only site with till parent material and is therefore not included in this plot. The error bars in panel (c) show the range of estimated SRT given an erosion rate of 17 ± 9 m My^{-1} for the Appalachian sites and 25 ± 17 m My^{-1} in Puerto Rico (see text). The symbols in panel (c) were determined using the average erosion rate for the Appalachian sites (17 m My^{-1}) and Puerto Rico (25 m My^{-1}) listed in Table 1. The data comprise two groups: a *moderately wet* group including NY, PA, VA, AL and TN (100 cm < MAP < 140 cm) and a *very wet* group including PR and Wales (MAP ~ 240 cm).
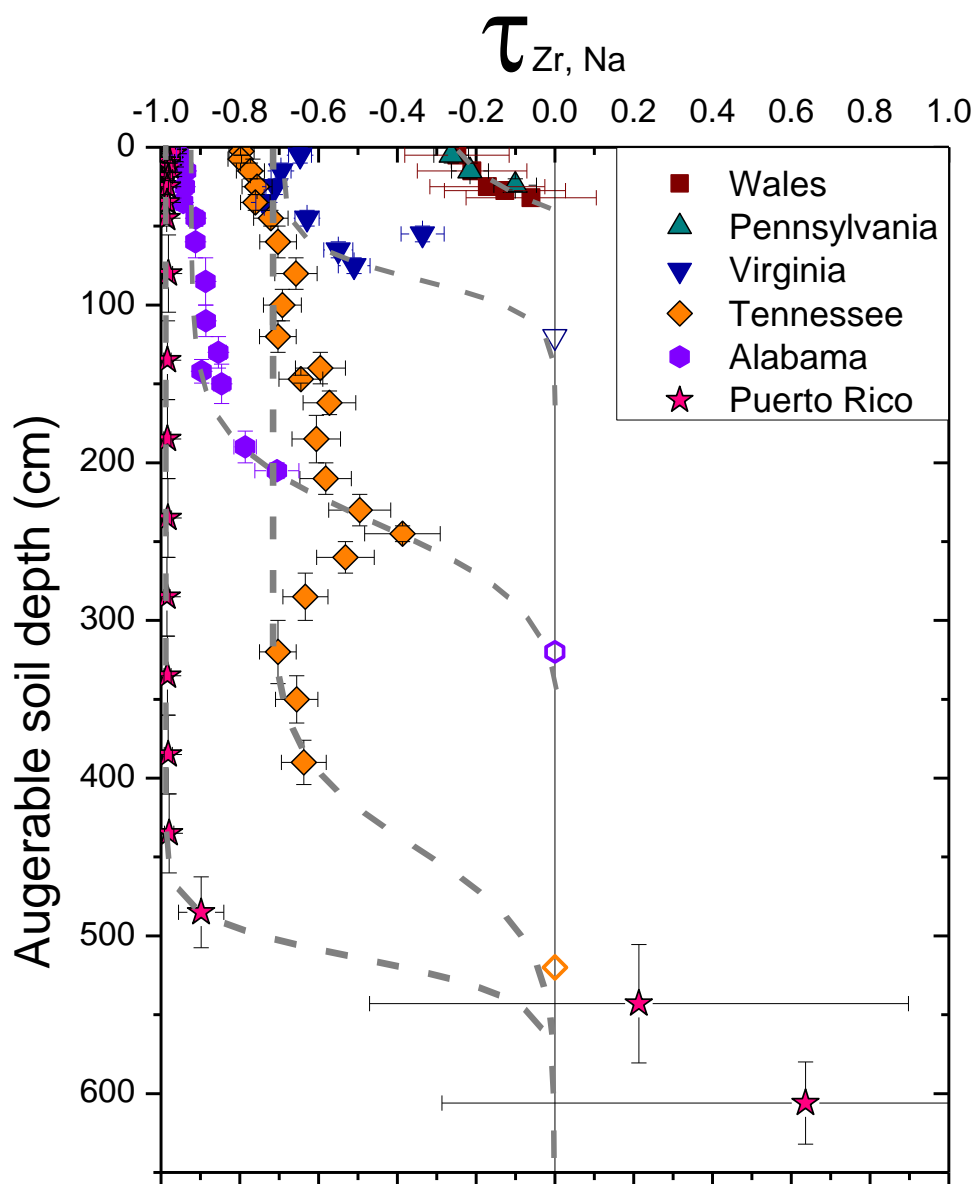
Figure 2-4. $\tau_{Zr, Na}$ plotted versus augerable soil depth for Wales, PA, VA, TN, AL and PR. For all symbols, Zr is the immobile element except VA, where Zr data were high, presumably due to residuum from weathering of an overlying sandstone layer (see text). For the VA site, we used a corrected Ti concentration as the immobile element concentration, assuming Ti mobility similar to that observed in TN. NY is not included due to till parent material. Curves are plotted based on geologic and weathering criteria as discussed in text. These sigmoidal lines are well described by Eq. (31) in Brantley et al. (2008). Closed symbols are $\tau_{Zr, Na}$ values calculated from measured concentrations. Open symbols represent our best estimate of true depth where $\tau_{Zr, Na}$ values return to 0 for profiles where augering did not reach parent. The shale layer in VA was thin enough that the shale was completely weathered: therefore, the depth to parent, L_{parent}, is greater than augered depth, L. The extreme difficulty of augering several meters into clay with rock fragments in TN may have precluded augering to parent. Likewise, chert in the AL soil precluded deeper augering.
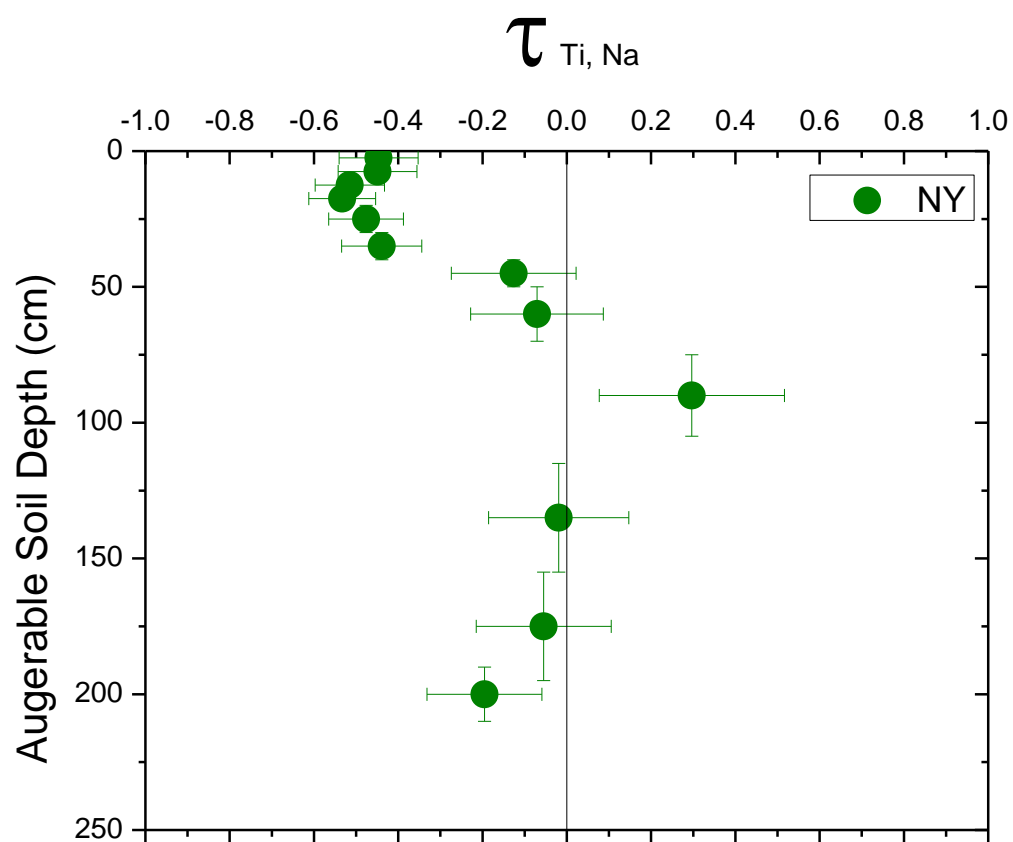
Figure 2-5. $\tau_{Ti, Na}$ plotted against augerable soil depth in NY using Ti as the immobile element (Zr was not measured in NY). The $\tau_{Ti, Na}$ profile more closely resembles the profile observed in VA (Fig. 2-4), although the climate is similar to PA (Table 2-1).
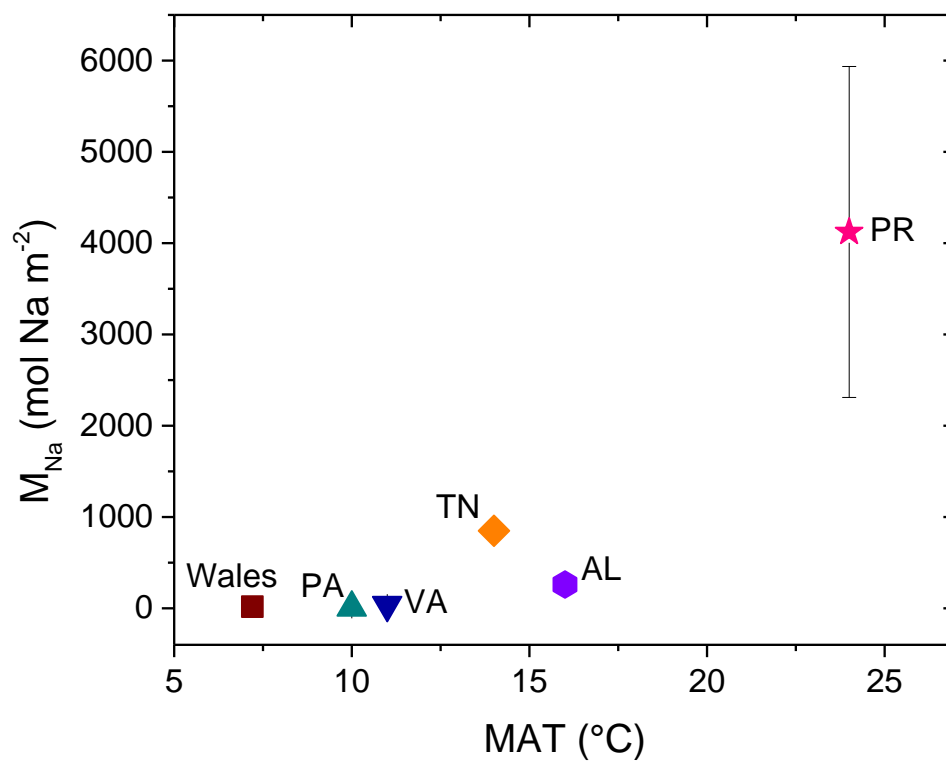
Figure 2-6. Total mass of Na lost (M_{Na}) from transect soil profiles (not including the NY till site) plotted as a function of mean annual temperature (MAT) at each site. VA, TN and AL are all minimum values, as soil depth may be greater than sampled and therefore the total mass loss over the soil profile is likely greater as shown with arrows (see text).
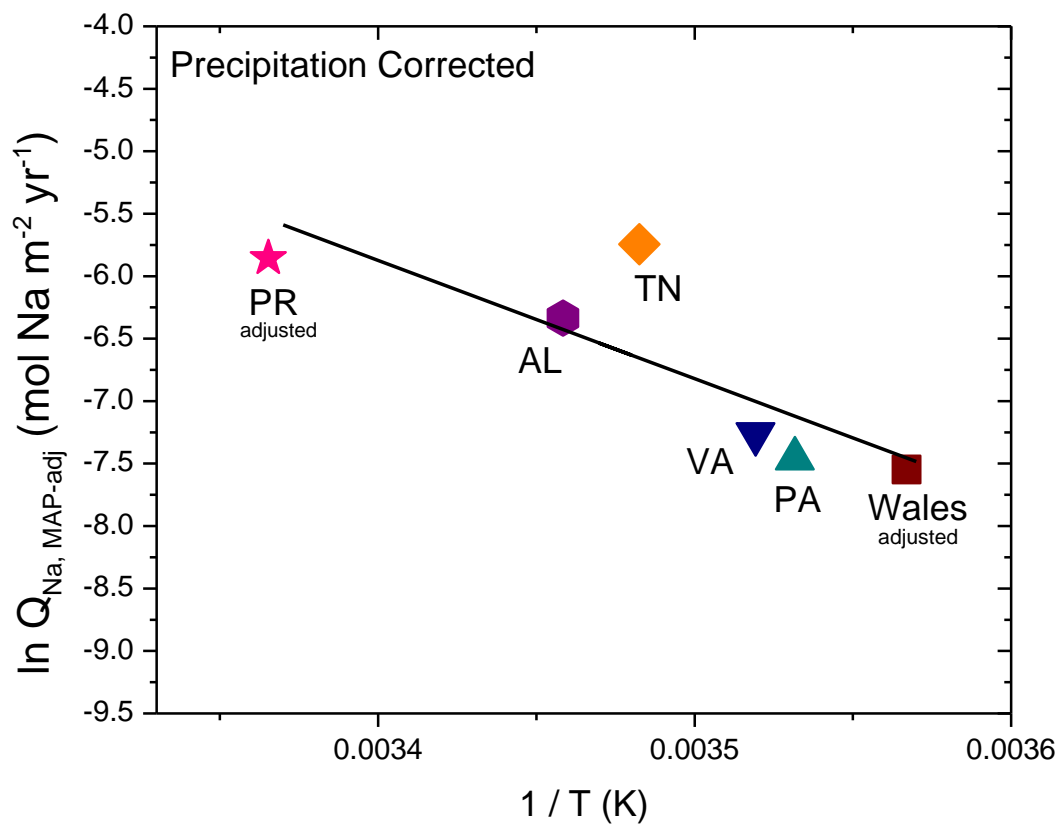
Figure 2-7. Pseudo-Arrhenius plot of Na loss rate (Q_{Na}) plotted for sites across the transect after adjustment for the difference in precipitation between moderately wet and very wet sites (see text). The slope of the line gives an apparent activation energy of 99 ± 15 kJ mol^{-1}.
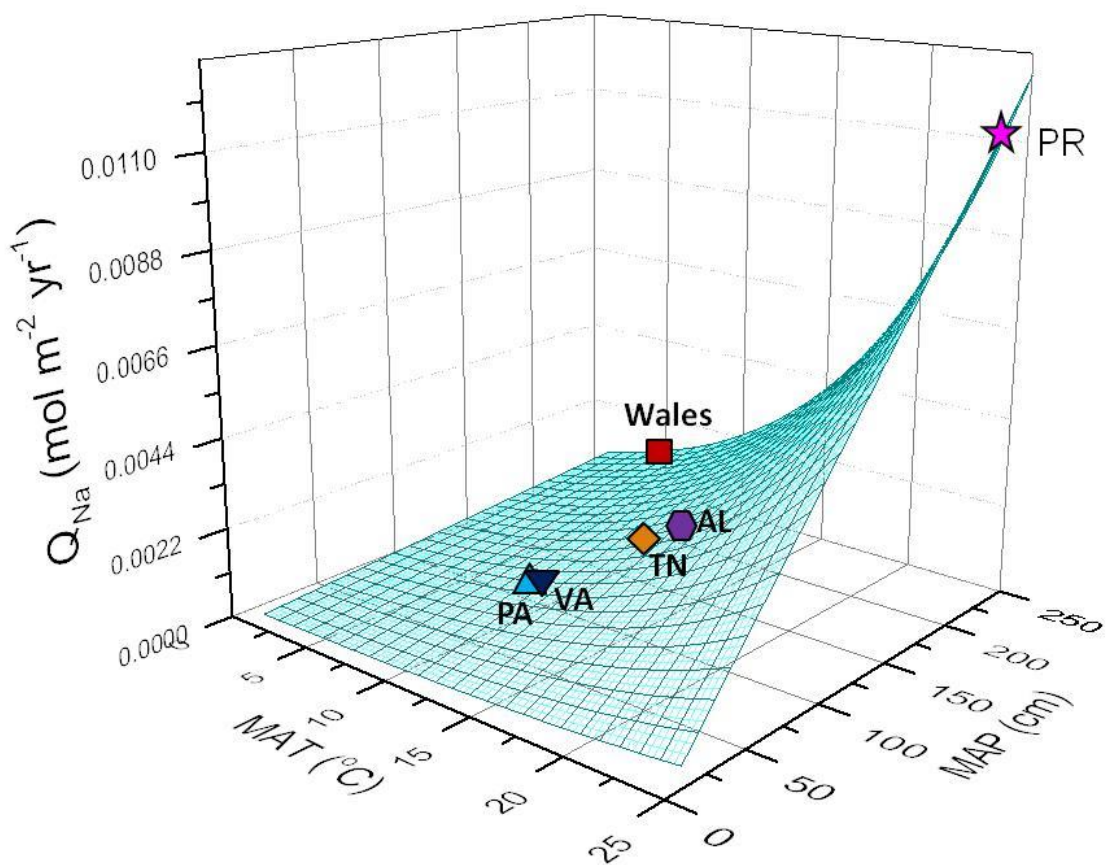
Figure 2-8. The average integrated rate of Na loss (Q_{Na}) plotted versus MAT and MAP for transect sites. The 3D curve was calculated using fit parameters obtained from fitting Eq. (11) to data. Transect sites are projected onto the surface using MAT and MAP values listed in Table 2-1.

Tables

Table 2-1. Shale transect site characteristics.

Site	Latitude	Longitude	Elevation	Relief	Slope	Strike	Dip	MAT	MAP	depth[a]	E[b]	SRT[c]	ρ_b^{0} [j]	ρ_b^{max} [k]	K[l]
			——— m ———					°C	—— cm ——		m Ma^{-1}	ka	—— g cm^{-3} ——		
Wales, UK	N52° 28.416	W3° 41.575	417	87	0.29	22	10°SE	7.2	250	35	---	10[i]	0.42	1.75	0.053
New York (NY)	N43° 1.739	W75° 16.609	269	85	0.18	341	6°SW	8.3	106	220[d]	---	10[i]	---[m]	---	---
Pennsylvania (PA)	N40° 39.931	W77° 54.297	297	40	0.10	70	25°NW	10	107	28	17[g]	17	0.80	1.75	0.050
Virginia (VA)	N37° 55.625	W79° 32.799	752	220	0.34	46	46°NW	11	106	80[e]	17[h]	47	0.70	1.75	0.050
Tennessee (TN)	N36° 16.414	W83° 54.809	418	71	0.30	62	32°SE	14	138	398	17[h]	234	1.01	1.75	0.035
Alabama (AL)	N34° 25.375	W86° 12.400	241	43	0.35	40	10°SE	16	136	220[f]	17[h]	129	0.90	1.75	0.020
Puerto Rico (PR)	N18 18.050	W66 54.401	366	25	0.16	68	5°NE	24	234	613	25[h]	253	0.80	1.75	0.025

[a] Augerable soil depth; [b] Estimated ridgetop erosion rate (E); [c] Soil residence time (SRT) calculated using erosion rate (E) and augerable soil depth (Eq. 1); [d] Glacial till parent material; [e] Augerable soil depth extended an additional 20 cm into underlying sandstone; [f] Lithology at this site includes chert ; [g] Erosion (E) estimate obtained from Be^{10} measurements (West et al., 2013); [h] Erosion estimates constrained to vary between 8 – 26 m My^{-1} in the Appalachians and 8 – 43 m My^{-1} in Puerto Rico (See Appendix A); [i] Estimated as time since soil began forming after the beginning of the recent interglacial; [j] Parameter for bulk density (ρ_b^{0}, Eq. 2); [k] Parameter for bulk density (ρ_b^{max}, Eq. 2); [l] Parameter for bulk density (K, Eq. 2); [m] Bulk density not modeled due to glacial till parent material

Table 2-2. Major elemental chemistry of shale collected across the transect and corresponding depth of sample (d) where applicable. All rock samples were collected at local outcrops with the exception of PlynQ-RF and ALD-10-158, which were recovered from the bottom of soil pits and ALD-10-432, which is a weathered shale chip recovered from the bottom of the augered core.

Site	Sample name	IGSN[a] Number	d m	Al	Ca	Fe	K	Mg	Mn %	Na	P	Si	Ti	Zr ppm	LOI[b]	LOI[c] %
Wales	PlynQ-RF	SSH0000GG	0.35	12.0	0.04	6.77	3.15	1.41	0.43	0.57	0.04	25.1	0.82	164	---	5.30
	ALD-10-01	SSH000STR	---	11.8	0.03	6.40	2.96	1.36	0.33	0.68	0.04	26.3	0.82	154	---	3.88
	ALD-10-02	SSH000STS	---	11.0	0.01	5.77	2.88	1.23	0.21	0.61	0.04	27.1	0.71	137	---	5.12
	ALD-10-03	SSH000STT	---	11.8	0.01	6.73	2.87	1.47	0.23	0.62	0.05	24.4	0.90	175	---	7.61
	ALD-10-04	SSH000STU	---	11.6	0.05	6.45	2.66	1.63	0.13	0.77	0.06	25.9	0.83	215	---	5.02
	ALD-10-06	SSH000STW	---	11.9	0.05	6.17	2.91	1.53	0.21	0.76	0.06	24.8	0.85	186	---	6.86
	ALD-10-07	SSH000STX	---	11.7	0.01	6.45	2.93	1.33	0.29	0.62	0.05	24.3	0.90	210	---	8.38
	ALD-10-08	SSH000STY	---	11.9	0.02	6.82	2.94	1.50	0.62	0.62	0.06	24.9	0.89	185	---	5.23
	ALD-10-09	SSH000STZ	---	11.2	0.07	6.51	2.77	1.41	0.27	0.64	0.06	24.1	0.84	167	---	9.72
	ALD-10-33	SSH000SU0	---	11.7	0.04	6.32	2.97	1.41	0.21	0.64	0.06	24.1	0.85	165	---	8.73
NY	OW-81308-3	---	---	12.0	0.29	5.96	5.19	1.44	0.03	0.08	0.01	25.1	0.77	---	5.10	---
PA	ALD-10-158	SSH000SUA	0.35	12.4	0.03	5.20	4.65	0.68	0.01	0.23	0.05	26.4	1.00	180	---	4.13
VA	TSW-1163	SSH00005C	27.0	12.0	0.03	3.50	5.11	0.89	0.01	0.18	0.05	26.1	0.91	227	5.73	---
	TSW-1164	SSH00005D	29.0	11.3	0.04	3.50	4.86	0.88	0.01	0.16	0.05	27.0	0.88	258	5.51	---
	TSW-1165	SSH00005E	30.0	11.3	0.10	5.37	4.98	1.13	0.30	0.16	0.05	24.7	0.85	200	5.47	---
	TSW-1162[d]	SSH00005B	26.0	6.43	0.23	2.46	2.71	0.58	0.01	0.08	0.11	34.7	0.77	679	2.75	---
	TSW-1165[d]	SSH00005F	36.0	5.19	0.14	7.09	2.29	0.45	0.01	0.07	0.10	33.3	0.68	881	2.37	---

Table 2-3. (cont.)

Site	Sample name	IGSN[a] Number	d m	Al	Ca	Fe	K	Mg	Mn %	Na	P	Si	Ti	Zr ppm	LOI[b] %	LOI[c]
TN	TSW-1212	SSH00006Q	28.0	10.2	0.50	4.41	4.41	1.31	0.06	0.47	0.06	26.9	0.88	257	5.79	---
	TSW-1213	SSH00006R	29.0	10.1	0.60	5.13	5.13	1.44	0.05	0.46	0.04	25.7	0.91	214	5.95	---
	TSW-1214	SSH00006S	30.0	9.19	0.70	3.50	3.62	1.27	0.06	0.54	0.03	27.4	0.90	260	5.61	---
	ALD-10-432	SSH000SUH	3.98	10.4	0.01	6.51	3.92	0.74	0.02	0.17	0.04	26.8	0.85	231	---	6.27
AL	ALD-10-2025	SSH00008J	37.5	9.67	0.17	6.61	4.20	1.08	0.16	0.20	0.05	25.7	0.80	163	6.61	---
	ALD-10-2026	SSH00008K	38.0	9.87	0.17	5.13	4.29	1.14	0.02	0.21	0.03	27.2	0.84	173	6.24	---
	ALD-10-2028	SSH00008M	41.0	9.68	0.08	4.88	4.12	1.03	0.15	0.17	0.04	27.6	0.85	182	6.16	---
PR	ALD-11-03	SSH000SUW	---	4.21	18.9	2.24	0.84	0.99	0.05	1.15	0.07	15.3	0.31	62.0	---	24.8
	ALD-11-93	SSH000SV6	---	4.10	20.6	2.73	0.58	1.24	0.04	0.52	0.05	12.9	0.30	79.7	---	27.7
	Average		---	10.5	1.92	5.30	3.37	1.24	0.18	0.50	0.05	24.7	0.81	182	---	---
	Standard deviation		---	2.24	5.78	1.42	1.17	0.24	0.16	0.26	0.01	3.63	0.17	49.6	---	---

[a] International Geo Sample Number, www.geosamples.org

[b] LOI measured by combustion

[c] LOI calculated by subtracting total oxides from 100

[d] Sandstone samples collected stratigraphically below (TSW-1162) and above (TSW-1165) shale samples used as parent at this site (TSW-1163, TSW-1164, TSW-1165)

Table 2-4. Bedrock plagioclase mineralogy calculated based on rock chemistry and by quantitative XRD using RockJock.

Site	Sample name	IGSN[a] number	Calculated albite	RockJock plagioclase	Full pattern degree of fit[b]
			———————— % ————————		
Wales	PlynQ-RF	SSH000GG	7.4	4.0	0.18
Pennsylvania	ALD-10-158	SSH000SUA	2.6	0.5	0.12
Virginia	TSW-1164	SSH00005D	1.8	3.1	0.18
Tennessee	TSW-1208	SSH00006M	5.6	5.5	0.14
Alabama	ALD-10-2026	SSH00008K	2.2	1.3	0.20
Puerto Rico	ALD-11-03	SSH000SUW	9.5	12.0	0.19

[a] International Geo Sample Number, www.geosamples.org

[b] Full pattern degree of fit between the calculated and measured pattern in RockJock (lower is better)

Table 2-5. Concentrations of Na, Ti and Zr and Loss on Ignition (LOI) for soils collected across the transect and corresponding tau values using Zr as an immobile element at all sites except VA, where corrected Ti values were used as the immobile element. Zr was not measured in NY.

Site	Sample	IGSN[a]	Interval cm	LOI[b]	LOI[c]	Na	Ti	Ti[d]	Zr ppm	$\tau_{Zr,j}$ values Na	Ti	CDF$_T$[f]
						%						
Wales	plnq0-10	SSH000SSM	0 - 10	---	19.4	0.47	0.81	---	166	-0.25	0.03	0.00
	plnq10-20	SSH0000HE	10 - 20	---	12.4	0.50	0.81	---	168	-0.21	0.02	
	plnq20-30	SSH0000HF	20 - 30	---	7.91	0.53	0.80	---	172	-0.17	-0.03	
	plnq30-31	SSH0000HG	30 - 31	---	7.57	0.56	0.77	---	170	-0.13	-0.05	
	plnq31-35	SSH0000HH	31 - 35	---	5.29	0.56	0.80	---	158	-0.06	0.06	
New York	ALD-10-61	SSH0000L8	0 - 5	7.37	---	0.32	0.62	---	---	-0.45[g]	---	0.19
	ALD-10-60	SSH0000L9	5 - 10	5.80	---	0.32	0.61	---	---	-0.45	---	
	ALD-10-59	SSH0000LA	10 - 15	5.35	---	0.30	0.65	---	---	-0.51	---	
	ALD-10-58	SSH0000LB	15 - 20	4.74	---	0.28	0.64	---	---	-0.53	---	
	ALD-10-57	SSH0000LC	20 - 30	4.29	---	0.28	0.57	---	---	-0.48	---	
	ALD-10-56	SSH0000LD	30 - 40	3.80	---	0.27	0.52	---	---	-0.44	---	
	ALD-10-55	SSH0000LE	40 - 50	3.31	---	0.36	0.44	---	---	-0.13	---	
	ALD-10-53	SSH0000LG	60 - 70	2.72	---	0.35	0.40	---	---	-0.07	---	
	ALD-10-49	SSH0000LK	100 - 110	2.12	---	0.50	0.41	---	---	0.30	---	
	ALD-10-45	SSH0000LO	140 - 150	1.64	---	0.41	0.44	---	---	-0.02	---	
	ALD-10-36	SSH0000LS	180 - 190	1.84	---	0.39	0.44	---	---	-0.05	---	
	ALD-10-38	SSH0000LU	200-210	---	---	0.34	0.45	---	---	-0.20	---	
Pennsylvania	ALD-10-163	SSH0000NL	0 – 10	---	6.60	0.21	1.02	---	216	-0.26	-0.15	0.12
	ALD-10-164	SSH0000NM	10 – 20	---	4.83	0.22	1.03	---	211	-0.22	-0.12	
	ALD-10-165	SSH0000NN	20 – 28	---	3.60	0.22	1.01	---	190	-0.10	-0.04	
Virginia[e]	MT-09-032	SSH0000PH	0 – 10	12.5	---	0.04	0.59	0.72	984	-0.71	---	0.33
	MT-09-033	SSH0000PI	10 – 20	4.22	---	0.03	0.60	0.73	661	-0.75	---	
	MT-09-034	SSH0000PJ	20 - 30	3.24	---	0.03	0.46	0.56	718	-0.76	---	
	MT-09-035	SSH0000PK	30 - 40	5.51	---	0.02	0.47	0.55	836	-0.77	---	
	MT-09-036	SSH0000PL	40 - 50	4.66	---	0.04	0.60	0.68	772	-0.67	---	
	MT-09-037	SSH0000PM	50 - 60	5.74	---	0.07	0.55	0.61	808	-0.40	---	
	MT-09-038	SSH0000PN	60 - 70	5.59	---	0.05	0.62	0.68	1244	-0.59	---	
	MT-09-039	SSH0000PO	70 - 80	5.76	---	0.07	0.72	0.75	908	-0.53	---	

Table 2-5 (cont.)

| Site | Sample | IGSN[a] | Interval cm | Elemental concentrations | | | | | | $\tau_{Zr,j}$ values | | CDF$_T$[f] |
| | | | | LOI[b] | LOI[c] | Na | Ti | Ti[d] | Zr | Na | Ti | |
						%			ppm			
Tennessee	ALD-09-17	SSH0000QC	0 - 5	---	16.0	0.13	0.89	---	315	-0.80	-0.22	0.21
	ALD-09-18	SSH0000QD	5 - 10	---	6.48	0.15	1.07	---	375	-0.80	-0.21	
	ALD-09-02	SSH0000QG	10 - 20	---	8.60	0.16	1.00	---	350	-0.77	-0.21	
	ALD-09-03	SSH0000QH	20 - 30	---	7.46	0.15	0.96	---	310	-0.76	-0.15	
	ALD-09-04	SSH0000QI	30 - 40	---	9.19	0.14	0.94	---	300	-0.76	-0.14	
	ALD-09-05	SSH0000QJ	40 - 50	---	9.03	0.16	0.93	---	285	-0.72	-0.11	
	ALD-09-07	SSH0000QL	60 - 70	---	6.72	0.16	0.93	---	280	-0.70	-0.09	
	ALD-09-09	SSH0000QN	80 - 90	---	7.22	0.18	0.93	---	265	-0.66	-0.04	
	ALD-09-11	SSH0000QP	100 - 110	---	7.28	0.16	0.92	---	270	-0.69	-0.07	
	ALD-09-13	SSH0000QR	120 - 130	---	7.53	0.15	0.85	---	255	-0.70	-0.09	
	ALD-09-15	SSH0000QT	145 - 150	---	8.26	0.17	0.90	---	215	-0.60	0.15	
	ALD-09-16	SSH0000QU	150 - 155	---	5.89	0.17	0.92	---	245	-0.64	0.03	
	ALD-10-64	SSH0000QY	160 - 170	---	7.23	0.18	0.88	---	209	-0.57	0.15	
	ALD-10-67	SSH0000R1	190 - 200	---	6.49	0.17	0.89	---	218	-0.61	0.12	
	ALD-10-70	SSH0000R4	210 - 220	---	6.41	0.18	0.91	---	217	-0.58	0.15	
	ALD-10-73	SSH0000R8	230 - 240	---	6.95	0.18	0.83	---	180	-0.50	0.26	
	ALD-10-75	SSH0000R9	240 - 250	7.67	---	0.19	0.80	---	160	-0.39	0.38	
	ALD-11-401	SSH0000RP	260 - 270	7.67	---	0.19	0.90	---	230	-0.53	0.01	
	ALD-11-404	SSH0000RS	290 - 300	7.62	---	0.17	0.86	---	238	-0.63	-0.01	
	ALD-11-426	SSH0000RW	330 - 340	8.94	---	0.16	0.91	---	270	-0.70	-0.08	
	ALD-11-429	SSH0000RZ	360 - 370	6.65	---	0.19	0.91	---	277	-0.66	-0.09	
	ALD-11-432	SSH0000S2	390 - 398	7.11	---	0.18	0.87	---	254	-0.64	-0.05	

Table 2-5 (cont.)

Site	Sample	IGSN[a]	Interval cm	LOI[b]	LOI[c]	Na	Ti	Ti[d]	Zr	Na	Ti	CDF_T[f]
							Elemental concentrations %		ppm	$\tau_{Zr,j}$ values		
Alabama	ALD-10-114	SSH0000T3	0 - 10	---	4.13	0.02	0.36	---	314	-0.95	-0.76	0.38
	ALD-10-115	SSH0000T4	10 - 20	---	8.44	0.02	0.56	---	331	-0.94	-0.65	
	ALD-10-116	SSH0000T5	20 - 30	---	6.58	0.03	0.62	---	380	-0.94	-0.66	
	ALD-10-117	SSH0000T6	30 - 40	---	6.96	0.02	0.54	---	265	-0.94	-0.57	
	ALD-10-118	SSH0000T7	40 - 50	---	5.76	0.02	0.60	---	236	-0.91	-0.47	
	ALD-10-121	SSH0000TA	60 - 70	---	7.99	0.02	0.63	---	224	-0.91	-0.41	
	ALD-10-123	SSH0000TC	90 - 100	---	6.55	0.02	0.58	---	197	-0.89	-0.39	
	ALD-10-125	SSH0000TE	110 - 120	---	8.94	0.02	0.60	---	187	-0.89	-0.33	
	ALD-10-127	SSH0000TG	130 - 140	---	9.04	0.03	0.62	---	168	-0.85	-0.24	
	ALD-10-129	SSH0000TI	150 - 155	---	7.31	0.01	0.35	---	129	-0.90	-0.44	
	ALD-11-506	SSH0000TP	170 - 180	6.68	---	0.03	0.55	---	153	-0.85	-0.25	
	ALD-11-508	SSH0000TR	190 - 200	8.04	---	0.04	0.57	---	172	-0.79	-0.32	
	ALD-11-510	SSH0000TT	200 - 210	7.30	---	0.06	0.54	---	172	-0.71	-0.35	

Table 2-5 (cont.)

Site	Sample	IGSN[a]	Interval cm	LOI[b]	LOI[c]	Na	Ti	Ti[d]	Zr ppm	$\tau_{Zr,j}$ values Na	Ti	CDF$_T$[f]
							Elemental concentrations %					
Puerto Rico	ald-11-13	SSH0000VO	0 - 8	---	21.5	0.05	0.69	---	139	-0.97	0.03	0.50
	ald-11-14	SSH0000VP	8 - 10	---	18.4	0.04	0.72	---	153	-0.98	-0.02	
	ald-11-15	SSH0000VQ	10 - 15	---	17.4	0.04	0.72	---	142	-0.98	0.06	
	ald-11-16	SSH0000VR	15 - 20	---	14.9	0.03	0.74	---	150	-0.98	0.02	
	ald-11-17	SSH0000VS	20 - 30	---	13.9	0.03	0.73	---	142	-0.98	0.07	
	ald-11-18	SSH0000VT	30 - 40	---	14.9	0.02	0.71	---	134	-0.98	0.10	
	ald-11-19	SSH0000VU	40 - 50	---	13.0	0.02	0.72	---	141	-0.99	0.06	
	ald-11-25	SSH0000W0	100 - 111	---	18.5	0.03	0.78	---	130	-0.98	0.24	
	ald-11-30	SSH0000W5	150 - 160	---	13.8	0.02	0.76	---	133	-0.98	0.18	
	ald-11-38	SSH0000WA	200 - 210	---	14.6	0.02	0.73	---	132	-0.98	0.16	
	ald-11-43	SSH0000WF	250 - 260	---	12.7	0.02	0.71	---	127	-0.98	0.17	
	ald-11-48	SSH0000WK	300 - 310	---	12.6	0.02	0.67	---	122	-0.99	0.14	
	ald-11-53	SSH0000WP	350 - 360	---	13.1	0.02	0.65	---	127	-0.98	0.06	
	ald-11-58	SSH0000WU	400 - 410	---	13.1	0.03	0.74	---	155	-0.98	-0.01	
	ald-11-63	SSH0000WZ	450 - 460	---	13.2	0.04	0.87	---	152	-0.98	0.19	
	ald-11-76	SSH0000X5	500 - 505	---	12.9	0.15	0.80	---	127	-0.90	0.31	
	ald-11-86	SSH0000XF	570 - 580	---	8.88	1.78	0.76	---	130	0.21	0.21	
	ald-11-92	SSH0000XL	625 - 632	---	8.24	2.20	0.77	---	120	0.64	0.33	

[a] International Geo Sample Number, www.geosamples.org

[b] LOI measured by combustion

[c] LOI calculated by subtracting total oxides from 100

[d] Recalculated Ti concentrations assuming loss of Ti similar to Ti depletion observed in the upper 80cm of TN

[e] VA tau values were calculated using reconstructed Ti as the immobile element

[f] CDF calculated for the upper 1 m of each soil profile using the equation CDF = $(1 - [Zr]_{rock} / [Zr]_{soil})$ (Riebe et al., 2004)

[g] Tau values for NY calculated using Ti as the immobile element (Zr data not available) and the average of the bottom four samples as parent

Table 2-6. Surface tau value ($\tau_{Na,surface}$), total mass loss of Na (M_{Na}) and Na loss rate (Q_{Na}) for each transect site.

Site	$\tau_{Na,surface}$	M_{Na} mol m^{-2}	Q_{Na} mol m^{-2} yr^{-1}
Wales	-0.25	18.0	0.0018
New York	-0.45	91.6	0.0092
Pennsylvania	-0.26	8.06	0.0005
Virginia	-0.71	37.4	0.0008
Tennessee	-0.80	850	0.0036
Alabama	-0.95	260	0.0020
Puerto Rico	-0.97	4100	0.0163

Chapter 3

Shale weathering and erosion across a latitudinal climosequence

Abstract

Regolith, the mantle of physically, chemically, and biologically altered material overlying parent material, covers much of Earth's continents but the rates and mechanisms of regolith formation are not well known. To quantify the influence of climate on shale weathering rates, a transect of study sites has been established on Silurian shale along a climatic gradient as part of the Susquehanna Shale Hills Critical Zone Observatory, PA, USA. The climate gradient is bounded by a cold/wet end member in Wales and a warm/wet end member in Puerto Rico; in between, temperature and rainfall increase to the south through New York, Pennsylvania, Virginia, Tennessee and Alabama. Soil depth and geochemistry were measured both on ridgetops (where inputs are only from the atmosphere) and hillslopes (where inputs are derived from upslope sediment transport and the atmosphere). The depth of ridgetop regolith, defined as the material which is hand-augerable, increases from north to south, with shallow regolith (~ 30 cm) in Wales and Pennsylvania and increasingly deep regolith to the south (632 cm in Puerto Rico). Regolith depth on slopes, however, vary less along the transect, ranging from 52–86 cm across the Appalachian sites. Thus, ridgetop regolith depth varies more with climate than slope regolith thickness. The extent of sodium depletion at the land surface (as determined by the mass transfer coefficient) in ridgetop and slope soils

increases from ~ 20% in the north to 100% depletion in the south, documenting a

transition from kinetic to increasingly transport limited systems. These observations are

roughly consistent with end members of a simple reactor-on-a-slope model, where

transport limited weathering produces thicker and highly depleted soils on both ridgetops

and slopes and kinetically limited weathering produces shallower, slightly depleted soils

at the ridgetop and slope surface. Transport limitation is more likely under warm and wet

climate conditions. With respect to Mg loss, a transition toward transport limitation is

also observed, but no site is completed depleted of Mg at the soil surface. This is likely

due to Mg dissolution from primary clay minerals and partial re-precipitation in Mg-

bearing secondary minerals. Meteoric ^{10}Be measurements at ridgetop sites document

increasing residence time for the total regolith from north to south across the transect (10

ky to 120 ky) but similar erosion rates within error (~40 m My^{-1}). Given the temperature

dependence of weathering of plagioclase and chlorite-like minerals as demonstrated in

elemental depletion in the soils, we conclude that climate is an important factor

controlling total regolith thickness on shale under steady state across this climate

gradient. These efforts help elucidate the role of climate on regolith and landscape

evolution and provide data to validate hillslope evolution models.

Introduction

The formation of regolith, the weathered material found along the upper meters of

the Earth's surface, influences landscape evolution, nutrient cycling and the delivery of

sediment to streams and oceans. Regolith formation is especially important to humans in

that this material provides the foundation for agriculture, which is tasked with feeding

Earth's increasing population (Buringh, 1989). Humans are depleting regolith at

unprecedented rates (Hooke, 2000; Wilkinson and McElroy, 2007) yet we are unable to

predict the rate of regolith formation that will counter these losses (Brantley et al., 2007).

The inability to predict regolith depth or formation rates presents a fundamental challenge

to the Earth sciences, one that is especially important to understand as climate changes in

the future may alter the balance of regolith production and denudation in many

landscapes (NRC, 2001).

Numerous researchers have worked toward quantifying regolith formation on

dominant lithologies including granite (e.g. Pavich et al., 1989; White et al., 1998; Riebe

et al., 2004; Dixon et al., 2009; Rasmussen et al., 2011) and basalt (e.g. Chadwick et al.,

2003; Ma et al, 2012). The formation of regolith on shale, although comprising

approximately 25% of continental lithologies (Amiotte-Suchet et al., 2003), has not been

as widely investigated. Shale is predominantly composed of clay minerals that weather

slowly but erode quickly (Hack, 1960), thus we might expect that shale weathering will

be kinetically limited, i.e., weathering is limited by mineral reaction rates rather than the

erosive transport rate of material from the system (Brantley and White, 2009). In fact,

kinetically limited weathering has been inferred in the shale catchment of the

Susquehanna Shale Hills Critical Zone Observatory (SSHO) located in central

Pennsylvania, USA (Jin et al., 2010).

The weathered profile, here referred to as regolith, is the material that has been

measurably altered by (biogeo)chemical and physical weathering of bedrock (Riebe et al.,

2003). Regolith can be further characterized by mobile and immobile layers, where the

mobile portion of the weathered regolith (roughly equivalent to the soil) moves

downslope and the immobile layer, often referred to as saprolite, is weathered but is not

transported downslope (Gilbert, 1909; Riebe et al., 2004; Heimsath et al. 2001). In some

cases the mobile layer is equivalent to the entire weathered profile (i.e. there is no

immobile saprolite) meaning all weathered material can be transported downslope. In

deeper regolith, however, only a portion of the profile is transported downslope and this

boundary can be difficult to define. Previous work has characterized mobile regolith

(soil) as material that has been influenced by physical mixing whereas immobile regolith

(saprolite) retains both inherited structure and mechanical strength from the bedrock

(Heimsath et al., 1999; Riebe et al., 2004). Here, we define mobile regolith as the layer

between the land surface and the depth at which sub-angular blocky pedogenic structure

is no longer observed. Below this depth, the structure of the parent material is often

visible (saprolite). The presence of mobile soil indicates that weathering, downslope

movement, and bioturbation erased much of the initial parent characteristic structure

whereas saprolite structure indicates weathering has not erased the initial parent material

structure.

The presence of regolith on hillslopes is influenced both by chemical weathering

that produces material and physical processes that remove it from the landscape (Gilbert,

1909; Kirkby, 1971). The use of cosmogenic ^{10}Be isotopes provides a way to link

chemical and physical weathering across landscapes (Riebe et al., 2004; Dixon et al.,

2009). Most studies rely on isotopic concentrations of *in situ* ^{10}Be that are measured in

stream sediment samples to infer an average erosion rate for a watershed (e.g. Brown et

al., 1995; Bierman and Steig, 1996; Granger et al., 1996). Using this approach, across a

variety of lithologies in the Appalachian Mountains erosion rates estimated from *in situ* cosmogenic ^{10}Be measurements range from 8 – 26 m My^{-1} (Portenga and Bierman, 2010). Alternatively, meteoric ^{10}Be, which is delivered via precipitation to Earth's surface and accumulates over the lifetime of the soil (Willenbring and von Blanckenburg, 2011), provides a powerful tool to quantify the regolith residence time (Pavich et al., 1986) as well as the downslope transport of regolith (McKean et al., 1993; West et al., 2013). Assuming steady state regolith thickness, where regolith production is balanced by removal via erosion, the inventory of meteoric ^{10}Be in regolith can be used to estimate weathering duration and erosion rate in stable or eroding landscapes (Brown et al., 1988). Such an approach has been employed at the SSHO to infer an erosion rate of 26 m My^{-1} at the ridgetops (West et al., 2013).

Recently, researchers have sought to use soil production models to explicitly explore the effect of climate variables such as precipitation on hillslope regolith (Pelletier and Rasmussen, 2009; Norton et al., 2014). In one set of models, regolith production on convex-up hillslopes provided insight into the end members of transport and kinetic weathering limitation (Lebedeva et al., 2010; Lebedeva and Brantley, 2013). In these models, weathering of a model rock (albite + quartz) underlying a hillslope results in regolith material (quartz + kaolinite) that moves downslope along the hillside. This modeling shows slightly enhanced chemical depletion at the land surface on ridgetops compared to the surface of hillslopes in kinetically limited weathering regimes. In contrast, the models show similar chemical depletion for ridgetop and slope surficial soils when the regime is transport limited.

Although such models can now explore the importance of climate variables, the relative importance of climate in controlling weathering and erosion is still debated. For example, Riebe et al. (2001), in a study of 14 granitic watershed in North America, concluded that long-term granite weathering rates were strongly correlated with physical erosion rates but only weakly correlated with climate. In contrast, our previous work on 7 shale sites in North America documented that the extent of feldspar weathering varied significantly with climate (Dere et al., 2013). We proposed that unlike the study by Riebe et al. (2001) that included tectonically active sites, the effects of climate on shale weathering could be observed because the sites experience similar erosion rates and minimal tectonic influences. Similarly, recent modeling efforts by Norton et al. (2014) concluded that the effects of climate on regolith thickness are most pronounced in model simulations of hillslope evolution where erosion is low and temperature and precipitation are high.

A transect of sites underlain by shale in a range of climates was established based on initial work at SSHO (Dere et al., 2013) (Fig. 3-1). Across these sites, mean annual temperature (MAT) increases fairly linearly from the coldest site in Wales, down the U.S.A. Appalachian Mountains in New York (NY), Pennsylvania (PA), Virginia (VA), Tennessee (TN) and Alabama (AL), with the warmest site in Puerto Rico (PR) (Table 3-1). Mean annual precipitation (MAP) increases to a lesser extent south through the Appalachian Mountains, with Wales and PR serving as two very wet end members (Table 3-1). In other words, as temperature increases from Wales to NY and south to PR, precipitation shows no such variation, but rather defines two sets, moderately wet sites (1 m < MAP < 2 m yr^{-1}) and extremely wet sites (MAP ~ 2.5 m yr^{-1}).

Initial efforts across the transect characterized weathering processes on ridgetops, where net fluid flow is, to first approximation, largely one-dimensional down to bedrock, at which point flow either recharges into bedrock or travels laterally (Jin et al., 2010). In contrast, at any position on the hillslope fluid flow is both vertical (in the unsaturated layers) and lateral (in saturated zones of relatively impermeable horizon boundaries) (Jin et al., 2011; Thomas et al., 2013). For a so-called "diffusive" system where transport is proportional to slope, the upper part of the idealized hillslope is convex-up and sediment transport is always downslope without accumulation of sediment. Conversely, the lower part of the hillslope is concave up, resulting in the accumulation of sediment. In this paper we focus on the convex-up part of the hillslope to consider how chemical weathering influences the depth and depletion of regolith as a function of position on the hillslope in different climates. In addition, we address the use of meteoric ^{10}Be isotopes measured in regolith across the transect to determine soil residence time (SRT), or the duration of weathering, as well as erosion rates.

Methods

Site characteristics

The transect of study sites was established in 2010 as part of the SSHO and is described in detail in Dere et al. (2013). The transect includes the Plynlimon experimental forest near Llanidloes, Wales, United Kingdom, sites in the Appalachian province (USA) including Chadwicks, New York (NY), Pine Grove Mills, Pennsylvania

(PA) (site of the SSHO CZO), Goshen, Virginia (VA), Norris, Tennessee (TN), Lake Guntersville, Alabama (AL) and Scottsboro, AL, and the lowest latitude site in Juncal, Puerto Rico (PR), USA (Fig. 3-1). The majority of the sites are underlain by organic-poor, iron-rich Silurian shale of the Rose Hill Formation (or stratigraphic equivalent), providing a parent material common to all sites. Exceptions are the site in NY, where Silurian shale is covered by glacial till and PR, where the study site is underlain by the Oligocene San Sebastian Formation. Extensive care was taken to locate sites where all variables other than climate were as similar as possible (Dere et al., 2013). Nonetheless Dere et al. noted several anomalous observations at the TN site, which prompted further investigation of the depth profiles in that location.

Slope samples were obtained from the convex-up hillslopes 50 – 280 m downslope of the ridgetop sampling sites (Table 3-1) at all transect sites except those described herein. Due to recent clearing of trees on the upper part of the slope in Wales, a sample was taken farther downslope on the concave upward part of the slope where vegetation was undisturbed. In VA, as described by Dere et al. (2013), the shale at the ridgetop is extremely thin and the slopes on either side of the ridge are underlain by sandstone: no slope samples were collected in VA. At the ridgetop in Alabama, regolith included large chert clasts originating from the parent shale at this latitude. Given this limitation, a slope was sampled on the opposite limb of the folded shale unit at the Scottsboro Solid Waste Authority in Scottsboro, AL, approximately 36 km northeast of the ridgetop sampling site. Shale beds at the AL slope site dip 30º NW; in contrast, at the ridgetop site, beds dip 10º SE (Table 3-1). Samples were also collected on a slope in NY and like the ridgetop site, the slope parent material is glacial till.

Regolith sampling

Regolith samples were collected by both hand augering and digging of pits (Table 3-1). At every ridgetop site, samples were collected from the mineral soil surface, defined as the layer initiating at the interface of the organic and mineral horizons down to the depth of refusal to hand augering, using a 5 cm diameter auger. Pits were also dug (maximum depth of 2 m) on ridgetops at all sites. In TN and AL, deeper sampling was completed by hand augering into the bottom of the soil pits. On the slopes, pits were excavated by hand to bedrock or the maximum depth possible. Samples were taken at 10 cm intervals from a side wall of each soil pit. In PR, the slope was sampled downslope from the ridgetop site by digging a trench vertically through a stream bank down to bedrock and collecting samples from the side of the trench as described above.

Regolith chemistry

Regolith samples were air dried and homogenized in a plastic bag before splitting the bulk sample four times with a riffle soil splitter. One split was ground and sieved to < 150 μm for geochemical analysis. For each ground sub-sample, 100 mg were fused with 1 g of lithium metaborate for 10 minutes at 950 °C followed by dissolution in 5% nitric acid (Medlin et al., 1969). Solutions were analyzed for major elements by inductively coupled plasma atomic emission spectroscopy (Perkin-Elmer Optima 5300DV ICP-AES, Waltham, MA) at the Materials Characterization Laboratory at Penn State University (MCL). Analytical error for each element was estimated at ± 3%.

To avoid the inclusion of minor fragments of gneiss from the Adirondack Mountains in the till, NY samples from the ridgetop site were analyzed using only the < 2 mm fraction rather than the bulk fraction. A Phillips PW2404 X-ray Fluorescence Spectrometer (PANalytical, Almelo, The Netherlands) at Colgate University, Hamilton, NY was used to determine elemental concentrations of ridgetop soil samples at this site, while the bulk soil was analyzed for slope samples at Penn State University (MCL) as described above.

Total soil carbon and nitrogen were analyzed by combustion on a CE Instruments Elemental Analyzer EA 1110 (CE Instruments Ltd., Lancashire, United Kingdom) (Bingham, 2012). Clay content was determined by wet sieving and centrifuging bulk soil samples, followed by laser diffraction analysis using a Malvern Mastersizer "S" V. 2.19 (Malvern Instruments Ltd., Malvern, United Kingdom) at the MCL (Jackson, 1974; Soil Survey Staff, 2004; Konert and Vandenberghe, 1997). See Chapter 4 for more details on this method.

[10]Be concentrations and soil residence time

[10]Be concentrations were measured on ridgetop sites to estimate the soil residence time (SRT). SRT was defined as the time particles spend in the weathered profile – here interpreted as the hand-augerable regolith. Depth-weighted splits of bulk regolith from ridgetop cores were amalgamated to produce one sample that represented the entire regolith thickness at all sites. No analysis was completed in NY due to the glacial till parent material. The entire sampled thickness was amalgamated in Wales, PA, VA, AL

and PR. In TN, samples from 0 – 160 cm and 160 – 398 cm depths were amalgamated

separately to measure ^{10}Be concentrations in the mobile and immobile layers,

respectively (see Results for more detail).

All samples and process blanks were prepared at the University of Vermont

cosmogenic nuclide extraction laboratory. Samples were powdered in a steel shatter box

and extracted for meteoric ^{10}Be following a modified flux fusion method (Stone, 1998).

Approximately 0.5 g of finely milled material was mixed with KHF, NaSO$_4$ and ~300 μg

of ^{9}Be- carrier (SPEX brand), which was then fused in a Pt crucible over a natural gas/O$_2$

flame for several minutes until the resulting melt was clear. Following cooling, the

solidified fusion cake and crucible were plunged into a Teflon beaker with Milli-Q (18.2

Mohm) water for a 24 hour leaching period. Excess K in the leachate was removed by

precipitation with HClO$_3$. The remaining Be was precipitated as a hydroxide and burned

to BeO, followed by mixing with an equimolar amount of Nb metal powder. Samples

were loaded into stainless steel cathodes and ^{10}Be/^{9}Be ratios were measured by

accelerator mass spectrometry (AMS) at the Center for Accelerator Mass Spectrometry,

Lawrence Livermore National Laboratory.

^{10}Be isobaric interference was reduced by obtaining multiple data acquisitions of

each target using post accelerator stripping. Target analyses were repeated two to four

times and three secondary standards were repeatedly run to verify isotopic linearity over

a range of ratios. All results were normalized to standards in the 07KNSTD series by

using a primary standard with a reported ^{10}Be/^{9}Be ratio of 2.85×10^{-12} (Nishiizumi et al.,

2007), with standard-corrected isotopic ratios ranging from 2.49×10^{-12} to 1.06×10^{-11}. A

blank correction was made by subtracting the average of the process blanks run with four

sample batches (n = 4, σ = 2.1 ± 3.2 x 10^{-14}) from each sample ratio, although most

samples contained abundant ^{10}Be with high average ratios rendering the blank correction

inconsequential. Ratios were converted to ^{10}Be concentrations (at g^{-1} sample) to represent

depth-average concentrations of meteoric ^{10}Be in ridgetop soils at each site.

Meteoric ^{10}Be inventories were calculated using the expression from Brown et al.

(1988),

$$I_{Be} = \int_{z_b}^{z} N\rho_p dz \tag{1}$$

where I_{Be} is the total inventory of ^{10}Be (at cm^{-2}) calculated for a given sample, z is the

elevation of the land surface (cm), z_b is the elevation of the bedrock-regolith interface

(cm), N is the measured ^{10}Be concentration (at g sample^{-1}), ρ_p is the depth-averaged

regolith density of the sample (g cm^{-3}), averaged from values in Table 3-2, and dz is the

sample depth interval (cm). The total sampling depth should extend to the deepest

penetration of meteoric ^{10}Be to calculate I_{Be}. If we assume a steady state regolith ^{10}Be

inventory where additions from delivery equal losses to solution and decay, the SRT (y)

can be calculated from (Pavich et al., 1985):

$$SRT = \left(\frac{-1}{\lambda}\right) \ln\left(1 - \frac{\lambda I_{Be}}{D}\right) \tag{2}$$

Here, λ is the radioactive decay constant for ^{10}Be (5.1 x 10^{-7} y^{-1}) (Nishiizumi et al., 2007)

and D is the delivery rate (at cm^{-2} y^{-1}). We assumed a constant D that could be calculated

from Graly et al. (2010), using latitude and modern MAP values reported by Dere et al.

(2013) for each site (Table 3-2). In Eq. 2, as long as sampling extends to the entire depth

of ^{10}Be penetration, soil can be considered a bucket collector for ^{10}Be: a longer SRT

means the bucket has been accumulating ^{10}Be over a longer period of time. However,

some loss of ^{10}Be can also occur due to solubilization or erosion; therefore, SRT estimated using Eq. 2 is a minimum value.

An alternate statement of mass balance can be developed assuming that the depth-averaged meteoric ^{10}Be concentration in the total regolith is *Cm* (at cm^{-3}) and chemical solubilization is minimal (Brown et al., 1988; West et al., 2014):

$$E = \frac{(D - \lambda I_{Be})}{C_m} \tag{3}$$

Here, E is the erosion rate (cm y^{-1}) and I_{Be} is the total inventory of ^{10}Be in the sampled regolith (Pavich et al., 1985). From E and the assumption that the mobile soil thickness is constant in time, we can solve for SRT as follows:

$$SRT = \frac{L}{E} \tag{4}$$

where *L* is the total thickness (cm) of the profile accumulating ^{10}Be. Once again, we assume that the augerable depth is equivalent to the depth to which meteoric ^{10}Be can penetrate. Implications of this assumption are discussed later. When the values of SRT and E are the same based on Eq. 2 and Eq. 4 (SRT) or Eq. 3 and 4 (E), the system is considered to be in steady state.

Results

Ridgetop and slope regolith depth

Augerable regolith depth, which is here defined either as the depth of auger penetration (on ridgetops) or of a hand-dug pit (on slopes), increases on the ridgetops

from north to south from Wales to PA (35 and 30 cm, respectively) to PR (632 cm) (Fig. 3-2, Table 3-1). NY soil depth is very deep (> 150 cm) and this is attributed to the unconsolidated nature of the glacial till parent material. In the northern sites (Wales and PA), auger refusal occurs at the top of bedrock. In contrast, at augering refusal in TN and AL, bedrock material was not recovered in the final augered sample. It is possible that a chert-rich layer in AL precluded deeper augering. In the most problematic case (VA), the soil and weathering front extends through shale into an underlying sandstone such that no unweathered shale parent material remained to be sampled. In NY, ridgetop and slope regolith are similarly thick (210 and 190 cm, respectively) and represent a fundamentally different parent material (till) weathering at this site. For this reason, NY is not included in subsequent calculations.

The thicknesses of regolith developed on hillsides downslope of the ridgetop profiles in this study also increases from north to south although the increase in thickness is much smaller than that observed for ridgetop regolith. Slope profiles increase from 52 cm in Wales to 90 cm in AL and are deepest in PR (400 cm) (Table 3-1). Although a north to south thickening was observed down the Appalachian sites, the variation was within one standard deviation of the mean (78 ± 17 cm). In Wales and PA, the thickness of hillslope regolith is equivalent to or slightly thicker than regolith on the ridgetop. For example, in the SSHO in PA where the largest dataset is available, more than 31 ridgetop and 18 hillslope sites have been investigated, with an average ridgetop depth of 32 ± 13 cm and slope depth of 42 ± 13 cm. In contrast, toward the south we observed slope regolith that was thinner than ridgetop sites.

To validate these observations across a larger scale we investigated soil depths reported in the gridded Soil Survey Geographic (gSSURGO) database (Soil Survey Staff, 2014). In general, the soil depths reported in this study are greater than those reported in the gSSURGO database because soils in that database are usually only investigated to a depth of 1.5 m (Fig. 3-3). Nevertheless gSSURGO shows that the depth to shale bedrock is < 75 cm in PA and >150 cm in AL and PR (e.g. Soil Survey Staff, 2012a, 2012b, 2012c, 2012d, 2012e, 2012f, 2014).

Mobile vs. immobile regolith

In the shallow soils of Wales and PA, auger refusal occurs at fractured bedrock. The entire augerable depth is therefore equivalent to the mobile layer at these sites. In VA and AL, sub-angular blocky structure is observed throughout the regolith so the total sampled depth is also the mobile layer. In PR, sub-angular blocky structure is observed only to a depth of 350 cm, defining the mobile/immobile boundary. In TN, as discussed below in more detail, sub-angular blocky structure is observed down to 160 cm, below which platy structure is observed. Thus, only the upper 160 cm is considered mobile.

In TN, examination of elemental geochemistry, clay, carbon and nitrogen content revealed unique observations (see Fig. 4-7 in Chapter 4). First, strong sub-angular blocky structure is observed in the upper 160 cm but platy structure similar to fractured shale bedrock is observed below. Second, clay films indicative of clay translocation are present as deep as 119 cm, then absent from 160 cm to 220 cm, and once again present from 220 – 330 cm. No clay films are observed below 330 cm. Third, clay minerals and carbon,

which often translocate and concentrate together, increase at the depths which contain

clay films. Fourth, redoximorphic features, including Fe and Mn concentrations and

depletions, are observed between 45 and 160 cm, below which the matrix is gleyed with

very few Fe and Mn concentrations. Abundant redoximorphic features are again observed

between 220 and 330 cm, below which point they are weakly developed in the gleyed

matrix. Fifth, coincident with the zone between 220 and 330 cm where clay films are

observed and clay content increases, Al, Fe, K, Si, and to a lesser extent Na and Mg, are

enriched.

Regolith profile chemistry

In general, concentrations of Mg, and to a lesser extent Na, increase with

increasing depth on both ridgetop and slope soils while Ti and Zr decrease with

increasing depth (Table 3-3). Parent shale chemistry for each site is derived from Dere et

al. (2013) based on local sampling of outcrops and/or rocks from the bottom of pits.

Meteoric ^{10}Be, soil residence time and erosion

Across the transect, ^{10}Be concentrations range from 2.1 to 4.9 x 10^8 at g^{-1}, with

the lowest concentrations at the end member sites (Wales and PR). Concentrations

decrease from PA to AL (Fig. 3-4a, Table 3-2). TN is an exception to this trend, with

^{10}Be concentration in the amalgamated total depth sample of 1.5 x 10^8 at g^{-1}. ^{10}Be

inventories increase systematically north to south across the transect from 8.0 x 10^9 at

cm^{-2} to 1.8 x 10^{11} at cm^{-2} (Fig. 3-4b, Table 3-2). Based on Eqn. 2, a doubling of the ^{10}Be inventory results in a two-fold increase in SRT. Therefore, both the ^{10}Be inventory in total regolith and SRT increase down the transect (Fig. 3-4b, c). ^{10}Be delivery rate is also significantly higher in Wales compared to all other sites (5.2 x 10^6 at cm^{-2} y^{-1}) (Table 3-2).

As calculated using Eq. 2, Wales has the shortest SRT at 1.6 ky and PR has the longest at 120 ky. SRT ranges in the Appalachian sites from 11 ky to 47 ky (Table 3-2, Fig. 3-4c). These soil residence times are about half as large as previously estimated based on average erosion rates from the literature across the Appalachian Mountains and PR (Dere et al., 2013). Briefly, Dere et al. used Eq. 4 to calculate SRT by using published estimates of E equal to 17 ± 9.0 m My^{-1} for sites in the Appalachian Mountains (excluding NY) and 25 ± 17 m My^{-1} in PR. For comparison, SRT calculated using this previous approach varied from 17 ky to 250 ky across the transect.

We also calculated values of E using Eq. 3. These values were observed to be constant within one standard deviation from PA to PR ($\sim 45 \pm 14$ m My^{-1}) except for TN where the value based on the total regolith was within two standard deviations (92 ± 26 m My^{-1}) (Fig. 3-4d, Table 3-2). Wales is the only outlier, with an estimated E of 220 ± 57 m My^{-1}. This E value in Wales is similar to rapid erosion rates globally (e.g., 270 ± 140 m My^{-1} reported for the Swiss Central Alps, Wittmann et al., 2007). With the exception of PA, the erosion rates calculated with Eq. 3 are slightly greater than values reported in the literature for sites in the Appalachian Mountains ($4 - 27$ m My^{-1}, Matmon et al., 2003; Clifton and Granger, 2005; Reuter, 2005; Sullivan, 2007; Hancock and Kirwan, 2007; Bierman et al., 2008, 2009; Duxbury, 2009; Portenga, 2011; Portenga and Bierman,

2011; Miller et al., 2013) but are within error of rates reported for PR (8 – 67 m My^{-1}) (Brown et al., 1995, 1998; Riebe et al., 2003; Portenga and Bierman, 2011). The slightly larger E values presented here could be a systematic difference based on the use of meteoric ^{10}Be since previous E estimates are largely derived from *in situ* ^{10}Be measurements; *in situ* ^{10}Be is produced from the interaction of cosmic radiation within mineral lattices in regolith near the surface (Willenbring and von Blanckenburg, 2010).

We can also use Eq. 4 to calculate SRT and E for each transect site assuming that *L* is equal to the total thickness of each profile. We observe similar values for SRT using Eq. 2 and Eq. 4 and for E using Eq. 3 and Eq. 4 at all sites (Fig. 3-4c, d; Table 3-2). SRT values reported in Table 3-2 are considered minima and the erosion rates are considered maxima because they are based on meteoric ^{10}Be inventories in the regolith. Without deeper samples it is impossible to ascertain if all ^{10}Be was retained in the sampled interval. We only have deeper samples in two sites. Specifically, measurement to a depth of 26 m in a drilled core from SSHO in PA showed that >80% of the total meteoric ^{10}Be inventory was retained in the uppermost meter of regolith and bedrock (West et al., 2013). This puts a constraint on the likely error in PA. Deeper^{10}Be sampled at the TN site is discussed extensively below.

Discussion

Ridgetop and slope regolith depth

The trend of increasing regolith depth at ridgetops as a function of increasing MAT was anticipated based on many observations by previous researchers in which higher temperatures in humid environments correlate with thicker weathered profiles (e.g. Strakhov, 1967). Similarly, the mobile soil thickness also increases across the transect. However, regolith on the slope positions across the Appalachians are equal within one standard deviation of the mean (Fig. 3-2). Thus ridgetop regolith thickness is a stronger function of MAT than hillslope regolith thickness.

The TN site is anomalous in terms of several characteristics: for example, the augerable depth at the ridgetop is thicker than the warmer AL site (Fig. 3-2). In addition, the presence of clay films at two different depth zones separated by a zone of no clay films is unusual. Given that soil profiles generally do not include a zone that lacks clay films at mid-depths, we considered several alternate explanations. First, we explored whether the deep regolith had developed as a paleosol during warmer and wetter conditions of the Sangamonian (Interglacial) Stage ($\sim$ 100 ky) (Cadwell and Muller, 2004). At that time, both clay and organic matter could have illuviated deep into the profile (Appendix B). Then, during the Last Glacial Maximum (LGM) ($\sim$ 25 ky), cold temperatures, reduced precipitation and permafrost (Clark and Ciolkosz, 1988; Cadwell and Muller, 2004) could have limited production of clays at the surface, eliminating the translocation of clay and creating a clay film-free zone overlying the deep clay film-containing zone (Appendix B). As temperature and precipitation increased following the

LGM (Cadwell and Muller, 2004), weathering could have produced new clays, creating the shallow zone of translocated clays near the land surface (Appendix B). The problem with this scenario is that the [10]Be inventory of the total TN profile yields an SRT of ~43 ky, i.e., younger than expected if the paleosol formed during the Sangamonian (Table 3-2).

An alternative interpretation of the observed patterns in TN is the introduction of laterally transported clay material moving along saprolite fractures at depth. Such a phenomenon has been hypothesized by other researchers near the TN site (Driese et al., 2001; McKay et al., 2005). For example, Driese et al. (2001), studying saprolite developed on Cambrian shale and limestone near Oak Ridge, TN, observed an upper zone devoid of clay films (1 m thick) overlying a zone (1.5 m thick) of extensive clay films as well as Fe/Mn oxide accumulation in saprolite fractures. They proposed that water moved through the highly fractured shale saprolite depositing clay and Fe/Mn oxides due to water moving laterally along saprolite fractures. Such lateral flow is possible in our TN site given the geometry of the hillslope and the sampling location (Appendix B).

Finally, the observed elemental enrichment at depth could result from variations in parent lithology, as we hypothesized earlier (Dere et al., 2013). In this scenario, however, it is difficult to explain the depth zoning of clay films and carbon enrichment. Given the complexity of this profile, in subsequent calculations we consider geochemical data from the total sampled profile (following previous work by Dere et al., 2013) as well as from the upper 160 cm (mobile depth) only.

Soil residence time and erosion

Uncertainties in SRT and E using Eqs. 2 and 3, respectively, for all sites were propagated by assuming a 20% uncertainty in the [10]Be delivery rate (D) (Willenbring and von Blanckenburg, 2010), 2% uncertainty in [10]Be concentration measurements (West et al., 2013) and 20 % error in the depth-averaged bulk density measurements (ρ_p). For Eq. 4, uncertainties in regolith depth were set at ±44% based on the variability of 22 ridgetop cores sampled at SSHO in PA (Jin et al., 2010; Herndon et al., 2011).

We do not observe a large difference in depth-averaged *Cm* values across all sites despite a large range of soil depths (30 – 632 cm) (Fig. 3-4a). This observation supports the idea that average *Cm* values are not biased by sample depth and that using amalgamated samples to obtain depth-averaged meteoric [10]Be concentrations is an acceptable approach. West et al. (2013) similarly concluded that depth-averaged *Cm* estimates were similar when calculated over a concentration-depth profile or from an amalgamated profile at SSHO. With this approach, however, we implicitly assume that the total augerable depth is equivalent to the deepest depth meteoric [10]Be could penetrate. This appears true at SSHO, where West et al. (2013) showed that >80% of the total meteoric [10]Be inventory was retained in the augerable regolith. Conversely, we also assume that meteoric [10]Be is likely to be present throughout the augerable material rather than concentrated just at the top (in which case we would have overestimated *L*).

The low SRT values in Wales (1.6 ± 0.28 ky) and PA (12 ± 1.6 ky) are expected. Glacial advance in Wales likely stripped soils to bare rock, effectively resetting the clock on [10]Be accumulation (Catt et al., 2006). Similarly, in PA, periglacial conditions during

the LGM likely resulted in near-frozen landscapes with intense freeze-thaw processes

that moved material, but did not necessarily result in stripping of all slopes (Ciolkosz et

al., 1986; Clark and Ciolkosz, 1988; Gardner et al., 1991). TN and AL were considerably

farther from the glacial margin and have higher SRT values than PA and VA.

In TN, where we measured meteoric ^{10}Be in the mobile and immobile regolith, if

we consider only the mobile TN layer, we obtain a SRT of 25 ky but if we consider the

total depth SRT approaches 43 ky. Thus, SRT as calculated in Eq. 2 strongly depends on

the depth of sampling that is used to assess the inventory of ^{10}Be in that profile. Given the

complications with this profile discussed earlier we can only conclude that 25 ky < SRT

< 43 ky. In AL, however, where we have hypothesized that chert may have limited hand-

augering, we assume that the entire meteoric ^{10}Be inventory may not have been sampled

and the SRT estimate is a lower limit. Regardless, erosion rates are likely not affected by

only sampling the mobile layer at this site, as discussed below.

When calculated from meteoric ^{10}Be and Eqn. 3, E across the transect is similar

within error (~40 m My^{-1}). Thus these sites (excluding NY for which we have no data)

are eroding at the same rate. In calculating E with Eq. 3, we used *Cm* depth-averaged

over the total profile depth, i.e. we followed the approach of West et al. (2014). They

concluded that *Cm* of the total profile at SSHO was the best way to assess the meteoric

^{10}Be inventory. In TN, we can use either ^{10}Be measured in the mobile or the

mobile+immobile layers to calculate E and SRT. In fact, although the SRT estimates are

different depending upon whether we use total or mobile layers only, E estimates are

similar within error. This is likely because, regardless of the complexity of the site, E has

been relatively constant during most of pedogenesis. Therefore, we conclude that using

Cm of the total regolith is appropriate for estimating E using Eq. 3.

Furthermore, we observe that although using *Cm* of the mobile or total regolith

impacts the total ^{10}Be inventory (*I$_{Be}$*), this has little bearing on the value of E because *I$_{Be}$*

is multiplied by decay in Eq. 3. Decay is a very small number (5.1 x 10^{-7} y^{-1}), making D

and *Cm* the dominant terms in Eq. 3. In other words, doubling *I$_{Be}$* does not appreciably

change E. ^{10}Be can be transported along with colloidal material in aqueous fluids (i.e.

illuviated with clay) (Willenbring and von Blanckenburg, 2010) and consequently

concentration-depth profiles can increase in clay-rich horizons, but the majority of ^{10}Be is

still retained in the upper part of the profile (Pavich et al., 1986).

The fact that SRT and E estimated using either Eqs. 2 and 4 or Eqs. 3 and 4,

respectively, are similar leads to the conclusion that the steady state assumption is

consistent with observations from PA to PR. In TN we used the mobile and total regolith

data to further test the use of Eq. 4, assuming various combinations of *Cm*, *I$_{Be}$* and *L*

values for the mobile or total regolith. Although we obtain different estimates of *E*

depending on the values of *Cm*, *I$_{Be}$* and *L* used in Eq. 3 or 4, the values are all within error

(Table 3-5; Fig. 3-4). In other words, separating out the mobile from the total regolith

does not impact estimated SRT or E within the uncertainty assumed in this approach.

The SRT in Wales stands out as surprisingly low for a site with 35 cm of soil

overlying fractured bedrock. In our previous treatment, we used an estimate of the SRT

of this site equal to 10 ky when the land became ice-free (Reynolds et al., 1987; Catt et

al., 2006). An SRT equal to 1.6 ky, is consistent with an extremely high erosion rate.

Such anomalously high rates would be surprising given the low MAT (~ 7 °C) and low

estimates of landscape denudation ($1 - 3$ m Ma^{-1}) calculated from watershed solute fluxes (Reynolds et al., 1987) (Appendix D). Erosion rates on the order of 220 m Ma^{-1} have been measured in recently glaciated, tectonically active areas such as the Swiss Alps (Wittmann et al., 2007) or the Oregon Coast (Reneau and Dietrich, 1990). The current tectonic quiescence in Wales does not support erosion rates of this magnitude (Brenchley and Rawson, 2006).

The low SRT measured with ^{10}Be in Wales may indicate ^{10}Be has been lost from the profile through leaching or human disturbance. Soil porewaters are acidic, with average organic and mineral horizon porewater pH of 3.5 and 4.0, respectively (Reynolds et al., 1988). Similarly, soils have an average pH of 3.5 (Reynolds et al., 1988). At pH > 4, ^{10}Be generally adsorbs readily to clay minerals and iron oxy-hydroxides but at pH < 4, however, Al^{3+} is also soluble and competes with other metals, including ^{10}Be, for exchange sites (Willenbring and von Blanckenburg, 2010). Under these circumstances, the low ^{10}Be inventory may result from leaching losses of ^{10}Be. Furthermore, the only other site along the transect with similarly low pH porewaters – PA – likely only had these low values for the last several decades of acid rain (Herndon et al., 2010). Indeed, no evidence of ^{10}Be leaching has been reported for SSHO in central PA (West et al., 2013).

Finally, human disturbance over the last 5 ky has been well documented in Wales and by some estimates the entire landscape was denuded of trees during Roman times (Barber et al., 1993; Catt et al., 2006). Evidence of large sediment accumulations dated to this time period (Harvey et al., 1981) as well as woodland species pollen underlying blanket peat in Wales (Walker, 1993) point to significant human disturbance during the

Holocene. Moreover, ample evidence of Roman-era mining activity has been noted at Plynlimon (Kirby et al., 1991). Soil loss of an unknown magnitude due to human activities could have removed some of the [10]Be inventory at this site. Given these uncertainties and the untenably low value of SRT in Wales, we conclude that meteoric [10]Be may not be an effective tool at this site. Thus, 10 ky is our best estimate of SRT in Wales based on the retreat of glaciers following the LGM (Reynolds et al., 1987; Catt et al., 2006). SRT calculated from Eq. 2 was used in subsequent calculations for all other sites.

Na and Mg depletion

With our estimates of SRT and E, it is now possible to address the importance of temperature in determining weathering rates. The Rose Hill Formation in PA and across the transect contains quartz, illite, 'chlorite' and lesser plagioclase feldspar, iron oxides, and kaolinite (Jin et al., 2010; Dere et al., 2013). Here, 'chlorite' represents either chlorite or minerals that share the same XRD peaks including vermiculite, hydroxy-interlayered vermiculite (HIV) or interstratification of these minerals. Na is largely present in plagioclase feldspar and Mg in 'chlorite' and, to a lesser extent illite. Thus, we use Na and Mg as proxies for the weathering of plagioclase and 'chlorite', respectively.

Geochemical profiles of Na and Mg with depth on ridgetop and slope profiles were evaluated using the dimensionless mass transfer coefficient:

$$\tau_{i,j} = \frac{c_{j,w} \, c_{i,p}}{c_{j,p} \, c_{i,w}} - 1 \tag{5}$$

Here, τ is a dimensionless coefficient representing the ratio of the concentration, *C*, of an element of interest (*j*) relative to an immobile element (*i*) in the weathered regolith (*w*) and the parent (*p*) (Brimhall and Dietrich, 1987; Anderson et al., 2002). When τ = 0, element *j* is neither enriched nor depleted with respect to element *j* in the parent; when τ < 0, the element has been lost relative to immobile element *i* in parent and τ > 0 indicates the element has been added to the profile relative to parent (Brantley and White, 2009). The weathering-resistant element Zr was used as the immobile element and the parent material was defined for each site using carefully selected average shale parent material compositions (Dere et al., 2013). Only in one site was the use of Zr problematic: Zr concentrations in VA reflected residual sandstone inputs from the previously overlying sandstone unit rather than the shale parent material (Dere et al., 2013). Therefore we used corrected Ti concentrations as the immobile element at this site as described in Dere et al. (2013).

In the ridgetop soils, the extent of Na depletion at the soil surface increases from roughly 20% depletion at the soil surface in Wales and PA to 100% depletion in PR (Fig. 3-5). In PR the profile is 100% depleted of Na at the regolith surface, consistent with a transport limited weathering regime. Such a profile develops when material is weathered faster than erosion can transport it away from the profile (Brantley and White, 2009).The Na depletion curves for Wales, PA, VA, TN and AL are incompletely developed profiles, where -1 < surface τ values < 0. Such profiles are consistent with kinetically limited weathering regimes or mixed control between kinetic and transport. Such profiles can develop when material has been removed before weathering away completely; however, they can also form when one mineral is dissolved and re-precipitated, maintaining surface

concentrations greater than zero (Lebedeva et al., 2007; Brantley and White, 2009). Slope profiles are similar, albeit shallower than ridgetop profiles (Fig. 3-5). Therefore between AL and PR there is a transition from kinetic to transport limited plagioclase weathering in both ridgetop and slope profiles (Fig. 3-6).

In contrast to these results for Na, surface τ_{Mg} on both ridgetop and slope profiles at all sites remains incompletely developed ($-1 < \tau < 0$) although they approach transport limitation ($\tau = -1$) toward the south (Fig. 3-6). These profiles likely result from both weathering of Mg out of 'chlorite' as well as incomplete re-precipitation of Mg as vermiculite and HIV phases. In fact, based on detailed bulk soil and clay mineralogy, we observe an increase in HIV and vermiculite content in the soil profiles from north to south, with ~8 % at the soil surface in Wales to 37% in PR (see Ch. 4 and Appendix D). In other words, Mg is dissolved from primary shale 'chlorite' (and to a lesser extent, illite) but is reincorporated into secondary minerals, maintaining Mg concentrations within the soil profile above zero even after Mg-containing primary minerals have largely been depleted. Furthermore, colloidal transport of clay may result in Mg loss and redistribution within the regolith (Jin et al., 2010; Yesavage et al., 2012). Thus, we conclude that 'chlorite' weathering is kinetically limited in the north and approaches transport limitation in the south, but that some re-precipitation of Mg in HIV and vermiculite phases retains Mg in the soil.

Model comparisons

We compare results from the transect to simulations from a simple hillslope reactive transport model by Lebedeva and Brantley (2013) (Fig. 3-8b). The model is used to simulate a convex hillslope as a parabolic profile where the land surface moves at a constant velocity downward due to a constant erosion rate. The modeled rock includes one non-reactive and one reactive mineral – albite – where the reactive mineral weathers to a kaolinite (Lebedeva et al., 2010). Model regolith, defined as any material containing the clay, is assumed to be formed by chemical weathering as the rock interacts with a constant rate of precipitation, where solute transport occurs by both diffusion and advection. Once regolith forms, it moves down the hillslope gradient following the transport law of Dietrich et al. (2003). In other words, all regolith formation is due to chemical weathering and all regolith is mobile. Thus, the change in regolith thickness over time depends on the rate of albite dissolution and the rate of regolith transport down the hillslope as the curvature of the hillslope evolves. As downslope transport occurs, the material continues to chemically weather. In the model, porefluid flow is strictly vertical as expected for the unsaturated zone and weathering is assumed to be isovolumetric.

In the model, the relative rates of weathering and erosion can be varied to simulate the kinetic or local equilibrium regimes (where weathering rate is limited by the transport of solutes) (Fig. 3-7b). In the kinetic regime, the weathering extent of surficial material (e.g. the negative of the τ value) is greatest at the ridgetop and decreases for soils down the convex-up part of a hillslope. At the ridgetop, soil is always present but at the bottom of the hillslope, bedrock can be exposed if τ approaches 0 when the capacity for

erosion is fast compared to the capacity for weathering. In the transport regime, the weathering extent of surficial material is similar at both ridgetop and hillslope positions.

Despite the simplifying assumptions made in the model, losses of Na (plagioclase) along the shale transect are largely consistent with model predictions of Na loss from the model rock (Fig.3-7a, b). In PR, the ridgetop and slope are both completely depleted of Na, consistent with the Lebedeva and Brantley model for transport limitation. In Wales and PA, the most northern sites in the transect, surface τ_{Na} values approach zero, similar to model predictions for kinetic limitation. All other sites fall between these kinetic and transport end members and progress toward transport limitation ($\tau = -1$) (Fig. 3-7a).

The model of Lebedeva and Brantley (2013) also predicts greater depletion on ridgetops compared to slopes in kinetically limited regimes. This is not observed: rather, the most kinetically limited sites (Wales and PA) have slightly thicker soils on the slope compared to the ridgetop. This is likely a result of sampling on the concave-up, rather than convex-up, portion of the hillslope. In fact, at the SSHO Jin et al. (2010) reported Mg depletion at the land surface decreased slightly from the ridgetop to the profile positioned at the bottom of the convex part of the hillslope but then increased down the rest of the slope, including the position reported here. Nonetheless, observations of surface Na depletion are roughly consistent with the simple reactive transport model of Lebedeva and Brantley, documenting increasing transport limitation of feldspar weathering from north to south across the transect.

Temperature dependence of weathering

Integrating the area under a τ plot gives the total mass of an element lost from a weathered profile (Chadwick et al., 1990; Egli and Fitze, 2000; Brantley and Lebedeva, 2011):

$$M_j = \rho_p C_{j,p} \int_0^L \frac{\tau_j(z)}{(\varepsilon_i(z) + 1)} dz \qquad (6)$$

Here, M_j (mol m^{-2}) is the total mass loss of element j from the profile, ρ_p is the density of the parent (g m^{-3}), $C_{j,p}$ is the concentration of element j in the parent (mol g^{-1}), ε_i the strain (dilation or compaction of the profile) and z the sample depth. Setting L equal to the total profile depth, the total loss of Na (M_{Na}) and Mg (M_{Mg}) is greater on ridgetops compared to slopes at sites where some of the total regolith is immobile (i.e. TN and PR) (Fig. 3-8).

Dividing M_j by the SRT yields a time-integrated elemental release rate from the profile (Q_j, mol m^{-2} y^{-1}). Here we follow our approach from Dere et al. (2013). We plot the natural log of the release rate as a function of inverse temperature to estimate the temperature dependence: in this pseudo-Arrhenius plot, the slope equals $-Ea/R$, where R is the universal gas constant and Ea is a pseudo-activation energy describing the temperature dependence of weathering release of Na. Previously we used SRT estimated from erosion rates in the literature and Eq. 4 (Dere et al., 2013) to make a similar calculation. Here, we use the updated SRT estimates determined from the new ^{10}Be values and Eq. 2. Given the uncertainties surrounding the complex TN profile, we calculated rates for both the mobile layer and the total profile using the respective SRT and M_j values for those layers. As described in Dere et al. (2013), differences in

precipitation across the transect were corrected by averaging Q_j values for the very wet

sites (Wales and PR = $Q_{j,\text{very wet}}$) and the moderately wet sites (PA, VA, TN, AL =

$Q_{j,\text{moderately wet}}$) and then scaling to the average MAP of the moderately wet sites to

calculate $Q_{j,\text{MAP-adj}}$:

$$Q_{j,MAP-adj} = Q_j - \left(Q_{j,very\,wet} - Q_{j,moderately\,wet}\right) \qquad (7)$$

Our previous estimate of the apparent activation energy (Ea) for Na derived from an

Arrhenius plot of ln $Q_{j,\text{MAP-adj}}$ versus 1/T was 99.0 ± 15.0 kJ mol^{-1} (Dere et al., 2013).

Using the new SRT values, the apparent activation energy of Na loss equals 115 ± 25.0 kJ

mol^{-1}, within error of the previous estimate (Fig. 3-9). This value is higher than the range

of laboratory-derived activation energies for albite dissolution (59 – 89 kJ mol^{-1}) but

similar to field estimates of the temperature dependence of plagioclase dissolution (77 -

109 kJ mol^{-1}) (Williams et al., 2010). Interestingly, using only the mobile TN layer (upper

160 cm) Na release rate and SRT (25 ky), the calculated apparent activation energy is

very similar (114 ± 22.7 kJ mol^{-1}, R^2 = 0.61) to that calculated from the Na release rate

and SRT using the total TN profile (115 ± 25.0 kJ mol^{-1}).

However, this interpretation from Fig. 3-9 is likely only valid for the sites that

approach kinetic limitation (Wales to AL). For example, Lebedeva et al. (2010) have

shown that the temperature dependence of release rates for a model rock at a ridgetop are

best described not by Ea but rather by the sum Ea + ΔH, for the controlling reactive

mineral reaction. Here, ΔH is the enthalpy change of the dissolution reaction. In contrast,

weathering at transport-limited sites (such as PR) are more influenced by equilibrium

solubility rather than dissolution kinetics (Maher, 2009; Brantley et al., 2008) and the

temperature dependence should approximate ΔH (Lebedeva et al., 2010). As previously

discussed in Dere et al. (2013), based on laboratory measurements of Ea and ΔH of albite dissolution (65.3 ± 3.4 kJ mol^{-1} and 79.8 kJ mol^{-1}, respectively) (Chen and Brantley, 1997; Johnson et al., 1992), for kinetically limited sites we would predict a temperature dependence for albite dissolution equal to 145.1 kJ mol^{-1} for strict kinetic limitation. This value is within error of 168 ± 50.8 kJ mol^{-1}, the Ea value we calculate from regressing only the kinetically limited sites (excluding PR). In summary, the temperature dependence of the observed Na loss is consistent with a transition from Ea + ΔH = 168 kJ mol^{-1} in the north to ΔH = 115 kJ mol^{-1} in the south as sites become increasingly transport limited with respect to plagioclase dissolution.

Applying Eq. 7 to Mg loss, we obtain an apparent activation energy of 64.0 ± 14.4 kJ mol^{-1} (Fig. 3-9). The Mg apparent activation energy calculated here is within the range of chlorite activation energies estimated in the laboratory ($40.5 - 94.3$ kJ mol^{-1}) (Ross, 1967; Lowson et al., 2007). Thus, we could conclude that the temperature dependence that describes Mg release rate across the climosequence is consistent with 'chlorite' weathering. However, as discussed above, Mg is not only dissolved from 'chlorite' but also re-precipitated in secondary 'chlorite' minerals instead of leaching from the profile. Thus the calculated temperature dependence is not strictly comparable to laboratory Ea estimates. More accurate estimates of Ea for this shale transect will only be possible using full reactive transport modeling.

The picture that emerges from this analysis is that, in kinetically limited weathering environments where erosion is sufficient to maintain a constant supply of weatherable minerals, increasing temperature results in faster weathering reactions and thicker regolith at ridgetops and the temperature dependence of this trend can be

described by the value of Ea + ΔH for the weathering reaction. When weathering

becomes transport limited, the capacity for erosion is small and the regolith thickness

grows until pore waters reach equilibrium solubility with respect to the weathering

minerals. For this case, the temperature dependence decreases to ΔH, the enthalpy of the

weathering reaction. In this local equilibrium case, either an increase in the rate of

precipitation or erosion is necessary to increase the weathering advance rate (which will

thicken ridgetop regolith) because an increase in the reaction rate constant alone does not

affect thickness where fluids are in chemical equilibrium. In contrast, the factors that

control the slope regolith thickness do not depend strongly on MAT (i.e. increasing MAT

only results in a slight thickening of slope regolith along the transect) (Fig. 3-2).

Therefore, our results suggest that slope regolith thickness is controlled by a factor other

than temperature. One hypothesis is that biota, especially through bioturbation, impact

slope regolith more than ridgetop regolith, resulting in a weaker temperature dependence

of slope regolith compared to ridgetops. Alternatively, differences in fluid fluxes or

overland flow between the ridgetop and slope could be responsible for thinner slope

regolith compared to ridgetop regolith.

Conclusions

A climosequence in the northern hemisphere was established to investigate the

effects of climate on shale weathering rates. Total regolith depth increases from north to

south down the transect, but the slope thickness does not increase markedly. Thus we

conclude that factors controlling the depth of ridgetop regolith are affected by MAT more

than factors controlling slope regolith thickness. Meteoric ^{10}Be measurements were used to determine soil residence times (SRT) and erosion rates (E) at all transect sites. SRT increases linearly from north to south while E remains constant ($\sim$40 m My^{-1}) within uncertainty. Wales is an exception, with low SRT and high E estimates, likely due to low pH conditions that facilitate the loss, rather than retention, of ^{10}Be in the regolith. However, all other sites appear to be operating such that the ^{10}Be remains constant in total concentration, i.e., steady state. The extent of Na and Mg depletion at the soil surface is similar on ridgetop and slope positions, indicating that the increased duration of weathering in surficial soil samples downslope compared to ridgetop samples is not a large factor in controlling weathering rates. Furthermore, we observe an apparent temperature dependence for plagioclase and 'chlorite' dissolution that can be fit to a pseudo-activation energy of 115 ± 25.0 kJ mol^{-1} and 64.0 ± 14.4 kJ mol^{-1}, respectively, values that are consistent with or slightly higher than previously published lab and field activation energies. The temperature dependence of plagioclase is best described as Ea + ΔH for kinetically controlled weathering and a transition to ΔH as weathering is increasingly transport-limited. Comparisons of data from the transect are roughly consistent with a simple reactive transport model, indicating increasing transport limitation for plagioclase dissolution rates from north to south across the transect. Data presented here will be useful in predicting landscape evolution and ultimately predict the depth of regolith in a variety of landscapes.

References

Amiotte-Suchet P., Probst J. L. and Ludwig W. (2003) Worldwide distribution of continental rock lithology: Implications for the atmospheric/soil CO_2 uptake by continental weathering and alkalinity in river transport to the oceans. *Global Biogeochem. Cyc*. **17**: 1038.

Anderson S. P., Dietrich W. E. and Brimhall G. H. (2002) Weathering profiles, mass-balance analysis, and rates of solute loss: Linkages between weathering and erosion in a small, steep catchment. *Geol. Soc. Am. Bull.* **114**:1143-1158.

Barber K. E. (1993) Peatlands as scientific archives of past biodiversity. *Biodiversity and Conserv.* **2**:474-489.

Bazilevskaya E., Lebedeva M., Pavich M., Rother G., Parkinson D. Y., Cole D. and Brantley S. L. (2012) Where fast weathering creates thin regolith and slow weathering creates thick regolith. *Earth Surf. Process. Landforms* DOI:10:1002/esp.3369.

Bierman P. R., Jungers, M., Reusser, L. and Pavich, M. (2008) Look again: meteoric 10-Be Is a useful tracer of hillslope and basin-scale process. *Geol. Soc. Am. Abstracts Program.* pp. 165–166.

Bierman P. R., Reusser, L. and Pavich, M. (2009) New ways of using an old isotopic system – meteoric 10-Be is back and ready to do geomorphology. *Geophys. Res. Abstracts* **11**:EGU2009-0.

Birkeland P. W. (1999) Soils and Geomorphology. Oxford University Press, New York. 430 p.

Brantley S. L. and Lebedeva M. (2011) Learning to read the chemistry of the regolith to understand the critical zone. *Annu. Rev. Earth Pl. Sci*. **39**:387-416.

Brantley S. L. and White A. F. (2009) Approaches to modeling weathered regolith. *Rev. Mineral. Geochem*. **70**:435-484.

Brantley S. L., Goldhaber M. B. and Ragnarsdottir K. V. (2007) Crossing disciplines and scales to understand the critical zone. *Elements* **3**:307–314.

Brantley S. L., Bandstra J., Moore J. and White A. F. (2008) Modeling chemical depletion profiles in regolith. *Geoderma* **145**:494-504.

Brenchley P. J. and Rawson P. F. (2006) England and Wales through geologic time. *In:* The Geology of England and Wales. (Eds.) Brenchley P .J. and Rawson P. F. The Geological Society of London, London, UK. pp. 1-7.

Brimhall G. H. and Dietrich W. E. (1987) Constitutive mass balance relations between chemical composition, volume, density, porosity, and strain in metasomatic hydrochemical systems: Results on weathering and pedogenesis. *Geochim. Cosmochim. Acta* **51**:567-587.

Brown L., Pavich M., Klein J. and Middleton R. (1988) Erosion of the eastern United States observed with [10]Be. *Earth Surf. Process. Landforms* **13**:441-457.

Brown E. T., Stallard R. F., Larsen M. C., Raisbeck G. M. and Yiou F. (1995) Denudation rates determined from the accumulation of in situ-produced 10Be in the Luquillo Experimental Forest, Puerto Rico. *Earth Plan. Sc. Lett*. **129**:193-202.

Buringh P. (1989) Availability of agricultural land for crops and livestock production. *In*: Food and Natural Resources. (Eds.) Pimental L.D. and Hall C.W. Academic Press, San Diego. pp. 69-83.

Catt J. A., Gibbard P. L, Lowe J. J., McCarroll D., Scourse J. D., Walker M. J. C. and Wymer J. J. (2006) Quaternary: ice sheets and their legacy. *In:* The Geology of England and Wales. (Eds.) Brenchley P. J. and Rawson P. F. The Geological Society of London, London, UK. pp. 429-467.

Chadwick O. A., Brimhall G. H. and Hendricks D. M. (1990) From a black to a gray box – a mass balance interpretation of pedogenesis. *Geomorph.* **3**:369-390.

Chadwick O. A., Gavenda R. T., Kelly E. F., Ziegler K., Olson C. G., Elliott W. C. and Hendrick D. M. (2003) The impact of climate on the biogeochemical functioning of volcanic soils. *Chem. Geol.* **202**:195-223.

Ciolkosz E. J., Cronce R. C. and Sevon W. D. (1986) Periglacial features in Pennsylvania. Pa. State Univ., Agron. Ser. 92. 52 p.

Clark G. M. and Ciolkosz E. J. (1988) Periglacial geomorphology of the Appalachian highlands and interior highlands south of the glacial border – a review. *Geomorph.* **1**:191-220.

Clark C. D., P. L. Gibbard and Rose J. (2004) Pleistocene glacial limits in England, Scotland and Wales. *In*: Quaternary Glaciations – Extent and Chronology. Part I: Europe. (Eds.) Ehlers J. and Gibbard P. L. Elsevier, Netherlands. pp. 47-82.

Clifton T. and Granger D. (2005). Erosion rate of the Appalachian plateau in the vicinity of the New River Gorge, West Virginia. *Geol. Soc. Am. Abstr. Prog.* **37**:18.

Dere, A. L., White T. S., April R. H., Reynolds B., Miller T. E., Knapp E. P., McKay L. D. and Brantley S. L. (2013) Climate dependence of feldspar weathering along a latitudinal gradient. *Geochim. Cosmochim. Acta*. **122**:101-126.

Dietrich W. E., Bellugi D. G., Sklar L. S., Stock J. D., Heimsath A. J. and Roering J. J. (2003) Geomorphic transport laws for predicting landscape form and dynamics. *In*: Prediction in Geomorphology, Geophys. Monogr. Ser. Vol. 135. (Eds.) Wilcock P. and Iverson R. AGU, Washington, D.C. pp. 103-132.

Dixon J. L., Heimsath A. M. and Amundson R. (2009) The critical role of climate and saprolite weathering in landscape evolution. *Earth Surf. Process. Landforms* **34**:1507-1521.

Driese, S. G., McKay L. D. and Penfield C. P. (2001) Lithologic and pedogenic influences on porosity distribution and groundwater flow in fractured sedimentary saprolite: a new application of environmental sedimentology. *J. Sedim. Res.* **71**:843-857.

Duxbury J. (2009) Erosion rates in and around Shenandoah National Park, VA, determined using analysis of cosmogenic 10Be: University of Vermont, 134 p.

Egli M. and Fitze P. (2000) Formulation of pedogenic mass balance based on immobile elements: a revision. *Soil Sci.* **165**:437-443.

Gardner T. W., Ritter J. B., Shuman C. A., Bell J. C. Sasowsky K. C. and Pinter N. (1991) A periglacial stratified slope deposit in the valley and ridge province of central Pennsylvania, USA: sedimentology, stratigraphy and geomorphic evolution. *Permafrost Periglac. Process.* **2**:141-162.

Gilbert G. K. (1909) The convexity of hilltops. *J. Geol.* **17**:344-350.

Graly J. A., Reusser L. J. and Bierman P. R. (2010) Short and long-term delivery rates of meteoric ^{10}Be to terrestrial soils. *Earth Planet. Sci. Lett*. **302**:329-336.

Hack J. T. (1960) Interpretation of erosional topography in humid temperate regions. *Am. J. Sci.* **258**A:80-97.

Hancock G. and Kirwan M. (2007) Summit erosion rates deduced from ^{10}Be: Implications for relief production in the central Appalachians. *Geol.* **35**:89-92.

Harvey A. M., Oldfield F. and Baron A. F. (1981) Dating of post-glacial landforms in the Central Howgills. *Earth Surf. Process. Landforms* **6**:401-412.

Heimsath A. M., Dietrich W. E., Nishiizumi K. and Finkel R. C. (1999) Cosmogenic nuclides, topography, and the spatial variation of soil depth. *Geomorph.* **27**:151-172.

Heimsath A. M., Dietrich W. E., Nishizumi K. and Finkel R. C. (2001) Stochastic processes of soil production and transport: erosion rates, topographic variation and cosmogenic nuclides in the Oregon Coast Range. *Earth Surf. Process. Landforms* **26**:531-552.

Herndon E. M., Jin L. and Brantley S. L. (2011) Soils reveal widespread manganese enrichment from industrial inputs. *Environ. Sci. Technol*. **45**:241-247.

Hooke R. L. (2000) On the history of humans as geomorphic agents. Geology. 28:843-846.

Jackson, M. L. (1974) Soil Chemical Analysis – Advanced Course 2nd edition. University of Wisconsin, Dept. of Soil Science, Madison, Wisconsin.

Jenny H. (1941) Factors of soil formation. McGraw Hill, NY. 281 p.

Jin L. Ravella R., Ketchum B., Heaney P. and Brantley S. L. (2010) Mineral weathering and elemental transport during hillslope evolution at the Susquehanna/Shale Hills Critical Zone Observatory. *Geochim. Cosmochim. Acta*. **74**:3669-3691.

Jin L., Rother G., Cole D. R., Mildner D. F. R., Duffy C. J. and Brantley S. L. (2011) Characterization of deep weathering and nanoporosity development in shale – A neutron study. *Amer. Min*. **96**:198-512.

Kirby, C., Newson M. D. and Gilman K. (1991) Plynlimon Research: The first two decades. Institute of Hydrology Report No. 109, Wallingford, UK.

Kirkby M. J. (1971) Hillslope process-response models based on the continuity equation. Institute of British Geographers Special Publication. **3**:15-30.

Konert M. and Vandenberghe J. (1997) Comparison of laser grain size analysis with pipette and sieve analysis: a solution for the underestimation of the clay fraction. *Sedimentology* **44**:523-535.

Lebedeva M. I. and Brantley S. L. (2013) Exploring geochemical controls on weathering and erosion of convex hillslopes: beyond the empirical regolith production function. *Earth Surf. Process. Landforms* **38**:1793-1807.

Lebedeva M. I., Fletcher, R. C. and Brantley, S. L. (2010) A mathematical model for steady-state regolith production at constant erosion rate. *Earth Surf. Process. Landforms* **35**: 508–524

Lebedeva M. I., Fletcher R. C., Balashov V. N. and Brantley S. L. (2007) A reactive diffusion model describing transformation of bedrock to saprolite. *Chem. Geol*. **244**:624-645.

Lowson R. T., Brown P. L., Josick Comarmond M. C. and Rajaratnam G. (2007) The kinetics of chlorite dissolution. *Geochim. Cosmochim. Acta*. **71**:1431-1447.

Lundberg L., Ticich T., Herzog G. F., Hughes T., Ashley G., Moniot R. K., Tuniz C., Kruse T. and Savin W.(1983) [10]Be and Be in the Maurice River-Union lakes system of southern New Jersey. *J. Geophys. Res*. **88**:4498-4504.

Ma L., Chabaux F., Pelt E., Blaes E., Jin L. and Brantley S. (2010) Regolith production rates calculated with uranium-series isotopes at Susquehanna/Shale Hills Critical Zone Observatory. *Earth Plan. Sc. Lett*. **297**:211-225.

Ma L., Chabaux F., Pelt E., Granet M., Sak P. B., Gaillardet J., Lebedeva M. and Brantley S. L. (2012). The effect of curvature on weathering rind formation: Evidence from Uranium-series isotopes in basaltic andesite weathering clasts in Guadeloupe. *Geochim. Cosmochim. Acta* **80**:92-107.

Ma L., Chabaux F., West N., Kirby E., Jin L. and Brantley S. (2013) Regolith production and transport in the Susquehanna Shale Hills Critical Zone Observatory, Part I: Insights from U-series isotopes. *J. Geophys. Res*. DOI:10.1002/jgrf.20037.

Matmon A. S., Bierman P. R., Larsen J. Southworth S., Pavich M., Finkel R. and Caffee M. (2003) Erosion of an ancient mountain range, the Great Smoky Mountains, North Carolina and Tennessee*. Amer. J. Sci*. **303**:817-855.

McKay L. D., Driese S. G., Smith K. H. and Vepraskas M. J. (2005) Hydrogeology and pedology of saprolite formed from sedimentary rock, eastern Tennessee, USA. *Geoderma* **126**:27-45.

Medlin J. H., Suhr N. H. and Bodkin J. B. (1969) Atomic Absorption Analysis of Silicates Employing LiBO2 Fusion. *Atomic Absorption Newsletter* **8**:25-29.

McKean J. A., Dietrich W. E., Finkel R. C., Southon J. R. and Caffee M. W. (1993) Quantification of soil production and downslope creep rates from cosmogenic [10]Be accumulations on a hillslope profile. *Geol.* **21**:343-346.

Miller S. R., Sak P. B, Kirby E. and Bierman P. R. (2013) Neogene rejuvenation of central Appalachian topography: Evidence for differential rock uplift from stream profiles and erosion rates. *Earth Planet. Sci. Lett.* **369**:1-12.

National Research Council (NRC) (2001) Basic Research Opportunities in Earth Science. National Academy Press, Washington, 154 p.

Nishiizumi K., Imamura M., Caffee M. W., Southon J. R., Finkel R. C. and McAninch J. (2007) Absolute calibration of ^{10}Be standards. Nucl. Instrum. Meth. Res. B. **258**:403-413.

Norton K. P., Molnar P. and Schlunegger F. (2014) The role of climate-driven chemical weathering on soil production. *Geomorph.* **204**:510-517.

Pavich M.J. (1989) Regolith residence time and the concept of surface age of the Piedmont "Peneplain". *Geomorph.* **2**:181-196.

Pavich M. J., Brown L., Harden J., Klein J. and Middleton R. (1986) ^{10}Be distribution in soils from Merced River terraces, California. *Geochim. Cosmochim. Acta* **50**:1727-1735.

Pavich M. J., Brown L. and Vallette-Silver J. N. (1985) ^{10}Be analysis of a quaternary weathering profile in the Virginia Piedmont. *Geol.* **1**:39-41.

Pelletier J. D. and Rasmussen C. (2009) Quantifying the climatic and tectonic controls on hillslope steepness and erosion rate. *Lithosphere* **1**:73-80.

Portenga E. W. (2011) Using ^{10}Be to constrain erosion rates of bedrock outcrops globally and in the central Appalachian Mountains: University of Vermont, 174 p.

Portenga E. W. and Bierman P. R. (2011) Understanding Earth's eroding surface with 10Be. *Geol. Soc. Am. Today* **21**:4-10.

Rasmussen C. and Tabor N. J. (2007) Applying a quantitative pedogenic energy model across a range of environmental gradients. *Soil Sci. Soc. of Amer. J.* **71**:1719-1729.

Rasmussen C., Southard R. J. and Horwath W. R. (2005) Modeling energy inputs to predict pedogenic environments using regional environmental databases. *Soil Sci. Soc. of Amer. J.* **69**:1266-1274.

Rasmussen C., Troch P. A., Chorover J., Brooks P., Pelletier J. and Huxman T. E. (2011) An open system framework for integrating critical zone structure and function. *Biogeochem.* **102**:15-29.

Reneau S. L. and Dietrich W. E. (1990) Erosion rates in the southern Oregon Coast Range: Evidence for an equilibrium between hillslope erosion and sediment yield. *Earth Surf. Process. Landforms* **16**:307-322.

Reuter J. M. (2005) Erosion rates and patterns inferred from cosmogenic 10Be in the Susquehanna River basin: University of Vermont. 172 p.

Reynolds B., Hornung M. and Stevens P. A. (1987) Solute budgets and denudation rate estimates for a mid-Wales catchment. *Catena* **14**:13-23.

Reynolds B., Neal C., Hornung M., Hughes S. and Stevens P. A. (1988) Impact of afforestation on the soil solution chemistry of stagnopodzols in mid-Wales. *Water, Air, and Soil Poll.* **38**:55-70.

Riebe C. S., Kirchner J. W. and Finkel R. C. (2003) Long-term rates of chemical weathering and physical erosion from cosmogenic nuclides and geochemical mass balance. *Geochim. Cosmochim. Acta* **67**:4411-4427.

Riebe C. S., Kirchner J. W. and Finkel R. C. (2004) Erosional and climatic effects on long-term chemical weathering rates in granitic landscapes spanning diverse climate regimes. *Earth Planet. Sc. Lett.* **224**:547-562.

Riebe C. S., Kirchner J. W., Granger D. E. and Finkel R. C. (2001) Strong tectonic and weak climatic control of long-term chemical weathering rates. *Geol.* **29**:511-514.

Reneau S. L. and Dietrich W. E. (1991) Erosion rates in the southern Oregon Coast Range: Evidence for an equilibrium between hillslope erosion and sediment yield. *Earth Surf. Process. Landforms* **16**:307-322.

Ross G. J. (1967) Kinetics of acid dissolution of an orthochlorite mineral. *Canadian J. Chem.* **45**:3031-3034.

Saxton K. E., Willey P. H. and Rawls W. J. (2006) Field and pond hydrologic analyses with the SPAW model. ASABE Paper No. 062108. St. Joseph, Michigan.

Soil Survey Staff (1993) National Soil Survey Handbook, Title 430-VI. U.S. Govt. Printing Office, Washington, D.C.

Soil Survey Staff. (2004) Soil survey laboratory methods manual. Soil Surv. Invest. Rep. 42. Version 4.0. USDA-NRCS, Washington, DC.

Soil Survey Staff. (2012a) Gridded Soil Survey Geographic (gSSURGO) Database for Alabama. United States Department of Agriculture, Natural Resources Conservation Service. Available online at http://datagateway.nrcs.usda.gov/. October 15, 2012 (FY13 official release).

Soil Survey Staff. (2012b) Gridded Soil Survey Geographic (gSSURGO) Database for New York. United States Department of Agriculture, Natural Resources Conservation Service. Available online at http://datagateway.nrcs.usda.gov/. October 15, 2012 (FY13 official release).

Soil Survey Staff. (2012c) Gridded Soil Survey Geographic (gSSURGO) Database for Pennsylvania. United States Department of Agriculture, Natural Resources Conservation Service. Available online at http://datagateway.nrcs.usda.gov/. October 15, 2012 (FY13 official release).

Soil Survey Staff. (2012d) Gridded Soil Survey Geographic (gSSURGO) Database for Puerto Rico. United States Department of Agriculture, Natural Resources Conservation Service. Available online at http://datagateway.nrcs.usda.gov/. October 15, 2012 (FY13 official release).

Soil Survey Staff. (2012e) Gridded Soil Survey Geographic (gSSURGO) Database for Tennessee. United States Department of Agriculture, Natural Resources Conservation Service. Available online at http://datagateway.nrcs.usda.gov/. October 15, 2012 (FY13 official release).

Soil Survey Staff. (2012f) Gridded Soil Survey Geographic (gSSURGO) Database for Virginia. United States Department of Agriculture, Natural Resources Conservation Service. Available online at http://datagateway.nrcs.usda.gov/. October 15, 2012 (FY13 official release).

Soil Survey Staff. (2014) National Value Added Look Up (valu) Table Database for the Gridded Soil Survey Geographic (gSSURGO) Database for the United States of America and the Territories, Commonwealths, and Island Nations served by the USDA-NRCS. United States Department of Agriculture, Natural Resources Conservation Service. Available online at http://datagateway.nrcs.usda.gov/. January 15, 2014 (FY2014 official release).

Stone J. (1998) A rapid fusion method for separation of beryllium-10 from soils and silicates. *Geochim. Cosmochim. Acta*. **62**:555-561.

Strakhov N. M. (1967) Principles of lithogenesis, Vol. 1. Oliver and Boyd Ltd., Edinburgh, 245 p.

Sullivan C. L. (2007) [10]Be erosion rates and landscape evolution of the Blue Ridge Escarpment, southern Appalachian Mountains: University of Vermont, 76 p.

Thomas E. M., Lin H., Duffy C. J., Sullivan P. L., Holmes G. H., Brantley S. L. and Jin L. (2013) Spatiotemporal patterns of water stable isotope compositions at the Shale Hills Critical Zone Observatory: Linkages to Subsurface Hydrologic Processes. *Vadose Zone J.* DOI: 10.2136/vzj2013.01.0029.

Walker M. J. C. (1993) Holocene (Flandrian) vegetation change and human activity in the Carneddau area of upland mid-Wales. *In:* Climate change and human impact on the landscape. (Ed.) Chambers F.M. Chapman and Hall, London, UK. pp. 146-156.

West N., Kirby E., Bierman P., Slingerland R., Ma L., Brantley S. and Rood D. (2013) Regolith transport on hillslopes in the Susquehanna Shale Hills Critical Zone Observatory inferred from meteoric [10]Be. *J. Geophys. Res-Earth*. **118**:1877-1896.

West N., Kirby E., Bierman P. and Clarke B. A. (2014) Aspect-dependent variations in regolith creep revealed by meteoric [10]Be. *Geol.* **6**:507-510.

White A. F., Blum A. E., Schulz M. S., Vivit D. V., Stonestrom D. A., Larsen M., Murphy S. F. and Eberl D. (1998) Chemical weathering in a tropical watershed, Luquillo Mountains, Puerto Rico: I. Long-term versus short-term weathering fluxes. *Geochim. Cosmochim Acta* **62**:209-226.

Wilkinson B. H and McElroy B. J. (2007) The impact of humans on continental erosion and sedimentation. *Geol Soc. Am. Bu*ll. **119**:140-156.

Williams J. Z., Bandstra J. Z., Pollard D. and Brantley S. L. (2010) The temperature dependence of feldspar dissolution determined using a coupled weathering-climate model for Holocene-aged loess soils. *Geoderma* **156**:11-19.

Willenbring J. K. and von Blanckenburg F. (2010) Meteoric cosmogenic Beryllium-10 adsorbed to river sediment and soil: Applications for Earth-surface dynamics. *Earth Sci. Rev*. **98**:105-122.

Wittmann H., von Blanckenburg F., Kruesmann T., Norton K. P. and Kubik P. W. (2007) Relation between rock uplift and denudation from cosmogenic nuclides in river sediment in the Central Alps of Switzerland. *J. Geophys. Res*. DOI: 10.1029/2006JF000729.

Yesavage T., Fantle M. S., Vervoort J., Mathur R., Jin L., Liermann L. J. and Brantley S. L. (2012) Fe cycling in the Shale Hills Critical Zone Observatory, Pennsylvania: An analysis of biogeochemical weathering and Fe isotope fractionation. *Geochim. Cosmochim. Acta* **99**:18-38.
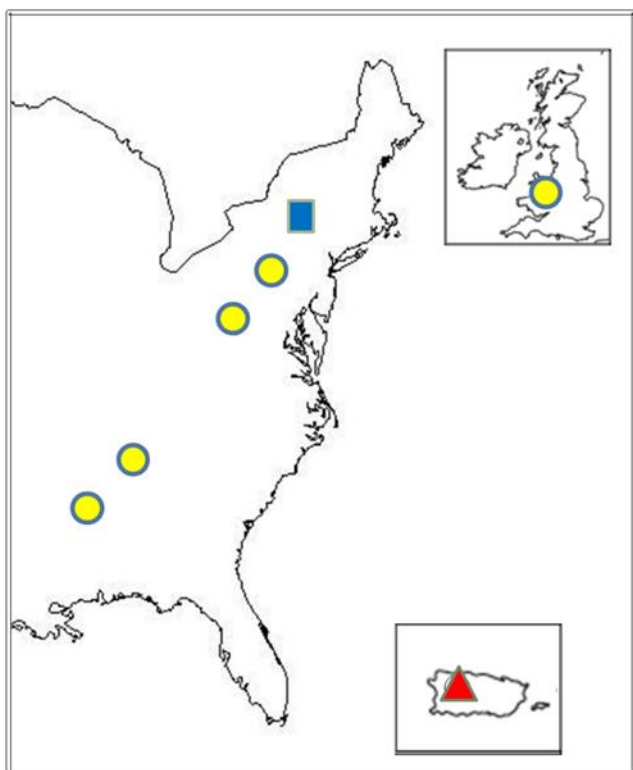
Figures

Figure 3-1. Map of shale transect sampling sites (Dere et al., 2013). Circles indicate transect sites underlain by Silurian Rose Hills Formation (or stratigraphic equivalent). New York (blue square), although underlain by the Rose Hill Formation, is covered with glacial till. The triangle represents the Oligocene San Sebastian Formation that is geochemically similar to the Rose Hill shale.
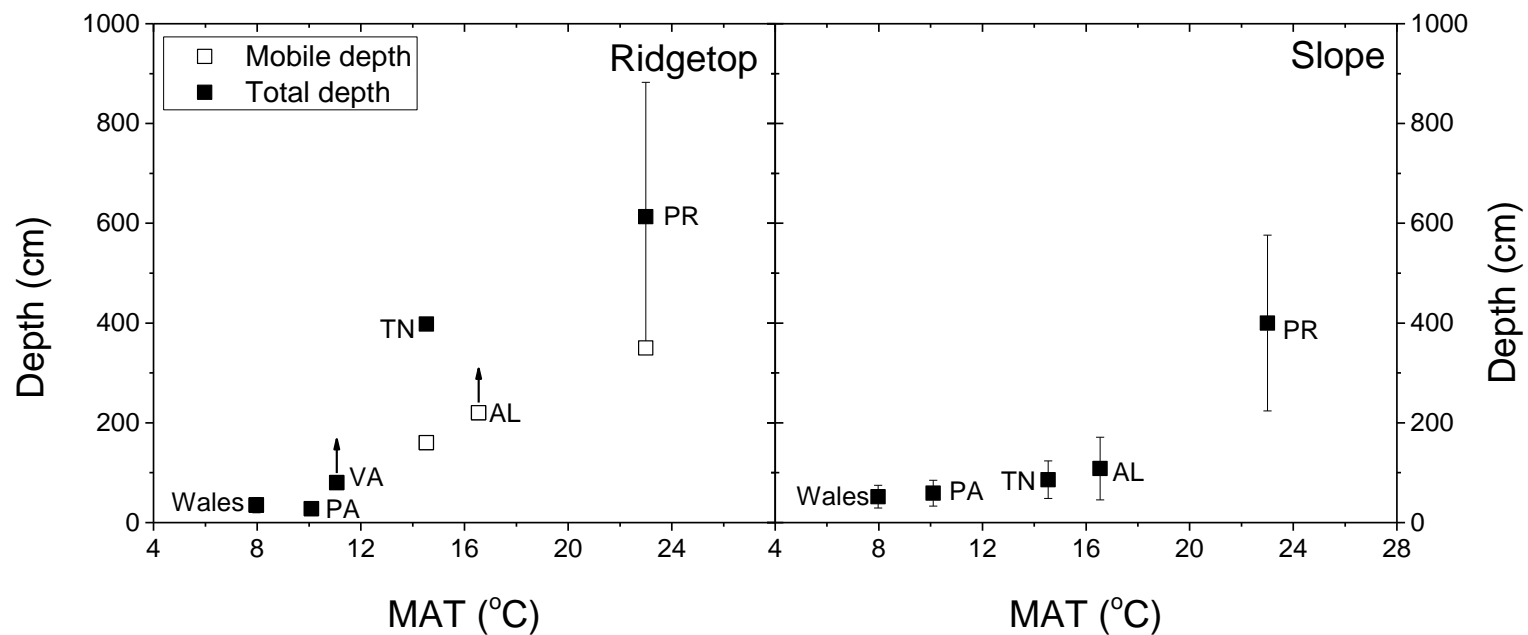
Figure 3-2. Regolith depth as a function of mean annual temperature (MAT) for ridgetop and slope sites on shale (NY not plotted because it is on till). Arrows indicate profiles that may be deeper than sampled (see text for more detail). Open squares represent the depth of mobile soil, closed squares are the total sampled depth. No slope site was sampled in VA. Note that some error bars are smaller than the symbol size.
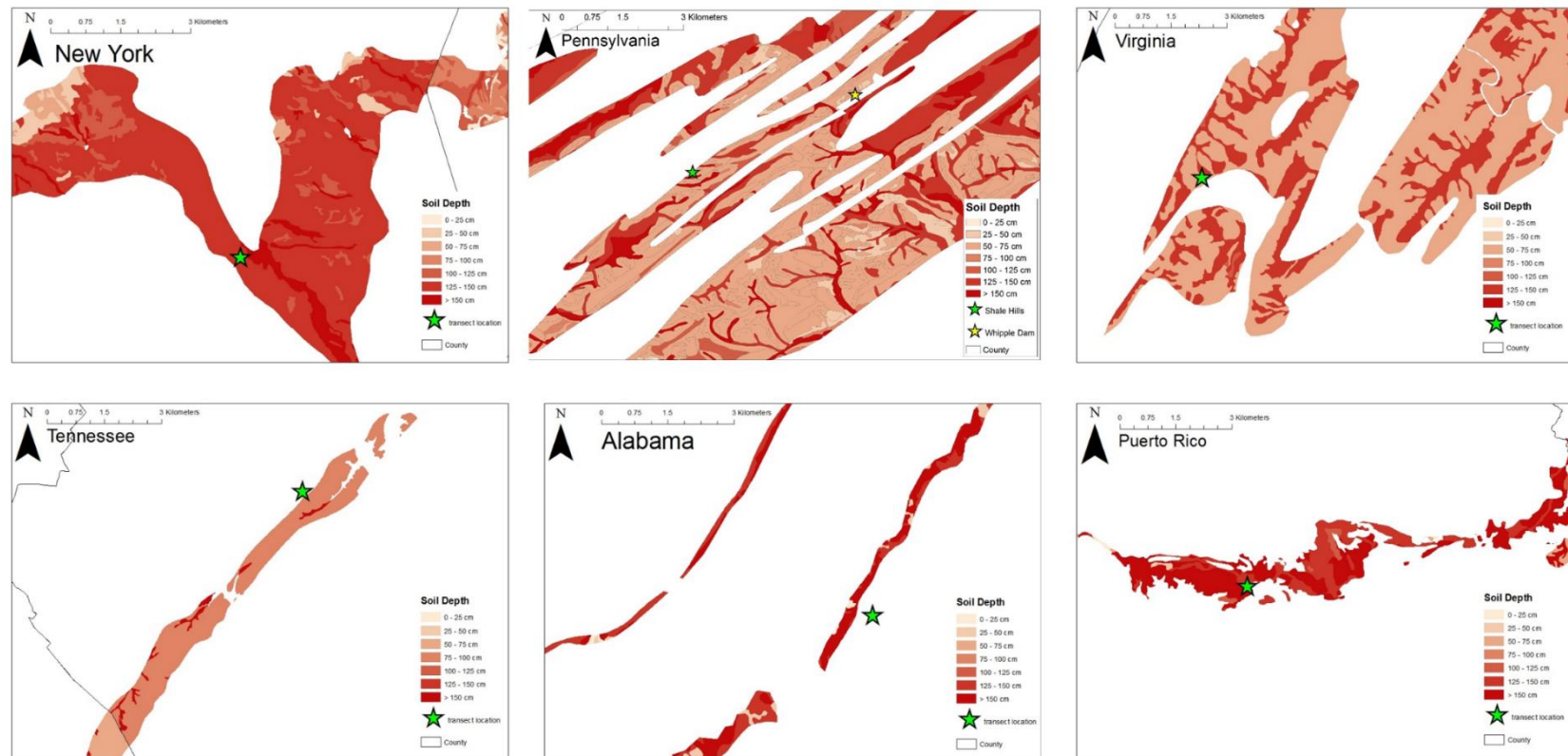
Figure 3-3. Soil depth on Silurian shale across the transect with lighter colors indicating shallower soils and darker red indicating deeper soils. The green stars show the locations of sampling sites (Fig. 3-1) (Soil Survey Staff, 2012a-f). The observations highlighted in Fig. 3-2 are consistent across the Appalachians, with deeper soils more prevalent in the southern Appalachians. Soils in New York have till parent material and are therefore deeper than expected for residual shale soils at this latitude.
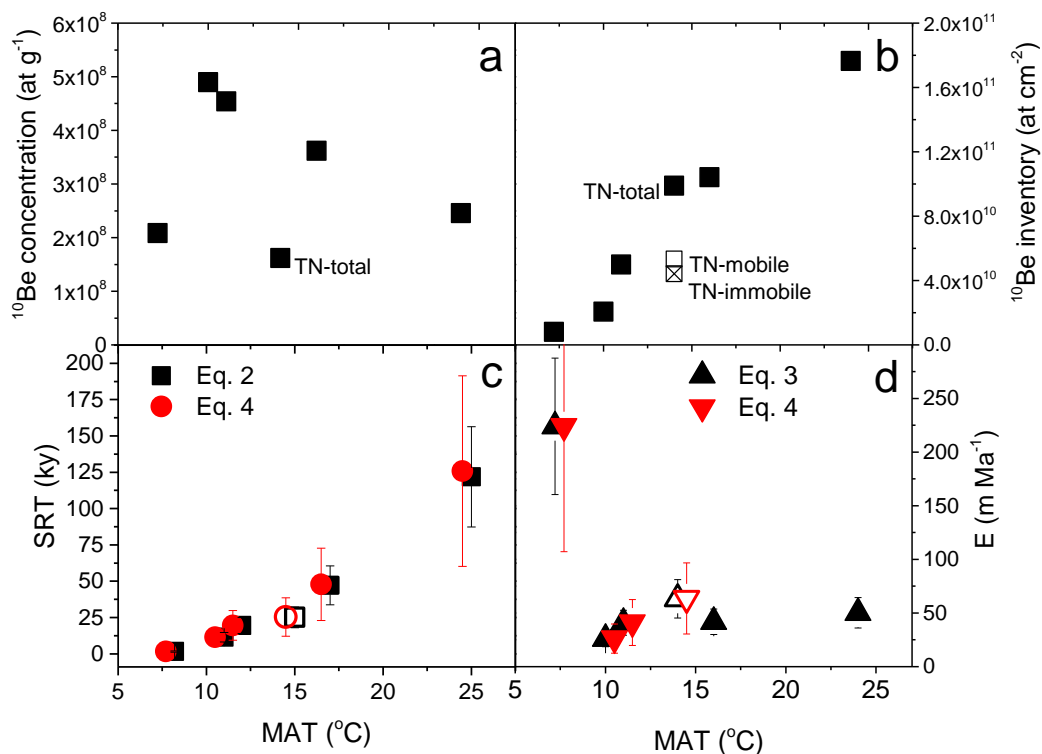
Figure 3-4. ^{10}Be concentrations (a), ^{10}Be inventory (b), SRT calculated using Eq. 2 and Eq. 4. (c) and E calculated using Eq. 3 and Eq. 4 (d) as a function of mean annual temperature (MAT) across the transect. Solid symbols represent calculations made using *Cm-total*, *I$_{Be}$-total* and *L-total*. In (b) open symbols represent the mobile layer in TN and the square with the X is the immobile layer. For TN in (c) and (d), the open symbols indicate only the mobile layer data were used (*Cm-mobile*, *I$_{Be}$-mobile,* and *L-mobile*). All data points are offset on the x-axis in (c) and (d).
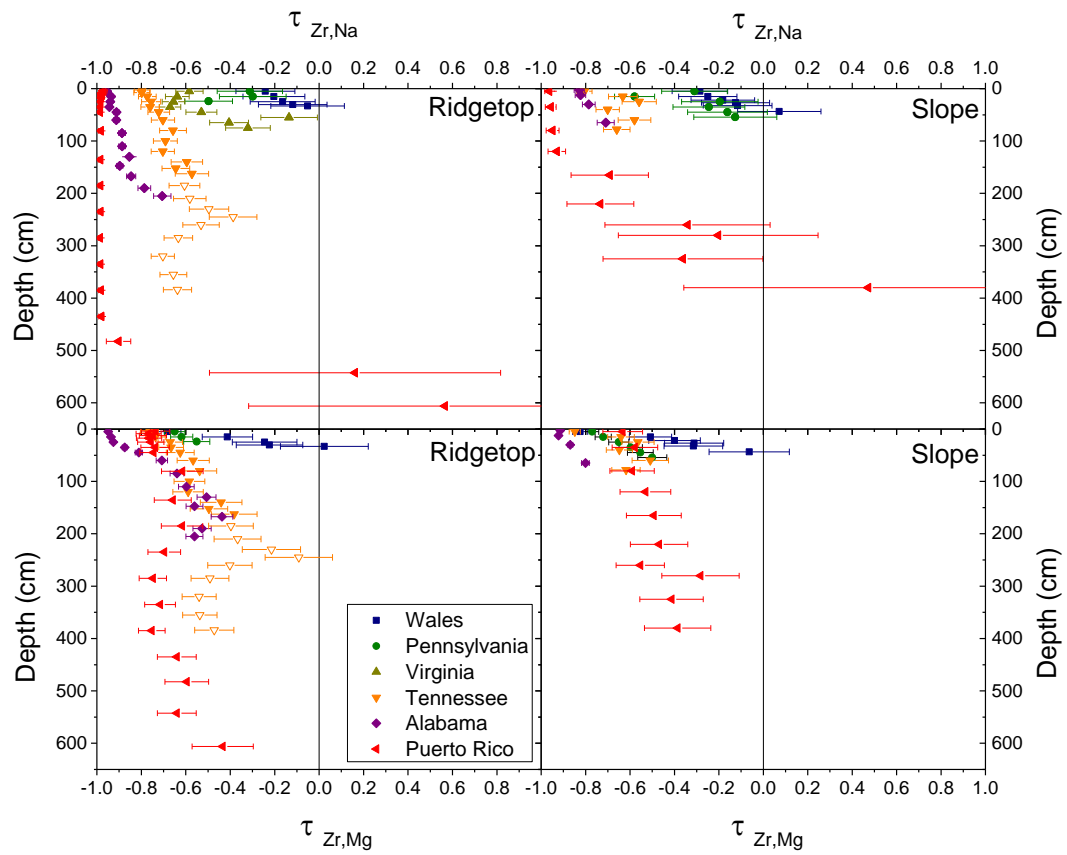
Figure 3-5. τ plots of Na and Mg for ridgetop and slope soils across the transect. Open symbols represent the immobile layer in TN (see text for more details). No slope soils were measured in VA. New York is not included due to glacial till parent material.
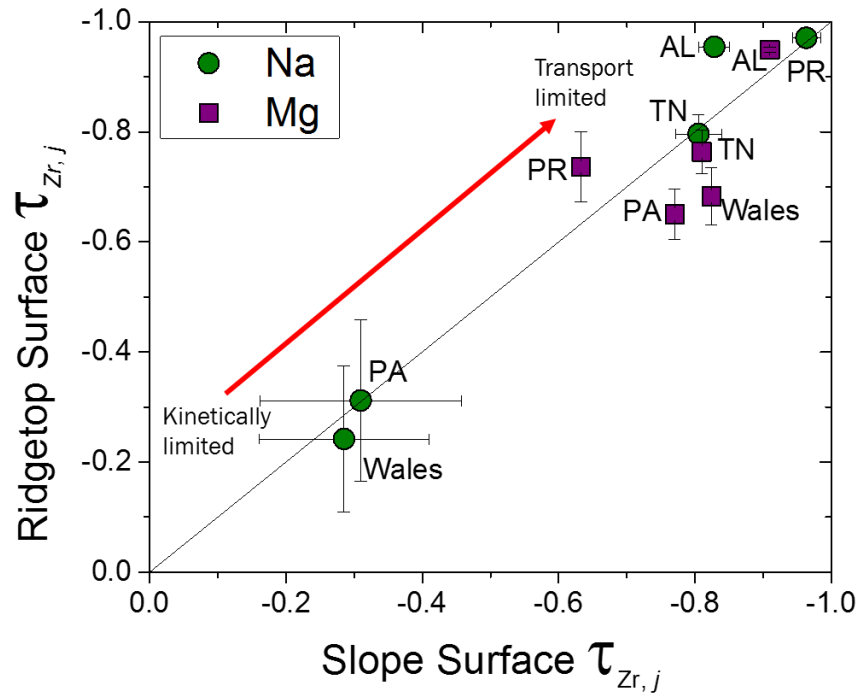
Figure 3-6. Surface $\tau_{Zr,Na}$ and $\tau_{Zr,Mg}$ values for ridgetop and slope soils across the transect. The solid line represents a 1:1 ratio where slope and ridgetop surface tau values are the same.
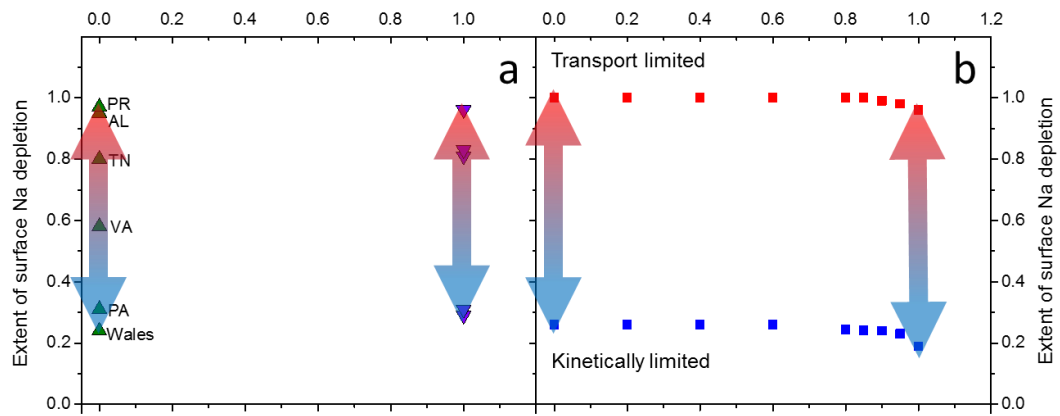
Figure 3-7. Extent of Na depletion measured (a) and modeled (b) as a function of dimensionless distance from the ridgetop. Modeled data for the extent of Na depletion were obtained from Lebedeva and Brantley (2013). Colored arrows indicate the range of measured values on ridgetop and slopes grading from kinetically limited (blue) to transport limited (red).
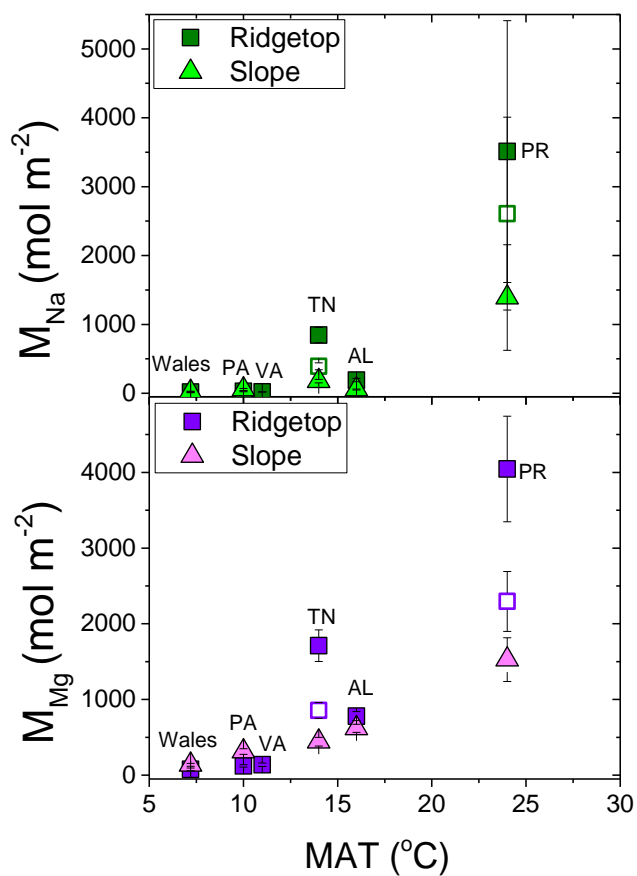
Figure 3-8. Total mass of Na and Mg (Mj) loss from ridgetop (squares) and slope (triangles) sites as a function of mean annual temperature (MAT) across the transect. Solid symbols are the total sampled depth and open symbols represent the mobile regolith. For all sites with no open symbol the total sampled depth was equivalent to the mobile depth.
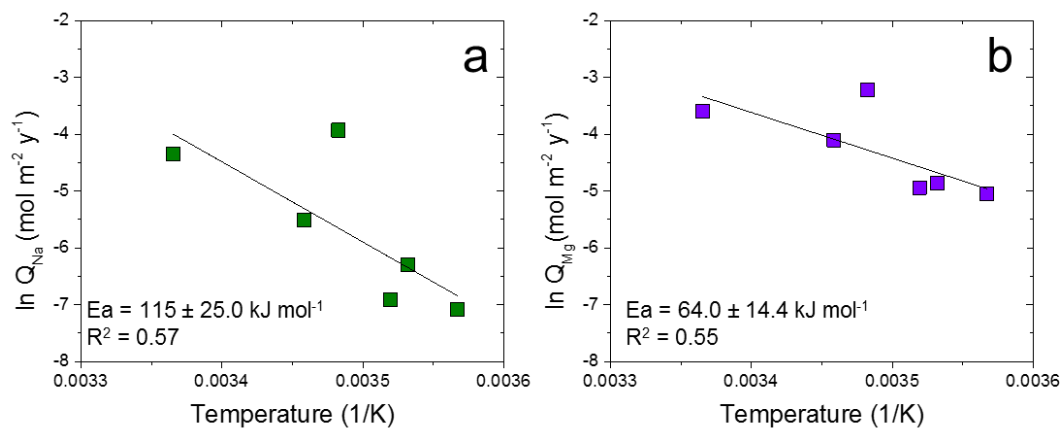
Figure 3-9. Natural log of the Na release rate (a) and Mg release rate (b) plotted against inverse temperature across the transect. Release rates have been corrected for precipitation differences across the transect (see text). Lines represent the best linear fit to the data.

Tables

Table 3-1. Site characteristics and total and mobile depth on ridgetops and slopes.

Site	Latitude	Longitude	MAT	MAP	Slope	Strike	Dip	Distance[a]	Ridgetop Total d	Mobile d	Slope d
			°C	cm	%			m	cm	cm	cm
Wales, UK	N52° 28.416	W3° 41.575	7.2	250	29	22	10ºSE	280	35	35	52
New York, USA (NY)	N43° 1.739	W75° 16.609	8.3	106	18	341	6ºSW	110	210	210	190
Pennsylvania, USA (PA)[b]	N40° 39.883	W77° 54.321	10	107	22	70	25ºNW	50	28	28	59
Virginia, USA (VA)[c]	N37° 55.625	W79° 32.799	11	106	34	46	46ºNW	---	80	80	---
Tennessee, USA (TN)	N36° 16.414	W83° 54.809	14	138	24	62	32ºSE	60	398	160	86
Alabama, USA (AL)[d] - ridgetop	N34° 25.375	W86° 12.400	16	136	33	43	10ºSE	---	220	220	---
Alabama, USA (AL) - slope	N34° 41.800	W85° 59.311	16	136	23	58	30ºNW	---	---	---	90
Puerto Rico, USA (PR)	N18 18.050	W66 54.401	24	234	16	68	5ºNE	122	632	350	400

[a] Distance between ridgetop and slope sampling site.
[b] Ridgetop and slope data from SHHO (Jin et al., 2010).
[c] No slope soil was sampled in VA due to the sandstone parent material on the slopes.
[d] The ridgetop and slope samples were collected at different locations in AL.

Table 3-2. Ridgetop soil residence time (SRT) and erosion rates (E) estimated from amalgamated cores at each site using Eq. 2 (SRT), Eq. 3 (E) or Eq. 4 (SRT and E). Tennessee was amalgamated by the mobile layer (TN-mobile, 0 – 160 cm) and the immobile layer (TN-immobile, 160 – 398 cm); TN-total is the sum of the mobile and immobile layers. Regular text means ^{10}Be concentration and inventory over the total profile depth (L) was used in all calculations. For the TN site, grey text indicates that only the ^{10}Be concentration of the mobile layer was used. Bold text indicates L = mobile layer. For all other sites with normal text, the ^{10}Be concentration, inventory and L of the total profile were used.

Site	^{10}Be Concentration (Cm)	Depth (L)	Depth-averaged density[b]	Latitude	MAP	^{10}Be delivery rate (D)	^{10}Be Inventory (I_{Be})	SRT$_{Eq.2}$	E$_{Eq\,3}$	SRT$_{Eq.4}$	E$_{Eq.4}$
	at g^{-1}	cm	g cm^{-3}	°	cm	at cm^{-2} y^{-1}	at cm^{-2}	ka	m My^{-1}	ka	m My^{-1}
Plynlimon	2.08 x 10^8	35	1.10	52	250	5.15 x 10^6	8.04 x 10^9	1.56 ± 0.44	224 ± 63.5	1.56 ± 0.81	224 ± 117
PA[a]	4.90 x 10^8	30	1.40	41	107	1.80 x 10^6	2.06 x 10^{10}	11.5 ± 3.25	26.1 ± 7.40	11.5 ± 5.99	26.2 ± 13.7
VA	4.54 x 10^8	80	1.37	38	106	2.58 x 10^6	4.99 x 10^{10}	19.4 ± 5.51	40.9 ± 11.6	19.5 ± 10.2	41.1 ± 21.5
TN-mobile	2.30 x 10^8	160	1.45	36	138	2.14 x 10^6	5.34 x 10^{10}	25.1 ± 7.13	63.2 ± 17.9	**25.3 ± 13.2**	**63.6 ± 33.2**
TN-immobile	9.34 x 10^7	238	1.59	36	138	2.14 x 10^6	4.42 x 10^{10}	---	---	---	---
TN-total	1.49 x 10^8	398	1.53	36	138	2.14 x 10^6	9.89 x 10^{10}	42.9 ± 12.2	91.8 ± 26.0	43.4 ± 22.6	92.8 ± 48.4
								62.7 ± 17.7	63.5 ± 33.1	92.8 ± 48.4	
								62.7 ± 17.7	**25.5 ± 13.3**	**37.3 ± 19.5**	
AL	3.62 x 10^8	200	1.44	35	136	2.23 x 10^6	1.04 x 10^{11}	47.2 ± 13.4	41.8 ± 11.9	47.8 ± 24.9	42.3 ± 22.1
PR	2.46 x 10^8	632	1.14	18	234	1.49 x 10^6	1.76 x 10^{11}	122 ± 34.6	50.3 ± 14.2	126 ± 65.6	51.9 ± 27.0

[a] Data from SSHO SPRT (West et al., 2013).

[b] Bulk density data for all sites except PA from Dere et al. (2013). PA bulk density data are from Jin et al. (2010).

Table 3-3. Elemental concentrations (C_j) of Na, Mg, Ti and Zr for ridgetop and slope soils across the transect. Zr was not measured on NY ridgetop soils.

Site	Sample	IGSN[a]	Depth cm	C_{Na} %	C_{Mg} %	C_{Ti} %	C_{Zr} ppm
Wales							
Ridgetop	Plnq0-10	SSH000SSM	0 - 10	0.47	0.43	0.81	166
	Plnq10-20	SSH0000HE	10 - 20	0.50	0.80	0.81	168
	Plnq20-30	SSH0000HF	20 - 30	0.53	1.06	0.80	172
	Plnq30-31	SSH0000HG	30 - 31	0.56	1.07	0.77	170
	Plnq31-35	SSH0000HH	31 - 35	0.56	1.31	0.80	158
Midslope	Plyn-bsf2 0-10	SSH0000HR	0 - 10	0.50	0.27	0.59	190
	Plyn-bsf2 10-20	SSH0000HS	10 - 20	0.57	0.82	0.65	205
	Plyn-bsf2 20-24	SSH0000HT	20 - 24	0.64	1.03	0.66	210
	Plyn bsf2 24-30	SSH0000HU	24 - 30	0.68	1.18	0.61	210
	Plyn-bsf2 30-35	SSH0000HV	30 - 35	0.69	1.17	0.59	210
	ALD-10-25	SSH0000JP	40 - 52	0.76	1.45	0.63	191
New York							
Ridgetop	ALD-10-61	SSH0000L8	0 - 5	0.32	0.48	0.62	---
	ALD-10-60	SSH0000L9	5 - 10	0.32	0.53	0.61	---
	ALD-10-59	SSH0000LA	10 - 15	0.30	0.68	0.65	---
	ALD-10-58	SSH0000LB	15 - 20	0.28	0.73	0.64	---
	ALD-10-57	SSH0000LC	20 - 30	0.28	0.69	0.57	---
	ALD-10-56	SSH0000LD	30 - 40	0.27	0.69	0.52	---
	ALD-10-55	SSH0000LE	40 - 50	0.36	0.49	0.44	---
	ALD-10-53	SSH0000LG	60 - 70	0.35	0.48	0.40	---
	ALD-10-49	SSH0000LK	100 - 110	0.50	0.37	0.41	---
	ALD-10-45	SSH0000LO	140 - 150	0.41	0.47	0.44	---
	ALD-10-36	SSH0000LS	180 - 190	0.39	0.53	0.44	---
	ALD-10-38	SSH0000LU	200-210	0.34	0.64	0.45	---
Midslope	ALD-11-225	SSH0000LZ	0 – 10	0.42	0.43	0.39	414
	ALD-11-224	SSH0000M0	10 – 20	0.39	0.43	0.38	407
	ALD-11-223	SSH0000M1	20 – 30	0.37	0.62	0.39	272
	ALD-11-221	SSH0000M3	40 – 50	0.37	0.71	0.37	291
	ALD-11-219	SSH0000M5	60 – 70	0.49	1.21	0.45	364
	ALD-11-216	SSH0000M8	90 – 100	0.48	1.48	0.46	322
	ALD-11-213	SSH0000MB	120 – 130	0.50	1.25	0.48	364
	ALD-11-210	SSH0000ME	150 – 160	0.46	2.49	0.42	299
	ALD-11-207	SSH0000MH	180 - 190	0.54	1.60	0.44	315
Pennsylvania							
Ridgetop [b]	SPRT0-10	SSH00001Q	0 – 10	0.38	0.51	0.62	273
	SPRT10-20	SSH00001R	10 - 20	0.39	0.56	0.64	275
	SPRT20-30	SSH00001S	20 - 30	0.25	0.59	0.67	246

Table 3-3 (cont.)

Site		Sample	IGSN	Depth cm	C_{Na}	C_{Mg}	C_{Ti}	C_{Zr}
						%		ppm
Tennessee								
	Midslope	ald-11-414	SSH0000SA	0 – 10	0.15	0.33	0.73	402
		ald-11-415	SSH0000SB	10 – 20	0.19	0.51	0.68	264
		ald-11-416	SSH0000SC	20 – 30	0.17	0.47	0.52	199
		ald-11-418	SSH0000SE	40 – 50	0.18	0.59	0.56	310
		ald-11-420	SSH0000SG	60 – 70	0.19	0.63	0.57	236
		ald-11-422	SSH0000SI	80 - 86	0.19	0.59	0.62	285
Alabama								
	Ridgetop	ALD-10-114	SSH0000T3	0 - 10	0.02	0.10	0.36	314
		ALD-10-115	SSH0000T4	10 - 20	0.02	0.13	0.56	331
		ALD-10-116	SSH0000T5	20 - 30	0.03	0.18	0.62	380
		ALD-10-117	SSH0000T6	30 - 40	0.02	0.21	0.54	265
		ALD-10-118	SSH0000T7	40 - 50	0.02	0.28	0.60	236
		ALD-10-121	SSH0000TA	60 - 70	0.02	0.41	0.63	224
		ALD-10-123	SSH0000TC	90 - 100	0.02	0.45	0.58	197
		ALD-10-125	SSH0000TE	110 - 120	0.02	0.47	0.60	187
		ALD-10-127	SSH0000TG	130 - 140	0.03	0.52	0.62	168
		ALD-10-129	SSH0000TI	150 - 155	0.01	0.35	0.35	129
		ALD-11-506	SSH0000TP	170 - 180	0.03	0.54	0.55	153
		ALD-11-508	SSH0000TR	190 - 200	0.04	0.51	0.57	172
		ALD-11-510	SSH0000TT	200 - 210	0.06	0.47	0.54	172
	Midslope	ald-10-800	SSH0000V6	0 - 5	0.06	0.17	0.42	308
		ald-10-802	SSH0000V8	10 - 20	0.08	0.21	0.65	421
		ald-10-804	SSH0000VA	30 – 40	0.09	0.33	0.64	399
		ald-10-806	SSH0000VC	50 - 60	0.10	0.38	0.45	305
Puerto Rico								
	Ridgetop	ald-11-13	SSH0000VO	0 - 8	0.05	0.58	0.69	139
		ald-11-14	SSH0000VP	8 - 10	0.04	0.56	0.72	153
		ald-11-15	SSH0000VQ	10 - 15	0.04	0.56	0.72	142
		ald-11-16	SSH0000VR	15 - 20	0.03	0.55	0.74	150
		ald-11-17	SSH0000VS	20 - 30	0.03	0.54	0.73	142
		ald-11-18	SSH0000VT	30 - 40	0.02	0.55	0.71	134
		ald-11-19	SSH0000VU	40 - 50	0.02	0.57	0.72	141
		ald-11-25	SSH0000W0	100 - 111	0.03	0.79	0.78	130
		ald-11-30	SSH0000W5	150 - 160	0.02	0.72	0.76	133
		ald-11-38	SSH0000WA	200 - 210	0.02	0.80	0.73	132
		ald-11-43	SSH0000WF	250 - 260	0.02	0.60	0.71	127
		ald-11-48	SSH0000WK	300 - 310	0.02	0.48	0.67	122
		ald-11-53	SSH0000WP	350 - 360	0.02	0.57	0.65	127
		ald-11-58	SSH0000WU	400 - 410	0.03	0.60	0.74	155
		ald-11-63	SSH0000WZ	450 - 460	0.04	0.86	0.87	152
		ald-11-76	SSH0000X5	500 - 505	0.15	0.81	0.80	127
		ald-11-86	SSH0000XF	570 - 580	1.78	0.74	0.76	130
		ald-11-92	SSH0000XL	625 - 632	2.20	1.07	0.77	120

Table 3-3 (cont.)

Site	Sample	IGSN	Depth cm	C_{Na}	C_{Mg} %	C_{Ti}	C_{Zr} ppm
Puerto Rico							
Midslope	PRT1-0.1	SSH0000Y9	0 – 10	0.06	0.78	0.51	135
	PRT1-0.6	SSH0000YA	50 – 60	0.07	0.89	0.52	134
	PRT1-1.0	SSH0000YB	90 – 100	0.08	0.87	0.52	136
	PRT1-1.4	SSH0000YC	130 – 140	0.10	0.90	0.49	122
	PRT1-1.9	SSH0000YD	180 – 190	0.46	1.01	0.43	126
	PRT1-2.5	SSH0000YE	240 – 250	0.37	0.98	0.45	118
	PRT1-2.7	SSH0000YF	260 – 270	1.10	1.00	0.42	142
	PRT1-2.9	SSH0000YG	280 – 290	0.95	1.15	0.37	102
	PRT1-3.6	SSH0000YH	350 – 360	0.82	1.01	0.37	110
	PRT1-4.0	SSH0000YI	390 - 400	1.94	1.08	0.40	112

[a] International Geo Sample Number, www.geosamples.org

[b] Data from Jin et al. (2010)

[c] Corrected Ti concentrations (Dere et al., 2013).

Table 3-4. Ridgetop and slope $\tau_{Zr,j}$ and M_j and ridgetop Q_j values for samples across the transect.

Site	Ridgetop surface		Slope surface		Ridgetop		Slope		Ridgetop	
	$\tau_{Zr,Na}$	$\tau_{Zr,Mg}$	$\tau_{Zr,Na}$	$\tau_{Zr,Mg}$	M_{Na}	M_{Mg}	M_{Na}	M_{Mg}	Q_{Na}	Q_{Mg}
					——————— mol m^{-2} ———————				mol m^{-2} y^{-1}	
Wales	-0.24	-0.68	-0.29	-0.82	18.5	77.2	20.1	137	0.002	0.008
NY	-0.45	-0.33	-0.34	-0.81	65.0	20.0	53.4	522	0.007	0.002
PA	-0.31	-0.65	-0.31	-0.77	29.2	123	55.0	313	0.003	0.011
VA[a]	-0.58	-0.73	---	---	19.4	139	---	---	0.001	0.007
TN-total	-0.80	-0.76	-0.81	-0.85	845	1710	178	443	0.020	0.040
TN-mobile	---	---	---	---	392	856	---	---	0.016	0.034
AL	-0.95	-0.95	-0.83	-0.91	191	781	55.0	620	0.004	0.017
PR	-0.97	-0.74	-0.96	-0.63	3510	4050	1390	1530	0.029	0.033

[a] Slope soil not sampled in VA.

Chapter 4

Mineralogical transformations and effective energy and mass transfer in shale weathering from Wales to Puerto Rico

Abstract

Soil is the material that sustains most terrestrial life on Earth, yet the processes by which soil forms from parent material are not well quantified. To investigate factors controlling soil formation, we established a climosequence as part of the Susquehanna-Shale Hills Critical Zone Observatory (SSHO). To minimize variables influencing soil production, sites were located on organic-poor, iron-rich Silurian-aged shale, and include cold and wet sites in Wales, New York and Pennsylvania and warm and wet sites in Virginia, Tennessee and Alabama. A site in western Puerto Rico provides a warm/wet end member for the climosequence but is underlain by a younger shale than the other transect sites. Here, we present geochemical and quantitative mineralogical data to characterize weathering processes and mineral transformations across this transect. Parent shales across the climosequence have a mineral assemblage dominated by quartz, illite and 'chlorite', which represents a mixture of chlorite, vermiculite and hydroxy-interlayered vermiculite (HIV). One exception is the site in Puerto Rico, where the parent shale contains up to 45% calcite in contrast to the < 2% calcite observed at the other sites. Sodium is largely present in plagioclase feldspar, which generally constitutes < 12% of the shale mineralogy at all sites. Plagioclase feldspar weathering increases from north to south, with 20% of plagioclase feldspar weathered at the soil surface in Wales and 100% of plagioclase feldspar weathered in Puerto Rico soil profiles. Soils in Alabama and

Puerto Rico – the most intensely weathered sites in the transect – show considerable mineral transformations from the parent rock to the soil surface. For example, kaolinite increases upward in the soil by 20 to 30% and iron oxides increase by up to 10%. In comparison, the northern sites exhibit upward increases of roughly 5% and 2% of kaolinite and iron oxides, respectively.

Variations in soil characteristics along the climosequence can be attributed to climate variables. To quantify these variables into one parameter, we tested the use of the effective energy and mass transfer (EEMT) model across the climosequence. EEMT includes terms for biotic inputs and rainfall and increases toward the southern end of the climosequence. Estimating the loss of precipitation to surface runoff is especially important in calculating EEMT; surface runoff may account for as much as 50% of incoming precipitation in Wales but is assumed to be negligible at all other sites. According to the EEMT model, the contribution of net primary production to soil development is almost constant along this shale climosequence. For soils such as those studied here where the majority of the EEMT parameter is dominated by the precipitation term, increasing EEMT correlates with enhanced chemical weathering and soil development. This conclusion appears valid for granite landscapes described in the literature as well as the shale climosequence presented here. In Wales and PA, however, EEMT is not a good predictor of chemical weathering. This is likely due to the geologic history at these sites: recent glaciations resulted in freezing and thawing and a young residence time (< 15 ky), processes that are not explicitly accounted for in the EEMT model. Therefore across the climosequence mean annual temperature is a better predictor of soil development across this climosequence than EEMT itself.

Introduction

Quantifying changes in the Critical Zone (CZ), especially soil development and function, is important for predicting the future of soils (NRC, 2001). The CZ extends from the top of the vegetation canopy to freshwater aquifers beneath Earth's surface and is the focus of most ecosystem processes that support terrestrial life (Brantley et al., 2007). The formation of soil within this zone involves complex coupling between physical, chemical and biological processes that are not well quantified (Amundson, 2004). Efforts to predict how future changes in climate and land use will modify the CZ are ongoing and important aspects of developing adaptation and management plans for human society.

Many researchers investigating soil development have used the state factor approach introduced by Dokuchaev (1883) and formalized by Jenny (1941) where a soil property or function is the result of various environmental factors, including climate, biota, topography, parent material and time. Identifying relationships among soils and the environment has long been used as the basis for qualitative soil field mapping efforts (Buol et al., 2003). Quantifying these relationships, however, is still a challenge. The use of environmental gradients to isolate the influence of one soil forming factor is a common and practical approach (Runge, 1973; Birkeland, 1999).

Background

The characterization of soils is a necessary step toward creating and validating models quantifying CZ evolution. Soil horizonation, although inherently a qualitative

observation, is in part created by soil hydrology, impacting both aboveground and belowground ecology as well as chemical weathering rates and the removal of weathered material (Simonson, 1959). Likewise, the development of pedogenic soil structure, often observed as granular or subangular blocky aggregates, opens porosity that drives water and air deeper into the soil (Brady and Weil, 2008). The development of structure is related to root growth and soil organisms (both macro- and micro-) that accumulate, distribute and break down organic matter. Redoximorphic features are created by the reduction, movement and oxidation of Fe and Mn compounds in soils that are periodically saturated with water, providing information about water flow, or lack thereof, through parts of the solum (Vepraskas, 2001). The clay content of soils tends to increase as soil is broken into smaller materials through physical and chemical weathering (Brady and Weil, 2008). While some of these observations are qualitative in nature, they nonetheless provide information about the developmental history of a soil and provide the basis for more quantitative measurements.

Mineralogical transformations are fundamental to the production of soil, especially in systems where colluvial, alluvial or eolian inputs are minimal (Minasny et al., 2008). In the case of residual parent material, solid rock is broken down through chemical and physical processes. Chemical weathering produces fine-grained, crystalline silicates with layered structures (Drever, 1997). In general, primary minerals, including feldspars, muscovite and chlorite, are transformed to secondary clay minerals such as vermiculite, kaolinite and iron oxides while resistant quartz minerals tend to remain unaltered (Wilson, 2004). Physical processes, such as frost action or root growth, also

contribute to the breakdown of rock into smaller particles, thereby increasing the surface area of material subject to attack by weathering (Anderson et al., 2012).

The bulk chemical composition of the soil relative to the initial rock composition can be a useful indicator of the mineralogical transformations that have taken place during weathering (Brantley and White, 2009). For example, Na is largely found in the mineral plagioclase and is not taken up by plants or reincorporated into secondary minerals; thus the loss of Na from the soil is indicative of plagioclase dissolution (Klute, 1986; Jin et al., 2010; Dere et al., 2013). Mg is predominantly found in 'chlorite' minerals, while illite is dominated by K; thus the loss of Mg and K from the soil profile can be an indicator of clay dissolution (Bain et al., 1993). In general, the production of secondary clay minerals is greatest in highly weathered soils (Buol et al., 2003).

Climate plays an important role in mineral weathering in that more intense weathering is associated with high temperatures and precipitation rates (White and Brantley, 2009). Water is necessary to facilitate the mineral transformation reactions and the temperature of water is important in controlling the kinetics of the system, whereby weathering reactions occur more rapidly in the presence of warm rather than cool water (Kump et al., 2000). The relationship between deeper and more weathered soils and warmer, wetter climates has long been recognized (Strakhov, 1967; Ruhe, 1984; Brady and Weil, 2008) but modeling these relationships with climate has been challenging (Amundson, 2004; Minasny et al., 2008).

Numerous pedogenic models have attempted to quantify soil structure and function based on soil forming factors and basic soil or environmental measurements (Minasny and McBrantney, 2001; Minasny et al., 2008). Recently, strong correlations

have been shown between soil properties and the effective energy and mass transfer

(EEMT) within the CZ (Rasmussen et al., 2005, 2011b; Rasmussen and Tabor, 2007).

The EEMT model is based on the hypothesis that soil systems self-organize to dissipate

the flux of energy within the system and therefore invokes thermodynamic principles to

quantify the flux of mass and energy through the system (Odum, 1983; Rasmussen et al.,

2005). In other words, soil processes such as carbon (C) accumulation, horizonation, clay

illuviation and the formation of soil structure and secondary minerals will reach a higher

level of development, or organization, in warmer/wetter environments with high energy

fluxes (Smeck et al., 1983).

EEMT represents a tool to calculate the climate and biotic conditions during soil

formation as one parameter that ostensibly describes the net energy that is transferred to

the subsurface where work can be done to modify the structure of the CZ (Rasmussen et

al., 2005). The dominant energy inputs to the subsurface are derived from 1) effective

precipitation (E_{PPT}), which is the energy associated with water fluxed to the subsurface

and 2) biota (E_{BIO}), which characterizes photosynthetic energy transferred to the

subsurface (Rasmussen, 2012). Together these terms describe the dominant pathways by

which radiative energy is converted to chemical and heat energy that is transferred to the

subsurface to perform work on the system. Previous work by Rasmussen et al. (2005,

2011b) and Rasmussen and Tabor (2007) showed significant correlation between EEMT

and CZ characteristics, including soil depth, clay and carbon content and chemical

alteration, at both regional and global scales. Furthermore, the researchers reported that

EEMT was a better predictor of soil properties than either MAT or MAP alone, providing

a better approach to quantify the effect of climate on soil development. As such, EEMT

provides a means by which climate, including seasonal or annual temperature and precipitation, can be used to estimate soil depth or chemical weathering.

In an effort to quantify soil formation as a function of climate, a climosequence of sites was established on residual shale parent material in the Northern Hemisphere (Dere et al., 2013). In previous treatments of the soils along this climosequence (Chapters 2 and 3), we did not observe consistent trends as a function of MAP but many characteristics showed trends based on MAT. The aim of this paper is to provide a more detailed characterization of weathering reactions and soil development in the previously studied climosequence of shale-derived soils and to test whether the use of the EEMT model 1) works well for shale landscapes and 2) elucidates the role of climate in soil development. Mineralogical, chemical and physical characterization of sites across a range of climate regimes will ultimately help us move toward more quantitative predictions of CZ evolution and structure.

Methods

Transect locations

The climosequence spans 34º of latitude in the northern hemisphere, including the following sites: Plynlimon, Wales, United Kingdom; Chadwicks, New York (NY), USA; Whipple Dam State Park and SSHO, Pennsylvania (PA), USA; Goshen National Wildlife Management Area, Virginia (VA), USA; Big Ridge State Park, Tennessee (TN), USA; Lake Guntersville State Park, Alabama (AL), USA; and Juncal, Puerto Rico (PR), USA

(see Fig. 4-1; Table 4-1). These sites were previously described in detail in Dere et al. (2013). An additional site in a grassland-dominated catchment adjacent to the forested Plynlimon site is also presented here. Mean annual temperature (MAT) and mean annual precipitation (MAP) vary across the climosequence, with the two end member sites, Wales and PR, exhibiting the greatest difference in climate (Table 4-1). The majority of the sites are underlain by Silurian iron-rich, organic-poor Clinton Group shale. In NY, PA and VA, the shale is part of the Rose Hill Formation (Gillette, 1947; Folk, 1960; Kozak, 1965), while the shale formations in TN and AL are called the Rockwood Formation and Red Mountain Formation, respectively (Finlayson, 1964; Sanford, 1966). The shale in Wales is part of the Gwestyn Formation (British Geological Survey, 2005). PR does not have Silurian shale therefore an Oligocene shale (Tobish and Turner, 1971) was sampled at this site. Residual soil profiles were sampled at all sites except NY. Although this site is underlain by Rose Hill shale, the region is covered by a thick layer of locally derived, mostly shale till, providing a different parent material for soil formation.

Vegetation varies across the climosequence, as would be expected across any climatic gradient. The Appalachian Mountains are dominated by mixed deciduous forests with coniferous vegetation most prominent in NY. The vegetation in Wales consists of spruce plantations on the slopes and moorland grasses in the upper reaches of the watershed. PR has tropical species including banana and palm trees. Although we attempted to sample sites undisturbed by humans, we recognize that the Appalachian Mountains have been deforested several times in the last 300 years (Walter and Merritts,

2008). PR was managed as a farm as recently as 40 years ago and Wales is an active
spruce plantation.

Aside from human disturbances, the greatest climatic disturbance over the soil
residence time (SRT), or the time soils have been forming, at each site was the Last
Glacial Maximum (LGM), where glaciers covered Wales and NY and PA was subjected
to periglacial conditions until about 15 ka (Ciolkosz et al., 1986; Cadwell et al., 2004;
Catt et al., 2006). Although periglacial features have been reported throughout much of
the Appalachian Mountains (King and Ferguson, 1960; Clark and Ciolkosz, 1988;
Gardner et al., 1991), we did not observe these features in the soils at the sites other than
in central PA.

Soil and rock sampling

Soil samples were collected from the mineral soil surface to as deep as physically
possible using a 5 cm diameter hand auger. The interface between the organic and
mineral horizon was defined as 0 cm. Samples were collected approximately every 10
cm throughout the augerable profile and placed in a plastic bag for storage. Soil pits were
dug by hand up to two meters deep and described (Soil Survey Staff, 1993). Rock
samples were obtained from outcrops near soil sampling sites or from the bottom of soil
pits (see Dere et al., 2013 for locations). All samples were air dried and homogenized
prior to chemical and physical analyses.

Soil and rock chemistry

Bedrock and bulk soil sample splits were ground and passed through a 100-mesh sieve (< 150 μm). In preparation for chemical analysis, 1 g of lithium metaborate was fused with 100 mg of ground sample at 950 °C for 10 minutes followed by dissolution in 5 % nitric acid for thirty minutes (Medlin et al., 1969). The resulting solutions were analyzed for major elements by inductively coupled plasma atomic emission spectroscopy (ICP-AES) (Perkin-Elmer Optima 5300DV ICP-AES, Waltham, MA). These analyses were performed at the Materials Characterization Laboratory (MCL) at Penn State University with an estimated analytical error of ± 3 % for each element.

Elemental concentrations for NY soil samples were completed using a Phillips PW2404 X-ray Fluorescence Spectrometer (PANalytical, Almelo, The Netherlands) at Colgate University, Hamilton, NY. Only the < 2 mm fraction was analyzed to avoid minor fragments of Adirondack Mountains-derived gneiss in the till parent material.

Soil and rock samples were analyzed for total carbon and nitrogen by combustion on a CE Instruments Elemental Analyzer EA 1110 (CE Instruments Ltd., Lancashire, United Kingdom). Samples were weighed and loaded into tin vials for combustion and reference and duplicate samples were analyzed after every 10 samples (Bingham, 2012).

Soil particle size distribution

Soil particle size distribution (wt %) was measured by first sieving 15 g to remove any rock fragments (> 2 mm). Ten grams of the < 2mm fraction was then placed in a 250 ml centrifuge bottle and filled halfway with distilled water (Soil Survey Staff, 2004).

Samples were sonified for 10 min then placed on a shaker table for 30 min before pouring

the silt and clay suspension through a wetted 53 μm sieve and rinsing with approximately

500 ml distilled water to separate the sand fraction (2 mm – 53 μm) (Jackson, 1974; Soil

Survey Staff, 2004). The rock and sand fractions were dried overnight at 105 ºC and

weighed after cooling. The remaining silt and clay suspension was analyzed by laser

diffraction using a Malvern Mastersizer "S" V. 2.19 (Malvern Instruments Ltd., Malvern,

United Kingdom) at the MCL. This instrument has a size range of 0.05 to 900 μm and we

used a wavelength of 633 nm, beam length of 2.4 cm and a particle density of 2.65 g cm⁻

^{3}. DI water was used as the medium with a refractive index of 1.33 at 20°C and the

refractive index of illite (1.54) was used for the solid phase, with an obscuration of ~15 %

(Buurman et al., 1997). The laser diffraction method measures the variation in light

scattering intensity as a laser beam passes through a well dispersed sample, yielding a

volume distribution of particles sizes. This approach assumes that all particles are

spheres, which is unrealistic for clay particles exhibiting platy structure. Thus, we used

the fraction of material that was < 8 μm to define the clay sized fraction based on

previous work by Konert and Vandenberghe (1997) that compared the laser method to

the pipette method of particle size analysis. The percent volume of silt and clay obtained

by laser diffraction was converted to weight percent by subtracting the sand fraction from

the original mass of the sample (10 g) and dividing the remaining mass proportionally

between the silt and clay fraction so the sum of all three size fractions (sand, silt and clay)

totaled 100 %.

Separation of clay fraction

For select samples, the clay fraction was separated using the methods of Jackson (1974). Following removal of rock fragments and sand as described above, the silt and clay suspension (< 53 μm fraction) was transferred to 250 ml centrifuge bottles and centrifuged using a Sorvall Legend X1R Centrifuge (Thermo Fisher Scientific, Inc., Waltman, MA) at 750 rpm for 7 minutes to settle the silt fraction. The clayey suspension was transferred to a clean 250 ml centrifuge bottle and centrifuged at 3000 rpm for 45 min. The supernatant was decanted and the remaining clays suspended in approximately 40 ml of distilled water.

Quantitative bulk soil and rock mineralogy

Select soil and rock samples from sites across the climosequence were analyzed for mineralogy using x-ray diffraction (XRD). Ground bulk soil and rock samples (< 150 μm) were mounted onto a metal holder using a side loading technique to maximize random mineral orientation (Whittig and Allardice, 1986). Samples were analyzed using a Scintag PAD-V powder x-ray diffractometer (Scintag, Inc. (currently Thermo Scientific), Cupertino, CA) with a Ge solid state detector and Cu-K$_\alpha$ radiation (γ = 1.54178 Å). Voltage was set at 35 kV and current at 30 mA and diffraction patterns collected from 2° to 70° 2θ using a step size of 0.020° 2θ at 1° 2θ per minute. JADE software was employed to identify XRD peaks. Quantitative mineral analysis was accomplished by combining 1 g of ground sample with 0.25 g of corundum standard micromilled with ethanol using a McCrone mill (Eberl, 2003). Samples were dried

overnight and shaken for 10 min with Vertrel$^{©}$ solution, then passed through a 150 µm

sieve and mounted onto a side loading sample holder for XRD analysis as described

above. Quantitative mineral abundance estimates were obtained from the resulting

diffraction patterns using the USGS RockJock program (Eberl, 2003).

Clay X-ray diffraction

Clays were treated to identify clay mineralogy following the methods of Jackson

(1974), Poppe et al. (2002) and Deng et al. (2009). Treatments included i) ethylene glycol

atmosphere at 60 °C; ii) K saturation with a 1 N KCl solution followed by heat treatments

at 200, 350 and 530 °C in a muffle furnace; iii) Mg saturation with a 1 N MgCl$_2$ solution

followed by treatment with glycerol; and iv) acid (HCl) treatment. Descriptions of the

clay treatment methods are provided in Appendix C. Slides were prepared by pipetting

roughly 2 ml of the treated clay and water solution onto glass slides and air drying

overnight. Diffraction patterns were obtained using a PANalytical Empyrean X-ray

diffractometer (Almelo, The Netherlands) with Cu-K$_α$ radiation at 45 kV and 40 mA.

Samples treated with ethylene glycol, K, Mg and HCl were scanned from 4° to 32° 2θ

while heat treated K saturated samples and glycerol treated Mg samples were scanned

from 4° to 15° 2θ using a PIXcel detector in scanning mode with a PSD length of 3.35°

2θ and 255 active channels for a duration time of 7:48 and 3:09, respectively. A 10 mm

beam mask, a 1/4° divergence, and a 1/8° anti-scatter slit were used on the incident side

of the diffractometer. A 1/16° anti-scatter slit and a 0.02 mm nickel filter were used on

the diffracted side. Additionally, a beam knife was used to minimize beam scatter at low angles.

Meteorological stations

Basic meteorological/soil environmental monitoring stations were deployed across all climosequence sites except Wales and PA for the duration of this study. Meteorological stations were already installed in PA or Wales as part of the SSHO CZO and the Plynlimon Experimental Forest, respectively (Duffy, 2012; Kirby et al., 1991). Measurements at the deployed meteorological stations include precipitation (mm), air temperature ($^\circ$ C), relative humidity (%), solar radiation (W m^{-2}), wind speed (m s^{-1}), soil temperature ($^\circ$ C), soil moisture (% volumetric water content) and soil electrical conductivity (dS m^{-1}); measurements were recorded every two hours with instrument scans every 10 seconds. Stations were powered by a 20 W SP20 solar panel recharging a 12V PS100 battery (both Campbell Scientific, Logan, UT). A detailed description of the setup and instrumentation can be found in Appendix C.

Effective energy and mass transfer

Effective energy and mass transfer (EEMT) is a quantitative pedogenic energy model (QPEM) developed by Rasmussen et al. (2005, 2007, 2011b) to quantify the energy input fluxes driving pedogenesis. In the model, soils are considered open systems that are characterized by the state factors formalized by Jenny (1941). EEMT

characterizes soils based on two state factors, climate and biota, using non-equilibrium thermodynamic theory. Initially, bedrock-underlain systems consist of minerals far from chemical equilibrium at Earth's surface. As open systems, these soils develop structure and order (they self-organize) by minimizing the total entropy production calculated locally at every point. Thus, soils experiencing greater energy flow can develop greater ordering (Odum, 1983; Smeck et al., 1983; Addiscott, 1994). The EEMT calculation quantifies energy inputs in units of W m^{-2} or J m^{-2} yr^{-1} (Rasmussen et al., 2005). In the context of this work, the utility of EEMT - if it successfully predicts soil systems - would be to parameterize climate and biota in one variable. A drawback of the model is that, although soils are conceptualized as non-equilibrium systems, they are modeled for simplicity as if they are stationary and unchanging over time. As discussed later, there are two complications with this conceptualization: first, even under relatively constant energy inputs, soil structure changes slowly over time as the primary minerals evolve to secondary minerals, and second, over geologically long time periods, the energy inputs also change.

The dominant energy input to soils, energy from solar radiation, is input via precipitation and reduced carbon from biota (Rasmussen et al., 2005). Precipitation provides heat and water that chemically alter the parent material (Runge, 1973). Higher temperature water increases both chemical and biological reaction rates. Net primary production (NPP) can be used to quantify the production of reduced C compounds (and by implication, acids) that contribute to mineral weathering and soil structuring (Rasmussen and Tabor, 2007). In other words, NPP represents the radiative energy converted to chemical energy and stored in organic compounds.

In comparison to these energy inputs, the rate of energy input associated with direct radiation of sunlight on the ground is argued to be negligible (Rasmussen et al., 2011b). In addition, geophysical processes, including uplift and gravity-driven mass flow, are not incorporated because they are often orders of magnitude lower than precipitation or biotic energy fluxes (Rasmussen et al., 2011b). Moreover, sites considered in this study are located on topographic ridgetop positions where erosion is low. In addition, in the Appalachian Mountains, tectonic activity has been minimal over the last 10^8 years (Matmon et al., 2003). For simplicity, the current energy flux is assumed to represent the conditions under which the soil formed under steady state conditions.

EEMT was calculated for each site following the methods of Rasmussen et al (2005) and Rasmussen and Tabor (2007) using climate parameters measured at each site with the meteorological stations as well as Moderate Resolution Imaging Spectroradiometer (MODIS) data product MOD16A2 and MOD17A3 to determine ET and NPP from 2000 – 2010, respectively (ORNL DAA, 2009; Zhao and Running, 2010). EEMT (MJ m^{-2} yr^{-1}) is the sum of the energy fluxes associated with effective precipitation (E_{PPT}) and biological carbon mass flux (E_{BIO}):

$$EEMT = E_{PPT} + E_{BIO} \tag{1}$$

E_{PPT} includes all the water derived from precipitation that ultimately infiltrates the soil and is corrected for temperature:

$$E_{PPT} = W * c_w * \Delta T \tag{2}$$

Here, c_w is the specific heat of water (4.18 J g^{-1} K^{-1}) and ΔT is the change in temperature from 273 K to the MAT (Rasmussen and Tabor, 2007). W (cm yr^{-1}) is the water that infiltrates the subsurface:

$$W = P - ET - R \tag{3}$$

W is calculated from precipitation (P, cm yr^{-1}), water lost through evapotranspiration (ET, cm yr^{-1}) and quick surface runoff (R, cm yr^{-1}). R is important when the soil surface infiltration capacity is exceeded or when the subsurface is saturated in excess of the water holding capacity (Kirby et al., 1991). This component of the water balance, often insignificant in vegetated, well-drained upland systems, can be difficult to estimate (Bonell, 1998). Along the climosequence, Wales is the only site with measurements of R. In Wales, R was calculated through hydrograph separation of base flow and storm flow contributions to the stream in the Plynlimon watershed where our sampling site is located (Sklash et al., 1996). R was also measured directly during storm events (Chapman et al., 1997).

In effect, Eq. 2 describes E$_{PPT}$ as the enthalpy of water that infiltrates a given soil on average per year at standard pressure. The soil temperature is assumed equivalent to the ambient air temperature for any given month. The energy associated with frost action is not considered, nor is the kinetic energy from rainfall impact (rainfall is largely intercepted by vegetation). For all calculations, the specific density of water is equal to 1 g cm^{-3}. For months where temperature or W was negative ($\Delta T < 0$ and/or ET > P), E$_{PPT}$ is set to 0 because there is little water flowing through the soil (i.e. all water is diverted to biota or is frozen). With these assumptions, E$_{PPT}$ was summed over a year for each month where $W > 0$.

Precipitation data from the meteorological stations across the climosequence were averaged for each month over two years where complete data were available (Appendix C). At several sites (VA, AL and PR) malfunctions in the precipitation sensors, usually

due to leaves clogging the rain bucket, precluded the use of some data and these time

periods were augmented with data from the nearest NOAA station (Appendix C)

(NOAA, 2011). Monthly averages of two years of complete data were used for each site.

Although the meteorological stations provided an estimate of daily ET,

incomplete data collection of one or more parameters – usually precipitation as discussed

above – made many ET estimates unreliable. Instead, MODIS data were used for each

site to determine ET (kg m^{-2} d^{-1}) (ORNL DAA, 2009). The MODIS data have a 1 km

pixel resolution and use algorithms to include a suite of variables that affect NPP at any

given site, including shortwave solar radiation, radiation absorbed by plants, vapor

pressure deficit, temperature, light use efficiency and maintenance respiration (Running

et al., 2004). A 7 km by 7 km grid was centered on each study site and ET and NPP

values were averaged across all pixels in the grid containing the same land use

classification as the center study site pixel (thereby excluding any areas of no data,

including urban areas and water bodies). At most sites the land use classification was

similar for almost all pixels in the grid. In AL and PR, however, the surrounding area

includes water (AL) and urban areas (PR) so only the center pixels were used to obtain

annual estimates of ET and NPP (Appendix C). While there is uncertainty from the

coarse resolution of the MODIS data (1 km pixels), NPP estimated using this approach

seems reasonable and more applicable to the analysis of specific sites than using modeled

estimates of NPP (see Eq. 8 below).

The energy flux associated with NPP (E_{BIO}) was calculated by assuming all NPP

is input to the system and the flux only occurs when light is not limiting and water is

available in the soil:

$$E_{BIO} = NPP * h_{BIO} \tag{4}$$

NPP (g C m^{-2} yr^{-1}) is multiplied by h_{BIO}, the specific biomass enthalpy fixed at 22 kJ g dry matter^{-1} (i.e. the energy resulting from the production of 1 g of organic matter at standard temperature and pressure) (Lieth, 1975). NPP across the climosequence was determined from annual averages for 2000 – 2010 from the MODIS data for each site as described above (Appendix C).

An empirical form of the EEMT equation was derived from global weather station data to produce the following equation (Rasmussen and Tabor, 2007):

$$EEMT_E = 347{,}134 * exp\left\{-0.5\left[\left(\frac{MAT-21.5}{-10.1}\right)^2 + \left(\frac{MAP-4412}{1704}\right)^2\right]\right\} \tag{5}$$

Here, EEMT$_E$ (kJ m^{-2} yr^{-1}) is a function of only two parameters: MAT (ºC) and MAP (mm). This equation was derived as the best fit among EEMT, MAT and MAP using a global climate data set (Rasmussen and Tabor, 2007). The use of Eq. 5 provides a simpler method for calculating EEMT, especially when detailed climate data are not available, because it does not require the calculation of E$_{PPT}$ and E$_{BIO}$ on a monthly basis. Furthermore, this global empirical equation provides an alternative calculation of EEMT to assess the assumptions used in Eq. 1.

In earlier versions of the EEMT model, Rasmussen et al. (2005) and Rasmussen and Tabor (2007) used modeled input values to estimate EEMT, largely because data beyond MAT and MAP were not always available, especially when considering regional or global datasets. They used the following equation to determine effective precipitation:

$$P_{eff} = P - ET_p \tag{6}$$

Here P_{eff} is the effective precipitation fluxing to the subsurface, P is precipitation and ET_p is potential evapotranspiration estimated using the Thornthwaite equation (Thornthwaite, 1948). P_{eff} is similar to the W term of Eq. 2, but does not include an estimate of precipitation losses to quick surface runoff (R). The calculation of E_{PPT} was done as in Eq. 3, with P_{eff} instead of W:

$$E_{\text{PPT-MODELED}} = P_{eff} * c_w * \Delta T \tag{7}$$

As with Eq. 3, $E_{\text{PPT-MODELED}}$ was summed for all months where P_{eff} and ΔT were greater than zero.

In the initial formulations of the EEMT model, NPP was modeled for a given site by assuming air temperature is a proxy for plant physiological processes associated with solar irradiance. Therefore the NPP for a given month (i) was calculated using a modified empirical equation (Lieth, 1975):

$$NPP_i = \left\{ \frac{3000}{[1+exp(1.315-0.119MAT_i)]} \right\} * \left(\frac{days_i}{365 \, d \, yr^{-1}} \right) \tag{8}$$

Here, i is a month where F is positive and MAT_i is the mean monthly air temperature. Monthly values of NPP were summed over a year to determine an annual energy input associated with net primary production (E_{BIO}). $E_{\text{BIO-MODELED}}$ was then determined as in Eq. 4, where NPP is multiplied by the specific biomass enthalpy (J kg^{-1}) and summed for all months of $P_{eff} > 0$.

The determination of EEMT using Eqs. 6 – 8 results in a modeled EEMT value, referred to as $EEMT_M$, such that:

$$EEMT_M = E_{\text{PPT-MODELED}} + E_{\text{BIO-MODELED}} \tag{9}$$

Comparisons of EEMT calculated using MODIS data and Eqs. 2 – 4 and by using

modeled data (Eqs. 6 – 8) are discussed in Rasmussen and Gallo (2013). Eqs. 6 – 8 were

also used in this study to compare the results of the EEMT modeled estimates compared

to MODIS data.

Results

Soil morphology

Soils described across the climosequence are progressively more mature from

north to south (Fig. 4-2). The profiles in Wales and PA are underlain by fractured shale

bedrock (saprock) (Figs. 4-3, 4-4) not observed at the bottom of pits or soil cores at any

other site (Figs. 4-5 – 4-9). C horizons in TN, AL and PR are thus characterized as

saprolite, where shale has been weathered relative to bedrock and the C horizon has

inherited the stratified structure of the parent material. The soil-saprolite boundary was

difficult to identify in AL and PR; therefore the loss of pedogenic structure was used to

define this boundary (Figs. 4-8, 4-9). In TN, the saprolite boundary is more clearly

defined at 160 cm where inherited shale structure is observed (Fig. 4-7). In VA, the soil

profile (80 cm) developed from Rose Hill Formation shale overlying a sandstone bed

(Fig. 4-6). Denudation of the intercalated shale-sandstone ridgetop proceeded to the

present setting in which more resistant sandstone clasts are still readily observed at the

land surface in VA. TN is also unique in that we observe 1) an absence of clay films in

the center of the profile (160 – 220 cm) and then recurrence of the films at 220 cm depth;

2) geochemical profiles depleted of elements in the upper part of the soil but enriched in those same elements at depth; and 3) high total clay content (328 kg m^{-2}) relative to all other sites (6 – 260 kg m^{-2}) (Fig. 4-7). These observations lead to the conclusion that the base of the modern weathering profile is at 160 cm (see Chapter 3 for more details).

In Wales and NY, soils exhibit minimal development of B horizons (B$_w$). In PA, B$_t$ horizons are weakly developed. Soil profiles in VA, TN, AL and PR have well-developed B$_t$ horizons with moderately subangular blocky structure and greatest clay concentrations in the uppermost B$_t$ horizons (Figs. 4-6 – 4-9). In addition, redoximorphic features, including both concentrations and depletions, are present in VA, TN, AL and PR. The depth to redoximorphic features generally increases: from 40 cm in VA to 45, 100 and 60 cm in TN, AL and PR, respectively. These features are most pronounced in the TN soil. The saturated hydraulic conductivity (K$_{sat}$), estimated using bulk density, carbon and clay content (Saxton and Rawls, 2006), at these sites decreases in the B$_t$ horizons and also corresponds to the upper boundary of redoximorphic features.

The NY soil has formed from a different parent material (glacial till) than the other sites and therefore shows the most distinctly different morphology, including very low clay content (< 5 %) throughout the profile and a carbonate cemented horizon near the base of the sampled profile (2.2 m) (Fig. 4-4). Although C content was not measured in the NY samples, the 5-fold increase in loss on ignition (LOI) in the bottommost sample indicates a high C content at depth related to the carbonate cemented layer.

Soil chemistry

Soil chemistry is reported in Table 4-2 for major elements Al, Ca, Fe, K, Mg, Mn, Na, P, Si, C and N and the trace element Zr. Major elemental rock chemistry used as parent material was previously reported in Dere et al. (2013). Concentrations of Si, Al and Fe were greatest throughout all soil profiles while elements such as Ca and P were extremely low except at the bottom of the NY profile, where high Ca concentrations reflect the carbonate-cemented horizon. C and N concentrations are greatest in the surface horizons and decrease with depth, as expected for residual soil profiles with organic inputs at the surface.

Soil chemical profiles were interpreted using the dimensionless mass transfer coefficient:

$$\tau_{i,j} = \frac{C_{j,w} \, C_{i,p}}{C_{j,p} \, C_{i,w}} - 1 \tag{10}$$

where τ represents the ratio of the concentration of an element of interest (C_j) normalized to an immobile element (C_i) in the weathered soil (w) and unweathered parent material (p) (Brimhall and Dietrich, 1987; Anderson et al., 2002) (Appendix C). A τ value of zero indicates the element of interest has not changed from the initial parent rock, while a τ value greater than or less than zero indicates addition or depletion of an element relative to the initial parent composition, respectively (Brimhall and Dietrich, 1987). The τ value is a useful way to compare changes in elemental composition from weathering processes, especially given the variations, albeit small, in initial parent composition between sites along the climosequence (Dere et al., 2013). Parent material samples were carefully chosen for each site from local shale outcrops or rocks recovered from pits or boreholes.

In NY, the bottommost 4 samples, not including the carbonate cemented horizon, were used as the till parent material (Dere et al., 2013). Across the transect, Zr was observed to be less mobile than Ti and was therefore chosen as the immobile element in Eq. 6. In VA, however, Zr addition to the profile from once overlying sandstone precluded the use of Zr as the immobile element; instead, we used corrected Ti values to account for Ti mobility (Jin et al., 2010; Dere et al., 2013). Zr concentrations were not measured in NY therefore Ti concentrations were used as the immobile element instead.

The majority of elements exhibit depletion profiles using the terminology of Brantley and White (2009), i.e., the value of the mass transfer coefficient decreases toward the land surface. However, concentrations only return to parent composition at depth at the northern transect sites including Wales, NY and PA (Whipple Dam), and to some extent, VA (Figs. 4-3 – 4-9). The majority of elements in TN, AL and PR do not return to parent at the bottom of the sampled profile. Sodium τ profiles were previously presented in Dere et al. (2013) and show depletion profiles at all sites, with the extent of depletion at the soil surface increasing from the northern ($20 - 30$ % depletion in Wales and PA) to the southern end (100 % depletions in PR) of the climosequence. Mg also exhibits depletion profiles and the extent of surface Mg depletion also increases from north to south, although no sites are 100 % depleted in Mg at the soil surface (see Chapter 3). K is depleted from all soils but shows enrichment at depth in TN (Fig. 4-7). Fe is highly variable with depth and enriched in profiles at Wales, VA, TN and PR. Si is most variable in AL, where chert fragments inherited from the parent shale at this site are abundant (Dere et al., 2013). In PR, Al was also enriched throughout the entire profile with respect to initial parent concentrations (Fig. 4-9).

Rock and soil mineralogy

Parent shale mineralogy consists mainly of quartz, illite and 'chlorite', which

herein is used to describe a mixture of phases including chlorite, vermiculite and

hydroxy-interlayered vermiculite (HIV) that were not distinguishable in the XRD patterns

(Jin et al., 2010) (Table 4-3). The term chlorite (without quotation marks) is used only in

the case where XRD measurements were completed to definitively confirm the presence

of true chlorite. In contrast to the other soils which contained ≤ 2 % calcite, the parent

shale in PR contains up to 45 % calcite. This large difference in composition is not

unexpected given the different depositional history of the shale at this site (Tobish and

Turner, 1971). Calculations of calcite content based on bulk Ca concentrations (i.e.

assuming all Ca is present only as calcite) are similar to estimates from quantitative XRD

analysis in PR (47 %) and TN (1.5 %). In VA and AL, calcite determined from XRD

analysis is slightly higher than calcite determined from Ca concentration in the shale

(Table 4-3). No calcite was reported for quantitative XRD analysis in Wales and PA

although bulk Ca concentrations equate to 0.19 % calcite in PA and 0.08 % calcite in

Wales. The most likely interpretation of this is that Ca in PA and Wales is also present as

plagioclase feldspar, which is known to be present. Overall, quantitative XRD analyses of

calcite are in good agreement with bulk Ca concentrations, assuming Ca in the bedrock is

present largely as calcite.

Consistent with these observations at all sites, the X-ray diffractograms indicate

that plagioclase generally constitutes < 12 % of the parent mineralogy, similar to iron

oxides and K feldspar. There is also a small amount of kaolinite (< 5 %) in the VA, TN

and PR parent rocks. Kaolinite is not a primary mineral in the shale (Jin et al., 2010). The presence of small amounts of kaolinite in VA, TN and PR may indicate some weathering of the parent rock has occurred in the outcrop. Illite is the dominant mineral in the PA parent material, comprising 63 % of the parent mineralogy while the 'chlorite' fraction is considerably smaller (5 %) compared to all other parent rock samples (15 – 37 % of the parent mineralogy) from the climosequence. The mineralogy of the PA sample reported here is consistent with the previous quantification of Rose Hill shale mineralogy at the SSHO CZO located within 3 km (Jin et al., 2010). Furthermore, plagioclase calculations based on Na concentrations in the parent give plagioclase quantities similar to quantitative XRD estimates (Dere et al., 2013).

Throughout the transect, the mineralogy of the bulk soils largely reflects the parent mineralogy with the addition of secondary minerals kaolinite, iron oxides and additional 'chlorite' and loss of some weathering phases including calcite (PR), plagioclase, illite and 'chlorite' (Fig. 4-10; Table 4-4). Total 'chlorite' content at the surface of the soil profiles increases from north to south, from ~8 % in Wales to 37 % in PR. Similarly, all soils show kaolinite addition in the upper soil samples, with surface kaolinite content increasing toward the south (~6 % in Wales to 30 % in PR) (Table 4-4). The disappearance of plagioclase from the surface soil is most evident in the PR profile, where plagioclase content decreases from 19 % at the base of the profile and in the shale, to < 1 % plagioclase toward the soil surface. K feldspar shows little change throughout the soil profiles in Wales, PA and VA; in contrast, soil K feldspar decreases toward the soil surface in TN, AL and PR. Iron oxide content generally increases toward the soil surface, consistent with previous observations of iron oxide minerals in SSHO (Yesavage

et al., 2012). However, Fe shows high variability with depth, especially in the southern profiles (TN, AL and PR). Given the till parent material in NY, the mineralogy of this soil was not evaluated.

All of these mineralogical concentrations are based on quantitative XRD (Eberl, 2003). Uncertainties associated with quantitative mineralogical estimates can be as much as ± 5 % especially for clay minerals (Jenkins and Snyder, 1996; Hillier, 2000; Ferrier et al., 2010). Although many minerals such as plagioclase, K feldspar and iron oxides are present in quantities < 5 %, the presence of these minerals in both rock and soil samples was confirmed using JADE peak analysis software that compares known mineral diffraction patterns to measured patterns. In addition, although no data are reported here, each of these minerals has been identified in samples at SSHO using scanning electron microscopy and energy dispersive analysis. Thus, we use the quantitative XRD estimates to identify weathering reactions as a function of depth and location across the climosequence (Brantley and White, 2009).

Soil clay mineralogy

In addition to quantitative XRD, we completed a more detailed analysis of mineralogy in the clay fraction of selected soils across the climosequence to identify clay mineralogy. At all sites, the soil minerals present in the clay fraction are illite (10, 5 and 3.3 Å peaks), 'chlorite' (14, 7.2 and 3.6 Å peaks), quartz (4.3 and 3.3 Å peaks), and kaolinite (7.2 and 3.6 Å peaks), as well as vermiculite, hydroxy-interlayered vermiculite (HIV) and interstratified chlorite (Harris and White, 2008) (Appendix C). None of the

transect soil samples contain smectite, because no changes were observed in the apparent d-spacing of the 14 Å peak following ethylene glycol treatment or solvation of a Mg saturated sample with glycerol (Moore and Reynolds, 1997).

Kaolinite can be difficult to identify in the presence of 'chlorite' due to similar peak positions. Thus, soil samples were treated with 1N HCl to destroy the 'chlorite' (Jackson, 1974). Following acid treatment, the 14 Å peaks disappeared but the 7.2 Å peaks remained, confirming the presence of kaolinite in the soils at all sites except perhaps Wales. Furthermore, the 7.2 Å kaolinite peak disappeared following heat treatment of 530 ℃, which also indicates the presence of kaolinite in the soil samples (Deng et al., 2009). In Wales, it is possible that the presence of the 7.2 Å peak before acid treatment indicates only minimal kaolinite (Appendix C). The sharpest kaolinite peaks were observed in AL while the kaolinite peaks in PR are broader, consistent with a small kaolinite particle size at this site (Moore and Reynolds, 1998). Illite (10, 5 and 3.3 Å peaks) was unaffected by any of the treatments and is present in the clay fraction of all samples except in PR (40 – 50 cm depth). Similarly, a small amount of quartz is present in all samples (4.3 and 3.3 Å peaks).

The clay diffraction patterns highlight the highly interstratified nature of the chlorite minerals – and this is the reason for using the notation 'chlorite' (Jin et al. 2010). Wales is the only site where true chlorite is positively identified in the soils by the persistence of the 14 Å peak even after K saturation and heating to 530 ℃ (Appendix C). At all other sites, however, the 14 Å peak disappears with heat treatments, indicating true chlorite is not present in the selected soil samples analyzed for clays using XRD. Rather, there is evidence for more complex associations of minerals with similar peaks to true

chlorite. Vermiculite is present in all the selected soil samples, as shown by differences in

peak shapes between cation saturation treatments and a collapse of the 14 Å peak

following K saturation but not Mg saturation. HIV, indicated by small peak shifts with

cation saturation and a trend toward more diffuse 10 Å peaks with increasing heat, is

observed most notably in Wales, VA, and TN. Chlorite-vermiculite interstratification is

observed at all sites except PR, as interpreted from the sharpening of the 10 Å peaks

following heat treatment. A small peak at 3.2 Å in Wales could indicate albite in the clay

fraction, while the 4.7 Å peak and 4.5 Å peaks observed only at this site could be

secondary reflections of 'chlorite' and vermiculite, respectively (Harris and White, 2008).

EEMT

EEMT calculated using equation Eq. 2 from monthly data is the same within error

from Wales to TN, but increases from AL to PR (Table 4-1, Fig. 4-11a). Nonetheless,

EEMT increases from VA to PR. Using the empirically derived Eq. 5 yields higher EEMT

values than using monthly-averaged E_{PPT} and E_{BIO} inputs in Eq. 1 (Table 4-1). Most

notably, EEMT in Wales is estimated to be two times greater when Eq. 5 for $EEMT_G$ is

used (i.e., a calculation using only MAT and MAP but not ET or R) and compared to

EEMT from Eq. 1. This is largely because Eq. 1 allows subtraction of ET and R from

MAP.

The fraction of EEMT associated with E_{PPT} is greater than the E_{BIO} term across

the climosequence, with the greatest differences observed at the lowest latitudes (TN, AL

and PR) (Fig. 4-12b; Table 4-1). E_{PPT} generally increases from north to south and is

greatest in PR. Within error, E_{BIO} does not vary across the climosequence, with values ranging from 14 – 20 MJ m^{-2} yr^{-1} (Table 1). In fact, Wales and PR, which have the most distinctly different vegetation of the study (evergreen and tropical vegetation, respectively), have nearly equivalent E_{BIO} (20 MJ m^{-2} yr^{-1}). The Appalachian Mountain sites vary from 14 to 17 MJ m^{-2} yr^{-1} (Fig. 4-11b). F_{BIO}, the fraction of EEMT that is derived from E_{BIO} ($F_{BIO} = E_{BIO}$ / EEMT) (Rasmussen et al., 2011b), is the same within two standard deviations of the mean but decreases from north to south. All sites have an $F_{BIO} < 0.5$, confirming that E_{PPT} is the dominant term in estimating EEMT.

In the next section NY is not included in comparison to our other study sites due to the different parent material (till).

<div align="center">**Discussion**</div>

Mineralogical transformations across the transect

In PA, at the SSHO which lies within 3 km of our sample site, weathering reactions have been identified deeper than 20 m in boreholes drilled into bedrock (Brantley et al., 2013). For example, under the northern ridge of SSHO, the deepest reaction is oxidative dissolution of pyrite, followed closely by dissolution of the carbonate mineral ankerite. All the pyrite and ankerite are completely depleted by 23 meters depth under the ridge. Weathering of plagioclase and illite commences at 6 m and 0.5 m, respectively (Jin et al, 2010). Although we did not drill boreholes, it is possible that deep weathering reactions that remove pyrite and carbonate minerals also occur at

depths greater than 20 m along the transect studied here. Brantley et al. (2013) have used the term "profile-initiating" reaction to describe the chemical reaction that occurs deepest in the profile. Given the lack of drilled samples along the climosequence, it is impossible to delineate pyrite and carbonate reaction fronts south of PA or conclude which reaction is profile-initiating. However, consistent with the carbonate depletion model, PR is 100% depleted of carbonate despite calcite constituting almost half of the parent shale (Table 4-2). Thus, the dissolution of calcite to 632 cm is attributed to dissolution throughout the PR soil. Calcite is an extremely small proportion of shale at all other sites ($0 - 2$ %) and is present in the other soils is often below detection, indicating that the small fraction of calcite present in parent at these sites may also have dissolved.

Similarly, we also cannot conclusively identify the true depth to which Na is depleted in each profile. However, throughout the transect Na is largely present in plagioclase feldspar that weathers to kaolinite (Dere et al., 2013). Given that no other Na-bearing minerals were identified through XRD and the fact that Na is not taken up appreciably by vegetation, we conclude that the dissolution of plagioclase results in the loss of Na as solute from the weathered profile. Indeed, the extent of observed Na loss is consistent with enhanced plagioclase weathering as temperatures increase across the transect (Dere et al., 2013). Although plagioclase constitutes <12 % of the initial shale, this weathering reaction is the first and deepest reaction we identify (without drilled samples) in the weathering profile. This interpretation is consistent with work by Jin et al. (2010) at the SSHO CZO where analysis of shale chips in the soil revealed depletion of Na, but not elements present in clay minerals (K, Mg, Al, Fe). Therefore, plagioclase dissolution occurred deeper than measurable clay mineral dissolution. In this respect,

plagioclase dissolution can be considered the so-called "regolith-initiating reaction", i.e., the deepest reaction that occurs close to the point where bedrock disaggregates to grains < 2 mm, roughly equivalent to the augerable soil depth at these sites.

In the shale bedrock, Mg is largely found in 'chlorite', and to a lesser extent illite (< 5 %) (Jin et al., 2010). Smectite minerals, which can also contain Mg, were not observed in any soils across the climosequence, as expected for the humid climate regimes included in this study (Barshad, 1966; Helgeson et al., 1969). However, instead of disappearing along the transect to the south, the proportion of 'chlorite' in the soils increases from north to south, indicating a greater transformation of clay minerals in the bedrock to secondary 'chlorite' minerals in the soil (Fig. 4-10). Wales is the only site with true chlorite identified in the bedrock and soils. Based on the lack of true chlorite observed in shale or soils at SSHO and all other sites along the climosequence, we assume 'chlorite' is the dominant mineral participating in weathering reactions at these sites.

The transformation of 'chlorite', and to a lesser extent illite, to vermiculite or HIV complicates the interpretation of the τ profiles for Mg because unlike Na, Mg can be retained in vermiculite and HIV secondary minerals rather than leaving the profile (Klute, 1986; Chapman, 1986; Bain et al., 1993). In other words, using the τ profile it is difficult to interpret the proportion of Mg lost from the weathering of primary 'chlorite' because that Mg is not necessarily removed from the soil profile but is re-precipitated in vermiculite and HIV, maintaining -1 < τ surface < 0. Nonetheless, soils are increasingly Mg-depleted at the soil surface from north to south while the proportion of 'chlorite' at the land surface increases toward the south, consistent with the interpretation that Mg loss

from 'chlorite' is re-precipitated as vermiculite and HIV (Tables 4-4, Appendix C). The dissolution of 'chlorite', comprising roughly one third of the parent mineralogy, represents the dominant weathering reaction contributing to Mg loss and re-precipitation of vermiculite and HIV in these profiles.

Illite loses more Fe than 'chlorite' during weathering on ridgetops at SSHO (Yesavage et al., 2012) and is thought to weather prior to 'chlorite' at this site (Jin et al., 2010). However, K is almost entirely present in illite in shale-derived soils, transforming to vermiculite upon weathering (Bain et al., 1993). Previous research characterizing the mineralogy of the Rose Hill Formation shale at the SSHO CZO reported similar K and Mg depletion profiles, attributed to the congruent dissolution of illite and 'chlorite' (Jin et al., 2010). A similar observation describes K and Mg depletion profiles at most of our study sites. Once again, we attribute this to simultaneous dissolution of 'chlorite' and illite. In Wales, however, Mg is more depleted than K throughout the soil profile, consistent with previous interpretations that 'chlorite' weathers more rapidly than illite at this site (Chapman, 1986). TN is also anomalous in that K is half as depleted as Mg in the upper part of the profile and greatly enriched at depth (160 – 380 cm) before returning to parent composition at the bottom of the profile (Fig. 4-7). This profile is discussed in depth in Ch. 3.

Kaolinite is a stable secondary mineral phase resulting from the destruction of minerals in the 2:1 clay family or the dissolution of plagioclase minerals (Berner and Berner, 1996) and is increasingly abundant at the soil surface toward the south (> 30%), consistent with enhanced weathering at the southern sites (Figure 4-10). The initial plagioclase content of PR bedrock is 12 % but kaolinite constitutes up to 30 % of the bulk

mineralogy in the soils. Therefore the precipitation of kaolinite in this soil must not only result from plagioclase dissolution but also clay mineral weathering (i.e. HIV dissolution).

Iron oxides are present in the unweathered shale at all sites but are also precipitated through the weathering of 'chlorite' minerals. The contributions of iron oxides to the soil mineralogy does not show a clear trend with depth and is highly variable within each profile. However, iron oxides can be difficult to identify with XRD if crystallinity is poor (Ferrier et al., 2010). Furthermore, iron oxides appear to be mobilized as particulates rather than dissolved as solutes from shale weathering at the SSHO CZO (Jin et al., 2010; Yesavage et al., 2012). Nonetheless, even with the observed variability, a greater percentage of iron oxides are present in the southern soils (up to 10 % compared to < 3 % at northern sites), again consistent with more advanced weathering at these sites compared to the northern soils (Buol et al., 2003).

Quartz is not expected to be a very reactive mineral in these weathering systems and for some sites, including Wales, PA and PR, the abundance of quartz does not vary with depth (Table 4-4). In VA, TN and AL, quartz abundance is greatest near the soil surface, possibly as a result of the inclusion of sandstone material from the previously overlying sandstone unit in VA, quartzite present upslope of the TN site and the inclusion of chert in the shale at the AL site (Dere et al., 2013). In fact, Si is heavily enriched at the VA site where blocks of sandstone are present on the soil surface (Fig. 4-5 – 4-6).

In summary, the dominant weathering reactions in the sampled regolith profiles along the climosequence include: 1) the dissolution of plagioclase that produces kaolinite and releases Na ions that are lost in solution from the soil; and 2) the dissolution of

'chlorite' and illite that produces vermiculite and HIV that in turn weathers to form

kaolinite and iron oxides. In PR, however, the dissolution of calcite is assumed to have

occurred at depth beneath the soil: this reaction may also have occurred at depth at other

sites.

Energy associated with precipitation

The energy associated with precipitation (E_{PPT}) exerts a dominant control over

total EEMT at all of the climosequence sites, flushing water through the subsurface to

alter soil properties (Fig. 4-11a). E_{PPT} equals total precipitation minus losses from ET and

R but the term also accounts for MAT: the idea is that higher air temperatures increase

precipitation temperatures, carrying greater heat energy to the subsurface that enhances

chemical weathering. ET is also affected in part by temperature, with ET often increasing

at higher temperatures (Chapin et al., 2002). As expected, ET is relatively low in the cool

climate of Wales and increasingly higher toward the warmer climate of PR

(Thornthwaite, 1948) (Table 4-1).

Previous estimates of actual evapotranspiration (AET) at the Plynlimon watershed

in Wales, calculated as the balance between precipitation (PPT) and watershed discharge

(Q) (AET = PPT – Q), were 650 ± 120 kg m^{-2} yr^{-1} (Kirby et al., 1991), slightly larger than

values obtained from MODIS data (447 kg m^{-2} yr^{-1}). Furthermore, estimates of AET at

SSHO yields an ET value of 404 kg m^{-2} yr^{-1} (Banwart et al., 2011), slightly lower than the

MODIS-derived value of 531 kg m^{-2} yr^{-1}. In Wales, ET from a forested (Wales-forest)

catchment has higher ET compared to a grassland (Wales-grass) catchment as estimated

from MODIS data (447 and 315 kg m^{-2} yr^{-1}, respectively), consistent with previous measurements showing higher ET loss from the forest compared to the grassland (Kirby et al., 1991). Thus, the use of ET from MODIS data appears to be a reasonable value for estimating the ET component of E_{PPT}.

Surface runoff has not been generally observed at SSHO even following large snow melt or storm events, except at limited locations near the footslope and toeslope areas (Lin, 2006). Given that the other transect sites in the Appalachian Mountains and in PR have similar organic horizon thickness (5 – 8 cm) and are located in upland positions, we assume that R is also not a significant process at these sites.

In Wales, however, R plays a significant role in routing precipitation to streams. Previously a hydrograph separation work for Plynlimon yielded an estimate that 43% of precipitation became R (Robinson and Newson, 1986; Sklash et al., 1996) while R estimates at the Llyn Brianne forest near Plynlimon were 44 % of precipitation inputs (Robson and Neal, 1990). In fact, direct measurements of R during storm events at Plynlimon revealed 50 – 83 % of total storm runoff occurred via overland flow and macropore flow rather than subsurface flow (Chapman et al., 1997). Forested soils at Plynlimon have thick organic horizons (> 12 cm), while the upper reaches of the catchment are characterized by layers of peat (up to 2 m) through which large lateral macropore flow (e.g. pipe flow) is commonly observed (Kirby et al., 1991; Chapman et al., 1997). The peat soils tend to have very low hydraulic conductivity at depth, meaning water does not rapidly flow vertically through the soil profile. Rather, water is quickly transported through the uppermost surface layer of the peat, either as overland flow or through macropores, and does not reach the underlying bedrock to participate in

weathering reactions. If R is not considered in Wales, the combination of high MAP and

low ET at this site would grossly overestimate the fraction of energy from precipitation

that is available to do work in the subsurface because much of the water entering the

system never reaches the subsurface. For example, the use of Eq. 5 to calculate EEMT$_E$,

which uses only MAT and MAP values, estimates EEMT values of 66 MJ m^{-2} yr^{-1}, a

value that is most similar to the AL site in the south (Table 4-1). Thus, the inclusion of R

in the determination of E$_{PPT}$ in Wales, or at sites exhibiting similar soil hydrology, is

critical for calculating EEMT.

Energy associated with biota

Despite differences in vegetation across the climosequence, E$_{BIO}$ is constant

within two standard deviations of the mean (Table 4-1), implying that although

vegetation is an uncontrolled variable at these sites, the biota do not provide vastly

different amounts of energy to the system and are not the dominant control on soil

development. However, the contribution of biota could be more important in the northern

sites compared to the southern sites of the climosequence (Fig. 4-11b).

The determination of E$_{BIO}$ depends on the estimation of NPP and h_{BIO}, the average

specific enthalpy of organic material (assumed here to be 22 kJ g^{-1}) (Rasmussen, 2012).

Although the specific enthalpy varies with different litter types (Lieth, 1975), this value is

not highly variable at a regional scale and is unlikely to introduce large errors in

quantifying E$_{BIO}$. The estimation of NPP is therefore the largest source of error for the

E$_{BIO}$ term. Using an average of 10 years of MODIS data across a 7 km^2 grid centered on

each site yields NPP values within the global range reported by Lieth (1975) for temperate evergreen forests (600 – 2500 g C m^{-2} yr^{-1}). Measurements of NPP at SSHO, although variable, yield an NPP of 580 g C m^{-2} yr^{-1}, a value slightly lower than the MODIS estimate of 638 g C m^{-2} yr^{-1} (Smith, 2013). In Wales, the grassland site has lower NPP (700 g C m^{-2} yr^{-1}) compared to the forest (896 g C m^{-2} yr^{-1}), which is consistent with the general observation that forests have higher NPP than grassland systems (Chapin et al., 2003). Although Wales is at a high latitude with the lowest solar irradiation and coldest temperatures of any site in the study, NPP is not greatly limited here because the site is influenced by a maritime climate that is not subject to freezing or excessive temperatures, meaning precipitation is available year-round (Kirby et al., 1991).

Using Eq. 8, modeled NPP, and thus E_{BIO}, increases linearly across the climosequence, directly correlating with temperature. If this relationship holds, then E_{BIO} increases from 27.2 MJ m^{-2} yr^{-1} in Wales to 53.1 MJ m^{-2} yr^{-1} in PR and F_{BIO} is > 0.5 for all sites except PR. Modeled NPP therefore predicts a 27 % and 61 % higher estimate of NPP in Wales and PR, respectively, compared to the MODIS data. Rasmussen and Gallo (2013) tested using modeled NPP compared to MODIS-derived NPP for 83 watersheds in the USA and found that modeled NPP values were overestimated because only MAT is taken into account in Eq. 8. Therefore while there is likely uncertainty associated with using MODIS data to estimate site specific NPP, MODIS data appear be a better choice than modeled NPP for estimating NPP at specific sites.

Climate and soil development

Higher EEMT value sites studied at the southern end of the climosequence have deeper and better developed soil horizons (Figs. 4-6 – 4-9) than the northern sites (Figs. 4-3 – 4-5) and we observe correlations among soil depth, clay content, average kaolinite content and chemical depletion with EEMT. Soil depth, defined here as the depth of the mobile layer where pedogenic sub-angular blocky structure is observed, increases with increasing EEMT across the climosequence and can be described by a linear fit ($R^2 = 0.80$) (Fig. 4-12a). We also observe a relationship between total clay content and EEMT ($R^2 = 0.94$) (Fig. 4-12b). Similarly, Rasmussen and Tabor (2007) reported an increase in total clay content with increasing EEMT for the previously mentioned granite, basalt and andesite sites. The average depth-weighted kaolinite content in the soil profiles, an indicator of the extent of shale weathering as kaolinite is produced through clay and feldspar dissolution, also increases with higher EEMT across the climosequence ($R^2 = 0.83$) (Fig. 4-12c).

Likewise, the chemical depletion fraction (CDF), which describes the proportion of total denudation in a system that is attributed to chemical weathering (Riebe et al., 2004), generally increases with EEMT (Fig. 4-12d). Here, CDF was calculated as a depth-weighted value for the upper 1 m as described in Ch. 2. In fact, data from the shale climosequence plot well within the range of CDF and EEMT observations for granite sites of Riebe et al (2004) (Rasmussen at al., 2011a) (Fig. 4-13). Across the granitic sites, Rasmussen et al. noted a significant linear relationship ($R^2 = 0.50$) between CDF and EEMT at sites where $F_{BIO} < 0.5$ (but the relationship was not significant for sites with

higher F_{BIO}). All of the climosequence sites have an $F_{BIO} < 0.5$; therefore our data can be directly compared to the granitic sites (Riebe et al., 2004; Rasmussen et al., 2011a) (Fig. 4-13). The relationship of higher EEMT associated with more weathered (e.g. greater CDF) sites is observed in both granite and shale landscapes.

   As discussed earlier, however, the EEMT model does not include changes in energy fluxes over time and assumes the soil systems are stationary. This is unrealistic because over geologic time, soil properties are slowly changing and changes in climate would impact energy fluxes to that system. An example of how this drawback affects EEMT can be observed in the northern part of the transect, where sites exhibit similar EEMT values (~50 MJ m^{-2} yr^{-1}) despite increasing CDF values from north to south across the climosequence. If increasing EEMT correlates with higher CDF when $F_{BIO} > 0.5$, as predicted for granitic landscapes by Rasmussen et al. (2011a), we might expect Wales and PA would have lower EEMT values based on the low CDF values for these sites. This discrepancy, however, is likely related to the geologic history of these sites. During the LGM, Wales was glaciated while PA, and to a lesser extent VA, was impacted by intense freezing and thawing near the glacial margin (Ciolkosz et al., 1986; Cadwell et al., 2004; Catt et al., 2006). The EEMT model relies on the simplifying assumption that the energy associated with the current climate and primary production represents the conditions under which soils formed. For younger sites that were impacted by glaciers, for example, this assumption is not valid. Vegetation in Wales and PA would have been non-existent or more tundra-like during the LGM, which would impact the energy flux (Clark and Ciolkosz, 1988). Thus, the relatively high EEMT values estimated for Wales and PA

based on current conditions appear anomalous because the young soils have experienced these energy fluxes over a shorter timescale than other sites.

Furthermore, the EEMT model does not consider the energy associated with freezing and thawing or the potential energy associated with snow melt (Rasmussen et al., 2005). The energy associated with these processes represents an important parameter for sites at the northern end of the climosequence that is not presently quantified in the model. EEMT might be a better predictor of soil properties at sites in the northern part of the climosequence if long-term energy fluxes and the energy associated with freeze/thaw were included in the EEMT model.

We also tested the relationships among soil depth, clay content, average kaolinite and CDF with E_{BIO}, E_{PPT}, MAP and MAT. As expected, E_{BIO} does not correlate well with any soil property ($R^2 < 0.40$), again documenting that the biota are not strongly controlling the differences in soil properties across the climosequence (Fig. 4-14). Similar to EEMT, E_{PPT} correlates well with soil depth, total clay content and average kaolinite ($R^2 = \sim0.8$) and less strongly with CDF ($R^2 = 0.52$) (Fig. 4-15). MAP, however, does not correlate well with any soil property ($R^2 < 0.20$) (Fig. 4-16). If the time over which the soils have been receiving precipitation is considered, or the cumulative precipitation at each site (MAP * SRT), a stronger correlation is observed for the soil depth, clay and kaolinite content ($R^2 > 0.90$) compared to MAP alone (Fig. 4-17). The strong correlation is observed in this case because the duration of energy input is included in such an approach. Thus, time is an important variable to include in energy estimates because soils are slowly changing (i.e. they are not in a stationary state over geologic timescales) and climate change over time will alter energy fluxes to the soils.

Ultimately, MAT shows the strongest correlations with soil depth, clay content and average kaolinite ($R^2 > 0.94$). CDF increases with increasing temperature ($R^2 = 0.77$) (Fig. 4-18). This result points to temperature as a better predictor of soil development and shale weathering across this climosequence.

Conclusions

Detailed characterization of the morphology, geochemistry and mineralogy of shale-derived soils across a climosequence point to enhanced weathering and soil development with increasingly warm and wet climates across the climosequence. Although pyrite and carbonate weathering may be happening at depths in the bedrock that were not sampled in our study, the deepest weathering reaction observed in the regolith at these shale sites was dissolution of plagioclase feldspar followed by the transformation of 'chlorite' and illite to vermiculite and hydroxy-interlayered vermiculite. Secondary minerals are present at higher concentrations at the warmest sites of the climosequence.

The quantification of energy fluxes using the EEMT model combines multiple climate parameters including temperature, precipitation and seasonality. The application of the EEMT model to this shale climosequence highlights the importance of accounting for the proportion of MAP that is lost to surface runoff rather than infiltrating into the subsurface. Based on the model, the biota does not appear to be driving the observed differences in weathering and soil development despite differences in vegetation across the climosequence. Similar to previously studied granite soils, when the majority of

energy in a system is directed to the subsurface as infiltration rather than toward growth

of vegetation (as described by NPP), greater EEMT is associated with enhanced chemical

weathering: here, this was documented as greater clay and kaolinite content and deeper

soils to the south in the climosequence. However, across this climosequence where

precipitation exceeds evapotranspiration and the contribution of biota to EEMT does not

vary significantly, temperature is the best predictor of soil development. The EEMT

model does not include the energy associated with freezing, thawing and snow melt that

are important processes in northern landscapes. Furthermore, the model does not account

for the fact that energy fluxes at these northern sites were likely much lower during the

LGM when northern sites were glaciated or near glacial margins. Accounting for changes

in climate and primary production over the residence time of the soils as well as the

energy associated with physical processes would greatly improve the predictive ability of

EEMT, especially in northern latitudes.

References

Addiscott, T. M. (1994) Simulation, prediction, foretelling or prophecy? Some thoughts on pedogenetic modeling. *In:* (Eds.) Bryant R.B. and Arnold R.W. Quantitative modeling of soil forming processes. SSSA Spec. Publ. 39, SSSA, Madison, Wisconsin. pp. 1-17.

Amundson R. (2004) Soil formation. *In*: Treatise in Geochemistry (Eds.) Drever J. I., Holland H. D. and Turekian K. K. Elsevier, Amsterdam. pp. 1-35.

Anderson R. S., Anderson S. P. and Tucker G. E. (2012) Rock damage and regolith transport by frost: an example of climate modulation of the geomorphology of the critical zone. *Earth Surf. Proc. Landforms* DOI:10.1002/esp.3330.

Anderson S. P., Dietrich W. E. and Brimhall G. H. (2002) Weathering profiles, mass-balance analysis, and rates of solute loss: Linkages between weathering and erosion in a small, steep catchment. *GSA Bulletin* **114**:1143-1158.

Bain D. C., Mellor A., Robertson-Rintoul M. S. E. and Buckland S. T. (1993) Variations in weathering processes and rates with time in a chronosequence of soils from Glen Feshie, Scotland. *Geoderma* **57**:275-293.

Banwart S., Bernasconi S. M., Bloem J., Blum W., Brandao M., Brantley S., Chabaux F., Duffy C., Kram P., Lair G., Lundin L., Nikolaidis N., Novak M., Panagos P., Ragnarsdottir K. V., Reynolds B., Rousseva S., Ruiter P., van Gaans P., van Riemsdijk W., White T. and Zhang B. (2011) Soil processes and functions in Critical Zone Observatories: Hypotheses and experimental design. *Vadose Zone J.* **10**:974-987.

Barshad I. (1966) The effect of variation in precipitation on the nature of clay minerals formation in soils from acid and basic igneous rocks. Proc. Int'l Clay Cong. Jerusalem, Israel. **1**:167-173.

Barshad I. and Kishk F. M. (1969) Chemical composition of soil vermiculite clays as related to their genesis. *Contr. Mineral. Petrol*. **24**:136-155.

Berner E. K. and Berner R. A. (1996) Global environment: Water, air and geochemical cycles. Prentice-Hall, Inc., Upper Saddle River, New Jersey.

Berry J. and Bjorkman O. (1980) Photosynthetic response and adaptation to temperature in higher plants. *Ann. Rev. Plant Phys*. **31**:491-543.

Bingham N. (2013) C, N, and Mn in Shale Soil Profiles along a Climate Gradient. Bachelor of Science, The Pennsylvania State University.

Birkeland P. W. (1974) Pedology, weathering and geomorphological research. Oxford University Press, New York. 372 p.

Birkeland P. W. (1999) Soils and Geomorphology. Oxford University Press, New York. 430 p.

Bonell M. (1998) Selected challenges in runoff generation research in forests from the hill-slope to headwater drainage basin scale. *J. Am. Water Resour. Assoc*. **34**:765-785.

Brady N. C. and Weil R. R. (2008) The nature and properties of soils. 14th ed. Pearson-Prentice Hall, New Jersey. 965 p.

Brantley S. L. and Lebedeva M. (2011) Learning to read the chemistry of the regolith to understand the critical zone. *Annu. Rev. Earth Planet. Sc*. **39**:387-416.

Brantley S. B., Goldhaber M. B. and Ragnarsdottir K. V. (2007) Crossing disciplines and scales to understand the Critical Zone. *Elements* **3**:307-314.

Brantley S. L. and White A. F. (2009) Approaches to modeling weathered regolith. *Rev. Mineral. Geochem.* **70**:435-484.

Brimhall G. H. and Dietrich W. E. (1987) Constitutive mass balance relations between chemical composition, volume, density, porosity, and strain in metasomatic hydrochemical systems: Results on weathering and pedogenesis. *Geochim. Cosmochim. Acta* **51**:567-587.

British Geological Survey (2005) Digital Geological Map of Great Britain 1:10 000 scale (DiGMapGB-10) data [CD-Rom]. Version 1.11. Keyworth, Nottingham: British Geological Survey. Tile TQ69SW. Release date 20-04-2005.

Buol S. W., Southard R. J., Graham R. C. and McDaniel P. A. (2003) Soil genesis and classification. 5th ed. Iowa State Press, Iowa.

Buurman P., Pape T. and Muggler C. C. (1997) Laser grain-size determination in soil genetic studies 1. Practical problems. *Soil Sci.* **162**:211-218.

Cadwell D. H. and Muller E. H. (2004) New York glacial geology, U.S.A. *In:* Quaternary Glaciations – Extent and Chronology. Part II: North America. (Eds.) Ehlers J. and Gibbard P. L. Elsevier, Netherlands. pp. 201-205.

Catt J. A., Gibbard P. L, Lowe J. J., McCarroll D., Scourse J. D., Walker M. J. C. and Wymer J. J. (2006) Quaternary: ice sheets and their legacy. In The Geology of England and Wales. Eds. Brenchley P.J. and Rawson P.F. The Geological Society of London, London, UK. pp. 429-467.

Chapman, P. (1986) Geochemical and mineralogical studies of the weathering of Silurian argillaceous rocks. Ph.D. Dissertation. University of North Wales, Bangor.

Chapman P. J., Reynolds B. and Wheater H. S. (1997) Sources and controls of calcium and magnesium in storm runoff: the role of groundwater and ion exchange reactions along water flowpaths. *Hydrol. Earth Syst. Sci*. **1**:671-685.

Clark G. M. and Ciolkosz E. J. (1988) Periglacial geomorphology of the Appalachian highlands and interior highlands south of the glacial border – a review. *Geomorph.* **1**:191-220.

Ciolkosz E. J., Cronce R. C. and Sevon W. D. (1986) Periglacial features in Pennsylvania. Pa. State Univ., Agron. Ser. 92. 52 p.

Chapin F. S., Matson P. A. and Mooney H. A. (2002) Principles of Terrestrial Ecosystem Ecology. Springer, New York. 436 p.

Deng Y., White G. N. and Dixon J. B. (2009) Soil Mineralogy Laboratory Manual. 11th edition. Department of Soil and Crop Sciences, Texas A&M University, College Station, TX.

Dere, A. L. and White T. S. (2013) Meteorological data for the shale transect. Available at: http://www.czo.psu.edu.

Dere, A. L., White T. S., April R. H., Reynolds B., Miller T. E., Knapp E. P., McKay L. D. and Brantley S. L. (2013) Climate dependence of feldspar weathering along a latitudinal gradient. *Geochim. Cosmochim. Acta* **122**:101-126.

Dokuchaev V. V. (1883) Russian chernozems (Russkii chernozem). Israel Prog. Sci. Trans., Jerusalem, 1967. Transl. from Russian by N. Kraner. Available from U.S. Dep. Of Commerce, Springfield, Virginia.

Drever, J. L. (2003) The Geochemistry of Natural Waters. Prentice Hall, NJ. 436 p.

Duffy C. (2012) Meteorological data. Available at: http://www.czo.psu.edu.

Eberl D. D. (2003) User's guide to RockJock – a program for determining quantitative mineralogy from powder x-ray diffraction data. U.S. Geological Survey, Open-file report 03-78.

Ferrier K. L., Kirchner J. W., Riebe C. S. and Finkel R. C. (2010) Mineral-specific chemical weathering rates over millennial timescales: Measurements at Rio Icacos, Puerto Rico. *Chem. Geol*. **277**:101-114.

Finlayson C. P. (1964) Geology map and mineral resources summary of the White Hollow quadrangle, Tennessee. Tennessee Div. Geol. Geologic Map GM-145-SW.

Folk R. L. (1960) Petrography and origin of the Tuscarora, Rose Hill, and Keefer Formations, Lower and Middle Silurian of Eastern West Virginia. *J. Sedim. Res*. **30**:1-58.

Gardner T. W., Ritter J. B., Shuman C. A., Bell J. C. Sasowsky K. C. and Pinter N. (1991) A periglacial stratified slope deposit in the valley and ridge province of central Pennsylvania, USA: sedimentology, stratigraphy and geomorphic evolution. *Permafrost Periglac. Process.* **2**:141-162.

Gillette T. (1947) The Clinton of western and central New York. N.Y. State Mus. Bull. 341.

Harris W. and White G.N. (2008) X-ray diffraction techniques for soil mineral identification. *In:* Methods of Soil Analysis. Part 5. Mineralogical Methods. SSA Book Series, no. 5. (Eds.) Ulery A. L. and Drees L. R. Madison, Wisconsin.

Helgeson H. C., Garrels R. M., and MacKenzie F. T. (1969) Evaluation of irreversible reactions in geochemical processes involving minerals and aqueous solutions—II. Applications. *Geochim. Cosmochim. Acta* **33**:455-481.

Hillier S. (2000) Accurate quantitative analysis of clay and other minerals in sandstones by XRD: comparison of a Rietveld and a reference intensity ratio (RIR) method and the importance of sample preparation. *Clay Min*. **35**:291-302.

Holiday A. S., Martindale W., Alred R., Brooks A. L. and Leegood R. C. (1992) Changes in activities of enzymes of carbon metabolism in leaves during exposure of plants to low-temperature. *Plant Physiol*. **98**:1105-1114.

Jackson, M. L. (1974) Soil Chemical Analysis – Advanced Course 2nd edition. University of Wisconsin, Dept. of Soil Science, Madison, Wisconsin.

Jenkins R. and Snyder R. L. (1996) Introduction to X-ray Powder Diffractometry. John Wiley and Sons, Inc., New York. 403 p.

Jenny H. (1941) Factors of soil formation: a system of quantitative pedology. 1st ed. McGraw-Hill, Inc., New York. 281 p.

Jin L., Andrews D. M., Holmes G. H., Lin H. and Brantley S. L. (2011) Opening the "black box": Water chemistry reveals hydrological controls on weathering in the Susquehanna Shale Hills Critical Zone Observatory. *Vadose Zone J.* **10**:928-942.

Jin L. Ravella R., Ketchum B., Heaney P. and Brantley S. L. (2010) Mineral weathering and elemental transport during hillslope evolution at the Susquehanna/Shale Hills Critical Zone Observatory. *Geochim. Cosmochim. Acta.* **74**:3669-3691.

King P. B. and Ferguson H. W. (1960) Geology of northeasternmost Tennessee: U.S. Geol. Survey Prof. Paper 311. 136 p.

Kirby, C., Newson M. D. and Gilman K. (1991) Plynlimon Research: The first two decades. Institute of Hydrology Report No. 109, Wallingford, UK.

Klute A. (1986) Methods of Soil Analysis. Part I. Physical and Mineralogical Methods. 2nd ed. SSSA Book Series 9. Soil Sci. Soc. Amer., Wisconsin.

Konert M. and Vandenberghe J. (1997) Comparison of laser grain size analysis with pipette and sieve analysis: a solution for the underestimation of the clay fraction. *Sedimentology* **44**:523-535.

Kozak S. J. (1965) Geology of the Millboro Quadrangle, Virginia. Virginia Div. Mineral. Resources Rep. Invest. 8. 19 p.

Kump L. R., Brantley S. L. and Arthur M. A. (2000) Chemical weathering, atmospheric CO2, and climate. *Ann. Rev. Earth Planet. Sci*. **28**:611-667.

Lieth H. (1975) Primary production of the major vegetation units of the world. *In:* Primary Productivity of the Biosphere. (Eds.) Lieth H. and Whittaker R. H. Springer-Verlag, New York. pp. 203-215.

Lin H. (2006) Temporal stability of soil moisture spatial pattern and subsurface preferential flow pathways in the Shale Hills catchment. *Vadose Zone J*. **5**:317-340.

Medlin J. H., Suhr N. H. and Bodkin J. B. (1969) Atomic Absorption Analysis of Silicates Employing LiBO2 Fusion. *Atomic Absorption Newslett.* **8**:25-29.

Minasny B. and McBrantney A. B. (2001) A rudimentary mechanistic model for soil formation and landscape development II. A two-dimensional model incorporating chemical weathering. *Geoderma* **103**:161-179.

Minasny B., McBrantney A. B. and Salvador-Blanes (2008) Quantitative models for pedogenesis – a review. *Geoderma* **144**:140-157.

Monteith J. L. (1965) Evaporation and environment. *In:* Symposium of the Society for Experimental Biology, The State and Movement of Water in Living Organisms. (Ed.) Fogg G. E. Academic Press, Inc., New York. pp. 205-234.

Moore D. M. and Reynolds R. C. (1997) X-ray diffraction and the identification and analysis of clay minerals. 2nd edition. Oxford University Press, New York.

Mu Q., Zhao S and Running W. (2011) Improvements to a MODIS Global Terrestrial Evapotranspiration Algorithm. *Remote Sensing of the Env*. **115**:1781-1800.

National Oceanographic and Atmospheric Administration (NOAA) (2011) Climate Data Online: Monthly Observational Data. U.S. Department of Commerce, National Oceanic and Atmospheric Administration, National Environmental Satellite Data and Information Service, National Climatic Data Center. http://www.ncdc.noaa.gov/cdo-web/

National Research Council (NRC). (2001) Basic opportunities in Earth Sciences. National Research Council, Washington, D.C.

National Research Council (NRC). (2010) Landscapes on the edge: New horizons for research on the Earth's surface. The National Academies Press, New York. 163 p.

Oak Ridge National Laboratory Distributed Active Archive Center (ORNL DAAC). 2009. MODIS subsetted land products, Collection 5. Available on-line [http://daac.ornl.gov/MODIS/modis.html] from ORNL DAAC, Oak Ridge, Tennessee, U.S.A. Accessed November 25, 2013.

Odum H. T. (1983) Systems ecology: An introduction. John Wiley & Sons, New York.

Pelletier J. D. and Rasmussen C. (2009) Quantifying the climatic and tectonic controls on hillslope steepness and erosion rate. *Lithosphere.* **1**:73-80.

Poppe, L. J., Paskevich V. F., Hathaway J. C. and Blackwood D. (2002) A laboratory manual for X-ray powder diffraction. U.S. Geological Survey Open File Report 01-041. U.S. Geological Survey, MA.

Rasmussen C. (2012) Thermodynamic constraints on effective energy and mass transfer and catchment function. *Hydrol. Earth Syst. Sci*. **16**:725-739.

Rasmussen C. and Gallo E. L. (2013) Technical note: A comparison of model and empirical measures of catchment-scale effective energy and mass transfer. *Hydrol. Earth Syst. Sci*. **17**:3389-3395.

Rasmussen C. and Tabor N. J. (2007) Applying a quantitative pedogenic energy model across a range of environmental gradients. *Soil Sci. Soc. Amer. J*. **71**:1719-1729.

Rasmussen C., Southard R. J. and Horwath W. R. (2005) Modeling energy inputs to predict pedogenic environments using regional environmental databases. *Soil Sci. Soc. Amer. J*. **69**:1266-1274.

Rasmussen C., Brantley S., Richter D. D., Blum A., Dixon J. and White A. F. (2011a) Strong climate and tectonic control on plagioclase weathering in granitic terrain. *Earth Planet. Sci. Lett*. **301**:521-530.

Rasmussen C., Troch P. A., Chorover J., Brooks P., Pelletier J. and Huxman T. E. (2011b) An open system framework for integrating critical zone structure and function. *Biogeochem.* **102**:15-29.

Riebe C. S., Kirchner J. W. and Finkel R. C. (2004) Erosional and climatic effects on long-term chemical weathering rates in granitic landscapes spanning diverse climate regimes. *Earth Planet. Sc. Lett*. **224**:547-562.

Robson A. and Neal C. (1990) Hydrograph separation using chemical techniques: an application to catchments in mid-Wales. *J. Hydrol.* **116**:345-363.

Robinson M. and Newson M. D. (1986) Comparison of forest and moorland hydrology in an upland area with peat soils. *Int. Peat J*. **1**:49-68.

Ruhe R. V. (1984) Loess-derived soil of the Mississippi Valley region: II. Soil-climate system. *Soil Sci. Soc. Am. J*. **48**:864-867.

Runge E. C. A. (1973) Soil development sequences and energy models. *Soil Sci*. **115**:183-193.

Running S. W., Nemani R. R., Heinsch F. A., Zhao M. S., Reeves M. and Hashimoto H. (2004) A continuous satellite-derived measure of global terrestrial primary production. *Biosci.* **54**:547-560.

Sanford T. H. (1966) Generalized geologic map of Marshall County, Alabama. Alabama Geol. Survey Map 60.

Simonson R. W. (1959) Outline of a generalized theory of soil genesis. *Soil Sci. Soc. of Amer. J.* **23**:152-156.

Slash M. G., Beven K. J., Gilman K. and Darling W. G. (1996) Isotope studies of pipeflow at Plynlimon, Wales, UK. *Hydrol. Process*. **10**:921-944.

Smeck N. E., Runge E. C. A. and Mackintosh E. E. (1983) Dynamics and genetic modeling of soil systems. *In*: Pedogenesis and Soil Taxonomy. (Eds.) Wilding L. P, Smeck N. E. and Hall G. F. Elsevier, New York. pp. 51-81.

Smith L. A. (2013) Aboveground carbon distribution across a temperate watershed. MS Thesis, The Pennsylvania State University.

Soil Survey Staff (1993) National Soil Survey Handbook, Title 430-VI. U.S. Govt. Printing Office, Washington, D.C.

Soil Survey Staff (1999). Soil Taxonomy: A basic system of soil classification for making and interpreting soil surveys. USDA-NRCS, Washington, DC.

Soil Survey Staff. (2004) Soil survey laboratory methods manual. Soil Surv. Invest. Rep. 42. Version 4.0. USDA-NRCS, Washington, DC.

Strakhov N. M. (1967) Principles of lithogenesis, Vol. 1. Oliver and Boyd Ltd., Edinburgh, 245 p.

Thornthwaite C. W. (1948) An approach toward a rational classification of climate. *Geographical Rev*. **38**:55-94.

Tobish O. and Turner M. (1971) Geologic map of the San Sebastian Quadrangle, Puerto Rico. Puerto Rico: U.S. Geol. Survey Misc. Invest. Series Map I-661.

Vepraskas M. J. (2001) Morphological features of seasonally reduced soils. *In*: Wetland soils: Genesis, hydrology, landscapes, and classification. (Eds.) Vepraskas MJ., Craft C.B. and Richardson J.L. pp 163-182.

Walter R. C. and Merritts D. J. (2008) Natural streams and the legacy of water-powered mills. *Science* **319**:299-304.

White A. F. and Brantley S. L. (1995) Chemical weathering rates of silicate minerals: An overview. *In*: Chemical Weathering Rates of Silicate Minerals, Reviews in Mineralogy. Mineralogical Society of America, Washington, D.C. pp. 1-22.

Whittig L. D. and Allardice W. R. (1986) X-ray diffraction techniques. *In:* Methods of Soil Analysis, Part 1: Physical and Mineralogical Methods. (Ed.) Klute A. Soil Sci. Am. Book Series No. 9. ASA and SSSA, Madison, WI.

Wilson M. J. (2004) Weathering of the primary rock-forming minerals: processes, products and rates. *Clay Min.* **39**:233-266.

Yesavage T., Fantle M. S., Vervoort J., Mathur R., Jin L., Liermann L. J. and Brantley S. L. (2012) Fe cycling in the Shale Hills Critical Zone Observatory, Pennsylvania: An analysis of biogeochemical weathering and Fe isotope fractionation. *Geochim. Cosmochim. Acta* **99**:18-38.

Zhao M. S. and Running S. W. (2010) Drought-induced reduction in global terrestrial net primary production from 2000 through 2009. *Science* **329**:940-943.

Figures

Figure 4-1. Map of sampling sites in the shale climosequence.
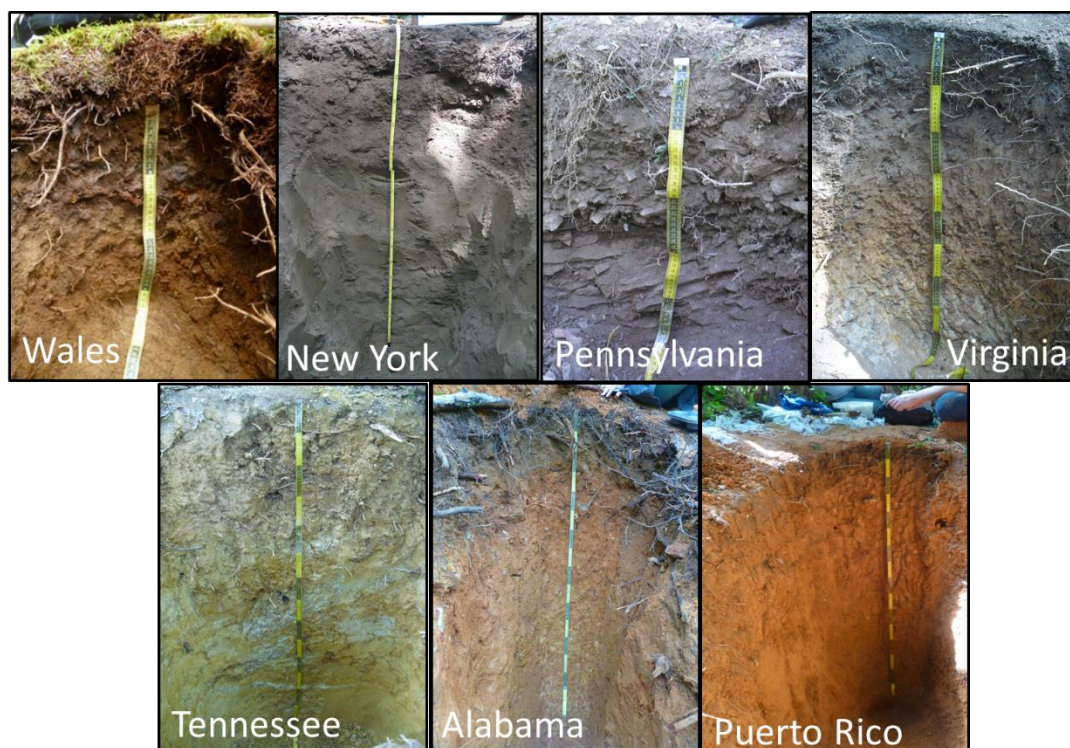
Figure 4-2. Photographs of ridgetop soils from each site in the climosequence.
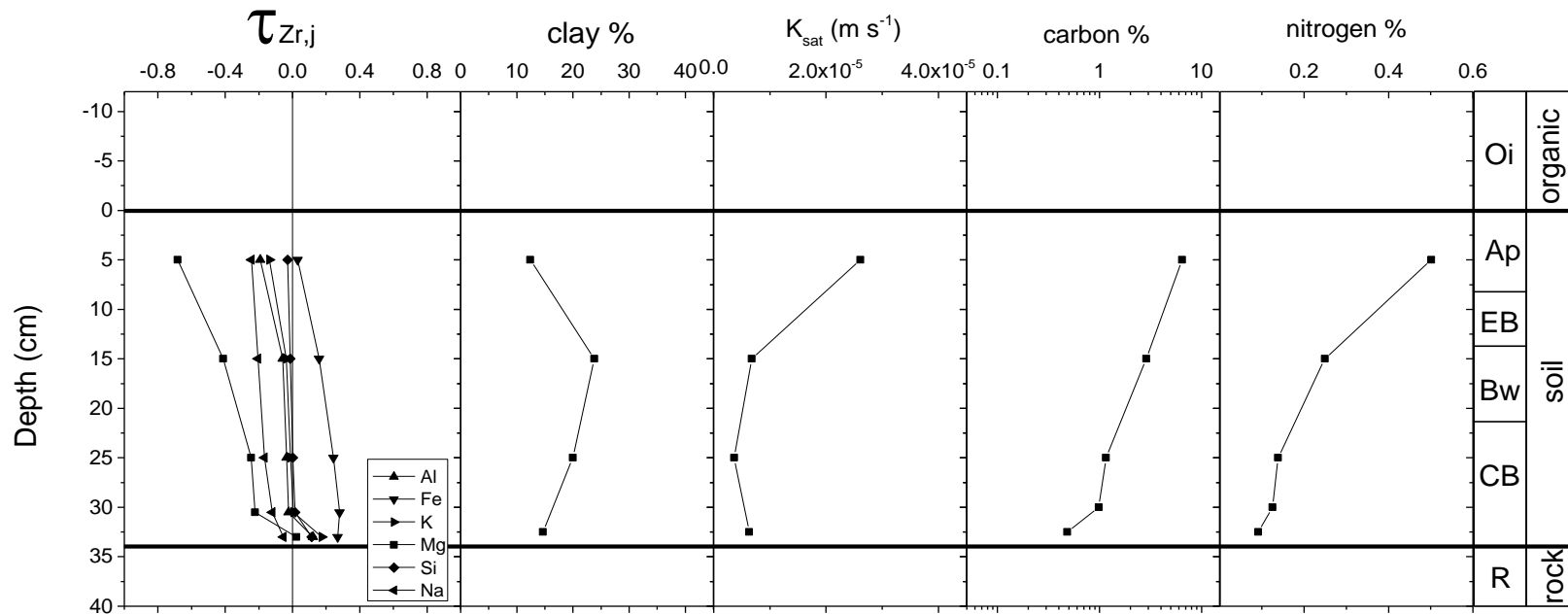
Figure 4-3. Wales ridgetop elemental τ profiles, clay , carbon and nitrogen content and estimated saturated hydraulic conductivity as a function of depth. No clay films or redoximorphic features were observed in the soil profile. Highly fractured shale in the CB horizon is underlain by more coherent rock. Saturated hydraulic conductivity (Ksat) was estimated using the SPAW model (Saxton and Rawls, 2006). The negative depth values correspond to the organic horizon above the mineral soil surface (depth = 0) and consists of largely undecomposed roots and mosses.
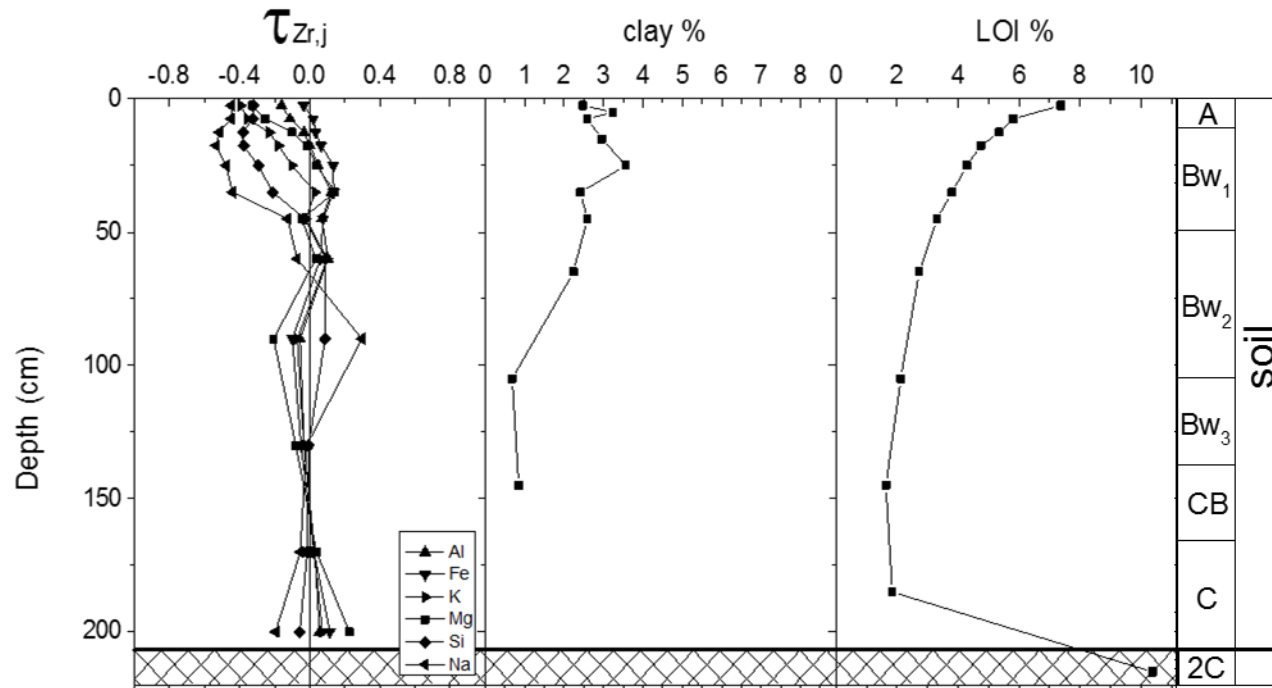
Figure 4-4. New York ridgetop elemental τ profiles, clay, rock fragment and LOI content as a function of depth. No clay films or redoximorphic features were observed in the profile. The entire profile consists of glacial till, with a calcium carbonate cemented layer at depth indicated by the hachured area. No carbon data were available, therefore loss on ignition (LOI) data is presented (Dere et al., 2013).
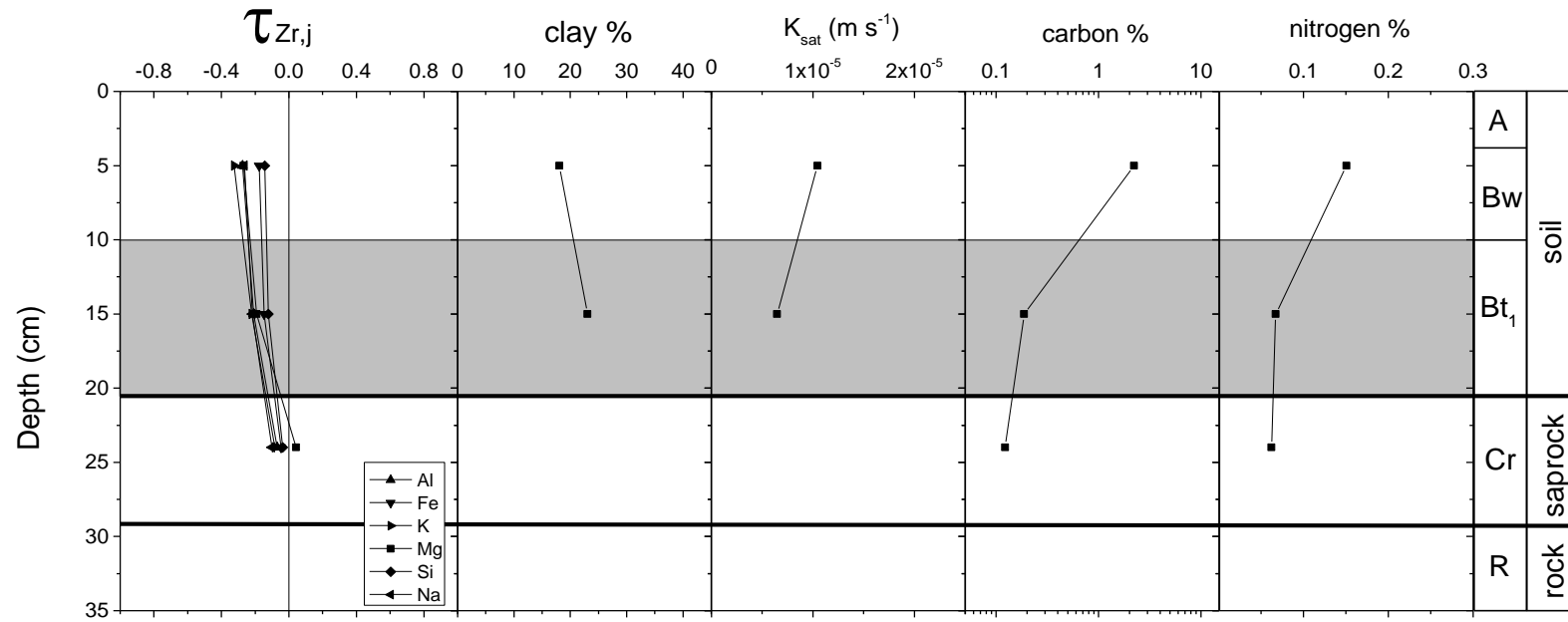
Figure 4-5. Pennsylvania (Whipple Dam) ridgetop elemental τ profiles, clay, carbon and nitrogen content and estimated saturated hydraulic conductivity as a function of depth. Grey shaded areas indicate the presence of clay films; no clay films were observed in unshaded areas. No redoximorphic features were observed. Highly fractured saprock is underlain by more coherent rock. Saturated hydraulic conductivity (Ksat) was estimated using the SPAW model (Saxton and Rawls, 2006).
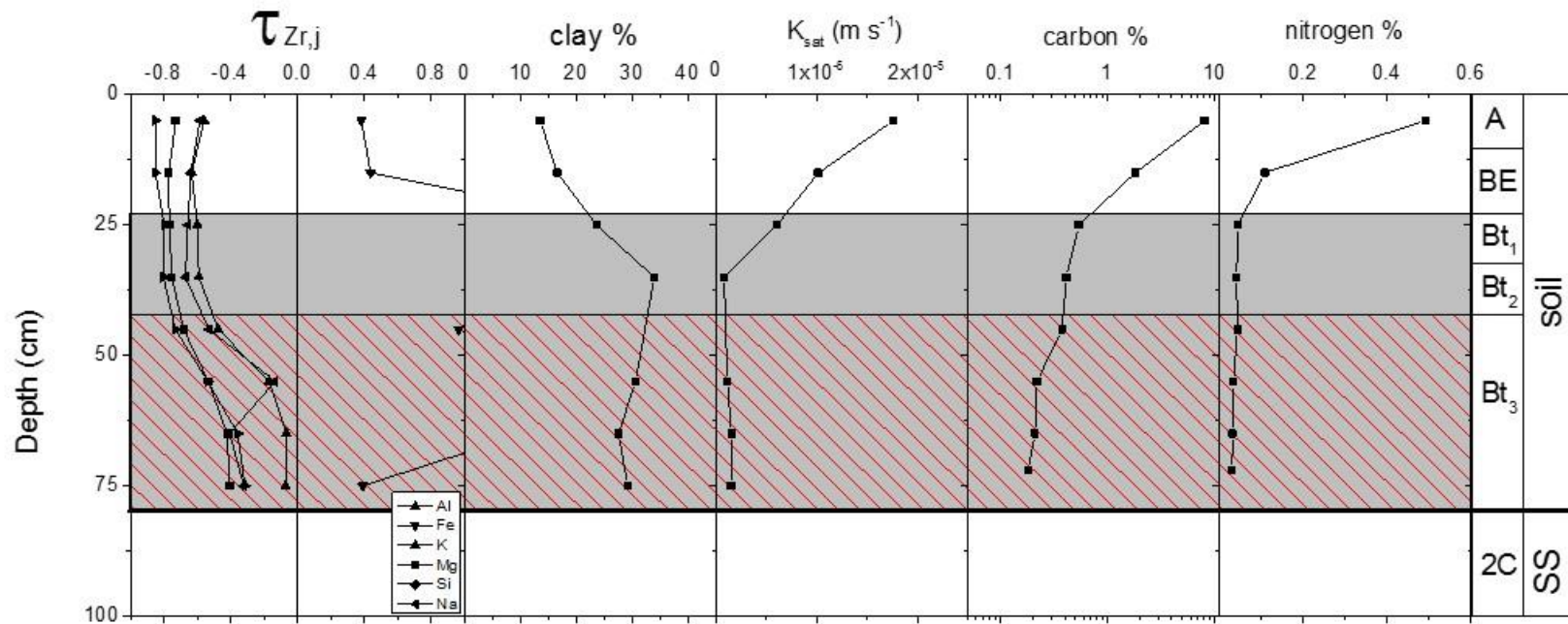
Figure 4-6. Virginia ridgetop elemental τ profiles, clay, carbon and nitrogen content and estimated saturated hydraulic conductivity as a function of depth. Grey shaded areas indicate the presence of clay films; no clay films were observed in unshaded areas. Hachured areas have moderately prominent redoximorphic features including both concentrations and depletions. Sandstone saprolite (SS) is present below 80 cm and represents a different parent material from the upper 80 cm of the profile (see text). Saturated hydraulic conductivity (Ksat) was estimated using the SPAW model (Saxton and Rawls, 2006).
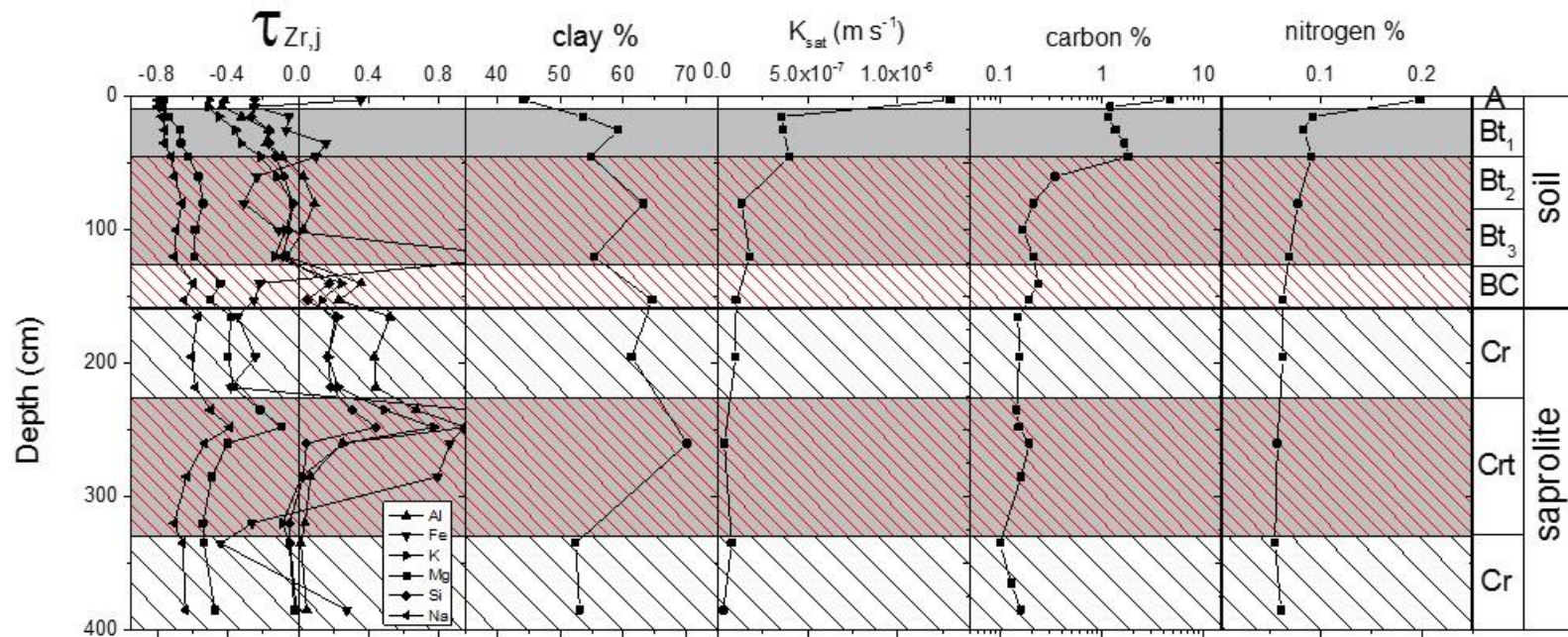
Figure 4-7. Tennessee ridgetop elemental τ profiles, clay, carbon and nitrogen content and saturated hydraulic conductivity as a function of depth. Grey shaded areas indicate the presence of clay films; no clay films were observed in unshaded areas. Sparsely hachured areas have a gleyed matrix with few to no concentrations while densely hachured areas have prominent redoximorphic features including both concentrations and depletions. Saprolite structure is present below 160 cm. Saturated hydraulic conductivity (Ksat) was estimated using the SPAW model (Saxton and Rawls, 2006).
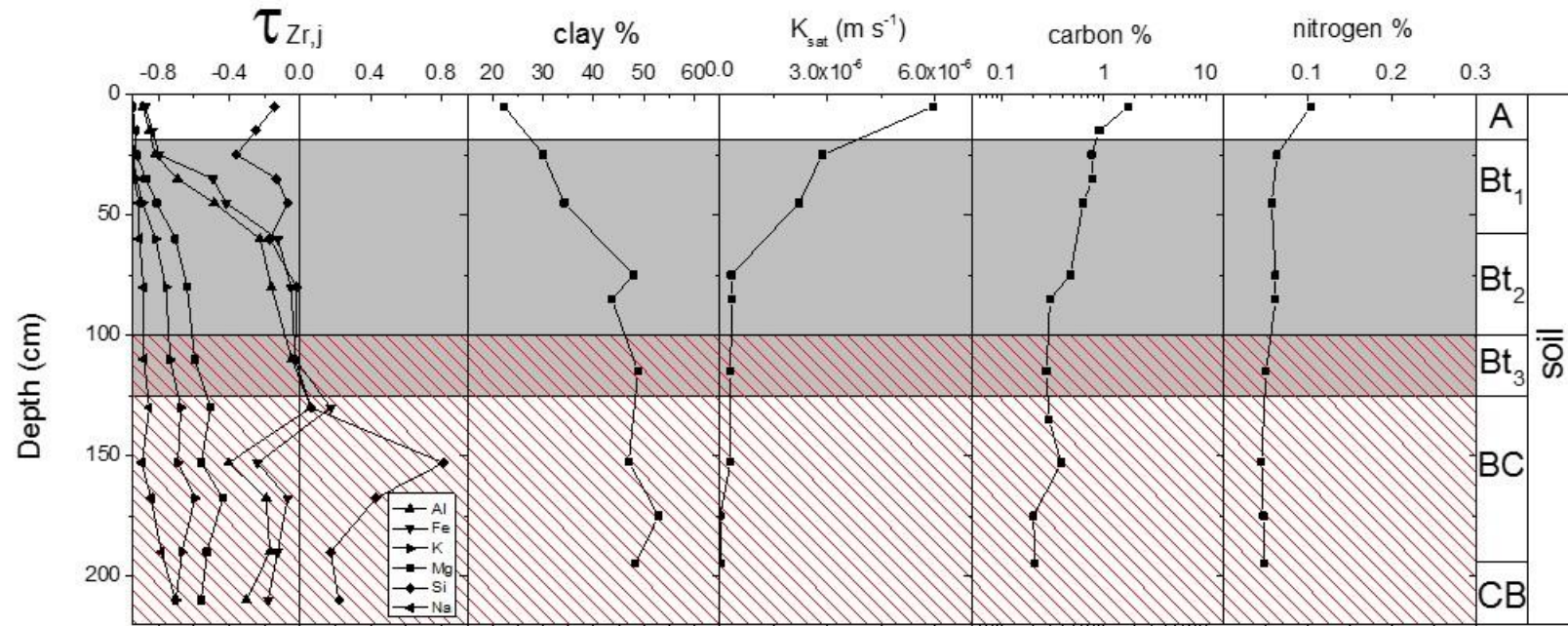
Figure 4-8. Alabama ridgetop elemental τ profiles, clay, carbon and nitrogen content and saturated hydraulic conductivity as a function of depth. Grey shaded areas indicate the presence of clay films; no clay films were observed in unshaded areas. Hachured areas have prominent redoximorphic features including both concentrations and depletions. Saprolite structure was not observed in this soil core and is likely deeper than the sampled depth. Saturated hydraulic conductivity (Ksat) was estimated using the SPAW model (Saxton and Rawls, 2006).
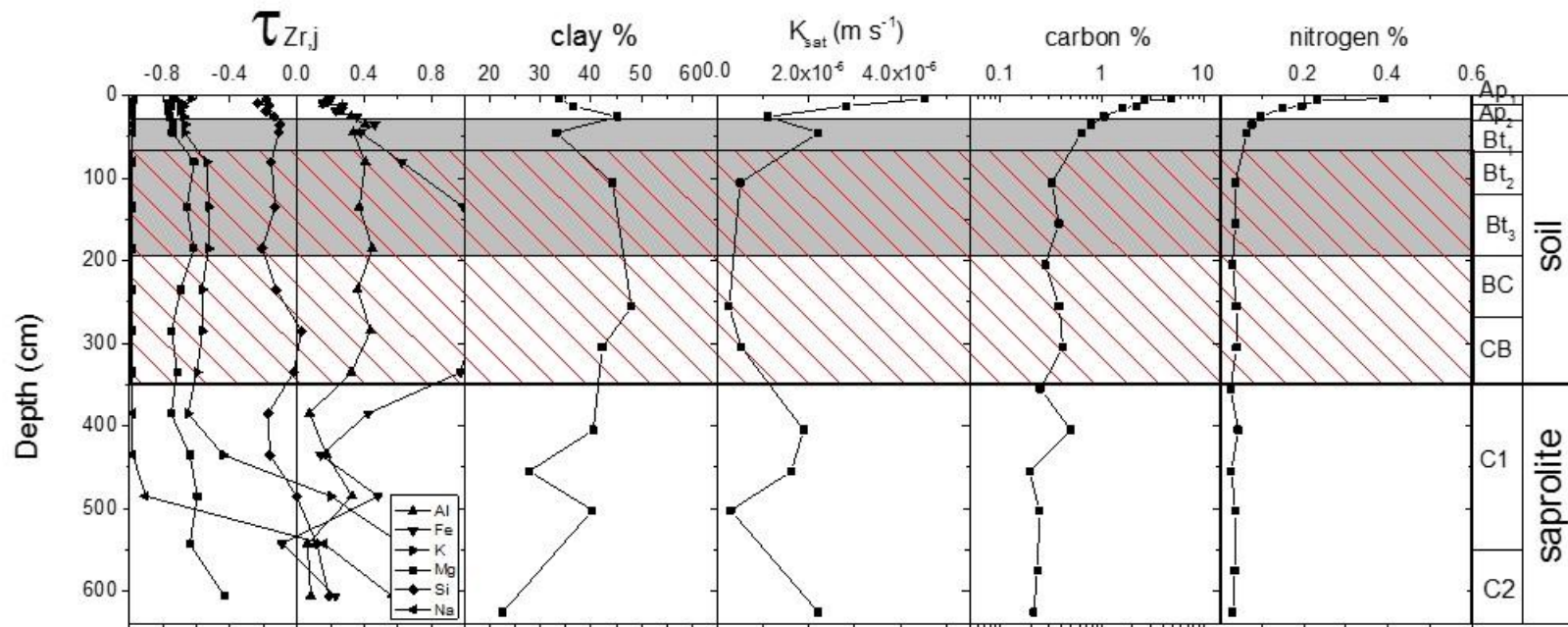
Figure 4-9. Puerto Rico ridgetop elemental τ profiles, clay, carbon and nitrogen content and saturated hydraulic conductivity as a function of depth. Grey shaded areas indicate the presence of clay films; no clay films were observed in unshaded areas. Hachured areas have redoximorphic features including both concentrations and depletions. Saprolite structure was not observed in this soil core so the boundary between soil and saprolite was defined by a lack of pedogenic structure (sub-angular blocky structure). Saturated hydraulic conductivity (Ksat) was estimated using the SPAW model (Saxton and Rawls, 2006).
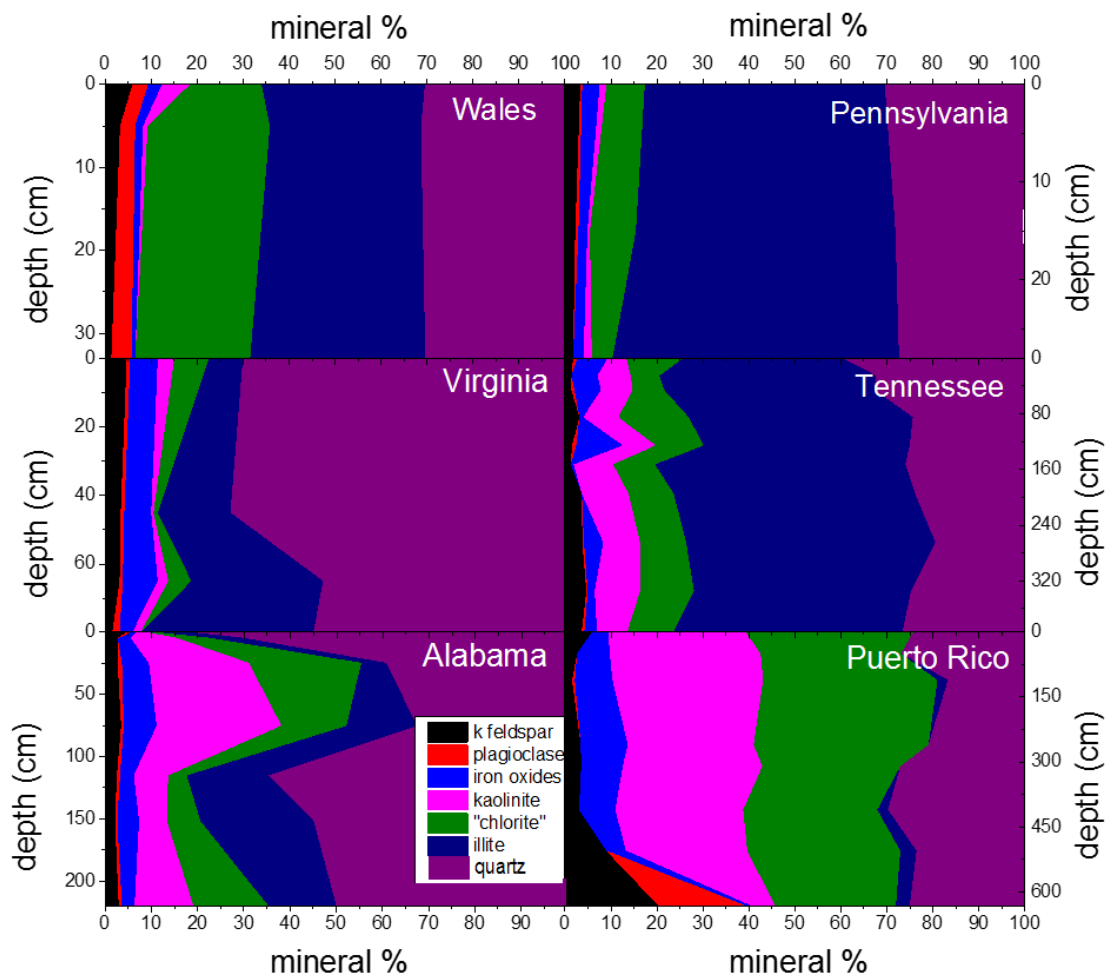
Figure 4-10. Bulk soil mineralogy as a function of depth across the climosequence. 'Chlorite' refers to secondary vermiculite and hydroxy-interlayered vermiculite (HIV). NY mineralogy was not analyzed due to till parent material.
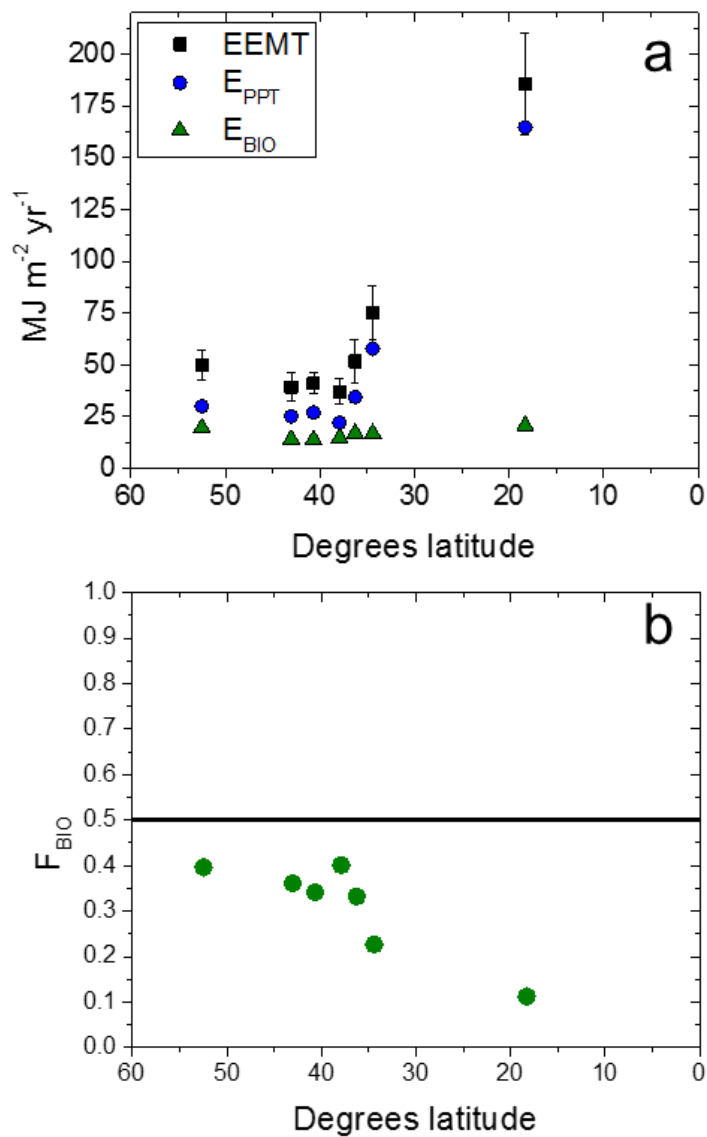
Figure 4-11. EEMT, E_{PPT} and E_{BIO} (a) and F_{BIO} as a function of latitude across the climosequence. The solid line in (b) represents an $F_{BIO} = 0.5$, below which systems are dominated by E_{PPT}, resulting in more energy flux via precipitation to the subsurface. Error bars for EEMT values represent the error associated with MAT and MAP at each site.
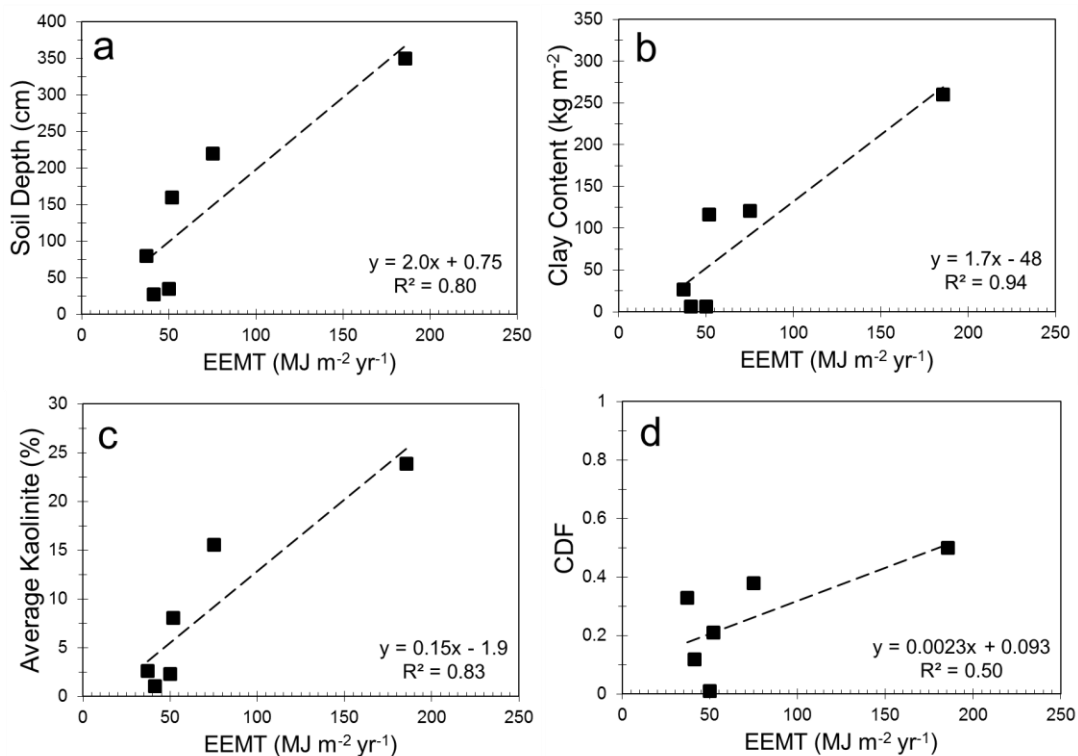
Figure 4-12. Soil depth (a), total clay content (b), depth-weighted average kaolinite content (c) and chemical depletion fraction CDF (d) as a function of effective energy mass transfer (EEMT) across the transect. New York is not plotted due to till parent material.
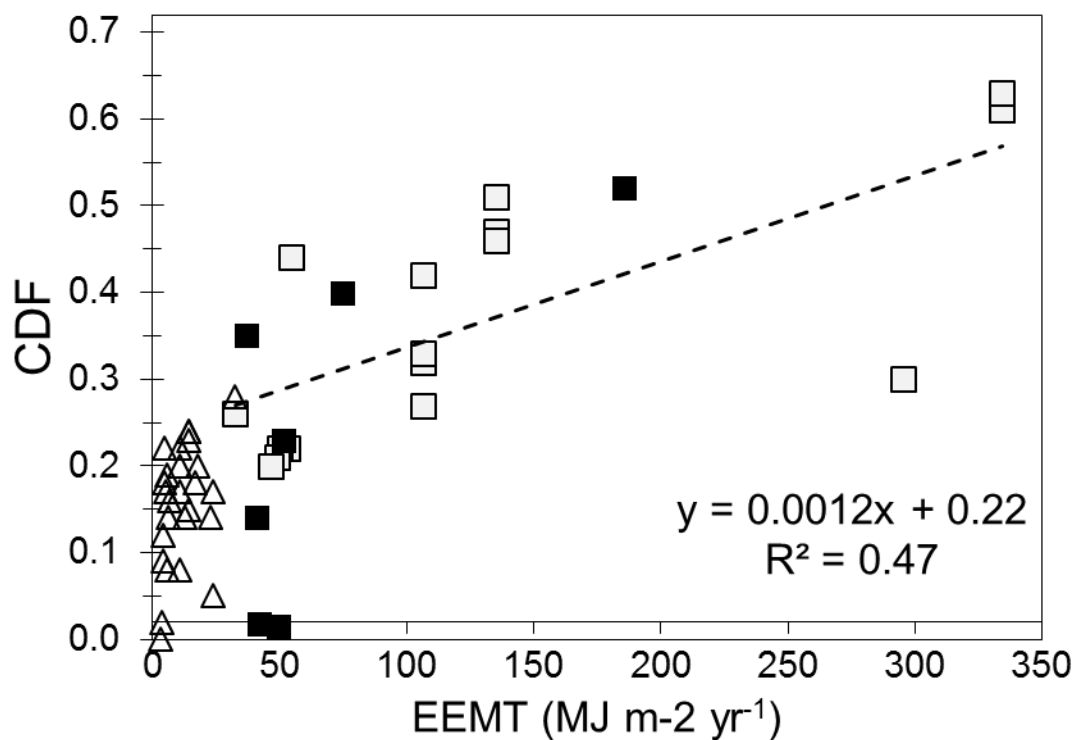
Figure 4-13. Chemical depletion fraction (CDF) as a function of effective energy mass transfer (EEMT). Closed squares are shale data from this study. Open symbols are granite data from Riebe et al. (2004) and used by Rasmussen et al. (2011) to calculate EEMT (following Rasmussen and Tabor, 2007). Open squares represent granite sites where $F_{BIO} < 0.5$ and triangles are granite sites where $F_{BIO} > 0.5$. The dashed line is the linear fit of granite and shale data for sites where $F_{BIO} < 0.5$. The two squares plotting near zero CDF are from the grassland and forested catchments at Plynlimon, Wales. NY is not plotted due to till parent material.
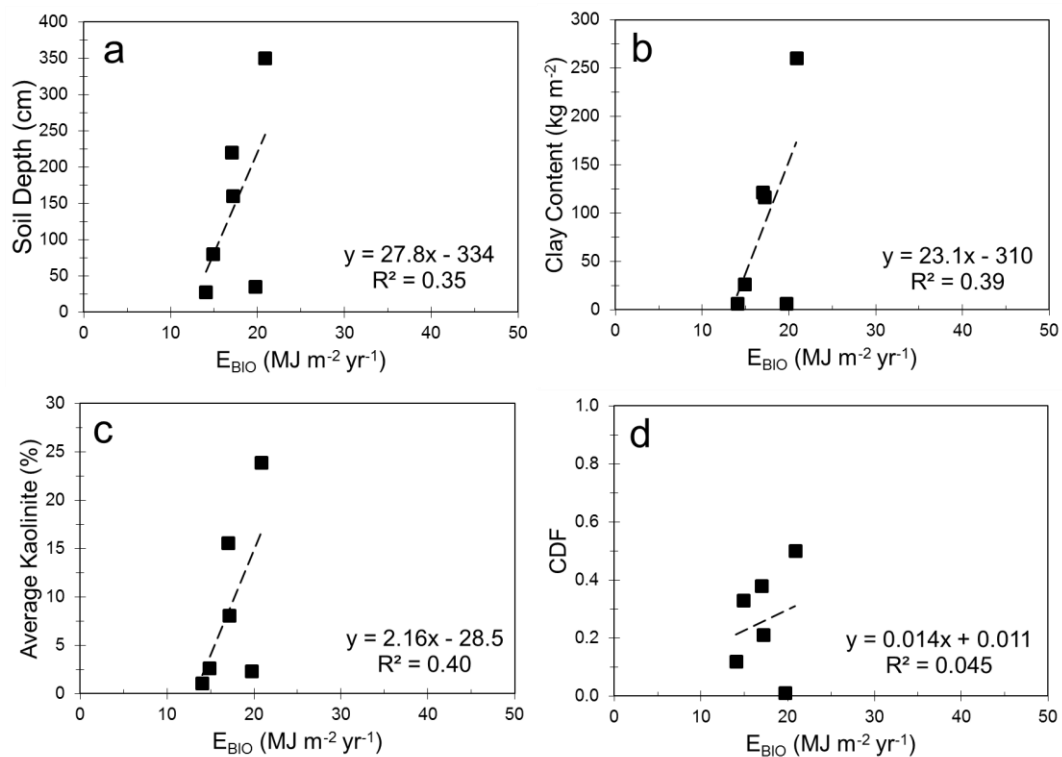
Figure 4-14. Soil depth (a), total clay content (b), depth-weighted average kaolinite content (c) and chemical depletion fraction CDF (d) as a function of E_{BIO} across the climosequence. New York is not plotted due to till parent material.
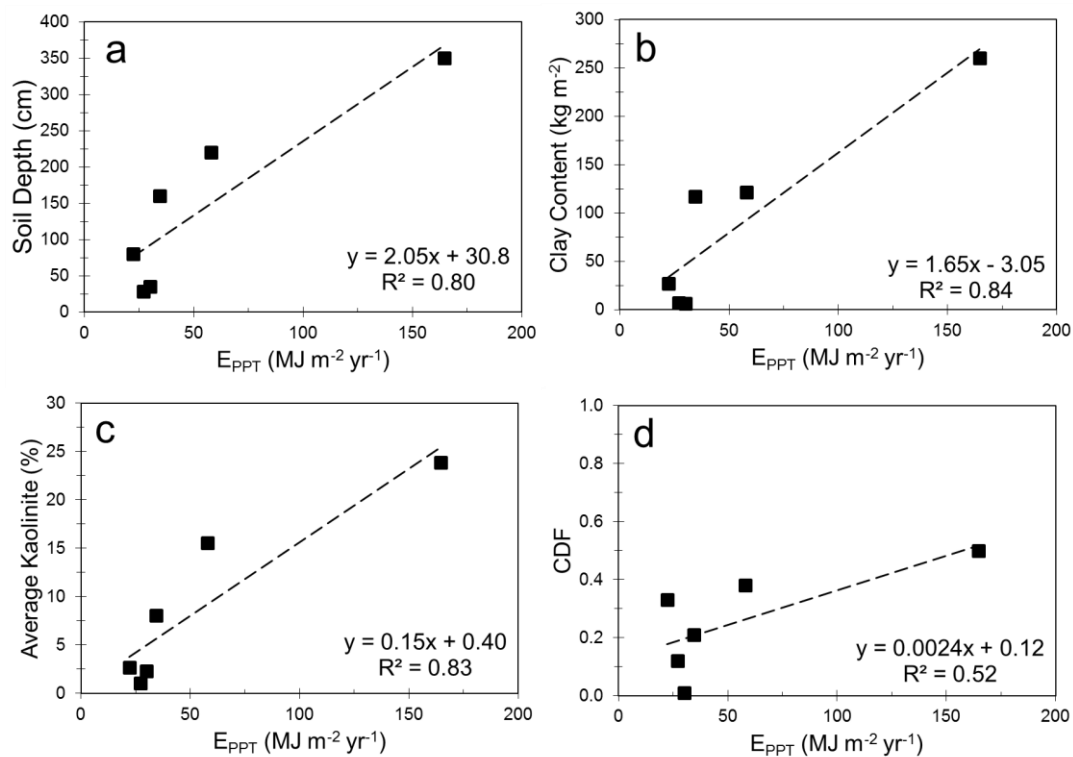
Figure 4-15. Soil depth (a), total clay content (b), depth-weighted average kaolinite content (c) and chemical depletion fraction CDF (d) as a function of E_{PPT} across the climosequence. New York is not plotted due to till parent material.
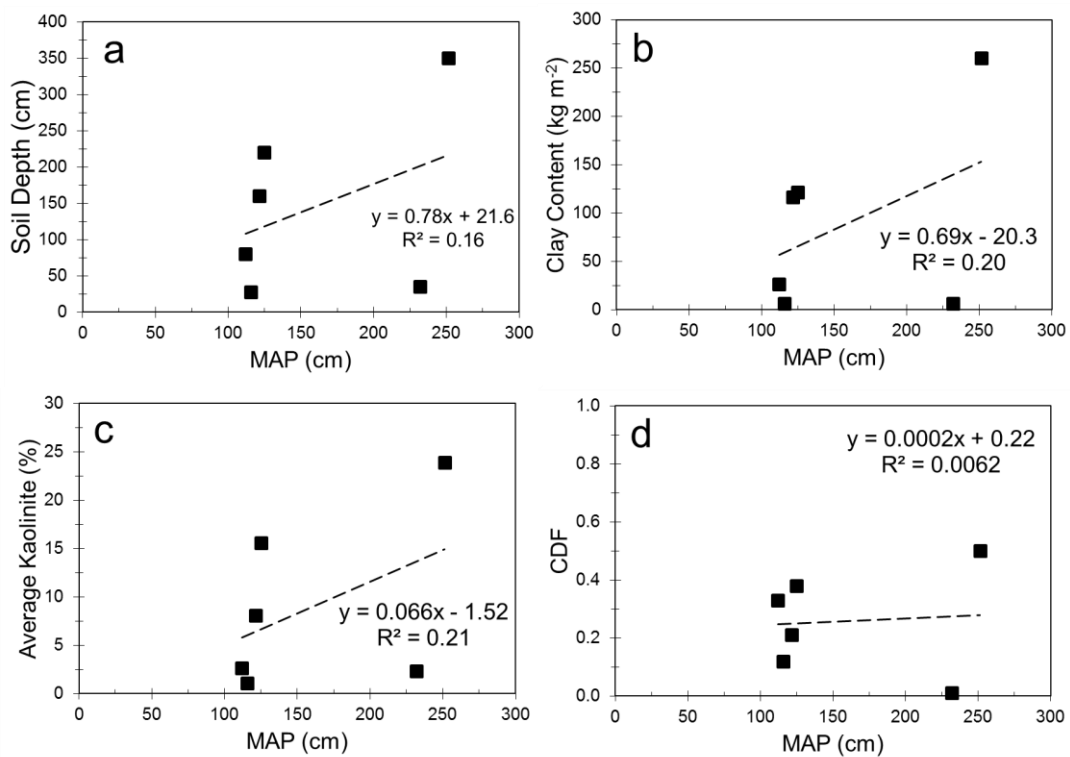
Figure 4-16. Soil depth (a), total clay content (b), depth-weighted average kaolinite content (c) and chemical depletion fraction CDF (d) as a function of MAP across the transect. New York is not plotted due to till parent material.
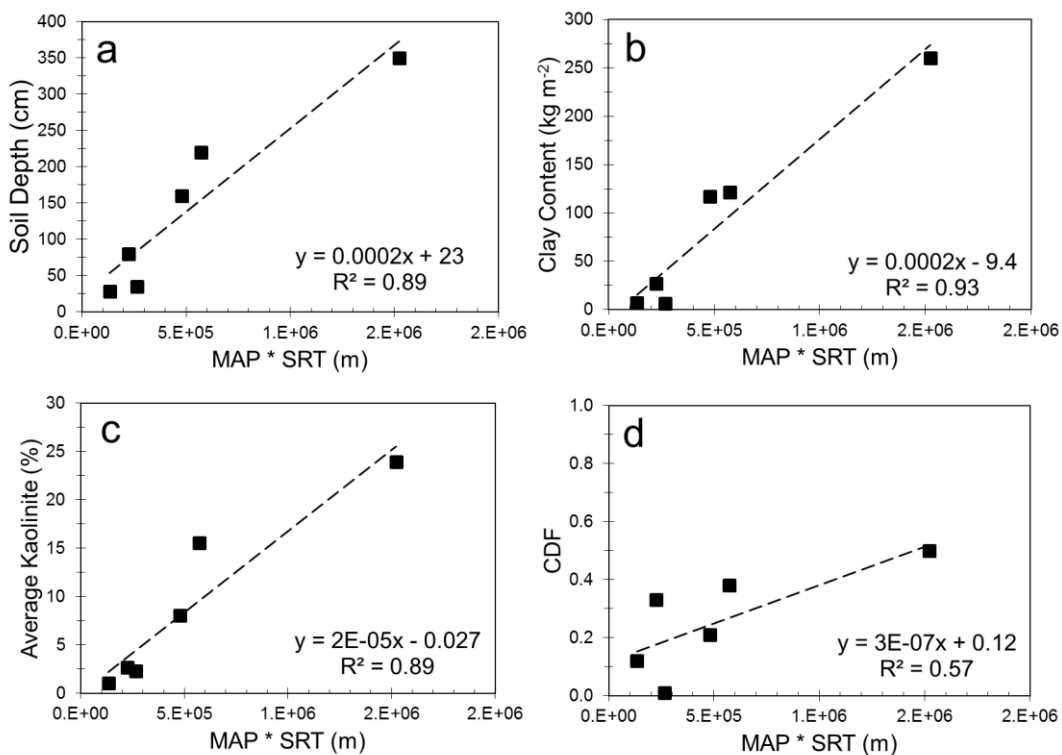
Figure 4-17. Soil depth (a), total clay content (b), depth-weighted average kaolinite content (c) and chemical depletion fraction CDF (d) as a function of MAP multiplied by the soil residence time (SRT) across the climosequence (see Ch. 3 for SRT data and discussion). In effect, this is the cumulative precipitation each site has received over the duration of soil formation. New York is not plotted due to till parent material.
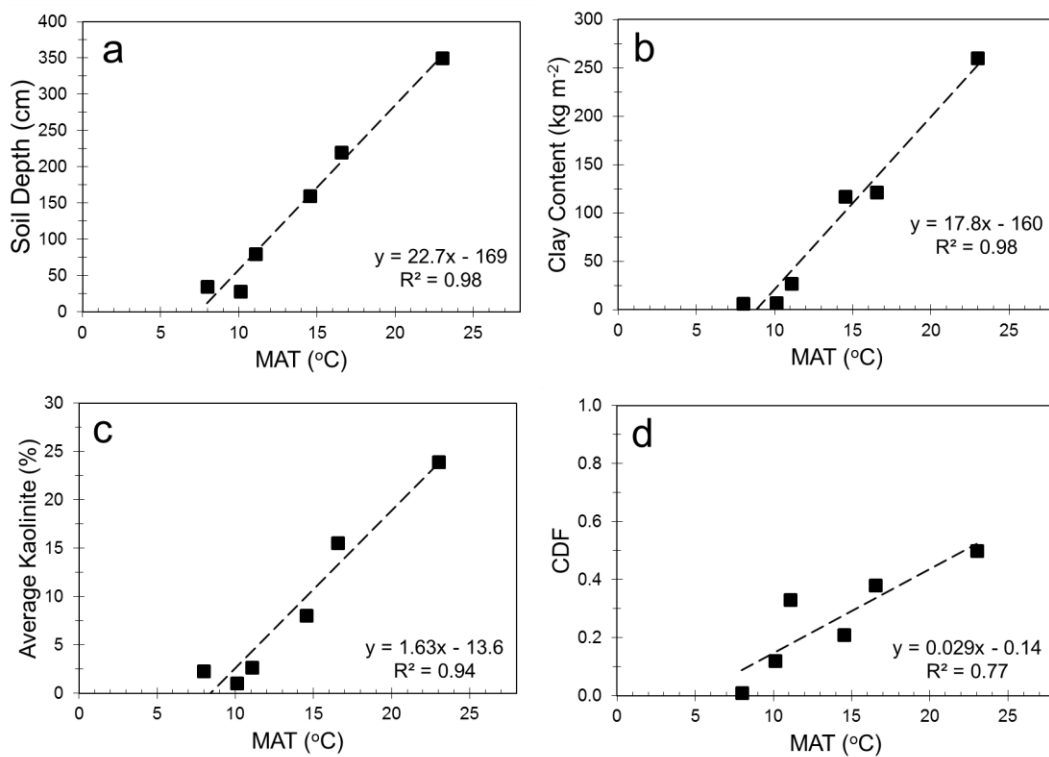
Figure 4-18. Soil depth (a), total clay content (b), depth-weighted average kaolinite content (c) and chemical depletion fraction CDF (d) as a function of MAT across the climosequence. New York is not plotted due to till parent material.

Tables

Table 4-1. Site locations, mean annual temperature (MAT) and precipitation (MAP) and values of evapotranspiration (ET) and net primary production (NPP) used to calculate energy associated with reduced carbon (E_{BIO}), effective precipitation (E_{PPT}) and total energy to the system (EEMT) for each transect site. F_{BIO} is the fraction of total EEMT associated with E_{BIO}. $EEMT_M$ and $EEMT_E$ are alternate methods for determining EEMT presented by Rasmussen et al. (2005) and Rasmussen and Tabor (2007), respectively. EEMT was calculated for a forest and grassland at the Plynlimon catchment in Wales.

Site	Latitude	Longitude	MAT[a] °C	MAP[a] mm yr^{-1}	ET[h] kg m^{-2} yr^{-1}	NPP[h] g C m^{-2} yr^{-1}	E_{BIO}	E_{PPT} —— MJ m^{-2} yr^{-1}——	EEMT[i]	F_{BIO}	$EEMT_M$[j] — MJ m^{-2} yr^{-1}—	$EEMT_E$[k]
Wales-Forest	52.47360	-03.69292	7.98[b]	2320[b]	447	896	19.7	30.0	49.8	0.40	57.2	66.6
Wales-Grass	52.46165	-03.74763	7.98[b]	2664[b]	315	700	15.4	26.7	42.1	0.37	53.9	83.7
New York	43.02895	-75.27682	8.50	1170	539	647	14.2	25.1	39.4	0.36	51.9	24.8
Pennsylvania	40.66552	-77.90495	10.1[c]	1160	531	638	14.0	27.1	41.1	0.34	56.2	29.5
Virginia	37.92708	-79.54665	11.1[d]	1180[e]	566	675	14.9	22.2	37.1	0.40	54.0	31.5
Tennessee	36.27357	-83.91348	14.5	1210	639	780	17.2	34.5	51.7	0.33	73.4	47.0
Alabama	34.42292	-86.20667	16.5	1580[f]	699	772	17.0	57.9	74.9	0.23	100	55.0
Puerto Rico	18.30083	-66.90668	23.0	2510[g]	812	948	20.9	165	186	0.11	218	184

[a] Mean annual temperature (MAT) and mean annual precipitation (MAP) determined over two years of data from transect meteorological stations

[b] Data from CEH (2009-2010) (www.ceh.ac.uk/sites/bangor.html)

[c] Data from Huntingdon NOAA station 364159 (2010-2011)

[d] Only one year of complete data available from deployed weather station

[e] Data from Hot Springs NOAA station 444128 (2011-2012)

[f] Data from Guntersville NOAA station 013573 (2011-2012)

[g] Data from Arecebo Observatory NOAA station 660426 (2011-2012)

[h] Net primary production (NPP) and evapotranspiration (ET) data from MODIS (2000-2010) (http://daac.ornl.gov)

[i] EEMT calculated using Eq. 2 and MODIS data for each site

[j] Modeled EEMT as described in equations 6 – 8.

[k] EEMT calculated using the empirically derived Eq. 5 and MAT and MAP

Table 4-2. Major elemental soil chemistry and Zr concentrations across the climosequence. C and N data are from Bingham (2012).

Site	IGSN[a]	Sample	d cm	Al	Ca	Fe	K	Mg	Mn	Na	P	Si	Ti	C	N	Zr ppm
									%							
Wales	SSH000SSM	plnq0-10	0 - 10	8.89	0.02	6.27	2.37	0.43	0.17	0.47	0.08	22.9	0.81	6.5	0.50	166
	SSH0000HE	plnq10-20	10 - 20	10.5	0.02	7.13	2.67	0.80	0.46	0.50	0.05	23.6	0.81	2.9	0.25	168
	SSH0000HF	plnq20-30	20 - 30	11.0	0.02	7.83	2.81	1.06	0.40	0.53	0.05	24.5	0.80	1.2	0.14	172
	SSH0000HG	plnq30-31	30 - 31	11.0	0.03	7.97	2.82	1.07	0.36	0.56	0.07	24.6	0.77	0.99	0.12	170
	SSH0000HH	plnq31-35	31 - 35	11.7	0.03	7.34	3.06	1.31	0.44	0.56	0.04	25.0	0.80	0.48	0.091	158
NY	SSH0000L8	ALD-10-61	0 - 5	4.82	0.14	4.37	1.40	0.48	0.13	0.32	0.07	36.9	0.62	---	---	---
	SSH0000L9	ALD-10-60	5 - 10	5.06	0.14	4.59	1.48	0.53	0.13	0.32	0.06	36.4	0.61	---	---	---
	SSH0000LA	ALD-10-59	10 - 15	5.82	0.16	4.92	1.87	0.68	0.12	0.30	0.05	35.4	0.65	---	---	---
	SSH0000LB	ALD-10-58	15 - 20	5.94	0.11	4.99	1.97	0.73	0.13	0.28	0.04	35.1	0.64	---	---	---
	SSH0000LC	ALD-10-57	20 - 30	5.56	0.13	4.75	1.92	0.69	0.12	0.28	0.04	35.5	0.57	---	---	---
	SSH0000LD	ALD-10-56	30 - 40	5.42	0.14	4.32	2.00	0.69	0.10	0.27	0.03	36.0	0.52	---	---	---
	SSH0000LE	ALD-10-55	40 - 50	4.38	0.21	3.48	1.61	0.49	0.08	0.36	0.04	37.8	0.44	---	---	---
	SSH0000LG	ALD-10-53	60 - 70	4.08	0.19	3.09	1.64	0.48	0.08	0.35	0.04	38.2	0.40	---	---	---
	SSH0000LK	ALD-10-49	100 - 110	3.57	0.29	2.69	1.41	0.37	0.08	0.50	0.04	38.9	0.41	---	---	---
	SSH0000LO	ALD-10-45	140 - 150	3.96	0.28	3.07	1.59	0.47	0.09	0.41	0.05	38.6	0.44	---	---	---
	SSH0000LS	ALD-10-36	180 - 190	4.21	0.31	3.31	1.69	0.53	0.09	0.39	0.05	38.3	0.44	---	---	---
	SSH0000LU	ALD-10-38	200-210	4.41	0.59	3.67	1.80	0.64	0.10	0.34	0.06	37.3	0.45	---	---	---
	SSH0000LV	ALD-10-39	220	4.23	7.12	3.29	1.74	1.64	0.09	0.33	0.05	32.6	0.43	---	---	---
	SSH0000LW	ALD-10-40	230	3.74	5.72	2.91	1.52	1.38	0.09	0.38	0.05	34.3	0.39	---	---	---
PA	SSH00001Q	ALD-10-163	0 – 10	10.8	0.02	5.17	3.77	0.60	0.16	0.21	0.08	27.1	1.02	2.2	0.15	216
	SSH00001R	ALD-10-164	10 - 20	11.5	0.01	5.21	4.26	0.65	0.02	0.22	0.06	27.1	1.03	0.77	0.087	211
	SSH00001S	ALD-10-165	20 - 30	12.2	0.03	5.25	4.51	0.75	0.01	0.22	0.07	26.8	1.01	0.50	0.079	190
VA	SSH0000PH	MT-09-032	0 – 10	3.26	0.07	2.32	0.37	0.18	1.56	0.06	0.07	33.8	0.72[c]	4.6	0.26	---
	SSH0000PI	MT-09-033	10 – 20	2.66	0.04	2.27	0.41	0.16	0.43	0.06	0.05	33.5	0.73	0.91	0.066	---
	SSH0000PJ	MT-09-034	20 - 30	3.03	0.04	2.69	0.56	0.17	0.36	0.07	0.05	38.6	0.56	---	---	---
	SSH0000PK	MT-09-035	30 - 40	2.94	0.05	2.48	0.46	0.17	0.58	0.06	0.07	37.6	0.55	1.7	0.082	---
	SSH0000PL	MT-09-036	40 - 50	3.98	0.03	3.28	0.86	0.21	0.25	0.07	0.06	36.6	0.68	0.94	0.067	---
	SSH0000PM	MT-09-037	50 - 60	6.14	0.04	4.70	1.41	0.30	0.15	0.08	0.06	32.9	0.61	0.82	0.062	---
	SSH0000PN	MT-09-038	60 - 70	6.30	0.04	5.39	1.93	0.33	0.04	0.07	0.11	32.7	0.68	0.48	0.047	---
	SSH0000PO	MT-09-039	70 - 80	6.14	BDL[b]	3.43	1.99	0.35	0.03	0.08	0.05	34.6	0.75	0.37	0.046	---

Table 4-2 (cont.)

Site	IGSN[a]	Sample	d cm	Al	Ca	Fe	K	Mg	Mn	Na	P	Si	Ti	C	N	Zr
									%							ppm
TN	SSH0000QC	ald-09-17	0 - 5	7.25	0.02	7.48	2.38	0.40	0.03	0.13	0.09	25.4	0.89	4.6	0.20	315
	SSH0000QD	ald-09-18	5 - 10	8.46	0.01	4.94	2.82	0.48	0.03	0.15	0.05	30.1	1.07	1.20	0.092	375
	SSH0000QG	ald-09-02	10 - 20	9.42	0.03	5.82	2.96	0.50	0.06	0.16	0.07	27.6	1.00	1.2	0.083	350
	SSH0000QH	ald-09-03	20 - 30	10.2	0.01	5.06	3.07	0.55	0.15	0.15	0.05	27.8	0.96	1.3	0.091	310
	SSH0000QI	ald-09-04	30 - 40	9.73	0.01	6.09	3.10	0.54	0.07	0.14	0.06	26.8	0.94	1.7	0.077	300
	SSH0000QJ	ald-09-05	40 - 50	10.3	0.01	5.51	3.45	0.58	0.01	0.16	0.05	26.6	0.93	1.8	0.069	285
	SSH0000QL	ald-09-07	60 - 70	11.4	0.01	3.76	3.79	0.66	BDL	0.16	0.04	27.6	0.93	0.34	0.063	280
	SSH0000QN	ald-09-09	80 - 90	11.5	BDL	3.21	3.94	0.66	BDL	0.18	0.03	27.6	0.93	0.21	0.062	265
	SSH0000QP	ald-09-11	100 - 110	11.0	BDL	4.21	3.85	0.61	BDL	0.16	0.04	27.4	0.92	0.16	0.057	270
	SSH0000QR	ald-09-13	120 - 130	9.47	BDL	10.1	3.40	0.57	BDL	0.15	0.08	25.0	0.85	0.21	0.056	255
	SSH0000QT	ald-09-15	145 - 150	11.6	BDL	2.94	4.11	0.65	BDL	0.17	0.02	27.1	0.90	0.24	0.061	215
	SSH0000QU	ald-09-16	150 - 155	12.0	BDL	3.22	4.27	0.67	BDL	0.17	0.03	27.6	0.92	0.19	0.062	245
	SSH0000QY	ald-10-64	160 - 170	12.6	0.00	2.40	3.94	0.70	0.00	0.18	0.03	27.1	0.88	0.15	0.060	209
	SSH0000R1	ald-10-67	190 - 200	12.4	0.00	2.90	3.92	0.71	0.00	0.17	0.03	27.3	0.89	0.15	0.064	218
	SSH0000R4	ald-10-70	210 - 220	12.4	0.01	2.36	4.10	0.74	0.01	0.18	0.03	27.6	0.91	---	---	217
	SSH0000R8	ald-10-73	230 - 240	11.9	0.01	6.27	4.11	0.77	0.01	0.18	0.04	25.1	0.83	0.14	0.063	180
	SSH0000R9	ald-10-75	240 - 250	12.4	0.00	5.45	4.36	0.79	0.08	0.19	0.04	24.7	0.80	0.15	0.069	160
	SSH0000RP	ald-11-401	260 - 270	12.4	0.02	7.82	4.39	0.79	0.01	0.19	0.06	26.9	0.90	0.19	0.064	230
	SSH0000RS	ald-11-404	290 - 300	10.1	0.01	7.48	3.72	0.66	0.01	0.17	0.05	26.3	0.86	0.16	0.060	238
	SSH0000RW	ald-11-426	330 - 340	11.1	0.02	3.50	3.79	0.67	0.02	0.16	0.04	27.5	0.91	0.098	0.058	270
	SSH0000RZ	ald-11-429	360 - 370	11.1	0.01	2.71	4.03	0.69	0.03	0.19	0.04	28.3	0.91	0.13	0.059	277
	SSH0000S2	ald-11-432	390 - 398	10.6	0.01	5.68	3.83	0.73	0.05	0.18	0.05	27.0	0.87	0.16	0.056	254
	SSH00001R	ALD-10-164	10 - 20	11.5	0.01	5.21	4.26	0.65	0.02	0.22	0.06	27.1	1.03	0.77	0.087	211
	SSH00001S	ALD-10-165	20 - 30	12.2	0.03	5.25	4.51	0.75	0.01	0.22	0.07	26.8	1.01	0.50	0.079	190

Table 4-2 (cont.)

Site	IGSN[a]	Sample	d cm	Al	Ca	Fe	K	Mg	Mn	Na	P	Si	Ti	C	N	Zr ppm
AL	SSH0000T3	ald-10-114	0 - 10	1.93	0.09	1.22	0.28	0.10	0.09	0.02	0.04	41.6	0.36	1.7	0.10	314
	SSH0000T4	ald-10-115	10 - 20	2.71	0.04	1.74	0.38	0.13	0.21	0.02	0.04	38.3	0.56	0.90	0.064	331
	SSH0000T5	ald-10-116	20 - 30	3.83	0.04	2.45	0.44	0.18	0.07	0.03	0.04	37.7	0.62	0.76	0.058	380
	SSH0000T6	ald-10-117	30 - 40	4.59	0.05	4.31	0.48	0.21	0.05	0.02	0.06	35.6	0.54	0.78	0.063	265
	SSH0000T7	ald-10-118	40 - 50	6.82	0.04	4.39	0.61	0.28	0.09	0.02	0.05	33.9	0.60	0.63	0.063	236
	SSH0000TA	ald-10-121	60 - 70	9.76	0.03	6.29	0.98	0.41	0.02	0.02	0.08	28.7	0.63	0.47	0.051	224
	SSH0000TC	ald-10-123	90 - 100	9.31	0.05	6.00	1.15	0.45	0.02	0.02	0.07	29.9	0.58	0.30	0.045	197
	SSH0000TE	ald-10-125	110 - 120	10.1	0.04	5.85	1.20	0.47	0.01	0.02	0.08	28.1	0.60	0.27	0.048	187
	SSH0000TG	ald-10-127	130 - 140	10.1	0.04	6.34	1.33	0.52	0.02	0.03	0.08	27.6	0.62	0.29	0.049	168
	SSH0000TI	ald-10-129	150 - 155	4.33	0.02	3.14	0.96	0.35	0.01	0.01	0.04	36.2	0.35	0.38	0.043	129
	SSH0000TP	ald-10-506	170 - 180	6.97	0.03	4.57	1.51	0.54	0.01	0.03	0.06	33.9	0.55	0.20	0.045	153
	SSH0000TR	ald-10-508	190 - 200	8.03	0.04	4.82	1.39	0.51	0.10	0.04	0.07	31.2	0.57	0.21	0.044	172
PR	SSH0000VO	ald-11-13	0 - 8	9.58	0.78	5.85	0.51	0.58	0.02	0.05	0.10	22.5	0.69	4.7	0.39	139
	SSH0000VP	ald-11-14	8 - 10	10.4	0.59	6.18	0.47	0.56	0.02	0.04	0.08	23.2	0.72	2.6	0.23	153
	SSH0000VQ	ald-11-15	10 - 15	10.6	0.56	6.34	0.46	0.56	0.02	0.04	0.08	23.4	0.72	2.2	0.20	142
	SSH0000VR	ald-11-16	15 - 20	10.9	0.49	6.47	0.45	0.55	0.02	0.03	0.08	24.2	0.74	1.6	0.15	150
	SSH0000VS	ald-11-17	20 - 30	11.0	0.44	6.79	0.45	0.54	0.01	0.03	0.07	24.4	0.73	1.1	0.097	142
	SSH0000VT	ald-11-18	30 - 40	11.1	0.42	6.90	0.44	0.55	0.01	0.02	0.07	23.8	0.71	0.78	0.077	134
	SSH0000VU	ald-11-19	40 - 50	11.0	0.42	6.82	0.46	0.57	0.01	0.02	0.08	24.8	0.72	0.63	0.065	141
	SSH0000W0	ald-11-25	100 - 111	10.7	0.45	7.43	0.60	0.79	0.01	0.03	0.07	21.8	0.78	0.32	0.038	130
	SSH0000W5	ald-11-30	150 - 160	10.7	0.23	9.32	0.63	0.72	0.02	0.02	0.07	22.9	0.76	0.38	0.037	133
	SSH0000WA	ald-11-38	200 - 210	11.2	0.13	11.51	0.62	0.80	0.02	0.02	0.06	20.7	0.73	0.28	0.030	132
	SSH0000WF	ald-11-43	250 - 260	10.1	0.09	12.78	0.55	0.60	0.02	0.02	0.08	22.0	0.71	0.38	0.040	127
	SSH0000WK	ald-11-48	300 - 310	10.3	0.06	8.72	0.53	0.48	0.02	0.02	0.09	24.7	0.67	0.41	0.025	122
	SSH0000WP	ald-11-53	350 - 360	9.86	0.06	8.82	0.51	0.57	0.04	0.02	0.11	24.7	0.65	0.25	0.044	127
	SSH0000WU	ald-11-58	400 - 410	9.76	0.10	7.74	0.54	0.60	0.03	0.03	0.09	25.4	0.74	0.49	0.045	155
	SSH0000WZ	ald-11-63	450 - 460	10.5	0.11	6.11	0.85	0.86	0.02	0.04	0.08	25.3	0.87	0.20	0.028	152
	SSH0000X5	ald-11-76	500 - 505	9.91	0.26	6.62	1.53	0.81	0.02	0.15	0.09	25.1	0.80	0.24	0.037	127
	SSH0000XF	ald-11-86	570 - 580	8.12	0.43	4.16	2.11	0.74	0.02	1.78	0.09	28.8	0.76	0.23	0.037	130
	SSH0000XL	ald-11-92	625 - 632	7.58	0.64	5.16	2.16	1.07	0.03	2.20	0.09	28.2	0.77	0.21	0.031	120

[a] International Geo Sample Number, www.geosamples.org
[b] Below detection limit
[c] Corrected Ti values as reported in Dere et al. (2013)

Table 4-3. Shale bedrock mineralogy for select samples at each site.

Site	Sample	IGSN[a]	Quartz	K feldspar	Plagioclase	Illite	'Chlorite'[b]	Kaolinite	Iron oxides	Calcite	Pattern fit[c]
								%			
Wales	PlynQ-RF	SSH000GG	30	1.1	4.0	39	25	---	0.70	---	0.18
PA	ALD-10-58	SSH000SUA	26	2.4	0.5	63	4.6	---	3.8	---	0.12
VA	TSW1164	SSH00005D	19	2.7	3.1	40	26	4.6	4.0	0.60	0.18
TN	TSW1208	SSH00006M	28	4.1	5.5	29	22	4.2	5.6	1.1	0.14
AL	ALD-10-2026	SSH00008K	16	6.2	1.3	30	37	---	7.4	2.2	0.20
PR	ALD-11-03	SSH000SUW	14	9.0	12	2.6	15	1.6	0.40	45	0.19

[a] International Geo Sample Number, www.geosamples.org
[b] 'Chlorite' refers to chlorite, vermiculite, hydroxy-interlayered vermiculite (HIV), and interstratified chlorite minerals
[c] Full pattern degree of fit between the calculated and measured pattern in RockJock (lower is better)

Table 4-4. Soil mineralogy for select samples at each site. 'Chlorite' refers to vermiculite and hydroxy-interlayered vermiculite (HIV) minerals.

Site	Sample	IGSN[a]	Depth	Quartz	K feldspar	Plagioclase	Illite	'Chlorite'	Kaolinite	Iron oxides	Pattern fit[b]
			cm				%				
Wales	plnq0-10	SSH000SSM	0 - 10	31	5.8	3.4	36	15.6	6.1	3.0	0.13
	plnq20-30	SSH0000HF	20 - 30	32	3.1	3.3	33	26.6	1.0	1.7	0.16
	plnq31-35	SSH0000HH	31 - 35	31	1.2	4.4	38	25.0	---	0.8	0.16
PA	ALD-10-163	SSH0000NL	0 – 10	30	2.6	0.7	49	8.3	1.5	3.8	0.14
	ALD-10-164	SSH0000NM	10 – 20	27	2.1	0.5	59	10	0.6	1.9	0.12
	ALD-10-165	SSH0000NN	20 – 28	26	0.8	0.1	59	4.5	1.8	2.3	0.12
VA	MT-09-032	SSH0000PH	0 – 10	69	4.5	0.8	7.3	7.5	3.6	5.9	0.18
	MT-09-036	SSH0000PL	40 - 50	73	3.2	0.8	16	0.9	0.5	5.8	0.16
	MT-09-038	SSH0000PN	60 - 70	53	3.0	0.7	28	5	2.3	7.5	0.21
	MT-09-039	SSH0000PO	70 - 80	55	1.4	1.6	37	---	1.8	2.7	0.15
TN	ALD-09-17	SSH0000QC	0 - 5	40	1.6	0.9	35	12	4.1	6.6	0.14
	ALD-09-03	SSH0000QH	20 - 30	33	1.3	---	47	6.3	7.2	5.6	0.13
	ALD-09-05	SSH0000QJ	40 - 50	33	1.2	0.7	46	6.8	6.9	5.8	0.13
	ALD-09-09	SSH0000QN	80 - 90	25	3.0	---	49	15	7.7	0.8	0.12
	ALD-09-13	SSH0000QR	120 - 130	25	1.4	0.9	45	11	7.2	10	0.13
	ALD-09-16	SSH0000QU	150 - 155	26	1.1	---	55	9.1	8.6	0.6	0.12
	ALD-10-67	SSH0000R1	190 - 200	24	3.5	---	53	9.8	10	---	0.13
	ALD-11-401	SSH0000RP	260 - 270	20	3.6	0.4	54	10	8.0	4.2	0.13
	ALD-11-426	SSH0000RW	330 - 340	25	4.5	0.3	47	12	9.9	1.5	0.12
	ALD-11-432	SSH0000S2	390 - 398	27	3.4	0.6	50	9.8	6.2	2.9	0.14
AL	ALD-10-114	SSH0000T3	0 - 10	83	4.4	1.0	7.4	1.6	1.6	1.2	0.21
	ALD-10-116	SSH0000T5	20 - 30	70	2.5	0.1	7.2	7	9.9	2.8	0.18
	ALD-10-121	SSH0000TA	60 - 70	39	2.6	0.9	5.4	24	22	5.8	0.13
	ALD-10-125	SSH0000TE	110 - 120	32	3.3	0.6	15	14	27	7.1	0.15
	ALD-10-129	SSH0000TI	150 - 155	65	2.4	0.7	18	4	7.4	3.0	0.14
	ALD-11-506	SSH0000TP	170 - 180	55	2.0	0.5	25	7.3	6.0	4.7	0.14
	ALD-11-508	SSH0000TR	190 - 200	50	2.8	0.7	15	16	13	2.7	0.17

Table 4-4 (cont.)

Site	Sample	IGSN[a]	Depth	Quartz	K feldspar	Plagioclase	Illite	'Chlorite'	Kaolinite	Iron oxides	Pattern fit[b]
			cm				%				
PR	ald-11-13	SSH0000VO	0 - 8	25	5.7	---	---	37	30	3.6	0.14
	ald-11-19	SSH0000VU	40 - 50	27	2.5	---	---	31	33	7.1	0.13
	ald-11-25	SSH0000W0	100 - 111	17	1.4	0.6	2.2	38	33	8.2	0.12
	ald-11-43	SSH0000WF	250 - 260	21	3.3	---	---	38	27	10	0.16
	ald-11-48	SSH0000WK	300 - 310	27	3.4	---	---	30	30	9.0	0.15
	ald-11-58	SSH0000WU	400 - 410	30	2.9	---	2.3	29	28	7.9	0.13
	ald-11-76	SSH0000X5	500 - 505	24	8.8	---	3.5	33	26	4.3	0.12
	ald-11-92	SSH0000XL	625 - 632	25	20	19	3.0	26	5.3	1.2	0.12

[a] International Geo Sample Number, www.geosamples.org
[b] Full pattern degree of fit between the calculated and measured pattern in RockJock (lower is better)

Appendix A

Chapter 2 Supplementary Material
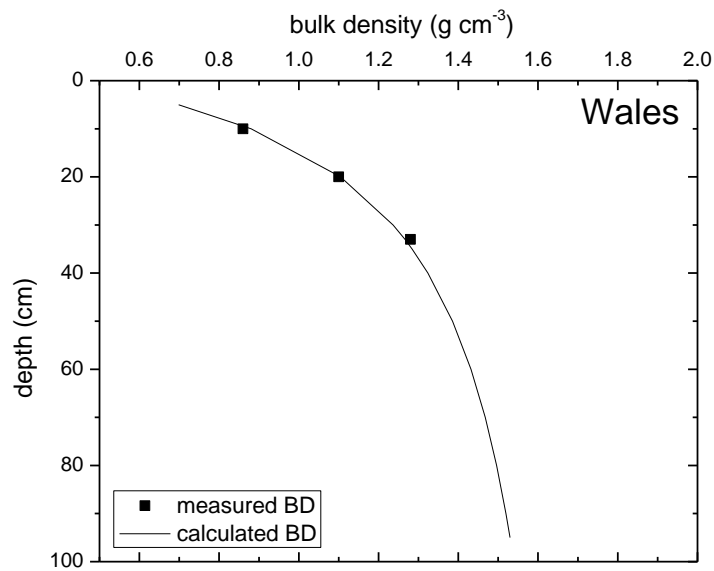
Figures

Figure A-1. Measured and calculated bulk density using Eq. (2) at the Wales transect site. Fit parameters are in Table 1.
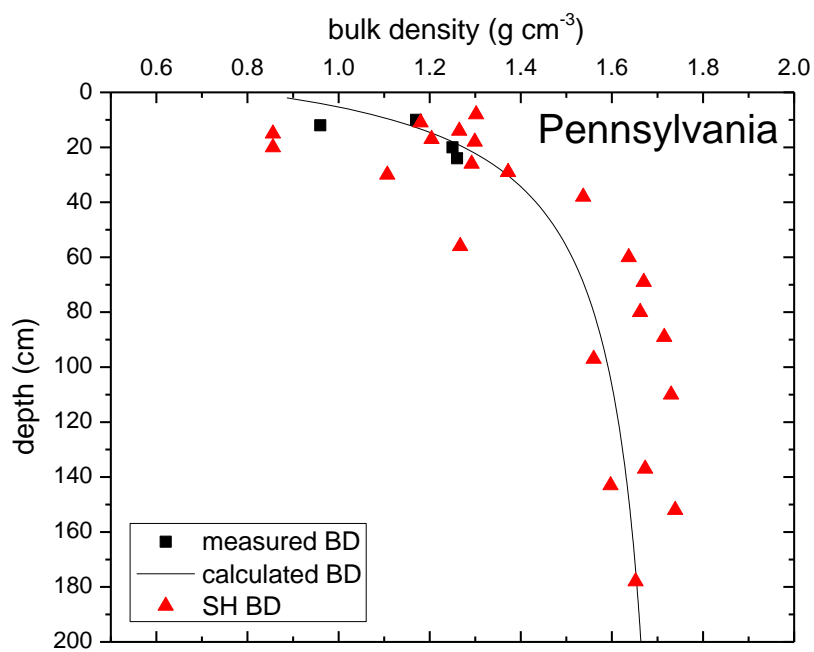
Figure A-2. Measured and calculated bulk density at the Pennsylvania transect site. Squares represent bulk density measured using the core method for samples from the shale transect site. Triangles represent bulk density measurements collected at the Susquehanna Shale Hills Critical Zone Observatory (SSHO) reported by Lin et al. (2006) for ridgetop, slope and valley floor sites.
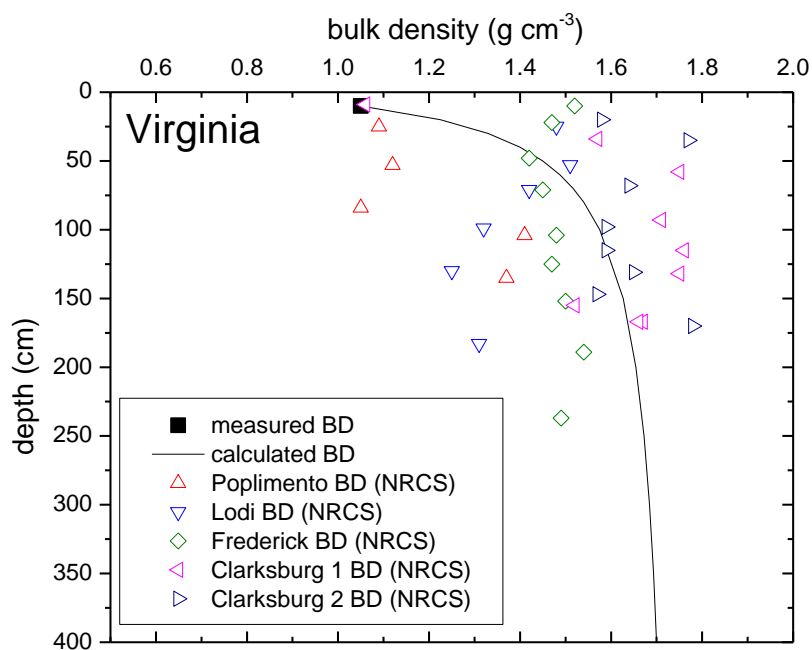
Figure A-3. Measured and calculated bulk density at the Virginia transect site. Squares represent bulk density measured using the core method. Triangles represent bulk density measurements obtained from the NRCS Soil Survey for shale-derived soils near the Virginia transect site. Open symbols indicate bulk density measurements of soils that were derived from shale but not directly comparable in classification (Alfisols) and land use (forest) to the transect site. NRCS soil series (with classification and land cover in parentheses) included in this plot are: Clarksburg (Oxyaquic fragiudult, hardwood pasture); Poplimento (Ultic hapludalf, hardwood pasture); Lodi (Typic hapludalf, cropland); Frederick (Vertic paleudult, hayfield). The large scatter in the NRCS bulk density data are attributed to differences in land cover (i.e. pasture and cropland) and differences in soil features (i.e. fragic, aquic or vertic properties). Since no directly comparable data were available, all plotted NRCS bulk density data were used to constrain the bulk density fit despite the large scatter.
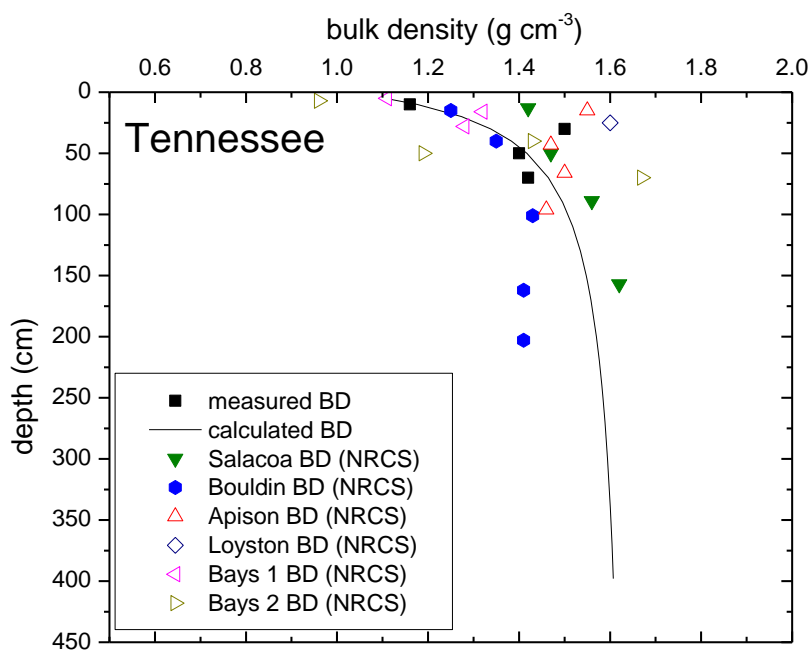
Figure A-4. Measured and calculated bulk density at the Tennessee transect site. Squares represent bulk density measured using the core method. Other symbols represent bulk density measurements obtained from the NRCS Soil Survey for shale derived soils near the transect site. Closed symbols indicate soil bulk density measurements that were comparable in classification (Ultisols) and land use (forest) to the shale transect site and were used to constrain the fit. Open symbols indicate bulk density measurements of soils that were derived from shale but not directly comparable in classification and land use to the transect site. NRCS soil series (with classification and land cover in parentheses) included in this plot are Apison (Typic hapludult, pasture); Salacoa (Typic hapludult, oak woodland); Bouldin (Typic paleudult, hardwood forest); Loyston (Lithic hapludulf, mixed hardwood); Bays (Dystric eutrochrept, grass and hardwood forest). Only the Salacoa and Bouldin soils are similar in soil classification and land use to the transect site and are therefore the best two available profiles with which we can fit our measured values.
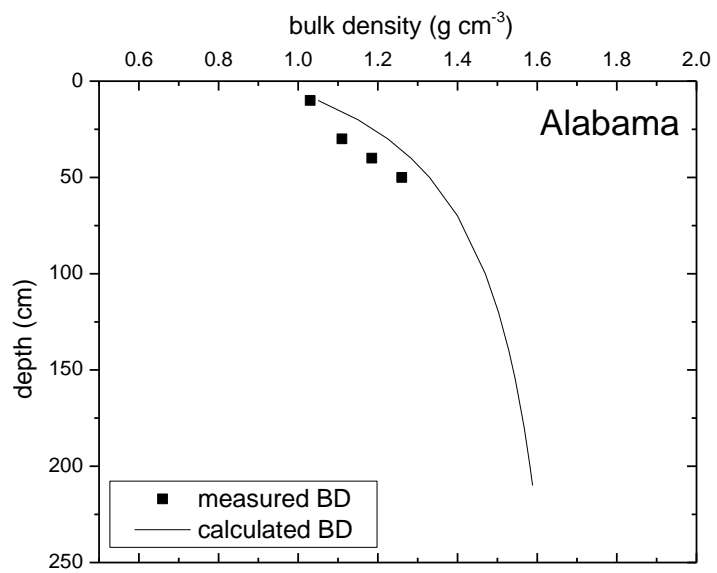
Figure A-5. Measured and calculated bulk density at the Alabama transect site. Squares represent bulk density measured using the core method. No data were available in the NRCS Soil Survey for shale-derived soils near the Alabama transect site.
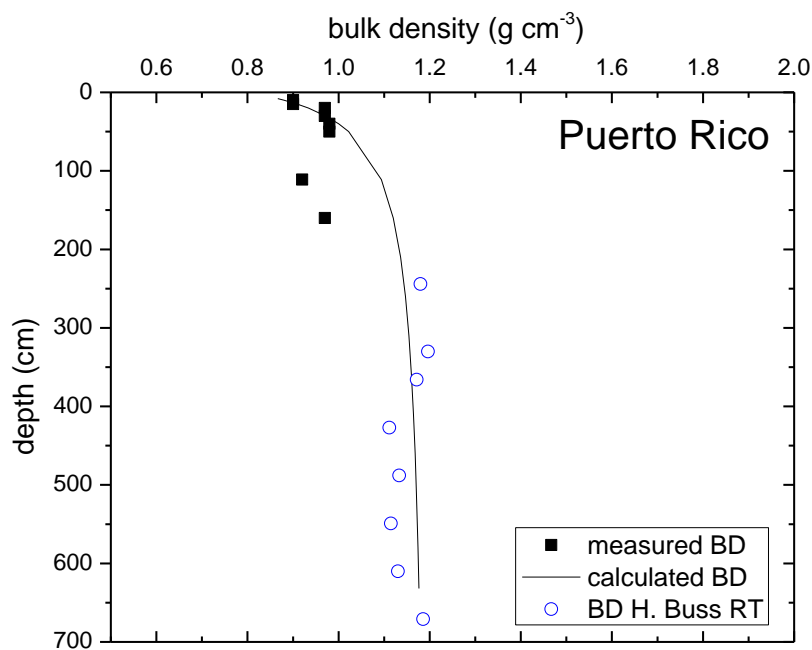
Figure A-6. Measured and calculated bulk density at the Puerto Rico transect site. Squares represent bulk density measured using the core method. The open circles represent deep bulk density measurements collected on a ridgetop (RT) site on volcano-clastic rocks by H. Buss at a ridgetop (RT) site in the Luquillo Critical Zone Observatory (CZO) (pers. comm.). No additional bulk density measurements were available in the NRCS Soil Survey for shale-derived soils near the Puerto Rico transect site.
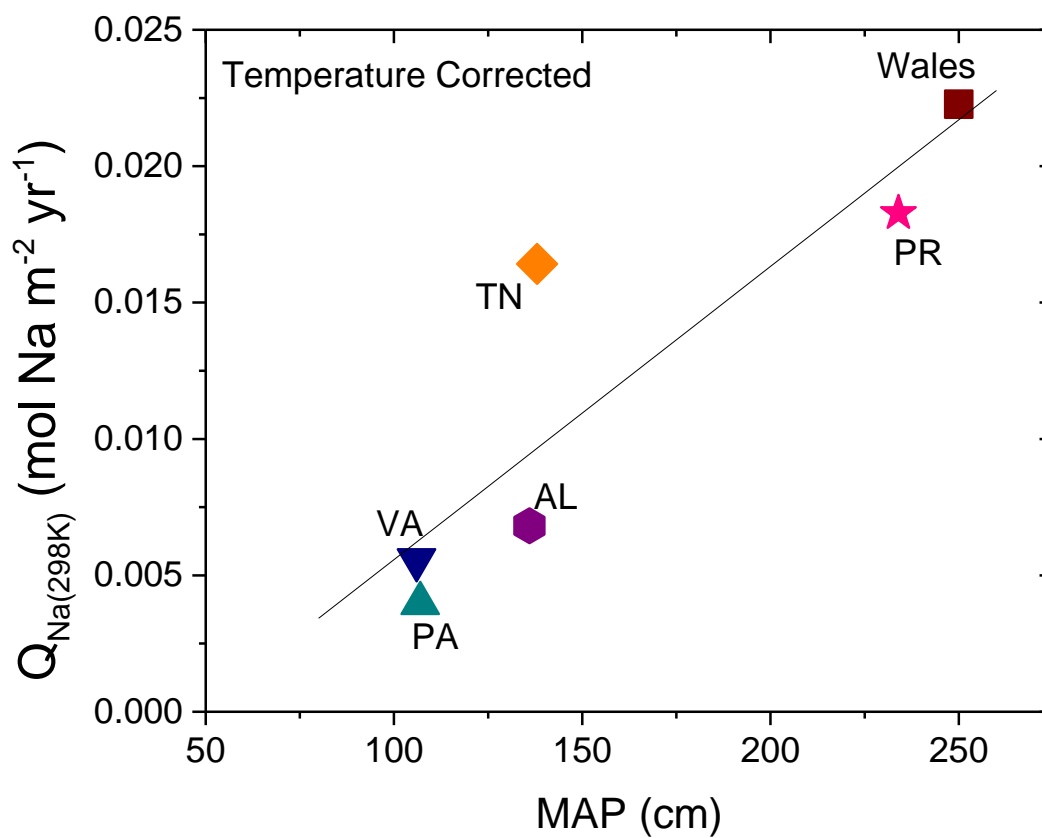
Figure A-7. Na loss rate (Q_{Na}) adjusted to 298 K for all transect sites plotted against mean annual temperature (MAT). A linear regression of the data gives a slope of 0.01 (MAP) - 0.005 mol Na m^{-2} yr^{-1}.

Tables

Table A-1. NOAA weather stations used to determine mean annual temperature (MAT) and mean annual precipitation (MAP) at the transect sites. Weather stations were chosen close to the study site, at a similar elevation and with at least 20 years of complete data records. Wales MAT and MAP data from Reynolds et al. (1997). Pennsylvania MAT and MAP data from Jin et al. (2010).

Site	Station name[a]	Station number	Latitude	Longitude	Elevation m	Distance to site km	Years data available	MAT[b] years	MAP[b] years
New York	Utica	308739	43°05'N	75°12'W	177	8.7	1948-1990	26	34
Virginia	Hot Springs	444128	38°00'N	79°50'W	682	26	1931-2011	49	55
Tennessee	Norris	406619	36°13'N	84°04'W	338	15	1953-2010	34	44
Alabama	Guntersville	013573	34°20'N	86°20'W	176	15	1954-2010	18	34
Puerto Rico	Lares	665175	18°17'N	66°53'W	451	3.2	1931-1989	21	53

[a] National Oceanic and Atmospheric Administration (NOAA) weather station

[b] Number of years used to calculate MAT or MAP. Years including estimated or missing monthly averages were not included in MAT or MAP calculations.

Table A-2. Compilation of published erosion rates (E) for the Appalachian Mountains and Puerto Rico from cosmogenic [10]Be analyses.

Site	Author(s)	Province	Type	Lithology	Mean Elevation m	Mean Slope °	Mean E m My[-1]
SSHO CZO[a], Pennsylvania, USA	West et al., 2013	Ridge/Valley	soil, N slope	shale	305	15 ± 1.7	16 ± 5.6
			soil, S slope	shale	285	20 ± 3.3	19 ± 6.2
SSHO CZO[a], Pennsylvania, USA	Bierman et al., 2008; 2009	Ridge/ Valley	sediment	shale	285 ± 20	17.7	15
Appalachian Mountains, USA	Portenga and Bierman, 2011	—	sediment	multilithology	—	—	17 ± 9
Shenandoah River, Pennsylvania, USA	Reuter, 2005	Ridge/ Valley	sediment	shale	226 ± 59	8.8 ± 3.7	12 ± 5.6
			sediment	sandstone	503 ± 66	9.5 ± 5.3	13 ± 7.2
Susquehanna and Potomac River basins, Pennsylvania and Virginia, USA	Portenga, 2011	Ridge/Valley	bedrock	multilithology [b]	639 ± 229	6.1 ± 1.7	16 ± 1.2
		Blue Ridge	bedrock	multilithology [c]	421 ± 156	5.1 ± 1.1	8.2 ± 0.64
		Plateau	bedrock	multilithology [d]	733 ± 167	4.4 ± 2.8	21 ± 1.6
		Piedmont	bedrock	multilithology [e]	144	1.6	6.2 ± 0.48
Shenandoah National Park, Virginia, USA	Duxbury, 2009	Blue Ridge	sediment	granite	291 ± 75	18 ± 3	15 ± 1.9
			bedrock	granite	835	—	7.8 ± 1.0
			sediment	metabasalt	473 ± 141	15 ± 2	8.9 ± 1.2
			bedrock	metabasalt	860	—	13 ± 1.7
			sediment	multilithology	312 ± 119	12 ± 10	10 ± 1.3
			bedrock	sandstone	692	—	3.6 ± 0.5
			sediment	siliciclastic	460 ± 82	6 ± 6	11 ± 1.4
			bedrock	siliciclastic	811	—	13 ± 1.6
			sediment	quartzite	440 ± 101	4 ± 4	8.0 ± 1.0
			bedrock	quartzite	518	—	2.4 ± 0.3
Brevard Fault Zone, Virginia and North Carolina, USA	Sullivan, 2007	Blue Ridge	basin	metamorphic	855 ± 106	12 ± 5	11 ± 1.4
		Blue Ridge E[f]	basin	metamorphic	644 ± 65	22 ± 2	20 ± 2.5
		Blue Ridge E[f]	bedrock	gneiss	—	—	25 ± 3.4
		Piedmont	basin	metamorphic	513 ± 97	15 ± 4	13 ± 1.7
Dolly Sods, West Virginia, USA	Hancock and Kirwan, 2007	Plateau	bedrock	sandstone	1246 ± 15	—	6.0 ± 1.2
			bedrock	quartz congl.[g]	1223 ± 5	—	5.3 ± 1.0

Table A-2 (cont.)

Site	Author(s)	Province	Type	Lithology	Mean Elevation m	Mean Slope °	Mean E m My^{-1}
New River Gorge, West Virginia, USA	Clifton and Granger, 2005	Plateau	soil	sandstone	—	—	8.5 ± 1.5
			sediment	sandstone	—	—	7.5 ± 3.5
Great Smoky Mountains, Tennessee, USA	Matmon et al., 2003	Ridge/Valley	sediment	metamorphosed sedimentary	>1500	23	27 ± 4
Luquillo Experimental Forest, Puerto Rico, USA	Brown et al., 1995; 1998	—	sediment	quartz diorite	615	30	43
			Soil	quartz diorite	656 ± 26	—	25
Luquillo Experimental Forest, Puerto Rico, USA	Riebe et al., 2003	—	sediment	quartz diorite	692 ± 38	35 ± 12	67 ± 18
			soil	quartz diorite	717 ± 29	27 ± 2	33 ± 7.8

[a] Susquehanna Shale Hills Critical Zone Observatory

[b] Lithology includes quartzite, sandstone and conglomerate

[c] Lithology includes quartzite, quartz veins, sandstone, phyllite/quartzite

[d] Lithology includes sandstone and quartz conglomerate

[e] Lithology includes schist and schist with quartz veins

[f] Blue Ridge Escarpment

[g] Quartz conglomerate

Table A-3. Detailed rock sampling locations across the transect.

Site	Sample Name	IGSN[a] Number	Latitude	Longitude	Elevation m
Wales	PlynQ-RF	SSH000GG	N52° 28.416	W3° 41.575	417
	ALD-10-01	SSH000STR	N52° 28.241	W3° 41.553	323
	ALD-10-02	SSH000STS	N52° 28.247	W3° 41.549	327
	ALD-10-03	SSH000STT	N52° 28.296	W3° 41.528	358
	ALD-10-04	SSH000STU	N52° 28.295	W3° 41.464	364
	ALD-10-06	SSH000STW	N52° 28.338	W3° 41.242	369
	ALD-10-07	SSH000STX	N52° 28.332	W3° 41.327	385
	ALD-10-08	SSH000STY	N52° 28.416	W3° 41.575	417
	ALD-10-09	SSH000STZ	N52° 28.403	W3° 41.549	413
	ALD-10-33	SSH000SU0	N52° 28.292	W3° 41.539	413
NY	OW-81308-3	---	N43° 01.903	W75° 16.564	216
PA	ALD-10-158	SSH000SUA	N40° 39.931	W77° 54.290	297
VA	TSW-1163	SSH00005C	N37° 42.728	W79° 54.515	561
	TSW-1164	SSH00005D	N37° 42.728	W79° 54.515	561
	TSW-1165	SSH00005E	N37° 42.728	W79° 54.515	561
	TSW-1162	SSH00005B	N37° 42.728	W79° 54.515	561
	TSW-1166	SSH00005F	N37° 42.728	W79° 54.515	561
TN	TSW-1212	SSH00006Q	N36° 02.361	W84° 11.882	252
	TSW-1213	SSH00006R	N36° 02.361	W84° 11.882	252
	TSW-1214	SSH00006S	N36° 02.361	W84° 11.882	252
	ALD-10-432	SSH000SUH	N36° 16.411	W83° 54.819	422
AL	ALD-10-2025	SSH00008J	N34° 41.817	W85° 59.339	226
	ALD-10-2026	SSH00008K	N34° 41.817	W85° 59.344	227
	ALD-10-2028	SSH00008M	N34° 41.817	W85° 59.348	227
PR	ALD-11-03	SSH000SUW	N18° 18.071	W66° 54.326	356
	ALD-11-93	SSH000SV6	N18° 18.008	W66° 54.291	365

[a] International Geo Sample Number, www.geosamples.org

Table A-4. Loss on ignition (LOI) determined by combustion or subtraction from total major oxides in rock samples collected across the transect.

Site	Sample name	IGSN[a] Number	d m	LOI[b] —— % ——	LOI[c]
Wales	PlynQ-RF	SSH000GG	0.35	---	5.30
	ALD-10-01	SSH000STR	---	---	3.88
	ALD-10-02	SSH000STS	---	---	5.12
	ALD-10-03	SSH000STT	---	---	7.61
	ALD-10-04	SSH000STU	---	---	5.02
	ALD-10-06	SSH000STW	---	---	6.86
	ALD-10-07	SSH000STX	---	---	8.38
	ALD-10-08	SSH000STY	---	---	5.23
	ALD-10-09	SSH000STZ	---	---	9.72
	ALD-10-33	SSH000SU0	---	---	8.73
NY	OW-81308-3	---	---	5.10	---
PA	ALD-10-158	SSH000SUA	0.35	---	4.13
VA	TSW-1163	SSH00005C	27.0	5.73	7.24
	TSW-1164	SSH00005D	29.0	5.51	6.95
	TSW-1165	SSH00005E	30.0	5.47	8.13
	TSW-1162	SSH00005B	26.0	2.75	4.01
	TSW-1166	SSH00005F	36.0	2.37	3.73
TN	TSW-1212	SSH00006Q	28.0	5.79	7.42
	TSW-1213	SSH00006R	29.0	5.95	8.61
	TSW-1214	SSH00006S	30.0	5.61	9.51
	ALD-10-432	SSH000SUH	3.98	---	6.27
AL	ALD-10-2025	SSH00008J	37.5	6.61	8.43
	ALD-10-2026	SSH00008K	38.0	6.24	6.95
	ALD-10-2028	SSH00008M	41.0	6.16	7.20
PR	ALD-11-03	SSH000SUW	---	24.2	24.8
	ALD-11-93	SSH000SV6	---	---	27.7

[a] International Geo Sample Number, www.geosamples.org

[b] LOI measured by combustion

[c] LOI calculated by subtracting total oxides from 100

Table A-5. Loss on ignition (LOI) determined by combustion or subtraction from total major oxides in soil samples collected across the transect.

Site	Sample	IGSN[a]	Interval	LOI[b]	LOI[c]
			cm	—— % ——	
Wales	plnq0-10	SSH000SSM	0 - 10	19.4	19.1
	plnq10-20	SSH0000HE	10 - 20	---	12.4
	plnq20-30	SSH0000HF	20 - 30	---	7.91
	plnq30-31	SSH0000HG	30 - 31	---	7.57
	plnq31-35	SSH0000HH	31 - 35	---	5.29
New York	ALD-10-61	SSH0000L8	0 - 5	7.37	---
	ALD-10-60	SSH0000L9	5 - 10	5.80	---
	ALD-10-59	SSH0000LA	10 - 15	5.35	---
	ALD-10-58	SSH0000LB	15 - 20	4.74	---
	ALD-10-57	SSH0000LC	20 - 30	4.29	---
	ALD-10-56	SSH0000LD	30 - 40	3.80	---
	ALD-10-55	SSH0000LE	40 - 50	3.31	---
	ALD-10-53	SSH0000LG	60 - 70	2.72	---
	ALD-10-49	SSH0000LK	100 - 110	2.12	---
	ALD-10-45	SSH0000LO	140 - 150	1.64	---
	ALD-10-36	SSH0000LS	180 - 190	1.84	---
	ALD-10-38	SSH0000LU	200 - 210	---	---
Pennsylvania	ALD-10-163	SSH0000NL	0 – 10	6.56	6.60
	ALD-10-164	SSH0000NM	10 – 20	---	4.83
	ALD-10-165	SSH0000NN	20 – 28	---	3.60
Virginia[e]	MT-09-032	SSH0000PH	0 – 10	12.5	13.7
	MT-09-033	SSH0000PI	10 – 20	4.22	6.24
	MT-09-034	SSH0000PJ	20 - 30	3.24	5.63
	MT-09-035	SSH0000PK	30 - 40	5.51	6.71
	MT-09-036	SSH0000PL	40 - 50	4.66	6.62
	MT-09-037	SSH0000PM	50 - 60	5.74	7.83
	MT-09-038	SSH0000PN	60 - 70	5.59	6.71
	MT-09-039	SSH0000PO	70 - 80	5.76	7.41

Table A-5 (cont.)

Site	Sample	IGSN[a]	Interval cm	LOI[b] %	LOI[c] %
Tennessee	ALD-09-17	SSH0000QC	0 - 5	---	16.0
	ALD-09-18	SSH0000QD	5 - 10	---	6.48
	ALD-09-02	SSH0000QG	10 - 20	8.21	8.60
	ALD-09-03	SSH0000QH	20 - 30	---	7.46
	ALD-09-04	SSH0000QI	30 - 40	---	9.19
	ALD-09-05	SSH0000QJ	40 - 50	---	9.03
	ALD-09-07	SSH0000QL	60 - 70	---	6.72
	ALD-09-09	SSH0000QN	80 - 90	---	7.22
	ALD-09-11	SSH0000QP	100 - 110	---	7.28
	ALD-09-13	SSH0000QR	120 - 130	7.62	7.53
	ALD-09-15	SSH0000QT	145 - 150	---	8.26
	ALD-09-16	SSH0000QU	150 - 155	---	5.89
	ALD-10-64	SSH0000QY	160 - 170	---	7.23
	ALD-10-67	SSH0000R1	190 - 200	---	6.49
	ALD-10-70	SSH0000R4	210 - 220	---	6.41
	ALD-10-73	SSH0000R8	230 - 240	---	6.95
	ALD-10-75	SSH0000R9	240 - 250	7.67	7.78
	ALD-11-401	SSH0000RP	260 - 270	7.67	---
	ALD-11-404	SSH0000RS	290 - 300	7.62	6.74
	ALD-11-426	SSH0000RW	330 - 340	8.94	7.84
	ALD-11-429	SSH0000RZ	360 - 370	6.65	6.81
	ALD-11-432	SSH0000S2	390 - 398	7.11	6.62
Alabama	ALD-10-114	SSH0000T3	0 - 10	5.17	4.13
	ALD-10-115	SSH0000T4	10 - 20	---	8.44
	ALD-10-116	SSH0000T5	20 - 30	---	6.58
	ALD-10-117	SSH0000T6	30 - 40	---	6.96
	ALD-10-118	SSH0000T7	40 - 50	---	5.76
	ALD-10-121	SSH0000TA	60 - 70	---	7.99
	ALD-10-123	SSH0000TC	90 - 100	---	6.55
	ALD-10-125	SSH0000TE	110 - 120	9.23	8.94
	ALD-10-127	SSH0000TG	130 - 140	---	9.04
	ALD-10-129	SSH0000TI	150 - 155	---	7.31
	ALD-11-506	SSH0000TP	170 - 180	6.68	3.88
	ALD-11-508	SSH0000TR	190 - 200	8.04	7.24
	ALD-11-510	SSH0000TT	200 - 210	7.30	8.12

Table A-5 (cont.)

Site	Sample	IGSN[a]	Interval cm	LOI[b]	LOI[c]
				—— % ——	
Puerto Rico	ald-11-13	SSH0000VO	0 - 8	---	21.5
	ald-11-14	SSH0000VP	8 - 10	---	18.4
	ald-11-15	SSH0000VQ	10 - 15	---	17.4
	ald-11-16	SSH0000VR	15 - 20	---	14.9
	ald-11-17	SSH0000VS	20 - 30	---	13.9
	ald-11-18	SSH0000VT	30 - 40	---	14.9
	ald-11-19	SSH0000VU	40 - 50	13.6	13.0
	ald-11-25	SSH0000W0	100 - 111	---	18.5
	ald-11-30	SSH0000W5	150 - 160	---	13.8
	ald-11-38	SSH0000WA	200 - 210	---	14.6
	ald-11-43	SSH0000WF	250 - 260	---	12.7
	ald-11-48	SSH0000WK	300 - 310	---	12.6
	ald-11-53	SSH0000WP	350 - 360	---	13.1
	ald-11-58	SSH0000WU	400 - 410	---	13.1
	ald-11-63	SSH0000WZ	450 - 460	12.6	13.2
	ald-11-76	SSH0000X5	500 - 505	---	12.9
	ald-11-86	SSH0000XF	570 - 580	---	8.88
	ald-11-92	SSH0000XL	625 - 632	---	8.24

[a] International Geo Sample Number, www.geosamples.org

[b] LOI measured by combustion

[c] LOI calculated by subtracting total oxides from 100

Appendix B

Chapter 3 Supplementary Material

Figures

t = ~ 100 ky	t = ~ 25 ky	t = present
Warmer, wetter conditions during Sangamonian; profile highly weathered and clay films deposited deep	Colder, less precipitation during LGM; weathering shuts down, no clay is weathered or illuviated	Moderate temperature, precipitation; weathering and clay illuviation concentrated near surface
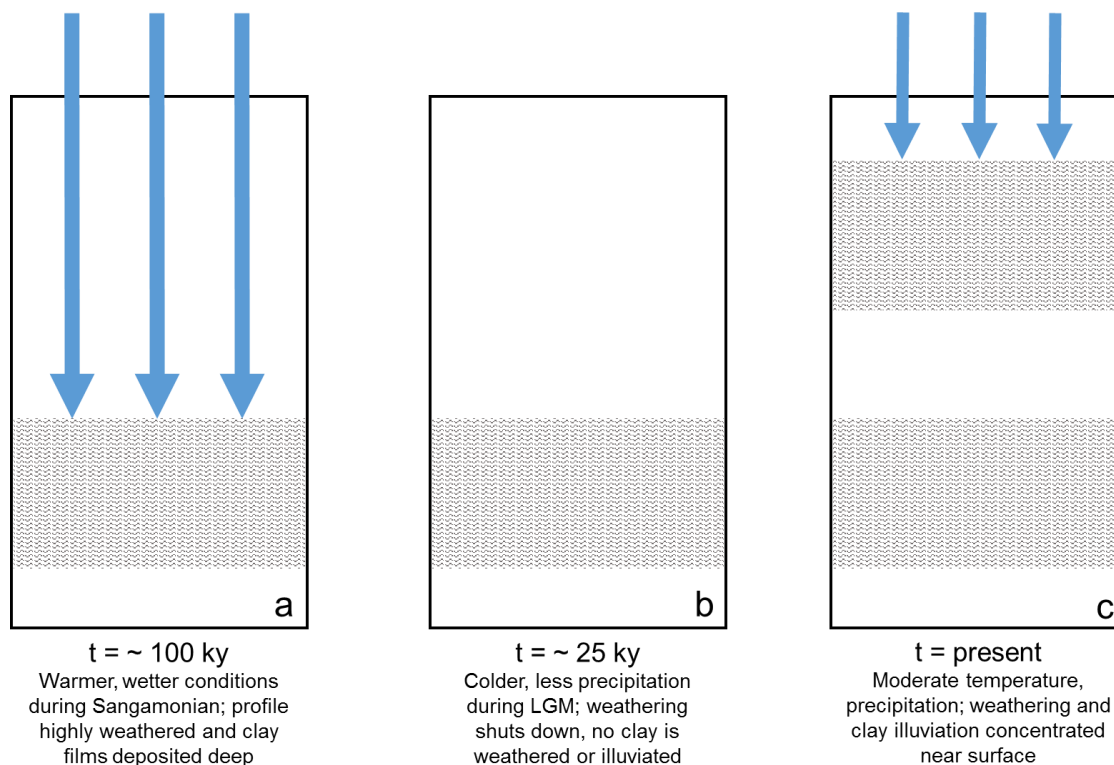
Figure B-1. Conceptual diagram of the evolution of the TN hillslope profile as a deeply weathered profile (paleosol). Arrows represent precipitation that moves clay and shaded areas represent zones of clay film accumulation. (a) Warmer and wetter climate conditions during the last interglacial results in fast weathering and deep translocation of clay. (b) As climate cools during the Last Glacial Maximum (LGM), cold temperatures and low precipitation shuts down weathering and the illuviation of clay throughout the profile. (c) Under modern climate conditions of moderate temperature and precipitation, modern weathering produces clay material and translocates clay only in the upper part of the profile; relict clay films are preserved at depth.
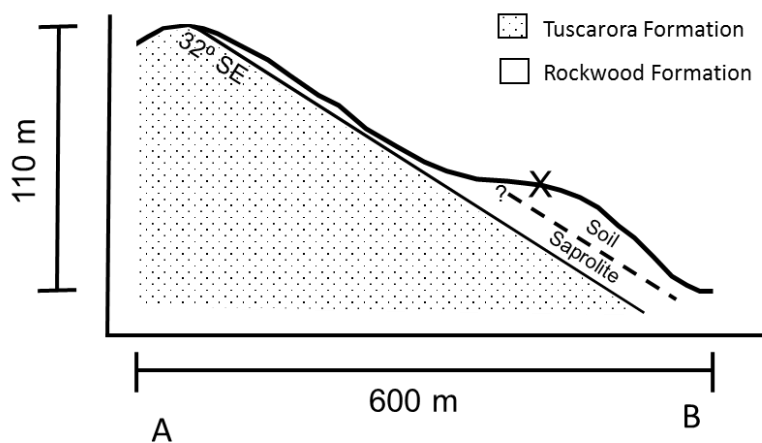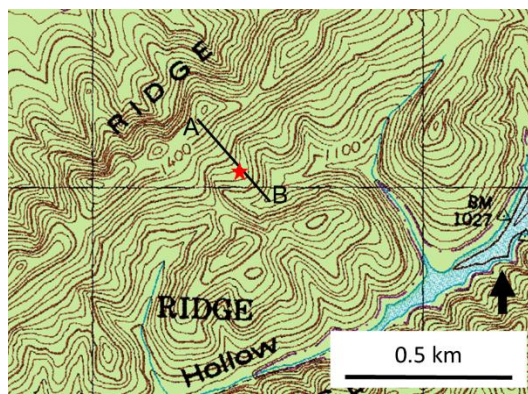
Figure B-2. Conceptual diagram of the TN hillslope profile with the Tuscarora Formation quartzite overlain by the Rockwood Formation shale (equivalent to the Rose Hill Formation in other parts of the climosequence). The X marks the sampling location of the ridgetop profile. Outcrop dipping 32^0 SE is observed at the top of the hillslope. Based on observations from the core, the soil-saprolite boundary can be identified by inherited shale structure in the saprolite. The boundary between the soil and saprolite upslope and downslope from the ridgetop sampling site is estimated.

Appendix C

Chapter 4 Supplementary Material

Clay XRD Methodology

Ethylene glycol treatment

Clays were mounted on a glass slide and dried overnight before scanning the following morning. The untreated slides were then placed in an ethylene glycol atmosphere overnight and scanned the following morning. A new untreated clay slide was prepared, scanned, then placed in an ethylene glycol atmosphere overnight at 60°C and scanned the following morning.

K saturation treatment

Approximately 6 ml of clay suspension and 6 ml of NaOAc buffer (pH 5) was added to a 15 ml test tube. The tube was corked and shaken vigorously, then warmed for 10 min in an 80°C water bath. Once removed, the tube was centrifuged at 2000 rpm for 5 min to settle material to the bottom and the supernatant was discarded. Approximately 7 ml of 1 N KCl was added to the test tube, shaken well by hand to re-suspend clay, then placed on a shaker table for 10 min. Upon removal from the shaker, the tube was again shaken and then centrifuged for 5 min at 2000 rpm and the clear supernatant discarded. The KCl treatment was repeated once, after which 10 ml of KCl was added to the tube, shaken and placed on a shaker table overnight. The tube was removed, shaken again then

centrifuged for 5 min at 2000 rpm. The first wash consisted of adding 10 ml of distilled

water, shaking, centrifuging for 5 min at 2000 rpm, then discarding the clear supernatant.

Secondly, 7 ml of methanol was added to the tube, shaken, then centrifuged for 5 min at

2000 rpm. The clear supernatant was discarded and the distilled water wash was

repeated. Finally, 6 ml of distilled water was added to the tube to re-suspend the clays.

Approximately 2 ml of treated clay suspension was pipetted onto a glass slide then dried

overnight. X-ray patterns were collected from the air dried K saturated slide and

immediately following heating slides to 200, 350 and 530°C.

Mg saturation treatment

Approximately 6 ml of clay suspension and 6 ml of NaOAc buffer (pH 5) was

added to a 15 ml test tube. The tube was corked and shaken vigorously, then warmed for

10 min in an 80°C water bath. Once removed, the tube was centrifuged at 2000 rpm for 5

min to settle material to the bottom and the supernatant was discarded. Approximately

10 ml of 1 N $MgCl_2$ was added to the test tube, shaken well by hand to re-suspend clay

then placed on a shaker table for 10 min. Upon removal from the shaker, the tube was

again shaken and then centrifuged for 5 min at 2000 rpm and the clear supernatant

discarded. The $MgCl_2$ treatment was repeated once, after which 10 ml of $Mg(Ac)_2$ (pH

7) was added, shaken and placed on a shaker table for 10 min. The tube was removed,

shaken, then centrifuged for 5 min at 2000 rpm. Approximately 10 ml of 1 N $MgCl_2$ was

then added to the tube, shaken and placed on a shaker table overnight. The tube was

removed from the shaker table, shaken and centrifuged 5 min at 2000 rpm, discarding the

clear supernatant. The first wash consisted of adding 10 ml of 50% methanol, shaking, centrifuging for 5 min at 2000 rpm then discarding the clear supernatant. Secondly, 7 ml of 95% ethanol was added to the tube, shaken then centrifuged for 5 min at 2000 rpm. The clear supernatant was discarded and the distilled water wash was repeated. Finally, 10 ml of distilled water was added to the tube, shaken by hand, then centrifuged for 5 min at 2000 rpm. After discarding the supernatant, approximately 6 ml of distilled water was added to the tube to re-suspend the clays. Approximately 2 ml of treated clay suspension was pipetted onto a glass slide then dried overnight.

For the Mg saturation with glycerol treatment, 5 ml of Mg saturated clay suspension was added to a 15 ml test tube. Eight to ten drops of 10% glycerol were added to the tube then shaken by hand. The clay suspension was applied to slides using a dropper and air dried overnight. Two hours prior to analysis, the slide was placed in a glycerol atmosphere at 60°C, then analyzed immediately following removal from the atmosphere.

Acid treatment

Approximately 10 ml of clay suspension and 130 ml of 1 N HCl was added to a 250 ml beaker, covered with a cover glass and heated to a boil for two hours. Clays were washed from the beaker into a centrifuge bottle and roughly 200 ml of distilled water was added. Bottles were centrifuged for 45 min at 3000 rpm and then the supernatant was discarded. 200 ml of distilled water was then added and the bottle shaken to re-suspend clays, centrifuged for 5 min at 2000 rpm and the supernatant discarded. The wash was

repeated once. Clays were transferred to a 1 ounce bottle for storage and a slide was prepared by dropping the clay suspension onto glass slides and drying overnight.

Meteorological instrumentation

Instruments at each site were mounted to a 3 m tall metal pole (8 cm2 dimensions) with a 1 m long crossbar affixed to the top of the pole. A metal base with angled edges was driven 0.5 m into the ground using a sledgehammer and the metal pole was inserted into the metal base and secured with screws. The datalogger and rechargeable battery were housed in a 10 x 12 x 4.5 in plastic enclosure (ENC10/12, Campbell Scientific, Logan, UT, USA) attached to the metal pole.

Precipitation (mm) was measured using a Texas Electronics Rain Gage (TE525-ET) (Texas Electronics, Dallas, TX, USA) instantaneously at each data time point (every 2 hr) as well as averaged over each sampling interval (2 hr). Wind speed (m s-1) was measured instantaneously as well as averaged every 2 hr with a Secondwind 3C Anemometer (Second Wind, Newton, MA, USA). Air temperature (°C) and relative humidity (%) were measured with a Campbell Scientific HMP45C Temperature and Relative Humidity Probe (Campbell Scientific, Logan, UT, USA). Solar radiation (W m-2) was measured with a Davis Instruments Vantage Pro2 Solar Radiation Sensor (Davis Instruments, Hayward, CA, USA). Volumetric water content (dielectric*50), electrical conductivity (dS) and soil temperature (°C) were measured with a Decagon 5TE Sensor (Decagon Devices, Pullman, WA, USA) buried 20 cm below the soil surface approximately 1 m from base of the station. To install the sensor, a small hole was dug

and the sensor was inserted laterally into the side of the pit to ensure contact with the soil. Wires for the sensor were enclosed in PVC piping and run back to the mounted datalogger. Volumetric Water Content (VWC, Θ) data require transformation of output units (dielectric*50) using the following equation:

$$\Theta = 3.11e^{-11} * \sigma^{-3} - 2.20e^{-7} * \sigma^2 + 5.84e^{-4} * \sigma - 5.3e^{-2} \qquad (1)$$

Here, θ is the volumetric water content in m3/m3, and σ is the data output from the soil moisture sensor (dielectric*50).

All data was recorded on a Campbell Scientific CR200x Datalogger (Campbell Scientific, Logan, UT, USA) and downloaded quarterly directly from the weather stations using a Gigaware® 6-ft. USB-A to Serial Cable and PC200W software (Campbell Scientific, Logan, UT, USA). Output data also included a daily average evapotranspiration (ETo), calculated using the daily average air temperature, relative humidity, wind speed and solar radiation measurements. All data, including notes on data quality, are available online (Dere and White, 2013).

Figures
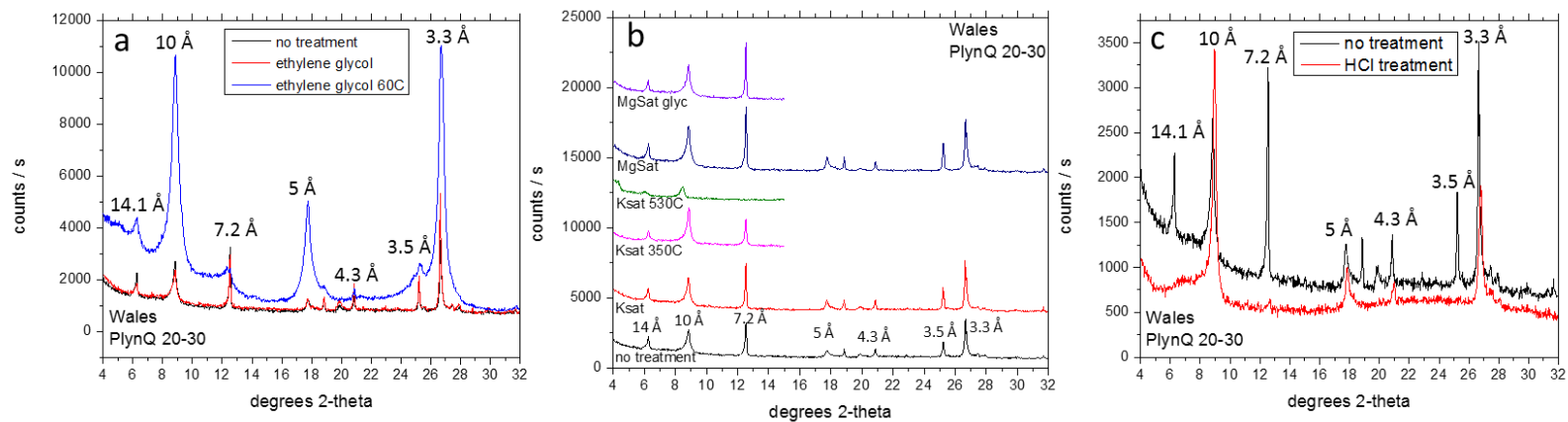
Figure C-1. Clay peaks for the 20 – 30 cm soil interval in Wales. The black line in each panel represents the untreated clay fraction (no treatment) diffraction pattern and colored lines represent the same samples subjected to different treatments: (a) samples submerged in an ethylene glycol atmosphere at room temperature and at 60 ºC; (b) samples saturated with K (Ksat) and heated to 350 ºC and 530 ºC or saturated with Mg (MgSat) and then Mg saturated and glycerol solvated (MgSat glyc); (c) samples treated with HCl. Numbers above peaks indicate the d-spacing associated with that peak.
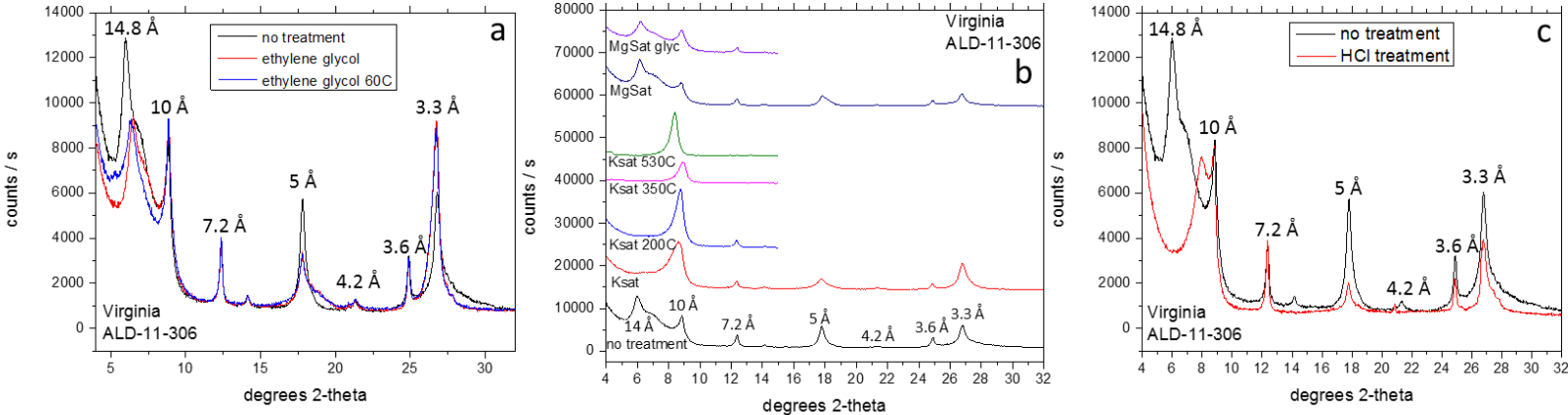
Figure C-2. Clay peaks for the 30 – 40 cm soil interval in Virginia. The black line in each panel represents the untreated clay fraction (no treatment) diffraction pattern and colored lines represent the same samples subjected to different treatments: (a) samples submerged in an ethylene glycol atmosphere at room temperature and at 60 ºC; (b) samples saturated with K (Ksat) and heated to 350 ºC and 530 ºC or saturated with Mg (MgSat) and then Mg saturated and glycerol solvated (MgSat glyc); (c) samples treated with HCl. Numbers above peaks indicate the d-spacing associated with that peak.
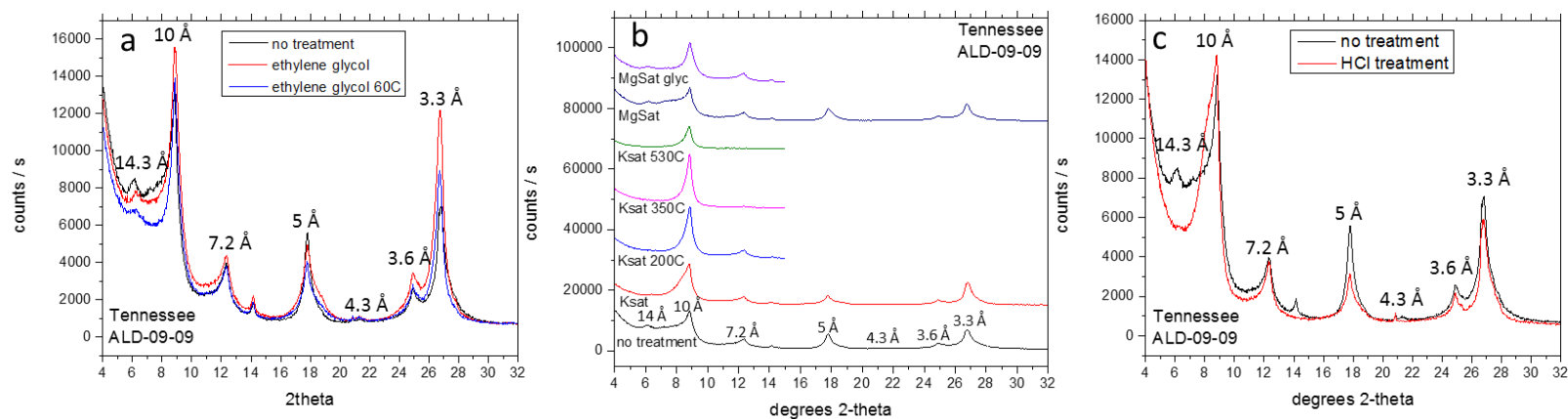
Figure C-3. Clay peaks for the 30 – 40 cm soil interval in Tennessee. The black line in each panel represents the untreated clay fraction (no treatment) diffraction pattern and colored lines represent the same samples subjected to different treatments: (a) samples submerged in an ethylene glycol atmosphere at room temperature and at 60 ℃; (b) samples saturated with K (Ksat) and heated to 350 ℃ and 530 ℃ or saturated with Mg (MgSat) and then Mg saturated and glycerol solvated (MgSat glyc); (c) samples treated with HCl. Numbers above peaks indicate the d-spacing associated with that peak.

Figure C-4. Clay peaks for the 250 – 260 cm soil interval in Tennessee. The black line in each panel represents the untreated clay fraction (no treatment) diffraction pattern and colored lines represent the same samples subjected to different treatments: (a) samples submerged in an ethylene glycol atmosphere at room temperature and at 60 ºC; (b) samples saturated with K (Ksat) and heated to 350 ºC and 530 ºC or saturated with Mg (MgSat) and then Mg saturated and glycerol solvated (MgSat glyc); (c) samples treated with HCl. Numbers above peaks indicate the d-spacing associated with that peak.

Figure C-5. Clay peaks for the 30 – 40 cm soil interval in Alabama. The black line in each panel represents the untreated clay fraction (no treatment) diffraction pattern and colored lines represent the same samples subjected to different treatments: (a) samples submerged in an ethylene glycol atmosphere at room temperature and at 60 °C; (b) samples saturated with K (Ksat) and heated to 350 °C and 530 °C or saturated with Mg (MgSat) and then Mg saturated and glycerol solvated (MgSat glyc); (c) samples treated with HCl. Numbers above peaks indicate the d-spacing associated with that peak.
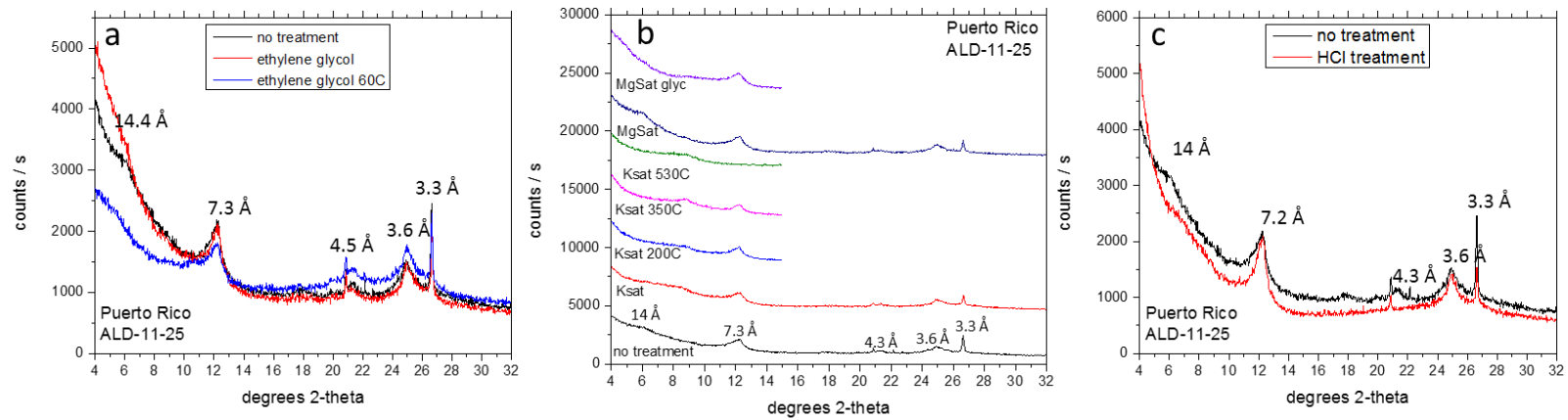
Figure C-6. Clay peaks for the 40 – 50 cm soil interval in Puerto Rico. The black line in each panel represents the untreated clay fraction (no treatment) diffraction pattern and colored lines represent the same samples subjected to different treatments: (a) samples submerged in an ethylene glycol atmosphere at room temperature and at 60 ℃; (b) samples saturated with K (Ksat) and heated to 350 ℃ and 530 ℃ or saturated with Mg (MgSat) and then Mg saturated and glycerol solvated (MgSat glyc); (c) samples treated with HCl. Numbers above peaks indicate the d-spacing associated with that peak.

Figure C-7. Particle size distribution of <2 mm fraction of soils with depth across the climosequence. NY is not included due to till parent material.

Tables

Table C-1. Data sources for EEMT calculation. Annual temperature (MAT) and precipitation (MAP) data were obtained from meteorological stations at each study site and/or nearby NOAA weather stations. Evapotranspiration (ET) and net primary productivity (NPP) data were obtained from MODIS data by averaging all pixels with the same land use as the center pixel, which was centered on the study site. In Alabama and Puerto Rico only the center pixel was used due to large variability in land use classification surrounding these sites.

Site	Dates of complete weather station data[a]	NOAA station	NOAA station #	Years	MODIS center pixel land use classification	Number of pixels in 7 km^2 grid with center pixel land use
Wales - Forest	6/29/08 – 6/29/10	---	---	---	Mixed forest	35/49
Wales - Grass	6/29/08 – 6/29/10	---	---	---	Grassland	32/49
New York	7/15/11 – 6/4/13	---	---	---	Cropland/natural vegetation mosaic	48/49
Pennsylvania[b]	7/29/10 – 7/30/11	Huntingdon	364159	2010-2011	Deciduous broadleaf forest	47/49
Virginia[c]	9/17/10 – 6/1/11 6/10/11 – 9/6/11	Warm Springs	444128	2010-2011	Deciduous broadleaf forest	49/49
Tennessee	11/8/11 – 11/9/13	---	---	---	Deciduous broadleaf forest	16/49
Alabama[c]	11/9/11 – 7/21/12 7/23/12 – 11/9/12 11/10/12 – 11/10/13	Guntersville	013573	2010-2012	Mixed forest	---
Puerto Rico[c]	5/29/11 – 5/29/13 3/24/13 – 6/16/13	Arecibo Observatory	660426	2010-2011	Cropland	---

[a] Dates of weather station data used to calculate mean annual temperature (MAT) and mean annual precipitation (MAP) at each site
[b] Temperature data obtained from NOAA station
[c] Precipitation data obtained from NOAA station

Table C-2. Transect soil tau values using Zr as an immobile element at all sites except VA, where corrected Ti values were used as the immobile element. Zr was not measured on NY soil samples therefore Ti is used as the immobile element.

Site	Sample	IGSN[a]	d cm	Al	Ca	Fe	K	Mg	Mn	Na	P	Si	Ti
Wales	plnq0-10	SSH000SSM	0 - 10	-0.19	-0.31	0.03	-0.14	-0.68	-0.38	-0.24	0.60	-0.03	-0.29
	plnq10-20	SSH0000HE	10 - 20	-0.06	-0.32	0.16	-0.04	-0.41	0.66	-0.20	0.05	-0.01	-0.30
	plnq20-30	SSH0000HF	20 - 30	-0.03	-0.34	0.24	-0.01	-0.24	0.40	-0.16	0.03	0.00	-0.33
	plnq30-31	SSH0000HG	30 - 31	-0.02	-0.10	0.28	0.01	-0.22	0.26	-0.12	0.39	0.02	-0.34
	plnq31-35	SSH0000HH	31 - 35	0.12	-0.04	0.27	0.17	0.02	0.68	-0.05	-0.07	0.11	-0.27
NY[b]	ALD-10-61	SSH0000L8	0 - 5	-0.16	-0.73	-0.03	-0.39	-0.33	0.04	-0.45	-0.07	-0.32	---
	ALD-10-60	SSH0000L9	5 - 10	-0.11	-0.72	0.02	-0.36	-0.25	0.05	-0.45	-0.14	-0.33	---
	ALD-10-59	SSH0000LA	10 - 15	-0.03	-0.71	0.03	-0.23	-0.10	-0.07	-0.51	-0.37	-0.38	---
	ALD-10-58	SSH0000LB	15 - 20	0.00	-0.80	0.06	-0.18	-0.02	0.00	-0.53	-0.51	-0.38	---
	ALD-10-57	SSH0000LC	20 - 30	0.05	-0.73	0.14	-0.10	0.04	-0.01	-0.48	-0.46	-0.29	---
	ALD-10-56	SSH0000LD	30 - 40	0.13	-0.69	0.14	0.03	0.14	-0.05	-0.44	-0.46	-0.21	---
	ALD-10-55	SSH0000LE	40 - 50	0.07	-0.44	0.08	-0.02	-0.04	-0.14	-0.13	-0.22	-0.03	---
	ALD-10-53	SSH0000LG	60 - 70	0.10	-0.43	0.06	0.10	0.03	-0.05	-0.07	-0.22	0.09	---
	ALD-10-49	SSH0000LK	100 - 110	-0.06	-0.17	-0.10	-0.07	-0.21	-0.07	0.30	-0.09	0.09	---
	ALD-10-45	SSH0000LO	140 - 150	-0.03	-0.26	-0.05	-0.03	-0.08	-0.06	-0.02	-0.09	-0.01	---
	ALD-10-36	SSH0000LS	180 - 190	0.03	-0.16	0.02	0.03	0.04	0.03	-0.05	0.03	-0.01	---
	ALD-10-38	SSH0000LU	200-210	0.06	0.56	0.11	0.07	0.23	0.09	-0.20	0.14	-0.06	---
PA	ALD-10-163	SSH0000NL	0 – 10	-0.27	-0.37	-0.18	-0.33	-0.27	18.37	-0.26	0.14	-0.14	-0.41
	ALD-10-164	SSH0000NM	10 – 20	-0.21	-0.59	-0.15	-0.22	-0.19	1.83	-0.22	-0.02	-0.12	-0.39
	ALD-10-165	SSH0000NN	20 – 28	-0.07	-0.15	-0.05	-0.08	0.04	0.57	-0.10	0.13	-0.04	-0.33
VA[c]	MT-09-032	SSH0000PH	0 – 10	-0.56	0.68	0.38	-0.85	-0.73	19.59	-0.58	0.65	1.32	-0.18
	MT-09-033	SSH0000PI	10 – 20	-0.63	-0.36	0.44	-0.85	-0.77	5.47	-0.64	0.65	1.59	-0.18
	MT-09-034	SSH0000PJ	20 - 30	-0.60	-0.52	2.00	-0.80	-0.77	3.45	-0.65	1.08	2.29	-0.17
	MT-09-035	SSH0000PK	30 - 40	-0.59	0.31	1.35	-0.80	-0.75	5.81	-0.67	1.98	2.43	-0.13
	MT-09-036	SSH0000PL	40 - 50	-0.47	-0.51	0.96	-0.73	-0.68	2.19	-0.53	0.65	1.67	-0.12
	MT-09-037	SSH0000PM	50 - 60	-0.17	-0.19	1.70	-0.54	-0.53	0.59	-0.14	1.11	1.73	-0.10
	MT-09-038	SSH0000PN	60 - 70	-0.07	-0.43	1.36	-0.36	-0.42	-0.49	-0.41	2.91	1.43	-0.08
	MT-09-039	SSH0000PO	70 - 80	-0.07	-0.89	0.39	-0.31	-0.41	-0.70	-0.32	0.85	1.20	-0.04

Table C-2 (cont.)

Site	Sample	IGSN[a]	d cm	Al	Ca	Fe	K	Mg	Mn	Na	P	Si	Ti
TN	ALD-09-17	SSH0000QC	0 - 5	-0.42	-0.97	0.35	-0.51	-0.76	-0.57	-0.80	0.67	-0.25	-0.46
	ALD-09-18	SSH0000QD	5 - 10	-0.43	-0.98	-0.25	-0.51	-0.77	-0.64	-0.80	-0.20	-0.25	-0.45
	ALD-09-02	SSH0000QG	10 - 20	-0.32	-0.97	-0.05	-0.45	-0.74	-0.22	-0.77	0.08	-0.27	-0.45
	ALD-09-03	SSH0000QH	20 - 30	-0.17	-0.98	-0.07	-0.36	-0.67	1.08	-0.76	-0.11	-0.16	-0.41
	ALD-09-04	SSH0000QI	30 - 40	-0.18	-0.98	0.16	-0.33	-0.67	0.02	-0.76	0.09	-0.17	-0.40
	ALD-09-05	SSH0000QJ	40 - 50	-0.09	-0.98	0.10	-0.21	-0.63	-0.88	-0.72	0.06	-0.13	-0.38
	ALD-09-07	SSH0000QL	60 - 70	0.03	-0.98	-0.24	-0.12	-0.57	-0.88	-0.70	-0.19	-0.08	-0.37
	ALD-09-09	SSH0000QN	80 - 90	0.09	-0.99	-0.31	-0.03	-0.54	-0.87	-0.66	-0.43	-0.03	-0.33
	ALD-09-11	SSH0000QP	100 - 110	0.03	-0.99	-0.11	-0.07	-0.58	-0.87	-0.69	-0.07	-0.05	-0.35
	ALD-09-13	SSH0000QR	120 - 130	-0.06	-0.99	1.27	-0.13	-0.59	-0.87	-0.70	0.77	-0.09	-0.37
	ALD-09-15	SSH0000QT	145 - 150	0.36	-0.99	-0.22	0.24	-0.44	-0.84	-0.60	-0.42	0.18	-0.20
	ALD-09-16	SSH0000QU	150 - 155	0.23	-0.99	-0.25	0.13	-0.50	-0.86	-0.64	-0.18	0.05	-0.29
	ALD-10-64	SSH0000QY	160 - 170	0.52	-0.99	-0.34	0.23	-0.38	-0.91	-0.57	-0.10	0.21	-0.20
	ALD-10-67	SSH0000R1	190 - 200	0.43	-0.99	-0.24	0.17	-0.40	-0.90	-0.61	-0.12	0.17	-0.22
	ALD-10-70	SSH0000R4	210 - 220	0.44	-0.99	-0.38	0.23	-0.37	-0.89	-0.58	-0.14	0.18	-0.21
	ALD-10-73	SSH0000R8	230 - 240	0.67	-0.97	0.99	0.49	-0.21	-0.81	-0.50	0.16	0.30	-0.12
	ALD-10-75	SSH0000R9	240 - 250	0.95	-0.99	0.94	0.77	-0.09	1.12	-0.39	0.29	0.44	-0.04
	ALD-11-401	SSH0000RP	260 - 270	0.25	-0.94	0.86	0.25	-0.40	-0.83	-0.53	0.14	0.05	-0.30
	ALD-11-404	SSH0000RS	290 - 300	0.07	-0.99	0.79	0.02	-0.49	-0.83	-0.63	0.16	0.03	-0.31
	ALD-11-426	SSH0000RW	330 - 340	0.04	-0.96	-0.26	-0.09	-0.54	-0.61	-0.70	-0.11	-0.05	-0.36
	ALD-11-429	SSH0000RZ	360 - 370	0.01	-0.99	-0.44	-0.05	-0.54	-0.54	-0.66	-0.18	-0.05	-0.37
	ALD-11-432	SSH0000S2	390 - 398	0.05	-0.98	0.27	-0.02	-0.47	-0.14	-0.64	0.05	-0.01	-0.34

Table C-2 (cont.)

Site	Sample	IGSN[a]	d cm	Al	Ca	Fe	K	Mg	Mn	Na	P	Si	Ti
AL	ALD-10-114	SSH0000T3	0 - 10	-0.89	-0.67	-0.88	-0.96	-0.95	-0.58	-0.95	-0.52	-0.14	-0.84
	ALD-10-115	SSH0000T4	10 - 20	-0.85	-0.85	-0.84	-0.95	-0.94	-0.01	-0.94	-0.50	-0.25	-0.76
	ALD-10-116	SSH0000T5	20 - 30	-0.82	-0.86	-0.80	-0.95	-0.93	-0.72	-0.94	-0.56	-0.36	-0.77
	ALD-10-117	SSH0000T6	30 - 40	-0.69	-0.79	-0.49	-0.93	-0.87	-0.69	-0.94	-0.10	-0.13	-0.70
	ALD-10-118	SSH0000T7	40 - 50	-0.49	-0.80	-0.42	-0.89	-0.81	-0.39	-0.91	-0.05	-0.07	-0.63
	ALD-10-121	SSH0000TA	60 - 70	-0.23	-0.83	-0.12	-0.82	-0.71	-0.85	-0.91	0.57	-0.17	-0.59
	ALD-10-123	SSH0000TC	90 - 100	-0.16	-0.72	-0.05	-0.76	-0.64	-0.86	-0.89	0.62	-0.02	-0.58
	ALD-10-125	SSH0000TE	110 - 120	-0.05	-0.72	-0.03	-0.74	-0.60	-0.88	-0.89	0.95	-0.03	-0.54
	ALD-10-127	SSH0000TG	130 - 140	0.06	-0.69	0.17	-0.68	-0.51	-0.79	-0.85	1.15	0.06	-0.47
	ALD-10-129	SSH0000TI	150 - 155	-0.40	-0.83	-0.24	-0.69	-0.56	-0.89	-0.90	0.39	0.81	-0.61
	ALD-11-506	SSH0000TP	170 - 180	-0.19	-0.79	-0.07	-0.59	-0.44	-0.94	-0.85	0.78	0.43	-0.48
	ALD-11-508	SSH0000TR	190 - 200	-0.17	-0.71	-0.13	-0.67	-0.53	-0.05	-0.79	0.67	0.17	-0.53
	ALD-11-510	SSH0000TT	200 - 210	-0.31	-0.85	-0.18	-0.70	-0.56	-0.83	-0.71	0.22	0.22	-0.55
PR	ald-11-13	SSH0000VO	0 - 8	0.17	-0.98	0.20	-0.64	-0.74	-0.73	-0.97	-0.09	-0.19	-0.20
	ald-11-14	SSH0000VP	8 - 10	0.16	-0.99	0.15	-0.69	-0.77	-0.79	-0.98	-0.33	-0.23	-0.24
	ald-11-15	SSH0000VQ	10 - 15	0.27	-0.99	0.27	-0.68	-0.75	-0.79	-0.98	-0.34	-0.17	-0.18
	ald-11-16	SSH0000VR	15 - 20	0.25	-0.99	0.23	-0.70	-0.77	-0.82	-0.98	-0.37	-0.19	-0.21
	ald-11-17	SSH0000VS	20 - 30	0.32	-0.99	0.36	-0.68	-0.76	-0.83	-0.98	-0.41	-0.13	-0.17
	ald-11-18	SSH0000VT	30 - 40	0.41	-0.99	0.46	-0.67	-0.74	-0.82	-0.99	-0.38	-0.11	-0.15
	ald-11-19	SSH0000VU	40 - 50	0.34	-0.99	0.38	-0.67	-0.74	-0.83	-0.99	-0.29	-0.11	-0.18
	ald-11-25	SSH0000W0	100 - 111	0.41	-0.99	0.63	-0.54	-0.62	-0.83	-0.98	-0.36	-0.15	-0.04
	ald-11-30	SSH0000W5	150 - 160	0.37	-0.99	0.99	-0.53	-0.66	-0.73	-0.98	-0.34	-0.13	-0.08
	ald-11-38	SSH0000WA	200 - 210	0.45	-1.00	1.49	-0.53	-0.62	-0.69	-0.98	-0.40	-0.21	-0.10
	ald-11-43	SSH0000WF	250 - 260	0.36	-1.00	1.88	-0.57	-0.70	-0.71	-0.98	-0.24	-0.13	-0.09
	ald-11-48	SSH0000WK	300 - 310	0.44	-1.00	1.04	-0.57	-0.75	-0.66	-0.99	-0.10	0.02	-0.12
	ald-11-53	SSH0000WP	350 - 360	0.32	-1.00	0.98	-0.60	-0.72	-0.51	-0.98	0.02	-0.02	-0.18
	ald-11-58	SSH0000WU	400 - 410	0.07	-1.00	0.42	-0.65	-0.75	-0.65	-0.98	-0.32	-0.17	-0.23
	ald-11-63	SSH0000WZ	450 - 460	0.18	-1.00	0.14	-0.44	-0.64	-0.76	-0.98	-0.38	-0.16	-0.08
	ald-11-76	SSH0000X5	500 - 505	0.33	-0.99	0.48	0.20	-0.60	-0.71	-0.90	-0.18	0.00	0.02
	ald-11-86	SSH0000XF	570 - 580	0.06	-0.99	-0.09	0.62	-0.64	-0.77	0.16	-0.18	0.12	-0.06
	ald-11-92	SSH0000XL	625 - 632	0.08	-0.98	0.23	0.81	-0.43	-0.62	0.57	-0.07	0.19	0.03

International Geo Sample Number, www.geosamples.org   [b] Tau values for NY calculated using Ti as the immobile element (Zr data not available) and the average of the bottom four samples as parent   [c] VA tau values were calculated using reconstructed Ti as the immobile element (Dere et al., 2013)

Appendix D

Solute fluxes and weathering at Plynlimon, mid-Wales

Abstract

In an effort to quantify the influence of climate on shale weathering rates, a transect of study sites has been established on Silurian shales along a climatic gradient in the northern hemisphere as part of the Susquehanna Shale Hills Critical Zone Observatory, PA (USA). The coldest and most northerly site of this transect is the Hafren watershed in the headwaters of the River Severn, at Plynlimon, Wales, UK. The watershed, which is approximately 24 km from the west Wales coast, has an area of 7 km^2 and is 70% covered by Sitka spruce plantation forestry. The watershed has been extensively studied with continuous measurements of precipitation and runoff since 1968 and weekly monitoring of rain and stream water chemistry since 1983. These data provide an ideal opportunity to compare weathering rates derived from watershed mass balance to those derived from soil geochemical profiles; weathering rate estimates at the other transect locations are restricted to geochemical profiles alone. Annual watershed solute fluxes over the past 25 years were determined by subtracting stream output fluxes from precipitation input fluxes using Cl as a conservative tracer. Annual mass balance estimates for dissolved elements such as Si are relatively consistent over time (mean value 863 ± 25.2 mol Si ha^{-1} yr^{-1}) while those of Na are more variable (mean value 149 ± 51 mol Na ha^{-1} yr^{-1}) and show influence of variable sea salt input. Area-weighted release

rates of Mg (mean value 212 ± 11 mol Mg ha^{-1} yr^{-1}) are indicative of weathering rates of the abundant chlorite minerals (chlorite, vermiculite, hydroxyl interlayered vermiculite) in the shale. Weathering rates were also estimated from soil geochemical profiles, where elemental depletions relative to parent shale chemistry were used to calculate a weathering rate over the last 10 ky. Mg release rate estimates from soil ridgetop samples (77.2 ± 17 mol Mg ha^{-1} yr^{-1}) are approximately one third as large as rates estimated from watershed mass balance calculations. This is not surprising given the different scales of measurement and point to a system that may not be in steady state with respect to regolith formation and denudation. Similarly, Na release estimates from ridgetop samples (18.5 ± 8.7 mol Na ha^{-1} yr^{-1}) are roughly 8 times smaller than estimates from the whole watershed. The ratios of Na and Mg to Si and Al loss from the stream and the soils were compared to infer weathering reactions in the catchment. The ratio of Mg and Al release rates from the stream is close to 1, which is consistent with chlorite weathering to vermiculite and kaolinite. Likewise, the ratio of Na and Al release rates from the stream is close to 1, consistent with dissolution of plagioclase. Soil geochemical profiles record no net loss of Al or Si from the soil profiles. One explanation for the discrepancy between weathering rates inferred from soils and from streams could be related to differences in surface area. In other words, the watershed solute estimates for Mg and Na are influenced by large surface area in fragmented shale bedrock underlying the soil profiles in addition to the augerable regolith but also in the fragmented shale bedrock underlying the soil profile.

Introduction

Weathering is a fundamental process operating at the surface of the Earth to break down rock and produce soil that supports ecosystems and humans alike (Brantley et al., 2007). Efforts to quantify weathering are often approached by measuring changes as a function of the main factors responsible for soil formation, including lithology, climate, time, topography and biota (Jenny, 1941; Birkeland, 1999). While environmental gradients are commonly employed to design experiments aimed at quantifying weathering, the methods for measuring weathering are variable. For example, stream solute chemistry provides information about weathering reactions at the watershed scale (Garrels and Mackenzie, 1967) while bulk geochemical rock and soil measurements provide rates from the clast to pedon scale (Navarre-Sitchler and Brantley, 2007).

Geochemical analyses of soil and rocks are commonly used to estimate soil weathering rates, providing an integrated weathering rate over the time the soil has been forming is estimated (April et al., 1986; Brimhall and Dietrich, 1987; Brantley and White, 1999). This method involves comparing soil and unweathered rock concentrations relative to an immobile element not involved in weathering reactions. Once the mass loss of an element is determined, a weathering rate can be obtained from the estimated weathering duration (Brantley and White, 2009). The depletion of individual elements, such as Na or Mg, are often used as a proxy for mineral weathering reactions, i.e. Na loss can be attributed to feldspar weathering (White and Brantley, 2003) while Mg loss can represent chlorite weathering (Jin et al., 2010). However, this method requires a proper assessment of the original parent composition as well as the duration of weathering, both

of which can be difficult to constrain in natural systems. Nonetheless, this approach is relatively rapid once a suitable sampling site is located and has been extensively employed to determine weathering rates in a variety of lithologies (e.g. April et al., 1986; White et al., 2001; Chadwick et al., 2003; Jin et al., 2010).

Weathering estimates at the watershed scale are generally estimated using solute fluxes, including stream and precipitation chemistry (Garrels and Mackenzie, 1967). In this approach, elements leaving the watershed as stream solutes provide a watershed-integrated weathering signal provided inputs other than weathering are subtracted from the stream output. One advantage to this method is that catchments integrate large areas and thus provide a weathering estimate over a large scale. The method can be time consuming, however, as data must be collected at regular intervals and ideally over multiple years to avoid inter-annual variations in climate, such as wet or dry years (Reynolds et al., 1997).

The Plynlimon watershed in mid-Wales has been extensively studied since 1968, providing a substantial dataset of solute chemistry. The original purpose of the study was to assess the sustainability of water resources in the United Kingdom as upland sites were increasingly converted from grazing operations to plantation forestry (Kirby et al., 1991). Recently, data from the Plynlimon watershed have been used to assess the recovery of stream and soils following a decrease in atmospheric sulfate deposition over the last several decades (Hughes et al., 2012).

Watershed solute fluxes at Plynlimon have previously been employed to calculate weathering rates over $1 - 2$ yr timescales. Reynolds et al. (1997) estimated Mg weathering fluxes over a two year period (1987 – 1988) of 2.4 kg Mg ha^{-1} yr^{-1}. These

values were in good agreement with estimates of solute weathering fluxes by other workers in the Plynlimon watershed (Reynolds et al., 1987, 1989; Durand et al., 1994). Some elements, however, were reported to have large variability. For example, Na flux estimates range from 2.4 to 10.4 kg ha^{-1} yr^{-1} over multiple studies (Reynolds et al., 1989; Reynolds et al., 1997). This discrepancy is attributed in large part to variable precipitation chemistry impacted by wind directions that influence the quantity of seawater inputs (Reynolds et al., 1987). There is a need, therefore, to calculate elemental budgets over longer time scales to better understand long-term weathering rates. Furthermore, weathering rates using a soil geochemistry have not previously been estimated at Plynlimon. Estimating weathering rates at the catchment and pedon scale may help elucidate weathering reactions at this site. Furthermore, insights gained at this intensively studied site could be extrapolated to sites with fewer data.

An environmental gradient approach has been used to isolate the influence of climate on shale weathering rates across a latitudinal climosequence as part of the Susquehanna Shale Hills Critical Zone Observatory (SSHO) in central Pennsylvania, USA (Dere et al., 2013). The coldest and northernmost site of the climosequence lies in Plynlimon, Wales, UK. The extensive datasets available at this site provide a unique opportunity to compare weathering estimated from solute fluxes and soil geochemistry.

The main goals of this study are to 1) provide an updated elemental solute budget using stream and precipitation chemistry over a 25 yr period for Plynlimon and 2) determine weathering fluxes and reactions from solutes and soil geochemical profiles in the same catchment. Both stream budgets and soil profiles are common methods for

estimating field weathering rates and this site provides the unique opportunity to compare

weathering reactions using the two approaches simultaneously.

Methods

Site characteristics

The Plynlimon forest in mid-Wales, United Kingdom (UK), is a 7 km^2 catchment

at the headwater of the River Severn, approximately 24 km from the west coast

(Reynolds et al., 1997) (Fig. D-1). Plynlimon has been studied and monitored since 1968,

with continuous measurements of precipitation, stream flow and runoff collected since

1983 (Neil et al., 2011 and references therein). The two main sub-catchments within the

Plynlimon watershed are the Hore and the Hafren. The Hore (335 ha) is predominantly

forested (67%) with the upper reaches of the catchment covered by peat and moorland

vegetation (Neal et al., 1990). Similarly, the Hafren (347 ha) is 48% forested with 52%

peat and moorland vegetation, predominantly in the upper reaches of the watershed (Neal

et al., 1990).

Vegetation within the forest is predominantly evergreen Sitka spruce (*Picea*

sitchensis (Bong. Carr.), with some Norway Spruce (*Picea abies* Karst.) and Lodgepole

Pine (*Pinus contorta* Dougl.) (Kirby et al., 1991). The trees are periodically thinned and

harvested for lumber resources by the Forestry Commission and immediately replanted

following harvest. Moorland vegetation is dominated by cottongrass (*Eriophorum*

vaginaturm L. and *E. angustifolium* L.), heather (*Calluna vulgaris* L.) and matgrass (*Nardus stricta* L.).

The catchment is largely underlain by the Silurian-age Fe-rich, organic-poor Gwestyn formation. Elevations range from 319 – 738 m and slopes within the catchment range from 0° - 15^0 (Kirby et al., 1991; Kirchner, 2009). The catchment was glaciated during the Last Glacial Maximum (LGM) and some areas of the catchment contain locally derived glacial till (Reynolds et al., 1989). Because the site was glaciated, the soil residence time (SRT), or the time particles spend in the soil before removal by erosion, is estimated at 10 ky, or roughly the time since deglaciation (Reynolds et al., 1987; Cadwell et al., 2004; Clark et al., 2004).

Mean annual temperature (MAT) is 7.2 °C and mean annual precipitation (MAP) is 250 cm with an average pH of 4.98 ± 0.01 (Kirby et al., 1991). Precipitation is heavily influenced by marine-derived solutes, with wind direction impacting the quantity of seawater inputs, especially during autumn when storms arrive from the west and southwest (Reynolds et al., 1987). In fact, approximately 60% of the total annual precipitation falls between October and March (Kirby et al., 1991). Snowfall represents a small portion of the water budget at Plynlimon ($< 5\%$) but frost has been recorded in every month of the year (Reynolds et al., 1987; Kirby et al., 1991).

Given the similar parent material throughout the catchment, Plynlimon soils are largely characterized by their drainage conditions. Drainage is impeded on the upper plateau and wider interfluves where thick layers of organic peat have accumulated as well as in valley bottoms which tend to have peat overlying gleyed mineral soils; slope soils are more freely draining and podzolized (Kirby et al., 1991). The soils in the upper

reaches of the catchment are classified as Peat, valley bottom soils as Stagnohumic Gleys or Peaty Gleys and slope soils are generally classified as Stagnopodzols (Rudeforth et al., 1967).

Water sampling

Water sampling was conducted by the Centre for Ecology and Hydrology (CEH, formerly the Institute of Hydrology) in Bangor, UK and data are publicly available (Neal et al., 2013). Bulk precipitation was collected at the Carreg Wen meteorological station on the border between the Hore and Hafren sub-catchments (Fig. D-1). Bulk precipitation was analyzed weekly for major and trace ions (Reynolds et al., 1997). Weirs located at the base of each sub-catchment measured streamflow and runoff every 15 min while stream water grab samples were collected weekly and analyzed for major ions (Reynolds et al., 1990). Precipitation and stream water samples were passed through a prewashed 0.45 μm filter, acidified with 1% HNO_3 and analyzed by inductively coupled optical-emission spectrometry at CEH laboratories at Plynlimon, Wallingford, Bangor and Lancaster (Neal et al., 2011). Precipitation and stream pH were measured on unfiltered samples (Reynolds et al., 1987). For this study, precipitation and stream chemistry data for the Hore (Lower Hore) and Hafren (Lower Hafren) sub-catchments were analyzed from 1984-2009, the period over which complete datasets were available for all inputs and outputs.

Watershed solute mass balance

A classic geochemical mass balance approach was used to calculate average elemental loss rates from the catchment over a 25 yr period (Garrels and Mackenzie, 1967). To determine the weathering signal for element j, the catchment solute budget was calculated as the difference between the flux of stream outputs and precipitation inputs, assuming inputs from sources other than precipitation were minimal (Reynolds et al., 1987; Drever and Clow, 1995).

Annual average precipitation input fluxes of element j ($Ip_{,j}$, mol ha^{-1} yr^{-1}) were calculated by (Reynolds et al., 2007):

$$I_{p,j} = \left(\frac{\sum C_j * P}{P_{total}}\right) * MAP \tag{1}$$

Here, a weighted average of precipitation concentration was obtained from the product of the concentration of element j (Cj, mol m^{-3}) and precipitation recorded for that period (P, mm) summed over one year, P_{total} (mm ha^{-1} yr^{-1}) and divided by the total annual precipitation. The weighted precipitation concentration was then multiplied by the mean annual precipitation (MAP) (mm) to calculate the input flux from precipitation. We assumed a density of water of 1 g cm^{-3}. Annual average output fluxes of element j (O_j, mol ha^{-1} yr^{-1}) were calculated as follows (Neal et al., 2011):

$$O_j = \left(\frac{\sum C_j * Q}{Q_{total}}\right) * R \tag{2}$$

Here, Q (m^3 s^{-1}) is stream discharge recorded during that sampling period multiplied by Cj and summed over the entire year, Q_{total} (m^3 s^{-1}) is the total annual stream discharge and R is the total annual runoff (mm ha^{-1} yr^{-1}).

A cyclic salt correction was applied to output Na, K, Ca, Mg and SO_4 concentrations by assuming Cl is a conservative tracer in the watershed and the difference between measured inputs and outputs of Cl is a result of seawater input. The following correction ratios were applied: Na, 0.553; K, 0.942; Ca, 0.990; Mg, 3.346; and SO_4, 6.691. Elemental inputs from seawater (Is,j, mol ha^{-1} yr^{-1}) were subtracted from stream output fluxes (Oj) following standard approaches (Garrels and Mackenzie, 1967; Wright and Johannessen, 1980). Average annual solute budgets (Fj) were then determined as the difference between sea salt corrected stream output fluxes (Oj) and precipitation input fluxes (Ip,j) (mol ha^{-1} yr^{-1}). Average solute budgets were averaged over 25 years and for the lowest and highest 5% of flows, representing baseflow and stormflow conditions, respectively.

Soil sampling

Soil samples were collected from a ridgetop, midslope and footslope topographic positions on a south-facing planar forested slope just outside the boundary of the Hafren sub-catchment (Figs. D-1, D-2). A 5 cm diameter hand auger was used to collect samples from the mineral soil surface, defined as 0 cm, to the depth of auger refusal, which was coincident with the depth to fractured shale bedrock at the ridgetop site. The ridgetop site was previously described in detail in Chapter 4. Soil pits were dug at each site to bedrock and described (Soil Survey Staff, 1993). At the midslope and footslope sites, examination of soil pits revealed that auger refusal was encountered short of bedrock due to large rock fragments. Thus, the bottommost samples at the midslope and footslope sites were

collected from the base of the soil pit. A sampling interval of 10 cm was used although

the rocky nature of the soils sometimes necessitated the sampling of smaller intervals.

Before auguring, the organic horizon was collected by hand. Samples were stored in

plastic bags and allowed to air dry. Soil pH was measured on all samples in a 1:1 slurry

of soil and deionized water in the laboratory (Schofield and Taylor, 1955).

Soil elemental depletion

Weathering rates using soil chemistry were calculated using the dimensionless

mass transfer coefficient, τ, which represents the ratio of an elemental concentration (C)

of an element of interest (j) in the parent rock (p) to the weathered soil (w) relative to an

immobile element (i) (Brimhall and Dietrich, 1987; Anderson et al., 2002) as follows:

$$\tau_{i,j} = \frac{C_{j,w}\,C_{i,p}}{C_{j,p}\,C_{i,w}} - 1 \qquad (3)$$

Here, a τ value of zero indicates that element j has not been enriched or depleted relative

to element j in the parent. If τ is greater than zero, then element j has been added to the

profile; if τ is less than zero, then element j has been lost from the profile compared to the

original parent composition (Brantley and White, 2009). Thus, negative τ values

throughout the profile indicate depletion of an element (depletion profile) while positive τ

values near the surface that return to 1 at depth indicate enrichment (enrichment profile)

(Brantley and Lebedeva, 2011). For all soils, parent material was defined as an average of

9 rock samples collected from outcrops on the same slope as the soil pits and one rock

sample from the bottom of the ridgetop soil pit; parent chemical data are reported in Dere

et al. (2013). Zr was used as the immobile element for all profiles (Neaman et al., 2006).

Integrating the area under the τ curve yields the total mass (M, mol m^{-2}) of element j lost or added to the weathered profile (Chadwick et al., 1990; Egli and Fitze, 2000; Brantley and Lebedeva, 2011):

$$M_j = \rho_p C_{j,p} \int_0^L \frac{\tau_j(z)}{(\varepsilon_i(z)+1)} dz \tag{4}$$

where L is the depth of the weathered soil profile, z is the sampled depth interval, ρ_p represents the bulk density of the parent and ε_i is the strain; strain values greater than zero indicate rock volume expansion during weathering processes (Brimhall et al., 1992). Soil elemental flux rates for element j (F_j) were determined by dividing M_j by the estimated SRT. Following previous workers, the SRT was estimated at 10 ky, the estimated time since deglaciation (Reynolds et al., 1987; Cadwell et al., 2004; Clark et al., 2004).

Quantitative mineralogy

Ground bulk soil samples (< 150 μm) and one rock sample from the ridgetop site were analyzed for mineralogy using x-ray diffraction (XRD) on a Scintag PAD-V powder x-ray diffractometer (Scintag, Inc. (currently Thermo Scientific), Cupertino, CA). Samples were mounted using a side loading technique to ensure randomization (Whittig and Allardice, 1986). Samples were scanned from 2° to 70° 2θ at 1° 2θ per minute using a Ge solid state detector (35 kV voltage and 30 mA current), Cu-K$_\alpha$ radiation (γ = 1.54178 Å) and a step size of 0.020° 2θ at 1° 2θ per minute. Collected peak patterns were analyzed using JADE software. Quantitative XRD was accomplished by combining 0.25 g corundum standard with 1 g of ground sample, followed by micromilling with ethanol in a McCrone mill (Eberl, 2003). Samples were then shaken with Vertrel® solution,

sieved, and randomly mounted on a side loading sample holder. Mineral abundances were quantified from the resulting XRD peaks using the USGS program RockJock (Eberl, 2003).

<div align="center">**Results**</div>

Solute fluxes

Input fluxes (Ip,j mol ha^{-1} yr^{-1}) to both the Hore and Hafren sub-catchments decrease in the order Na > Mg > K, Ca (Table D-1). While precipitation input fluxes (Ij) of Na, Mg, K and Ca can vary up to three-fold on an inter-annual basis. Input fluxes of these elements averaged over 25 yr are not highly variable (RSD <10%), except for Al and Si inputs, which exhibit the largest variability (RSD ~ 26%) (Table D-1). Input fluxes are nearly identical between sub-catchments. Similar to input fluxes, output fluxes (Oj) from both catchments are dominated by Na, Mg and Ca. However, output fluxes are also characterized by large fluxes of Si and Al that constitute < 2% of precipitation input fluxes.

All elemental budgets show larger values of output compared to input fluxes, consistent with the contribution of elements from weathering within the watershed (Table D-1). For most elements, there is minimal difference in the elemental budgets between the two sub-catchments (RSD < 18%). Ca is a clear exception, with almost two times more Ca (394 mol ha^{-1} yr^{-1}) exiting the Hore sub-catchment compared to the Hafren (210 mol ha^{-1} yr^{-1}) despite similarly small Ca inputs (150 mol ha^{-1} yr^{-1}). K fluxes, although

much smaller in magnitude (< 30 mol ha^{-1} yr^{-1}), are also two times greater in the Hore compared to the Hafren sub-catchment.

Soil profiles and elemental fluxes

Soils are shallow at all sampling sites, increasing from 35 to 62 cm from the ridgetop to the footslope (Fig. D-3, Table D-2). The bottom of all soil profiles was coincident with fractured shale bedrock and all soils contained a large volume of rock fragments (up to 40% at the bottom of the profile) (Table D-2). Soil profiles were weakly developed and dominated by sandy loam soil textures, brown to yellow-brown hues and moderately subangular blocky structure (Table D-2). A 7 – 12 cm organic layer consisting largely of moss, twigs and needles with some humified material, was observed at the top of each profile.

For the majority of elements, parent rock chemistry did not vary substantially (RSD < 14%), although low concentration elements Ca, Mn and P were highly variable (RSD = 62.3%, 48.1% and 17.7%, respectively) (Table D-3). Concentrations of most elements in rocks were similar to the bottommost sample of each soil profile (Table D-3). Ca concentrations in rocks and soils were extremely low or below detection (Table D-3).

In the soil profiles, most elements exhibited minimal variation (RSD < 10 %) with depth and between profiles. Mg concentrations were most variable with depth (RSD 22 – 41 %). Soil pH values were very acidic (pH < 3.5) and slightly lower than previously measured values in similar Stagnopodzol soil types at Plynlimon (pH = 3.43 – 4.31) (Reynolds et al., 1988). All soil profiles were only slightly depleted ($\tau < 0$) of most

elements relative to original parent composition (Fig. D-4, Table D-4). Mg was the most highly depleted element, with $60 - 80$ % depletion at the soil surface. Na, K and Al were $10 - 20$ % depleted at the soil surface and all element concentrations returned to parent composition within error at depth. Fe showed an enrichment profile ($\tau > 0$) in the ridgetop soil profile, indicating an additional input of Fe not from bedrock. In the ridgetop and footslope soils, Si depletion was not detectable but Si was up to 33% depleted in the midslope soil. Ti was roughly 30% depleted at all depths in the soils relative to Zr. Although Ti is often considered an immobile element, the observed mobility at this site supported the use of Zr as the immobile element (Gardner, 1980; Cornu et al., 1999; Neaman et al., 2006) (Table D-4).

Estimates of the elemental fluxes lost from soils (*Fj*) were highly variable and for some elements, including Si, Al, K and Ca, *Fj* was zero (within error) at ridgetop and footslope sites (Table D-1). Soil elemental fluxes of Mg (M_{Mg}, Eq. 2) increased downslope, from 77.2 ± 17.4 mol Mg ha^{-1} yr^{-1} in the ridgetop soil to 137 ± 19.5 mol Mg ha^{-1} yr^{-1} and 174 ± 17.7 mol Mg ha^{-1} yr^{-1} in the midslope and footslope profiles, respectively. The flux of Na was similar in the ridgetop and midslope profiles (~ 20 mol Na ha^{-1} yr^{-1}) and zero within error in the footslope profile. The midslope profile exhibited the largest fluxes of Si, Fe, Al and K of all sites. We also observed a net addition of Fe to the ridgetop soil profile.

Discussion

Weathering reactions

The dominant weathering reactions at Plynlimon are the breakdown of 'chlorite' and illite through intermediate vermiculite and hydroxyl-interlayered vermiculite (HIV) phases to kaolinite and iron oxides (Chapman, 1986) (Table D-5). Here, the term 'chlorite' encompasses chlorite, vermiculite, HIV and interstratified chlorite-vermiculite mineral phases. Previous detailed rock and soil mineralogical investigations at Plynlimon reported that in unweathered shale, 'chlorite' contains on average 15% HIV and is most commonly observed as a mixture of true chlorite and HIV (Chapman, 1986). The mean 'chlorite' composition at Plynlimon was reported as (Chapman, 1986):

$$(Fe_{5.47}Mg_{2.61}Al_{3.53}Ti_{0.01}K_{0.08})(Si_{5.16}Al_{2.84})O_{20}(OH)_{16} + 1.21\ H_4SiO_{4\ (aq)} + 0.16\ H^+ \rightarrow$$

$$5.47\ FeOOH_{(s)} + 2.61\ Mg^{2+} + 0.08\ K^+ + 0.01\ Ti^{4+} + 3.185\ Al_2Si_2O_5(OH)_{4\ (s)} + 1.235\ H_2O \quad (3)$$
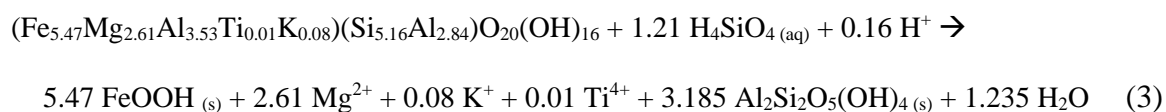
Here, 'chlorite' weathering releases Mg, K and a small amount of Ti to solution as written in Eq. 3. The dissolution of 'chlorite' also releases Fe as a solute which may precipitation as an iron oxide mineral. Al and Si can be transformed to kaolinite, but previous work at Plynlimon demonstrated that 'chlorite' initially weathers to HIV and then to trioctahedral vermiculite, which in turn dissolves or is altered to a non-crystalline phase (Chapman, 1986). During weathering processes in the soil, 'chlorite' loses the hydroxy interlayers to form a true vermiculite. Chapman (1986) also argued that vermiculite weathers rapidly in the soils at Plynlimon, leaving evidence of only small quantities of vermiculite in soils even though both 'chlorite' and illite pass through a vermiculite phase.

Previous studies of the stratigraphic equivalent Rose Hill shale at the Susquehanna Shale Hills Critical Zone Observatory (SSHO) in central Pennsylvania, USA, also showed that the 'chlorite' in shale includes vermiculite and hydroxyl-interlayered vermiculite (HIV) (Jin et al., 2010). Based on the characterization of the Rose Hill shale by Jin et al., (2010), a weathering reaction for 'chlorite' at SSHO was described as:

$$(Fe_{0.24}Mg_{0.38}Al_{0.38})_6(Si_{0.07}Al_{0.93})_4O_{10}(OH)_{8\ (s)} + 5.72\ H_4SiO_{4\ (aq)} + 4.56\ H^+ \rightarrow$$

$$1.44\ FeOOH_{\ (s)} + 2.28\ Mg^{2+} + 3\ Al_2Si_2O_5(OH)_{4\ (s)} + 11\ H_2O \qquad (4)$$
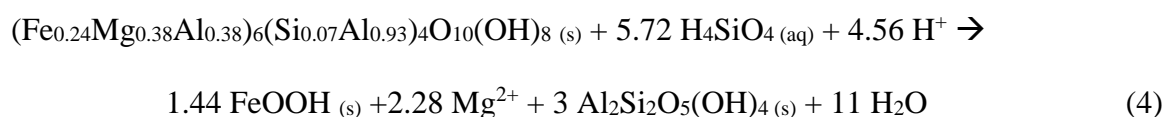
The SSHO 'chlorite' composition is similar to Plynlimon with respect to Mg and Al. The most notable difference in the 'chlorite' compositions is Fe. Iron constitutes a much larger fraction of the Plynlimon 'chlorite' (5.47) compared to the SSHO 'chlorite' (1.44) yet total Fe concentrations are only slightly larger in the Plynlimon shale ($6.44 \pm 0.31\%$) compared to the SSHO shale ($5.50 \pm 0.19\%$) (Jin et al., 2010). At SSHO, Yesavage et al. (2012) reported that ~22% of total Fe in the shale was in 'chlorite' and 10% of total Fe was found in (oxyhydr)oxide minerals; the remaining Fe was found in illite minerals.

In the soils, Yesavage et al. (2012) similarly concluded that ~20% of total Fe in the soils was found in 'chlorite', which is similar to the total Fe content in 'chlorite' in the parent shale (22%). Thus it appears little Fe has been lost from 'chlorite' at SSHO, consistent with the observation of minimal differences in 'chlorite' content in the bedrock and the soils (< 3 wt %). At Plynlimon, however, 'chlorite' content decreases from 25% in the rock to 15% in the upper soil, pointing to the loss of 'chlorite' as weathering occurs in the soil (Table D-5). Given that iron oxides only represent ~3% of the bulk mineralogy

in the upper soil horizon, it appears the majority of the Fe weathered from 'chlorite' is dissolved rather than precipitated as iron oxides at this site.

Chapman (1986) also determined a mean illite composition for shale at Plynlimon:

$$K_{1.71}(Fe_{0.27}Mg_{0.19}Al_{3.69}Ti_{0.04})(Si_{6.16}Al_{1.84})O_{20}(OH)_{4\ (s)} + 7.945\ H_2O \rightarrow$$

$$1.71\ K^+ + 0.27\ FeOOH_{\ (s)} + 0.19\ Mg^{2+} + 0.04\ Ti^{4+} + 2.765\ Al_2Si_2O_5(OH)_{4\ (s)} + 0.63\ H_4SiO_{4\ (aq)} +$$

$$6.04\ H^+ \tag{5}$$
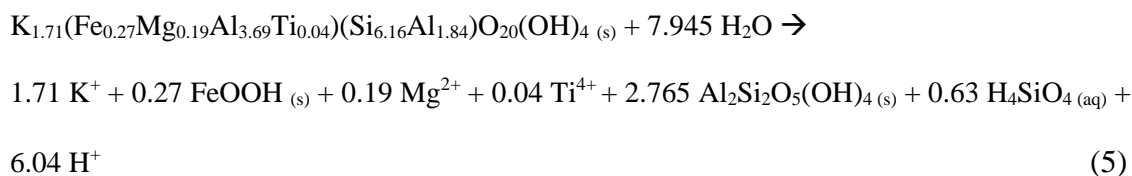
The dissolution of illite results in smaller losses of Mg ions than are lost from 'chlorite' and a small quantity of Ti. In addition, iron (oxyhydr)oxides and kaolinite can precipitate. Potassium, which is not present in 'chlorite' minerals, is also dissolved. In contrast to 'chlorite', illite in the Plynlimon shale transforms to vermiculite via an interstratified illite-vermiculite rather than via HIV (Chapman, 1986).

In contrast, the illite composition at SSHO was determined to be (Jin et al., 2010):

$$K_{0.77}(Fe_{0.48}Mg_{0.07}Al_{0.45})_6(Si_{0.30}Al_{0.70})AlSi_3O_{10}(OH)_{2\ (s)} + 3.235\ H_2O + 0.91\ H^+ \rightarrow$$

$$0.77\ K^+ + 0.48\ FeOOH_{\ (s)} + 0.07\ Mg^{2+} + 1.075\ Al_2Si_2O_5(OH)_{4\ (s)} + 1.15\ H_4SiO_{4\ (aq)} \tag{6}$$
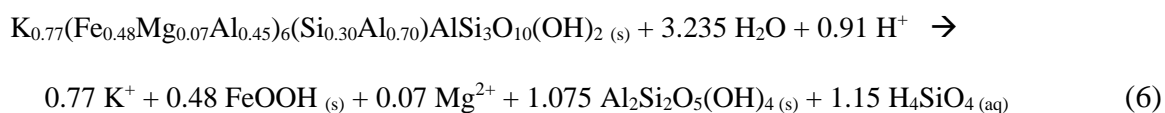
Fe in illite as reported by Jin et al. at SSHO is roughly 10 times greater and Mg two times greater than illite at Plynlimon. At SSHO, almost half of the total Fe in the soils is found in illite (Yesavage et al., 2012). Conversely, K is two times greater in Plynlimon illite compared to SSHO illite. However, parent shale K concentrations are slightly lower at Plynlimon compared to SSHO (2.90 ± 0.13 and 3.76 ± 0.16 wt%, respectively). Jin et al. (2010) identified that roughly 2% of the Mg concentrations and almost 100% of the dissolved K measured in streamwater chemistry at this site came from illite. In Plynlimon

soils, illite content does not vary from the bedrock to the soils while at SSHO illite decreases from ~60% in the shale to ~30% in the soils.

Thus, shale weathering at these two sites appear to be opposite: 'chlorite' dominates weathering at Plynlimon, while illite dominates weathering at SSHO. At Plynlimon, the transformation of 'chlorite' to HIV was observed at the bedrock-soil interface (49 cm below the surface) while illite transformation was not observed until 16 cm below the land surface (Chapman, 1986). Based on these observations, Chapman (1986) concluded that 'chlorite' weathering occurs at deeper depths and more rapidly than illite weathering. Conversely, at SSHO, Jin et al. (2010) concluded that 'chlorite' and illite dissolution occurred congruently and was initiated at ~50 cm below the soil surface within fractured shale bedrock underlying the soil. Interestingly, iron oxide content is similar between SSHO and Plynlimon soils but the Fe is weathered largely from illite at SSHO and 'chlorite' at Plynlimon, suggesting different shale weathering pathways at these sites.

Na loss in the catchments can be attributed to the dissolution of plagioclase as follows:

$$2NaAlSi_3O_8 + 2H_2CO_{3\,(aq)} + 9H_2O \rightarrow Al_2Si_2O_5(OH)_{4\,(s)} + 2Na^+ + 2HCO_3^- + 4H_4SiO_4 \qquad (7)$$
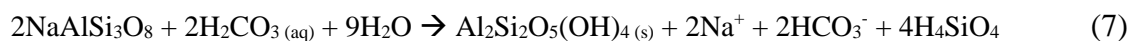
followed by the dissolution of kaolinite:

$$Al_2Si_2O_5(OH)_{4\,(s)} + 6H^+ \rightarrow 2Al^{3+} + 2H_4SiO_4 + H_2O \qquad (8)$$

resulting in the release of Na^+ and Al^{3+} ions in a roughly 1:1 molar ratio. It is assumed that Na is not precipitated in secondary minerals or taken up by biota, therefore the loss of Na from the catchment is inferred to result from plagioclase dissolution. The bulk

mineralogy of the shale contains roughly 4% plagioclase and approximately 6% kaolinite in the upper soil horizons (Table D-5); therefore both minerals are low in abundance.

Watershed fluxes

Fluxes reported here using 25 years of data from Plynlimon are similar in magnitude to previously published values in the same catchments, although variability is much lower. Reynolds et al. (1997) estimated base cation weathering rates using solute mass balance over a two year period (1987 and 1988). The authors reported that for some elements, such as Mg, solute budgets (226 mol Mg ha^{-1} yr^{-1}) were in good agreement with previous weathering studies at Plynlimon (Reynolds et al., 1987, 1989; Durand et al., 1994). Fluxes reported here for a 25 year period are similar to these previously reported fluxes (203 – 221 mol Mg ha^{-1} yr^{-1}) (Table D-1). However, fluxes of highly variable elements such as Na varied from 104 to 452 mol Na ha^{-1} yr^{-1} in the aforementioned studies (Reynolds et al., 1989; Reynolds et al., 1997), values that are up to three times greater than our calculations using 25 years of data. Reasons for this discrepancy include variations in annual climate, such as large storms or drought years, which can introduce an imbalance in the geochemical budgets of the catchment (Reynolds et al., 1987) (Fig. D-8). Therefore the long term dataset is necessary to constrain error in solute budgets for highly variable elements; short-term measurements introduce significantly more error in the budget calculations.

Soil weathering fluxes

Measurements of soil elemental chemistry at all topographic positions show approximately 60 - 80% depletion of Mg at the soil surface relative to original shale concentrations (Fig. D-3, Table D-3), consistent with the loss of Mg through 'chlorite' dissolution. Na is also depleted in the ridgetop and midslope soil profiles, with approximately 25% depletion at the soil surface (Fig. D-3, Table D-3) and is attributed to the dissolution of plagioclase as discussed above. All depletion profiles are incompletely developed, meaning elements are not 100% depleted at the land surface (Lebedeva et al., 2007; Brantley and White, 2009). Incompletely developed profiles can result from the loss of elements to solution or the dissolution then re-precipitation of an element, keeping soil concentrations greater than zero at the land surface. Incompletely developed profiles are consistent with kinetically limited weathering regimes, where material is transported out of the system before complete weathering occurs – this happens when erosion rates are fast and mineral dissolution rates are relatively slow (Brantley and Lebedeva, 2011). Such an interpretation has been made for shale weathering at the PA SSHO (Jin et al., 2010) and at sites across the Appalachians Mountains in the eastern USA (Dere et al., 2013). Reaction fronts in kinetically limited systems are often shallow, as observed here, and based on this observation, soil pore water is not likely in equilibrium with the reacting minerals in the regolith profile (Brantley and Lebedeva, 2011).

Both Si and Al, which are released during the weathering of clay minerals, show no depletion or enrichment within error as a function of depth in the ridgetop and footslope profiles (Fig. D-3, Table D-3). Biogenic Si cycling could play a role in

dampening the weathering signal of this element. However, no biogenic weathering profiles were observed: in biogenic profiles, biogenic cycling causes elements to become concentrated near the surface relative to original bedrock composition and depleted in the root zone (Brantley and White, 2009; Cornelis et al., 2011). In other words, Si and Al may be dissolving from clay minerals but re-precipitating in secondary minerals or taken up by biota such that the record of depletion is not recorded in the soil chemistry over the short time that the soils have been weathering (< 10 ky).

The midslope soil profile shows a higher extent of depletion at the land surface for most elements compared to the ridgetop and footslope soils, especially Mg, Al, Si and K (Fig. D-3, Table D-3). Similarly, midslope elemental fluxes for these elements are greater than at the ridgetop and footslope sites, consistent with higher weathering fluxes on this position (Table D-1). Enhanced weathering on the midslope position has also been observed in the central PA SSHO, where midslope soils are more depleted of all major weathering elements (Mg, Al, Si, Fe, K) compared to the ridgetop soil (Jin et al., 2010). The midslope soil, however, was collected downslope from a harvesting that occurred in 2005, one year prior to our sampling. This harvesting could have impacted the midslope profile chemistry (Fig. D-2).

Watershed vs. soil weathering fluxes

Weathering fluxes (mol ha^{-1} yr^{-1}) calculated using a watershed or soil profile mass balance approach are not the same (Table D-1). Assuming that Na and Mg loss from the soils or streams represents plagioclase and 'chlorite' weathering, respectively, this means

that measured weathering rates are higher when using a watershed mass balance approach compared to soil chemical profiles. The observed rate discrepancy is likely related to the differences in the method of calculating surface area between the watershed and soil profile. This discrepancy is attributed to using different "rulers" to measure surface areas at the watershed and pedon scales (Navarre-Sitchler and Brantley, 2008). In other words, the different weathering fluxes measured from the two approaches is a function of different surface area. Navarre-Sitchler and Brantley (2008) suggest that weathering advance rates at the watershed scale should be approximately 47 times faster than pedon scale rates, which is approximately seven times larger than the discrepancy observed here.

The ratios of elemental fluxes (mol ha^{-1} yr^{-1}) provide information about the stoichiometry of weathering reactions occurring within the watershed. Here, we compare Na and Mg elemental fluxes of Al and Si from soils or streams to infer mineral weathering reactions (Fig. D-5). In the case of Na, the proxy for plagioclase weathering, the ratio of Na to Al fluxes differs between the soils and stream waters (Fig. D-5). In the Hore and Hafren streams, the ratio of Na:Al lies between 1:1 and 1:2. This ratio is similar to the ratio derived from the complete dissolution of plagioclase (Eqs. 7 and 8). Ratios from the soil samples, however, approach infinity as the Al and Si flux from soils is zero within error (Fig. D-4). Therefore we cannot conclude weathering reactions from the stoichiometry of the soil chemistry in the ridgetop and footslope soils. The loss of Na and Mg from the soils, however, points to the dissolution of plagioclase and 'chlorite', respectively.

In the case of Mg:Al ratios, the Hore and Hafren ratios fall on the 1:1 line; for every mol of Mg lost, one mol of Al is also lost (Fig. D-5). This ratio could be attributed to the dissolution of one mol of 'chlorite' and the production of two mols of kaolinite, as in Eq. 3. Alternately, this could indicate that 'chlorite' is weathering to vermiculite or HIV, which is a more likely series of weathering reactions based on previous mineralogical analyses (Chapman, 1986). Soil Mg:Al ratios are closer to those derived from the watershed mass balance, but again soil Al fluxes are zero and an interpretation of the weathering reactions is difficult from the stoichiometry alone. The midslope soil profile is the exception, with high losses of Na and Mg relative to ridgetop and footslope soils (Fig. D-5).

An activity-activity diagram shows that under low flow conditions, the Hore and Hafren stream water are in equilibrium with respect to kaolinite, perhaps suggesting deeper weathering reactions contributing to the stream chemistry during baseflow conditions (Fig. D-6 and D-7). Under high flow conditions, stream water chemistry moves toward supersaturation with respect to kaolinite.

References

Anderson, S. P., Dietrich W. E., Brimhall G. H. (2002) Weathering profiles, mass-balance analysis, and rates of solute loss: Linkages between weathering and erosion in a small, steep catchment. *Geol. Soc. Amer. Bull.* **114**:1143-1158.

Brantley, S. L., Goldhaber M. B., and Ragnarsdottir K. V. (2007) Crossing disciplines and scales to understand the critical zone. *Elements* **3**:307–314.

Brantley, S. L. and Lebedeva M. (2011) Learning to read the chemistry of the regolith to understand the critical zone. *Annu. Rev. Earth Planet. Sci.* **39**:387-416.

Brantley, S. L. and White A. F. (2009) Approaches to modeling weathered regolith. *Rev. in Miner. Geochem.* **70**:435-484.

Breward, N. (1990) Geochemical cycling processes involving major and trace elements at Plynlimon, mid-Wales. Ph.D. Dissertation. The University of Leeds.

Brimhall, G. H. and Dietrich W. E. (1987) Constitutive mass balance relations between chemical composition, volume, density, porosity, and strain in metasomatic hydrochemical systems: Results on weathering and pedogenesis. *Geochim. Cosmochim. Acta* **51**:567-587.

Chadwick, O. A., Brimhall G. H., and Hendricks D. M. (1990) From a black to a gray box – a mass balance interpretation of pedogenesis. *Geomorph.* **3**:369-390.

Chapman, P. (1986) Geochemical and mineralogical studies of the weathering of Silurian argillaceous rocks. Ph.D. Dissertation. University of North Wales, Bangor.

Chapman, P. J., Clark J. M., Reynolds B. and Adamson J. K. (2008) The influence of organic acids in relation to acid deposition in controlling the acidity of soil and stream waters on a seasonal basis. *Environ. Poll.* **151**:110-120.

Cornu S., Lucas Y., Lebon E., Abrosi J. P., Luizao F., Rouiller J., Bonnay M. and Neal C. (1999) Evidence of titanium mobility in soil profiles, Manaus, central Amazonia. *Geoderma* **91**:281-295.

Cuttle, S. P. (1983) Chemical properties of upland peats influencing the retention of phosphate and potassium ions. *J. Soil Sci.* **34**:75-82.

Dere, A. L., White T. S., April R. H., Reynolds B., Miller T. E., Knapp E. P., McKay L. D. and Brantley S. L. (2013) Climate dependence of feldspar weathering along a latitudinal gradient. *Geochim. Cosmochim. Acta.* **122**:101-126.

Drever, J.L. (2003) The Geochemistry of Natural Waters. Prentice Hall, NJ.

Durand, P., Neal C., Jeffrey H. A., Ryland G. P. and Neal M. (1994) Major, minor and trace element budgets in the Plynlimon afforested catchments (Wales): general trends and effects of felling and climate variations. *J. Hydrol.* **157**:139-156.

Eberl, D. D. (2003) User's guide to RockJock – a program for determining quantitative mineralogy from powder x-ray diffraction data. U.S. Geological Survey, Open-file report 03-78.

Egli M. and Fitze P. (2000) Formulation of pedogenic mass balance based on immobile elements: a revision. *Soil Sci.* **165**:437-443.

Ferrier K. L., Kirchner J. W., Riebe C. S. and Finkel R. C. (2010) Mineral-specific chemical weathering rates over millennial timescales: Measurements at Rio Icacos, Puerto Rico. *Chem. Geol.* **277**:101-114.

Garrels R. M. and Mackenzie F. T. (1967) Origin of the chemical compositions of some springs and lakes. *In*: Equilibrium concepts in natural water systems. Advances in Chemistry. (Ed.) Strumm W. ACS, Washington, D.C.

Godsey S. E., Kirchner J. W., Clow D. W. (2009) Concentration-discharge relationships reflect chemostatic characteristics of US catchments. *Hydrol. Process.* **23**:1844-1864.

Hillier S. (2000) Accurate quantitative analysis of clay and other minerals in sandstones by XRD: comparison of a Rietveld and a reference intensity ratio (RIR) method and the importance of sample preparation. *Clay Min*. **35**:291-302.

Hughes S., Reynolds B. and Roberts J. D. (1990) The influence of land management on concentrations of dissolved organic carbon and its effects on the mobilization of aluminium and iron in podzol soils in Mid-Wales. *Soil Use and Manage*. **6:**137-145.

Jenny H. (1941) Factors of soil formation. McGraw Hill, NY. 281 p.

Jin, L., Ravella R., Ketchum B., Heaney P., and Brantley S. L. (2010) Mineral weathering and elemental transport during hillslope evolution at the Susquehanna/Shale Hills Critical Zone Observatory. *Geochim. Cosmochim. Acta* **74**:3669-3691.

Lebedeva M. I., Fletcher R. C., Balashov V. N. and Brantley S. L. (2007) A reactive diffusion model describing transformation of bedrock to saprolite. *Chem. Geol*. **244**:624-645.

Medlin, J. H., Suhr N. H. and Bodkin J. B. (1969) Atomic Absorption Analysis of Silicates Employing LiBO2 Fusion. *Atomic Absorption Newsletter* **8**:25-29.

Neal, C., Kirchner, J., Reynolds, B. (2013) Plynlimon research catchment hydrochemistry. NERC-Environmental Information Data Centre. DOI: 10.5285/44095e17-43b0-45d4-a781-aab4f72da025.

Neal, C., Reynolds B., Norris D., Kirchner J. W., Neal M., Rowland P., Wickham H., Harman S., Armstrong L., Sleep D., Lawlor A., Woods C., Williams B., Fry M., Newton G. and Wright D. (2011) Three decades of water quality measurements from the Upper Severn experimental catchments at Plynlimon, Wales: and openly accessible data resource for research, modelling, environmental management and education. *Hydrol. Process*. DOI:10.1002/hyp.8191.

Reynolds, B., Fowler D, Smith R. I. and Hall J. R. (1997) Atmospheric inputs and catchment solute fluxes for major ions in five Welsh upland catchments. *J. Hydrol.* **194:**305-329.

Reynolds, B., Hornung M. and Hughes S. (1989) Chemistry of streams draining grassland and forest catchments at Plynlimon, mid-Wales. *Hydrol. Sci. J*. **4**:667-686.

Reynolds, B., Hornung M. and Stevens P. A. (1987) Solute budgets and denudation rate estimates for a mid-Wales catchment. *Catena* **14**:13-23.

Reynolds, B., Neal C., Hornung M., Hughes S. and Stevens P. A. (1988) Impact of afforestation on the soil solution chemistry of stagnopodzols in mid-Wales. *Water, Air and Soil Poll*. **38:**55-70.

Schofield, R. K. and Taylor A. W. (1955) The measurement of soil pH. *Soil Sci. Soc. Amer. Proc.* **19**:164-167.

Shand P., Haria A. H., Neal C., Griffiths K. J., Gooddy D. C., Dixon A. J., Hill T., Buckley D. K. and Cunningham J. E. (2005) Hydrochemical heterogeneity in an upland catchment: further characterization of the spatial, temporal and depth

variations in soils, streams and groundwaters of the Plynlimon forested catchment, Wales. *Hydrol. Earth Syst. Sci.* **9**:621-644.

Soil Survey Staff (1993) National Soil Survey Handbook, Title 430-VI. U.S. Govt. Printing Office, Washington, D.C.

Stevens P. A., Reynolds B., Hughes S., Norris D. A. and Dickinson A. L. (1997) Relationships between spruce plantation age, solute and soil chemistry in the Hafren forest. *Hydrol. Earth Syst. Sci*. **1**:627-637.

White, A. F. and Blum A. E. (1995) Effects of climate on chemical weathering in watersheds. *Geochim. Cosmochim. Acta* **59**:1729-1747.

White, A. F., Blum A. E., Bullen T. D., Vivit D. V., Schulz M., and Fitzpatrick J. (1999) The effect of temperature on experimental and natural chemical weathering rates of granitoid rocks. *Geochim. Cosmochim. Acta* **63**:3277-3291.

White, A. F., Bullen T. D., Schulz M. S., Blum A. E., Huntington T. G. and Peters N. E. (2001) Differential rates of feldspar weathering in granitic regolith. *Geochim. Cosmochim. Acta* **65**:847-869.

Whittig, L. D. and Allardice W. R. (1986) X-ray diffraction techniques. *In*: Methods of Soil Analysis, Part 1: Physical and Mineralogical Methods. (Ed.) Klute A. Soil Sci. Am. Book Series No. 9. ASA and SSSA, Madison, WI.

Yesavage T., Fantle M. S., Vervoort J., Mathur R., Jin L., Liermann L. J. and Brantley S. L. (2012) Fe cycling in the Shale Hills Critical Zone Observatory, Pennsylvania: An analysis of biogeochemical weathering and Fe isotope fractionation. *Geochim. Cosmochim. Acta* **99**:18-38.
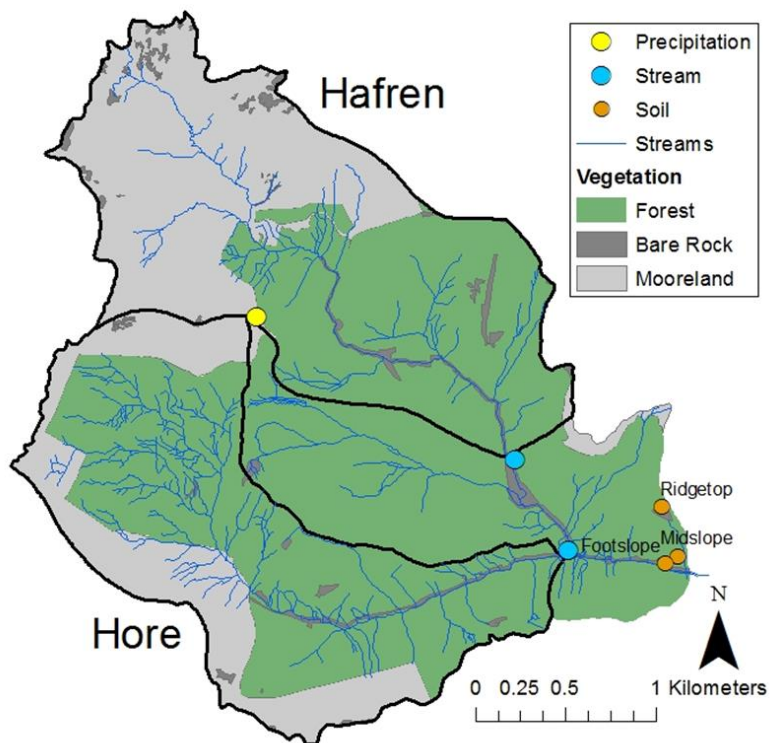
Figures

Figure D-1. Map of the Hafren and Hore sub-catchments at Plynlimon with precipitation, stream and soil sampling locations and dominant vegetation types.
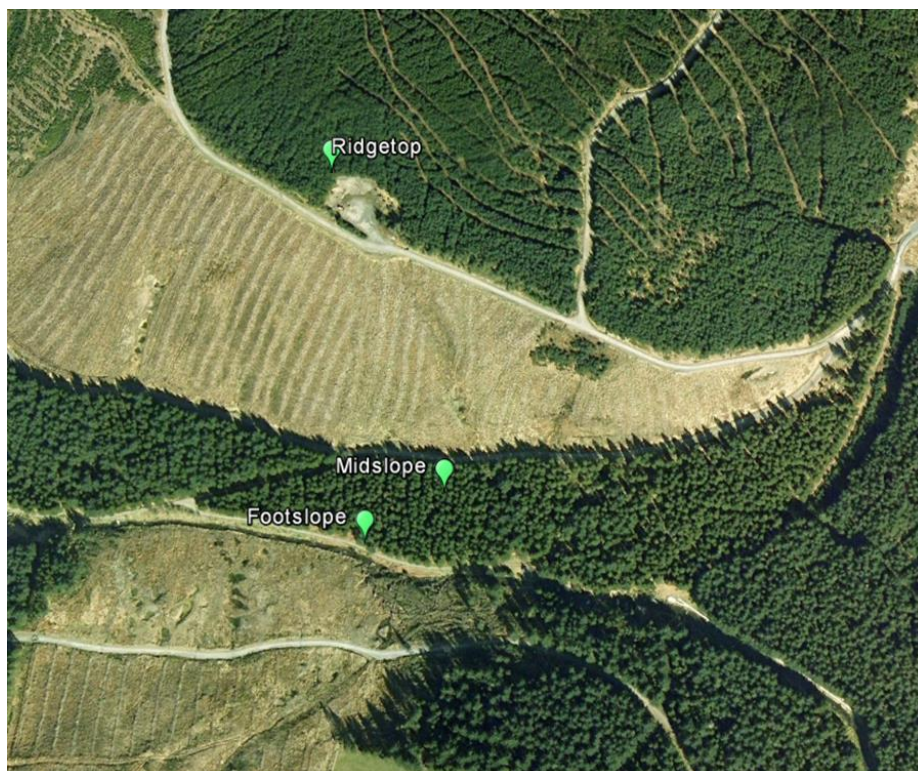
Figure D-2. Google Earth image showing the area of the slope clear cut in 2005, one year prior to soil sampling, indicated by the green dots. Distance between Ridgetop and Footslope sampling points is approximately 300 m.
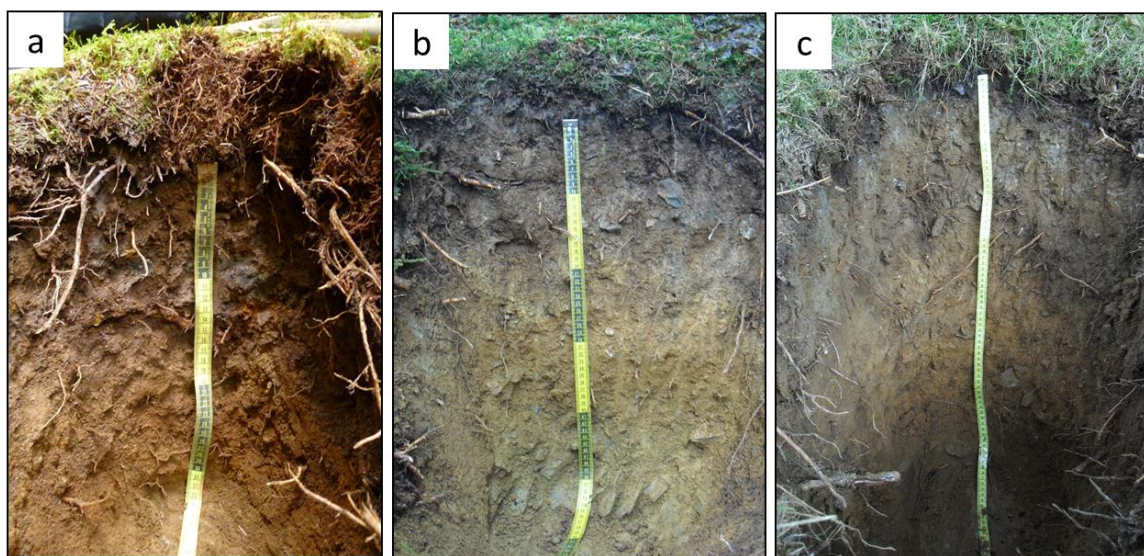
Figure D-3. Soil profiles from the ridgetop (a), midslope (b) and footslope (c) topographic positions on a planar hillslope in the Plynlimon forest. The color of the ridgetop photo is influenced by the dark lighting within the forest at this location; the lower forest density on the slope meant lighting conditions did not differ substantially between the midslope and footslope soils. The ridgetop soil was only slightly darker in color than the midslope or footslope soils (see profile descriptions in Table D-2).
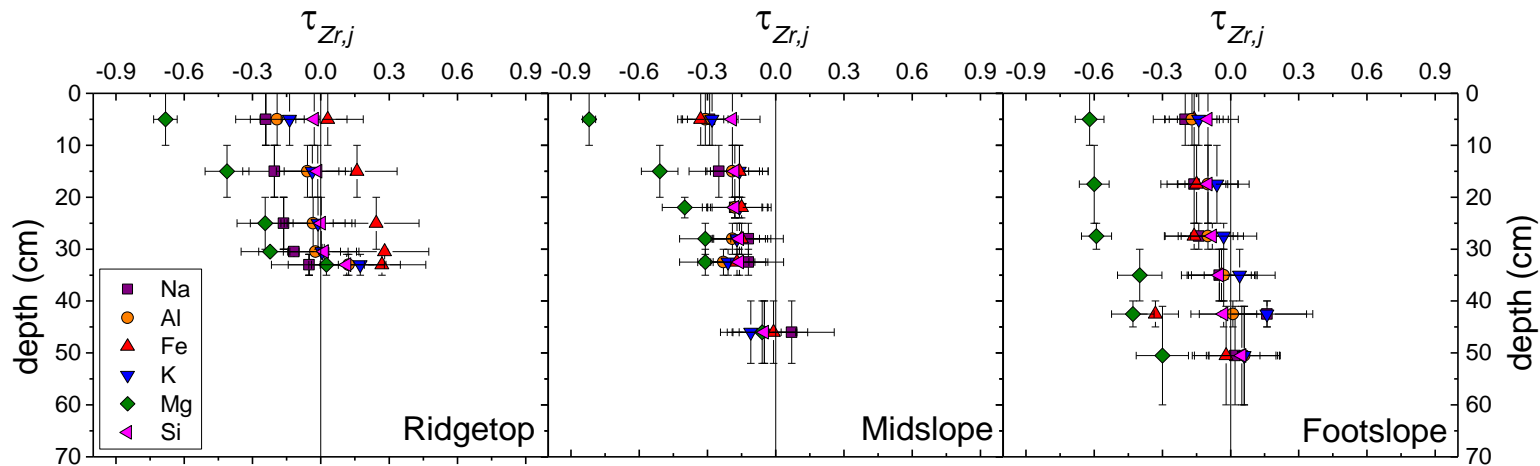
Figure D-4. Ridgetop, midslope and footslope soil τ depth profiles using Zr as the immobile element and an average of 10 rock samples as parent material. Elements return to parent composition at all hillslope positions except for Mg in the footslope profile and Fe in the ridgetop profile, which shows enrichment. In the footslope profile, Mg does not return to parent at depth and implies deeper Mg loss than observed in the soil (i.e. 'chlorite' begins dissolving at depth). In contrast, 'chlorite' weathering at SH starts in the fractured bedrock ~50 cm below soil surface, ~20 cm past augerable depth.
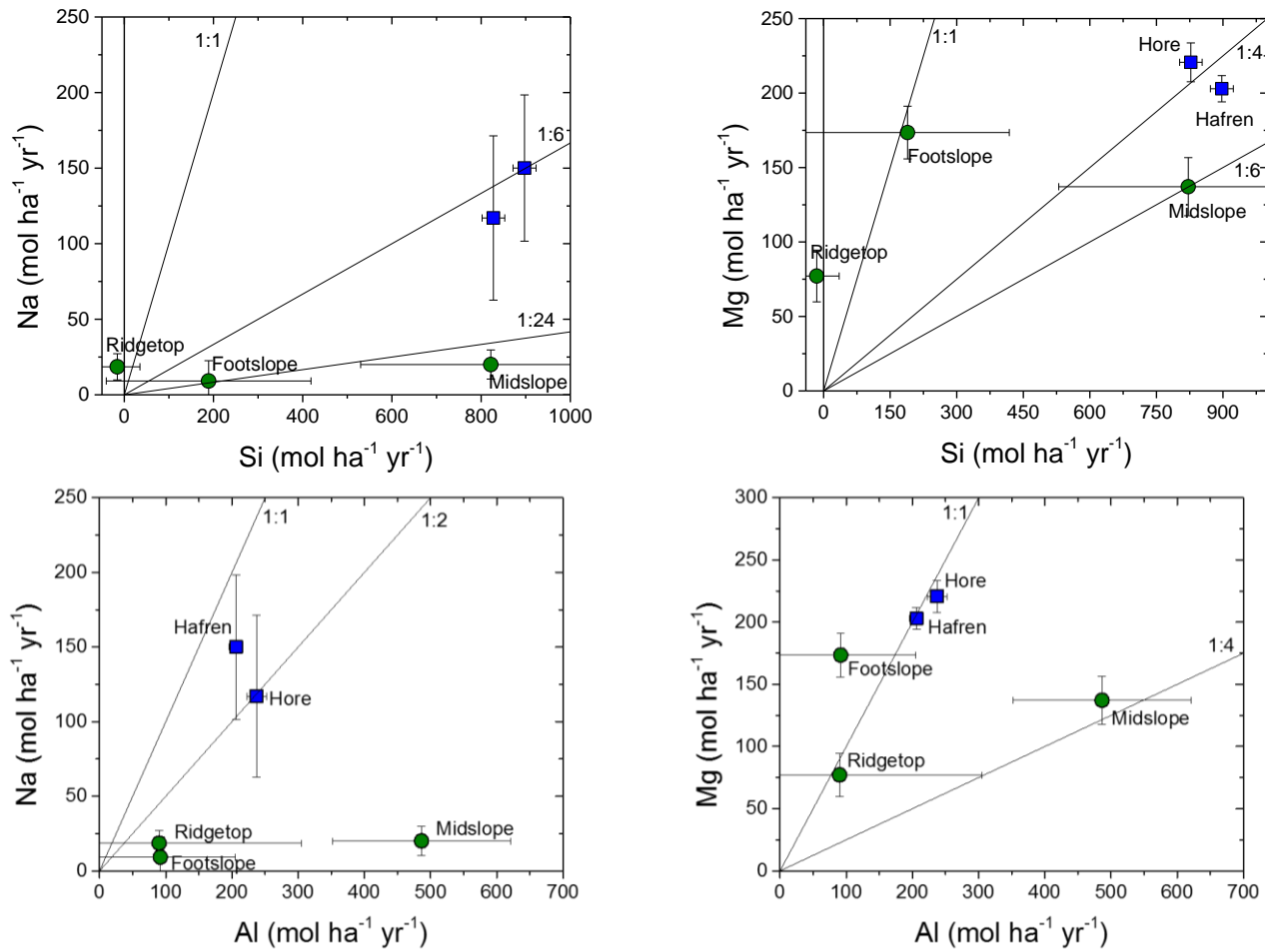
Figure D-5. Ratios of Na:Si, Mg:Si, Na:Al and Mg:Al loss recorded in stream budgets (Hore and Hafren, blue squares) and soil elemental profiles on ridgetop, midslope and footslope positions (green circles).
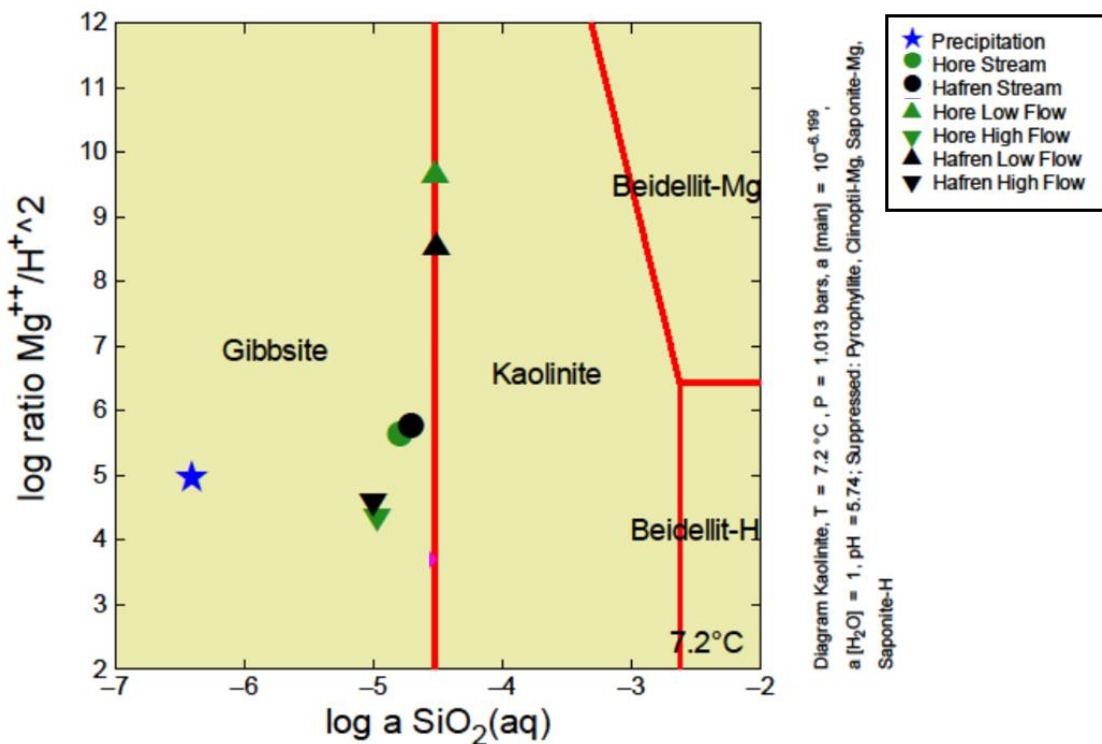
Figure D-6. Activity-activity diagram for precipitation, Hore and Hafren stream waters at Plynlimon. Hore and Hafren streams refer to the average stream composition at all flow conditions while high and low flow represents the highest and lowest 5% of flow conditions. Temperature was set as the mean annual temperature (MAT) at Plynlimon. Diagram was created using Geochemist's Workbench® software.
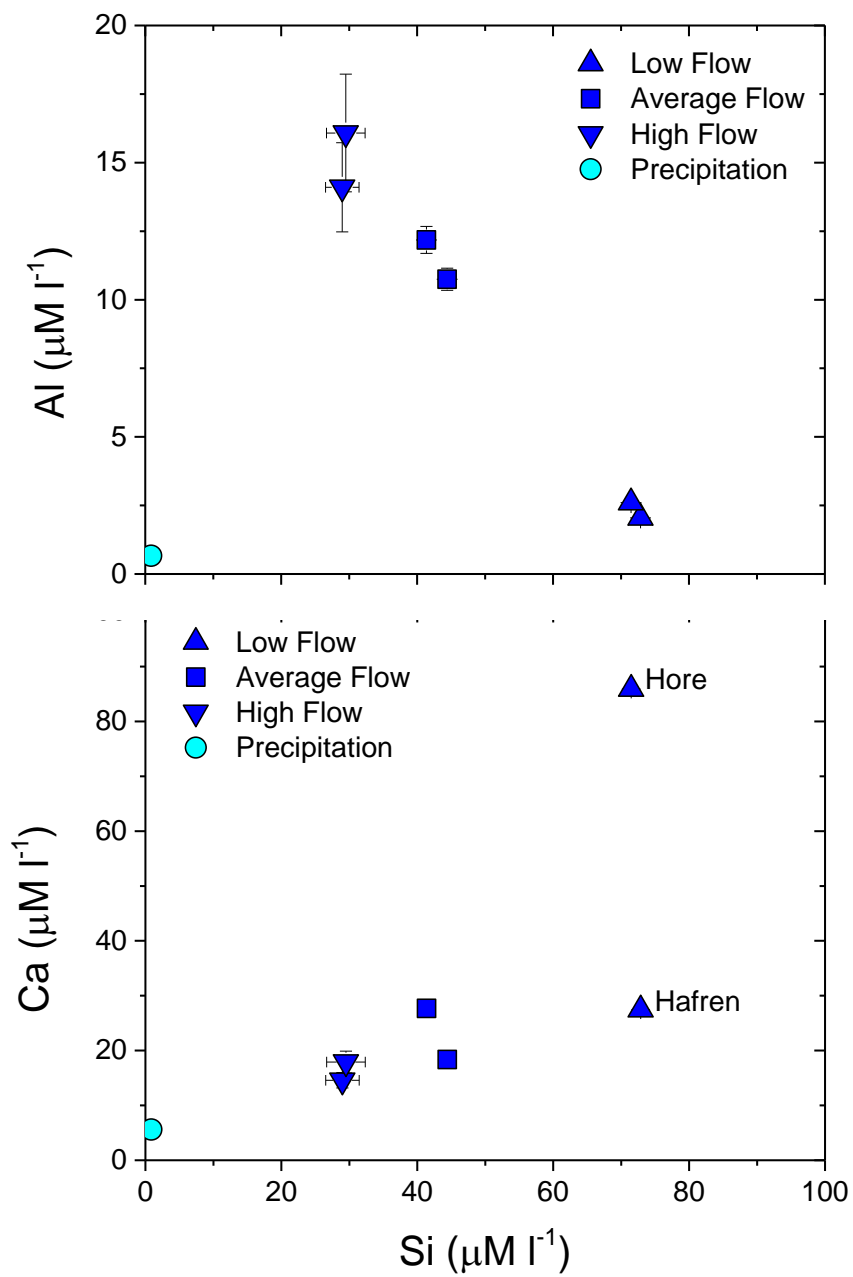
Figure D-7. Al, Ca and Si concentrations for precipitation and the lowest 5% (low flow), average and highest 5% (high flow) of flows from the Hore and Hafren streams.
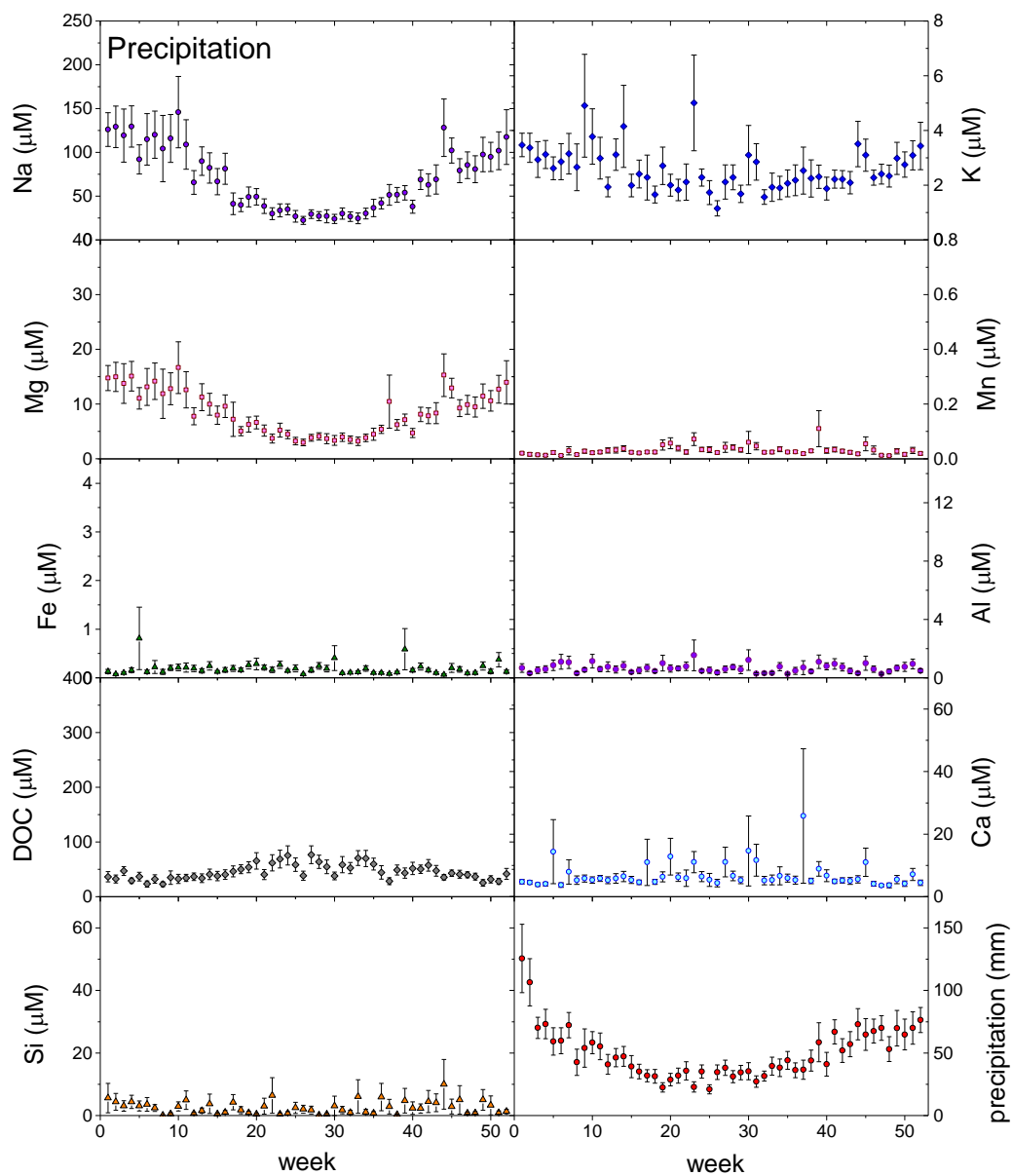
Figure D-8. Seasonality of precipitation chemistry in the Plynlimon forest.

Tables

Table D-1. Elemental fluxes (F*j*) calculated from soil profiles on ridgetop, midslope and footslope topographic positions and from the solute budgets of the Lower Hafren and Lower Hore streams (Outputs – Inputs). Budgets are corrected for sea salt input using Cl as a conservative element; inputs of Al, Fe and Si in sea salt are assumed to be negligible. Negative values indicate an additional flux of elements into the soil, positive values indicate a net flux of an element out of the catchment. Standard errors around the mean are reported.

Site	F*j*						
	Na	Mg	K	Ca	Al	Fe	Si
	mol ha^{-1} yr^{-1}						
Soils							
Ridgetop	18.5 ± 8.65	77.2 ± 17.4	6.48 ± 64.2	0.850 ± 0.921	90.0 ± 215	-74.4 ± 30.4	-15.5 ± 50.6
Midslope	20.1 ± 9.61	137 ± 19.5	85.9 ± 25.9	---	486 ± 135	102 ± 37.5	822 ± 292
Footslope	9.20 ± 13.4	174 ± 17.7	-4.10 ± 58.9	---	91.7 ± 113	83.3 ±32.0	189 ± 229
Hafren							
Inputs (*Ip,j*)	2590 ± 172	305 ±20.4	75.9 ± 4.02	149 ± 15.1	17.7 ± 4.36	3.62 ± 0.324	21.2 ± 5.84
Sea salt inputs (*Is,j*)	913	111	19.4	19.9	---	---	---
Outputs (*Oj*)	3660 ± 131	619 ± 18.4	109 ± 5.15	379 ± 9.24	224 ± 10.5	47.2 ± 2.71	919 ± 25.2
Total budget	150 ± 48.4	203 ± 8.81	13.5 ± 3.87	210 ± 15.2	206 ± 10.2	43.6 ± 2.62	897 ± 25.8
Hore							
Inputs (*Ip,j*)	2610 ± 172	307 ± 20.5	76.4 ± 4.02	150 ± 15.1	17.7 ± 4.35	3.64 ± 0.322	21.3 ± 5.89
Sea salt inputs (*Is,j*)	993	121	21.1	21.6	---	---	---
Outputs (*Oj*)	3720 ± 149	647 ± 22.4	126 ± 10.4	566 ± 14.8	255 ± 14.9	41.2 ± 3.08	849 ± 24.4
Total budget	117 ± 54.4	221 ± 13.0	28.6 ± 10.6	394 ± 17.2	237 ± 14.7	37.6 ± 2.98	828 ± 25.3

Table D-2. Soil profile descriptions for ridgetop, midslope and footslope topographic positions at Plynlimon. Depth is the bottom horizon, with d = 0 cm the mineral soil surface; positive (+) depth indicates organic depth above d = 0 cm. Rock fragment (RF) is percent by volume. Structure was either granular (gr) or subangular blocky (sbk) and moderately strong (mod) or weak.

Horizon	Depth	RF	Sand	Silt	Clay	Texture	Color	Structure
	cm			%				
Ridgetop								
Oi	+12	---	---	---	---	---	---	---
Ap	8	5	73	15	12	sandy loam	10YR 3/2	mod gr
EB	13	12	48	28	24	sandy loam	7.5YR 4/2	mod sbk
Bw	22	23	49	31	20	channery loam	10YR 4/4	mod sbk
CB	35	37	58	20	15	very channery sandy Loam	7.5YR 4/4	weak sbk
R	35+	---	---	---	---	---	---	---
Midslope								
Oi	+10	---	---	---	---	---	---	---
Ap	6	4	58	20	22	sandy clay loam	10YR 3/2	mod gr
Bw1	22	11	42	28	30	clay loam	7.5YR 3/4	mod sbk
Bw2	40	20	39	33	28	channery clay loam	7.5YR 4/6	mod sbk
BC	52	40	37	30	32	very channery sandy loam	10YR 4/6	weak sbk
Cr	52+	---	---	---	---	---	---	---
Footslope								
Oi	+7	---	---	---	---	---	---	---
Ap	5	---	66	17	17	sandy loam	7.5YR 2.5/1	weak gr
BE	24	10	46	26	28	sandy clay loam	7.5YR 3/4	mod sbk
Bw	49	31	56	20	24	channery sandy clay loam	7.5YR 4/6	mod sbk
CB	68	40	35	35	30	very channery clay loam	7.5YR 4/6	weak sbk
R	68+	---	---	---	---	---	---	---

Table D-3. Depth (d), bulk density (ρ_w), strain (ε), and elemental chemistry for ridgetop, midslope and footslope soils and average rock values at Plynlimon.

Position	Sample	IGSN[a]	d	ρ_w[b]	ε	Na	Mg	K	Ca	Al	Fe	Si	Ti	Zr	pH
			cm	g cm^{-3}					%					ppm	
Ridgetop	PLYNQ0-10	SSH0000HD	0 – 10	0.88	2.13	0.47	0.43	2.37	0.02	8.89	6.27	23.0	0.56	166	2.69
	PLYNQ10-20	SSH0000HE	10 – 20	1.10	1.47	0.50	0.80	2.67	0.02	10.5	7.13	23.7	0.56	168	3.36
	PLYNQ20-30	SSH0000HF	20 – 30	1.24	1.14	0.53	1.06	2.81	0.02	11.0	7.83	24.6	0.55	172	3.39
	PLYNQ30-31	SSH0000HG	30 – 31	1.27	1.12	0.56	1.07	2.82	0.03	11.0	7.97	24.6	0.53	170	---
	PLYNQ31-35	SSH0000HH	31 - 35	1.28	1.26	0.56	1.31	3.06	0.03	11.8	7.34	25.1	0.55	158	3.24
Midslope	PLYNBSF0-10	SSH0000HR	0 – 10	0.88	1.73	0.50	0.27	2.25	0.01	8.63	4.64	21.9	0.59	190	2.90
	PLYNBSF10-20	SSH0000HS	10 – 20	1.10	1.03	0.57	0.82	2.86	BDL[d]	11.0	6.29	23.9	0.65	205	3.21
	PLYNBSF20-24	SSH0000HT	20 – 24	1.16	0.88	0.64	1.03	2.92	BDL	11.4	6.57	24.6	0.66	210	3.32
	PLYNBSF24-30	SSH0000HU	24 – 30	1.24	0.76	0.68	1.18	2.88	0.01	11.3	6.52	25.1	0.61	210	3.13
	PLYNBSF30-35	SSH0000HV	30 – 35	1.28	0.70	0.69	1.17	2.75	0.01	10.8	6.40	25.3	0.59	210	3.36
	ALD-10-25	SSH0000JP	40 – 52	1.40	0.71	0.76	1.45	2.79	0.05	11.9	6.93	25.7	0.63	191	3.25
Footslope	PLYNFSOC0-10	SSH0000IB	0 – 10	0.88	1.89	0.53	0.56	2.57	0.01	9.85	5.53	23.0	0.58	180	3.14
	PLYNFSOC10-25	SSH0000IC	10 – 25	1.18	1.04	0.59	0.62	2.95	BDL	11.3	5.92	24.4	0.61	190	3.22
	PLYNFSOC25-30	SSH0000ID	25 – 30	1.24	0.99	0.59	0.61	2.96	BDL	11.0	5.72	24.3	0.61	185	3.25
	PLYNFSOC30-40	SSH0000IE	30 – 40	1.32	0.92	0.64	0.87	3.08	BDL	12.0	6.34	24.4	0.59	180	3.15
	PLYNFSOC40-45	SSH0000IF	40 – 45	1.36	0.82	0.79	0.86	3.55	BDL	12.4	4.52	25.7	0.62	185	3.28
	ALD-10-32	SSH0000JW	49 - 68	1.46	0.91	0.62	0.94	2.86	BDL	11.5	5.92	24.6	0.60	164	3.51
Rock[c]	---	---	---	2.70	---	0.65	1.43	2.90	0.03	11.7	6.44	25.1	0.84	176	---
std dev.	---	---	---	---	---	0.01	0.11	0.13	0.02	0.31	0.31	1.0	0.06	24.1	---

[a] International Geosample Number (www.sesar.org).

[b] Bulk density calculated using Eq. 2 in Dere et al., 2013.

[c] Average of 10 rock samples collected near the soil transect. Rock chemistry and sampling locations are listed in Dere et al., 2013.

[d] Below detection limit

Table D-4. $\tau_{Zr,j}$ values for ridgetop, midslope and footslope soils at Plynlimon.

Position	Sample	IGSN[a]	d	$\tau_{Zr,j}$							
				Na	Mg	K	Ca	Al	Fe	Si	Ti
			cm								
Ridgetop	PLYNQ0-10	SSH0000HD	0 – 10	-0.24	-0.68	-0.14	-0.31	-0.19	0.03	-0.03	-0.29
	PLYNQ10-20	SSH0000HE	10 – 20	-0.20	-0.41	-0.04	-0.32	-0.06	0.16	-0.01	-0.30
	PLYNQ20-30	SSH0000HF	20 – 30	-0.16	-0.24	-0.01	-0.34	-0.03	0.24	0.00	-0.33
	PLYNQ30-31	SSH0000HG	30 – 31	-0.12	-0.22	0.01	-0.10	-0.02	0.28	0.02	-0.34
	PLYNQ31-35	SSH0000HH	31 - 35	-0.05	0.02	0.17	-0.04	0.12	0.27	0.11	-0.27
Midslope	PLYNBSF0-10	SSH0000HR	0 – 10	-0.29	-0.82	-0.28	---	-0.31	-0.33	-0.19	-0.35
	PLYNBSF10-20	SSH0000HS	10 – 20	-0.25	-0.51	-0.16	---	-0.19	-0.16	-0.18	-0.34
	PLYNBSF20-24	SSH0000HT	20 – 24	-0.18	-0.40	-0.16	---	-0.18	-0.15	-0.18	-0.34
	PLYNBSF24-30	SSH0000HU	24 – 30	-0.12	-0.31	-0.17	---	-0.19	-0.15	-0.16	-0.39
	PLYNBSF30-35	SSH0000HV	30 – 35	-0.12	-0.31	-0.21	---	-0.23	-0.17	-0.16	-0.41
	ALD-10-25	SSH0000JP	40 – 52	0.07	-0.06	-0.11	---	-0.05	-0.01	-0.05	-0.31
Footslope	PLYNFSOC0-10	SSH0000IB	0 – 10	-0.20	-0.62	-0.14	---	-0.17	-0.16	-0.10	-0.33
	PLYNFSOC10-25	SSH0000IC	10 – 25	-0.16	-0.60	-0.06	---	-0.10	-0.15	-0.10	-0.33
	PLYNFSOC25-30	SSH0000ID	25 – 30	-0.14	-0.59	-0.03	---	-0.10	-0.16	-0.08	-0.31
	PLYNFSOC30-40	SSH0000IE	30 – 40	-0.05	-0.40	0.04	---	-0.03	-0.04	-0.05	-0.31
	PLYNFSOC40-45	SSH0000IF	40 – 45	0.16	-0.43	0.16	---	0.01	-0.33	-0.03	-0.30
	ALD-10-32	SSH0000JW	49 - 68	0.02	-0.30	0.06	---	0.06	-0.02	0.05	-0.24

[a] International Geosample Number (www.sesar.org).

Table D-5. Ridgetop soil and bedrock mineralogy calculated using quantitative XRD using RockJock. 'Chlorite' refers to a mixture of true chlorite, vermiculite and hydroxy-interlayered vermiculite.

Sample	Depth	IGSN[a]	Quartz	Illite	'Chlorite'	K Feldspar	Plagioclase	Fe oxides	Kaolinite	Degree of fit[b]
	cm					%				
PLYNQ0-10	0 – 10	SSH0000HD	30.6	35.5	15.6	5.8	3.4	3	6.1	0.1309
PLYNQ20-30	20 – 30	SSH0000HF	31.9	32.8	26.2	3.1	3.3	1.7	1.0	0.1639
PLYNQ31-35	31 – 35	SSH0000HH	31.1	38.1	24.5	1.2	4.4	0.8	0.0	0.1582
PlynQ-RF	Rock	SSH000GG	30.3	38.5	25.3	1.1	4.1	0.7	0.0	0.1816

[a] International Geo Sample Number, www.geosamples.org
[b] Full pattern degree of fit between the calculated and measured pattern in RockJock (lower is better)

Table D-6. Average annual precipitation elemental concentrations, pH and rainfall for the Hore and Hafren catchments.

Year	Na	K	Ca	Mg	Fe	Al	Si	pH	Precipitation Hore	Hafren
			—— mg l^{-1} ——		—— µg l^{-1} ——		mg l^{-1}		—— mm ——	
1984	2.44	0.140	0.200	0.311	13.9	10.3	0.110	4.82	2212	2174
1985	1.36	0.129	0.138	0.179	7.86	13.7	0.138	5.01	2423	2406
1986	2.47	0.118	0.152	0.312	6.13	8.00	0.0665	5.04	2776	2767
1987	1.90	0.091	0.155	0.237	6.47	8.43	0.0437	4.89	2330	2321
1988	2.81	0.126	0.192	0.349	5.80	7.89	0.0435	5.13	2628	2599
1989	2.37	0.108	0.191	0.292	5.22	6.57	0.0250	5.02	2545	2500
1990	3.69	0.154	0.205	0.451	4.30	5.41	0.0113	4.94	2907	2859
1991	3.29	0.141	0.224	0.399	5.69	6.88	0	4.96	2290	2227
1992	1.59	0.104	0.214	0.193	5.64	8.33	0	5.00	2709	2712
1993	2.22	0.109	0.332	0.252	5.43	7.11	0	4.91	2569	2452
1994	1.95	0.082	0.285	0.215	4.04	3.82	0	4.91	3230	3257
1995	2.39	0.119	0.189	0.289	5.82	4.86	0.0664	5.10	2193	2215
1996	1.77	0.108	0.245	0.215	7.61	7.20	0.0119	4.97	2213	2168
1997	1.64	0.087	0.246	0.199	5.64	4.34	0.0146	4.98	2300	2295
1998	2.85	0.126	0.213	0.345	6.26	5.46	0	5.12	3483	3460
1999	2.09	0.097	0.297	0.273	8.54	34.6	0.00683	5.00	3196	3199
2000	2.51	0.135	0.454	0.343	9.30	50.1	0	5.21	3496	3498
2001	1.56	0.074	0.567	0.209	20.5	107	0	5.15	2418	2414
2002	3.45	0.166	0.204	0.437	14.1	49.5	0.00346	4.95	2731	2787
2003	1.70	0.099	0.175	0.218	8.55	36.3	0.00113	4.17	2130	2112
2004	1.91	0.099	0.177	0.249	7.63	18.7	0.00812	4.99	2867	2820
2005	1.56	0.081	0.155	0.201	9.47	16.2	0.0097	5.06	2389	2369
2006	2.34	0.115	0.184	0.292	10.2	19.6	0.0323	4.85	2533	2529
2007	2.17	0.115	0.142	0.267	7.19	14.1	0.00766	4.93	2717	2685
2008	1.99	0.096	0.155	0.243	5.68	5.06	0.0239	5.05	3186	3146
2009	2.30	0.106	0.140	0.276	4.72	5.20	0.0087	5.02	2366	2433
Average	2.24	0.112	0.224	0.279	7.76	17.9	0.0243	4.97	2648	2631
Standard error	0.117	0.00447	0.0194	0.0145	0.715	4.44	0.00695	0.0367	78.2	79.1

Table D-7. Average annual stream elemental concentrations for the Lower Hore catchment.

Year	Na	K	Ca	Mg	Fe	Al	Si	pH	Runoff
			mg l⁻¹			μg l⁻¹	mg l⁻¹		mm yr⁻¹
1984	4.51	0.182	1.45	0.896	72.1	316	1.58	5.13	1529
1985	3.85	0.176	1.25	0.835	79.3	341	1.30	5.31	1900
1986	3.58	0.309	0.978	0.714	113	502	1.06	4.80	2209
1987	3.92	0.360	1.22	0.856	91.1	413	1.17	5.05	1946
1988	4.22	0.298	1.15	0.848	74.1	406	1.06	5.02	2171
1989	3.94	0.267	1.20	0.799	78.5	321	1.23	5.22	1943
1990	5.11	0.259	1.18	0.911	71.0	471	1.09	4.98	2083
1991	4.42	0.203	1.32	0.819	63.8	283	1.31	5.36	1960
1992	3.93	0.168	1.07	0.734	78.6	306	1.20	5.16	2091
1993	3.29	0.262	0.905	0.599	126	322	0.892	4.92	2106
1994	3.64	0.176	0.893	0.621	92.3	250	0.935	4.97	2681
1995	4.05	0.175	1.07	0.705	79.5	264	1.18	5.21	1613
1996	3.96	0.151	1.20	0.783	74.6	287	1.29	5.29	1614
1997	3.96	0.227	1.19	0.774	98.4	249	1.26	5.26	1646
1998	4.89	0.216	1.02	0.843	131	385	1.07	5.01	2762
1999	3.89	0.155	0.89	0.624	93.0	328	0.992	5.10	2355
2000	3.77	0.134	0.87	0.604	117	370	1.01	5.17	2859
2001	4.10	0.174	1.37	0.783	155	295	1.19	5.62	1949
2002	4.86	0.192	1.24	0.866	121	395	1.28	5.19	2334
2003	5.06	0.191	1.36	0.863	105	368	1.34	5.22	1560
2004	4.24	0.146	1.00	0.700	134	313	1.15	5.07	2171
2005	3.86	0.197	0.972	0.631	159	302	1.11	5.22	1729
2006	3.93	0.317	1.03	0.792	185	260	1.14	5.25	2039
2007	4.38	0.437	1.01	0.757	145	264	0.897	4.87	2142
2008	4.00	0.397	0.944	0.726	147	281	1.24	5.04	2648
2009	3.75	0.356	1.06	0.752	158	256	1.28	5.22	2008
Average	4.12	0.236	1.11	0.763	109	329	1.16	5.14	2079
Standard error	0.0895	0.0164	0.0319	0.0182	6.69	13.3	0.0303	0.0335	71.9

Table D-8. Average annual stream elemental concentrations for the Lower Hafren catchment.

Year	Na	K	Ca	Mg	Fe	Al	Si	pH	Runoff
	———————— mg l⁻¹ ————————				—— μg l⁻¹ ——		mg l⁻¹		mm yr⁻¹
1984	4.38	0.229	1.03	0.923	96.8	338	1.60	4.86	1659
1985	3.54	0.184	0.787	0.752	104	335	1.40	4.92	1987
1986	3.27	0.202	0.653	0.651	100	369	1.04	4.70	2217
1987	3.85	0.182	0.798	0.759	103	341	1.22	4.84	1881
1988	4.16	0.172	0.755	0.761	96.4	344	1.22	4.78	2101
1989	3.96	0.181	0.755	0.716	98.6	243	1.42	4.95	1853
1990	4.41	0.191	0.675	0.704	91.6	359	1.05	4.65	2069
1991	4.48	0.144	0.776	0.740	93.3	284	1.41	4.96	1910
1992	3.95	0.143	0.701	0.677	101	283	1.28	4.90	2083
1993	3.58	0.228	0.681	0.614	151	320	1.02	4.75	1989
1994	3.81	0.195	0.648	0.616	116	203	1.06	4.83	2590
1995	3.97	0.239	0.753	0.704	131	268	1.34	4.99	1643
1996	3.94	0.192	0.787	0.758	112	279	1.33	4.96	1651
1997	3.93	0.248	0.782	0.764	124	269	1.31	4.92	1668
1998	4.58	0.255	0.743	0.796	144	328	1.06	4.77	2713
1999	3.80	0.199	0.602	0.608	111	287	1.10	4.93	2378
2000	3.77	0.229	0.622	0.627	139	280	1.07	4.95	2867
2001	3.93	0.204	0.755	0.738	154	292	1.33	5.20	1968
2002	4.61	0.271	0.825	0.850	130	381	1.30	4.90	2327
2003	4.73	0.264	0.882	0.849	144	347	1.37	5.00	1554
2004	3.92	0.206	0.704	0.698	167	319	1.21	4.90	2213
2005	4.05	0.204	0.749	0.742	162	232	1.44	5.18	1882
2006	3.80	0.218	0.696	0.709	138	208	1.26	5.07	2216
2007	4.22	0.184	0.670	0.713	133	219	0.94	4.79	2205
2008	3.99	0.153	0.629	0.667	163	226	1.31	4.95	2709
2009	3.95	0.181	0.653	0.690	144	186	1.37	5.19	2089
Average	4.02	0.204	0.735	0.724	125	290	1.25	4.92	2093
Standard error	0.0678	0.00674	0.0181	0.0149	4.75	10.9	0.0318	0.0274	68.8

VITA

Ashlee Laura Denton Dere

EDUCATION
Ph.D., Geosciences, The Pennsylvania State University (2014)
  Dissertation: *Rates and mechanisms of shale weathering across a latitudinal climosequence*
M.S., Soil Sciences, The Pennsylvania State University (2009)
  Thesis: *Carbon and nitrogen dynamics in coal mine soils reclaimed with poultry manure*
French Language Certificate, Université Paul Cézanne Aix-Marseille III, Aix-en Provence, France (2006)
B.S., Earth Sciences (*summa cum laude*), California Polytechnic State University, San Luis Obispo (2005)
  Senior thesis: *Evidence for ancient shorelines in Montaña de Oro State Park, San Luis Obispo, CA*

PUBLICATIONS
Dere, A. L., White T. S.… and Brantley S. L. (2013) Climate dependence of feldspar weathering along a latitudinal gradient. *Geochim. Cosmochim. Acta.* 122:101-126.
Dere, A., Stehouwer R. … and McDonald K. (2012) Nutrient leaching and soil retention in mined land reclaimed with stabilized manure. J. Environ. Qual. 41:2001-2008.
Dere, A. and R. Stehouwer. (2011) Labile and stable nitrogen and carbon in mine soil reclaimed with manure-based amendments. Soil Sci. Soc. Am. J. 75:890-897.
Dere, A., R. Stehouwer, K. McDonald (2011) Nutrient leaching and switchgrass growth in mine soil columns amended with poultry manure. Soil Science. 176: 84-90.

FELLOWSHIPS
NSF GK-12 CarbonEARTH Fellow, PSU; 2012-2014
Chesapeake Energy Scholarship in Geosciences; 2013
Hiroshi and Koya Ohmoto Graduate Fellowship in Geosciences, PSU; 2010
Charles E. Knopf, Sr. Memorial Scholarship; PSU; 2009

AWARDS
22nd V.M. Goldschmidt Conference Outstanding Oral Presentation, Montreal, Canada; 2012
Geosciences Graduate Student Colloquium, Penn State University
        2nd place Oral Presentation by a Pre-comps student; 2010
        1st place Oral Presentation by a Pre-comps student; 2011
        1st place Oral Presentation by a Post-comps student-Peter Deines Memorial Lecture; 2014

SERVICE
Co-Chair, Geosciences Colloquium Committee; 2011-12
Advisor, Club Cross Country and Club Track and Field; 2011-2014

TEACHING EXPERIENCE
Instructor: 4th grade science at Philipsburg Elementary School; 2012-2014
Teaching Assistant: Introductory Physical Geology Laboratory, PSU; 2011-2012